Proton-Lambda Final State Interaction and Polarization Observables Measured in the $\vec{p}p \to pK\Lambda$ Reaction at $2.7\,\mathrm{GeV}/c$ Beam Momentum

Der Naturwissenschaftlichen Fakultät
der Friedrich-Alexander-Universität
Erlangen-Nürnberg

zur

Erlangung des Doktorgrades Dr. rer. nat.

vorgelegt von
Florian Hauenstein
aus Nürnberg

Als Dissertation genehmigt
von der Naturwissenschaftlichen Fakultät
der Friedrich-Alexander-Universität Erlangen-Nürnberg

Tag der mündlichen Prüfung: 20.11.14	
Vorsitzender des Promotionsorgans:	Prof. Dr. Jörn Wilms
Gutachter:	Prof. Dr. Wolfgang Eyrich
	Prof. Dr. Erhard Steffens

Abstract

In this thesis the analysis of a measurement of the $\vec{p}p \to pK^+\Lambda$ reaction with the COSY-TOF detector at the research facility Jülich is presented. In the measurement a polarized proton beam of $2.7\,\mathrm{GeV}/c$ momentum from the proton accelerator COSY is used to study features of the associated strangeness production close to the reaction threshold. The main goal of the presented analysis is the determination of the spin triplet $p\Lambda$ scattering length from the data with a new theoretical method based on a dispersion integral approach. The scattering length is an important parameter for the study of the hyperon-nucleon interactions, which suffer yet from the scarce data. In the determination procedure a decisive role is played by the kaon analyzing power, which can be measured due to the use of a polarized beam. The results for the other polarization observables e.g. Λ polarization and Λ analyzing power and unpolarized observables, such as the Dalitz plot and the angular distributions, are also shown in the thesis. The polarization observables, which are more sensitive to the properties of the associated strangeness production than the unpolarized observables, are studied in detail in this thesis, and they are analyzed using associated Legendre polynomials.

A data sample with high statistics and low background is obtained by a modification of the read out process of the detector components and the high-resolution and precise straw tube tracker (STT), which is the main sub detector in the upgraded COSY-TOF. The final $pK\Lambda$ data sample consists of 207,219 kinematically fitted events, extracted by optimized selection criteria. From Monte Carlo simulations it is obtained that the contribution of the most prominent background channel $\vec{p}p \to pK^+\Sigma^0$ in the data sample is only $(0.73 \pm 0.11)\,\%$. The beam polarization is determined by pp elastic scattered events to be $(79.0 \pm 1.1)\,\%$.

The obtained result for the Λ polarization is surprising. The Λ polarization as a function of $\cos(\theta_\Lambda^{\mathrm{CMS}})$ is opposite to the result from a previous COSY-TOF measurement at $2.95\,\mathrm{GeV}/c$ beam momentum. The detailed study of the polarization results from all available COSY-TOF data shows that the contribution of the P_2^1 associated Legendre polynomial to the Λ polarization changes smoothly from -0.030 to 0.188 with increasing beam momentum.

For the determination of the spin triplet $p\Lambda$ scattering length, the kaon analyzing power is analyzed in terms of associated Legendre polynomials and $p\Lambda$ invariant mass constraints in order to get the contribution of the symmetric P_1^1 polynomial as a function of the invariant mass. This contribution show nonzero values for low invariant masses (opposite to the previous measurement at $2.95\,\mathrm{GeV}/c$), and therefore the spin triplet

$p\Lambda$ scattering length could be extracted within this thesis. The obtained result is $a_{\mathrm{t}} = (-1.31^{+0.32}_{-0.49}{}_{\mathrm{stat.}} \pm 0.3_{\mathrm{theo.}} \pm 0.16_{\mathrm{syst.}})$ fm, which is compatible with recent theoretical predictions. In addition, an effective scattering length of $\tilde{a} = (-1.233 \pm 0.014_{\mathrm{stat.}} \pm 0.3_{\mathrm{theo.}} \pm 0.12_{\mathrm{syst.}})$ fm is obtained, which is also used to study systematic errors and the influence of N^* resonances on the extracted scattering lengths.

Zusammenfassung

In dieser Arbeit werden Analyse und Ergebnisse einer Messung der $\vec{p}p \to pK^+\Lambda$ Reaktion mit dem COSY-TOF Detektor am Forschungszentrum Jülich präsentiert. Die Messung zur Untersuchung von Eigenschaften der assoziierten Strangenessproduktion nahe der Reaktionsschwelle erfolgte mit einem polarisierten Protonstrahl des Beschleunigers COSY bei einem Strahlimpuls von $2,7\,\mathrm{GeV}/c$. Das wichtigste Ziel dieser Arbeit ist die Bestimmung der spin triplet $p\Lambda$-Streulänge unter Verwendung eines neuen theoretischen Verfahrens, welches auf einem Dispersionsintegralansatz basiert. Die Streulänge ist ein wichtiger Parameter für Untersuchungen der Hyperon-Nukleon Wechselwirkungen, wofür noch immer keine ausreichende Menge an Daten zur Verfügung stehen. Für die Bestimmung der spin triplet Streulänge ist die Kaonanalysierstärke entscheidend, welche mit Hilfe des polarisierten Strahls gemessen werden kann. Die Ergebnisse für die anderen Polarisationsgrößen, wie z.B. die Λ-Polarisation oder die Λ-Analysierstärke, und unpolarisierte Messgrößen, wie der Dalitz plot oder die Winkelverteilungen, werden ebenfalls in dieser Arbeit gezeigt. Die Polarisationsgrößen sind sensitiver auf Eigenschaften der assoziierten Strangenessproduktion als die unpolarisierten Messgrößen und werden deshalb in dieser Arbeit im Detail untersucht, indem assozierte Legendre Polynome an die Ergebnisse gefittet werden.

Das Datensample für die weitere Analyse besitzt eine hohe statistische Genauigkeit und einen geringen Anteil an Untergrundreaktionen, welche durch eine Modifikation des Datenauslesesystems und dem hochauflösenden und präzisen Straw-Tube-Tracker, der im COSY-TOF Detektor eine zentrale Rolle spielt, erreicht werden. Letztlich beinhaltet das Datensample 207.219 kinematisch gefittete $pK\Lambda$ Ereignisse, die durch optimierte Schnitte bestimmt wurden. Der Anteil der wichtigsten Untergrundreaktion, $\vec{p}p \to pK^+\Sigma^0$, wurde mittels Monte Carlo Simulationen bestimmt und beträgt nur $(0.73 \pm 0.11)\,\%$. Die Strahlpolarisation ist mit Hilfe von pp elastisch gestreuten Ereignissen bestimmt worden und beträgt $(79.0 \pm 1.1)\,\%$.

Das Ergebnis für die Λ-Polarisation ist überraschend. Im Vergleich zu einer früheren COSY-TOF Messung bei einem Strahlimpuls von $2,95\,\mathrm{GeV}/c$ ist das Verhalten der Polarisation als Funktion von $\cos(\theta_\Lambda^{\mathrm{CMS}})$ genau umgekehrt. Die detaillierte Untersuchung aller Ergebnisse zur Λ-Polarization von früheren COSY-TOF Messungen ergibt eine kontinuierliche Änderung des Beitrags des Polynoms P_2^1 zur Λ-Polarisation von -0.030 zu 0.188 bei Erhöhung des Strahlimpulses.

Ebenfalls wurde die Kaonanalysierstärke in Abhängigkeit der $p\Lambda$ invarianten Masse mittels assozierter Legendre Polynome gefittet. Dadurch erhält man den Beitrag des symmetrischen Polynoms P_1^1 zur Analysierstärke als Funktion der invarianten Masse für die Bestimmung der spin triplet $p\Lambda$-Streulänge. Im Vergleich zu einer früheren Messung bei $2,95\,\mathrm{GeV}/c$ ist dieser Beitrag für geringe Werte der invarianten Masse ungleich Null. Damit ist eine Bestimmung der spin triplet $p\Lambda$-Streulänge in dieser Arbeit möglich. Das Ergebnis ist $a_{\mathrm{t}} = (-1.31^{+0.32}_{-0.49}{}_{\mathrm{stat.}} \pm 0.3_{\mathrm{theo.}} \pm 0.16_{\mathrm{syst.}})\,\mathrm{fm}$. Dieses Ergebnis ist verträglich mit neueren theoretischen Vorhersagen. Die effektive $p\Lambda$-Streulänge $\tilde{a} = (-1.233 \pm 0.014_{\mathrm{stat.}} \pm 0.3_{\mathrm{theo.}} \pm 0.12_{\mathrm{syst.}})\,\mathrm{fm}$ wurde ebenfalls bestimmt und für die Untersuchung von systematischen Fehlern und den Einflüßen von N^* Resonanzen auf den Wert der extrahierten Streulänge herangezogen.

Contents

1. Introduction

The COSY-TOF experiment at the COSY accelerator facility at the research center Jülich is mainly dedicated to the measurement of strangeness production in proton-proton or deuteron-proton interactions close to the reaction threshold for NKY final states covering the full phase space of the reaction products. The detector was updated with the straw tube tracker, which improves the reconstruction efficiency and mass resolution significantly in comparison to the former setup as it was shown first in [Roe11]. These improvements are the basis of the proposed physics program for the associated strangeness production close to threshold with a polarized proton beam [CTOF07]. One part of this program is the study of the production mechanism and the influence of N^* resonances. The other goal is the measurement of the $p\Lambda$ spin resolved scattering length, which is an important parameter of the hyperon-nucleon interaction. This can be investigated by measuring the final state interaction in the reaction $\vec{p}p \to pK^+\Lambda$ and polarization observables like the analyzing power using the polarized proton beam.

This thesis presents the analysis of the reaction $\vec{p}p \to pK^+\Lambda$ measured in 2011 with a polarized proton beam at $2.7\,\mathrm{GeV}/c$ beam momentum. This measurement is the first one at COSY-TOF using a polarized proton beam with about 200,000 analyzed $pK\Lambda$ events, which is so far the largest data sample for this momentum. The high amount of collected data allows to extract the $p\Lambda$ spin triplet scattering length for the first time. Additionally, a high-resolution Dalitz plot, as well as angular and mass distributions, have been obtained. The polarization observables, and especially the Λ polarization, could be investigated in more detail compared to former COSY-TOF measurements.

The theoretical background is described in Chapter 2, including details about theoretical models, the Λ polarization and the hyperon-nucleon interaction. The detector and its components are shown in Chapter 3, paying special emphasis on the straw tube tracker and the modified experimental trigger.

Chapter 4 illustrates in the first part the reconstruction algorithm for the $pp \to pK^+\Lambda$ events, with the various steps from track finding up to the kinematic fit. The other part of the chapter focuses on the calibration of the straw tube tracker and the achieved spatial resolutions in the experiment.

Properties of the beam and the target size are derived from $\vec{p}p \to pp$ elastic events. Especially, the beam polarization is determined by these events. This is shown in Chapter 5 together with the elastic event selection.

In Chapter 6 the selection criteria for $\vec{p}p \to pK^+\Lambda$ events are described, together with the obtained data quality and statistics. The reconstruction efficiency and acceptance correction, as well as the resolution determined by Monte Carlo studies, are shown. Furthermore, the relative background contamination of the reaction $pp \rightarrow pK^+\Sigma^0$ is given.

The results for the various observables are shown in Chapter 7. This includes the Dalitz plot and invariant mass spectra, the angular distributions in various rest frames and the polarization observables. Special emphasis is given to the kaon analyzing power, since it is important for the determination of the $p\Lambda$ spin triplet scattering length. The results for the effective and the spin triplet scattering lengths, as well as the determination method, are shown in Chapter 8.

Chapter 9 gives a comparison of the results with measurements at other beam momenta and a discussion of the similarities and differences. Especially the striking differences of the Λ polarization from the measurements at different beam momenta are investigated in detail.

Finally, a summary and outlook is given in Chapter 10.

> Your theory is crazy, but it's not crazy enough to be true.
>
> *(Niels Bohr)*

2. Theoretical Background

2.1. Standard Model and SU(3) Symmetry

The "Standard Model of Particle Physics" is the actual theory of the constituents of matter and their interaction neglecting gravity. It is a relativistic quantum field theory with gauge invariance of different symmetry groups. It describes the electromagnetic, weak and strong interaction as an exchange of corresponding gauge bosons (photons, W- and Z-Bosons and gluons). The basic particles are six different quarks (up, down, strange, charm, top and bottom) and six leptons (electron, muon and tau and the corresponding neutrinos) grouped in three families. In addition, each of these particles has a corresponding anti particle with the opposite sign for all charge like quantum numbers and opposite intrinsic parity. In Figure 2.1 the particles and gauge bosons of the Standard model are shown with their mass, charge and spin. The electromagnetic and weak force interacts with all of these particles, while the strong force affects only the quarks. From an interaction with the recently observed Higgs-Boson [ATLAS12, CMS12] the particles acquire their masses.

The quarks carry color charge and can apparently not exist as free particles in nature (confinement of the strong interaction), so they are bound to colorless systems called hadrons. The easiest ways to achieve color neutralness are: Combining a quark and antiquark or three quarks together. The first kind of hadrons are called **mesons** and the second one **baryons**. In addition, there are theories which predict other systems with four or more quarks, but none of them has been observed in experiments without any doubts. The quarks which define the hadrons are named 'valence quarks'. From scattering experiments it was found that the hadrons are not only consisting of these valence quarks, but also of gluons and 'sea quarks' (virtual quark-antiquark pairs from the vacuum). This sea of quarks and gluons can be assigned to the valence quarks, which gain in this way an effective mass (constituent mass), and thus they are called constituent quarks. The theory of the strong interaction is called quantum chromodynamics (QCD).

The hadrons consisting of the three lightest quarks (up, down, strange) obey an additional SU(3) flavor symmetry. The quantum numbers for this symmetry are strangeness S[1], isospin I and the third component of the isospin I_3[2]. The ground state baryons

---

[1] Hadrons with a strange quark have $S = -1$ while hadrons with an antistrange quark have $S = 1$

[2] Only the up and down quark have isospin $I = 1/2$ while all other quarks have $I = 0$. The third component is $I_3 = +1/2$ for the up quarks and $I_3 = -1/2$ for the down quarks.

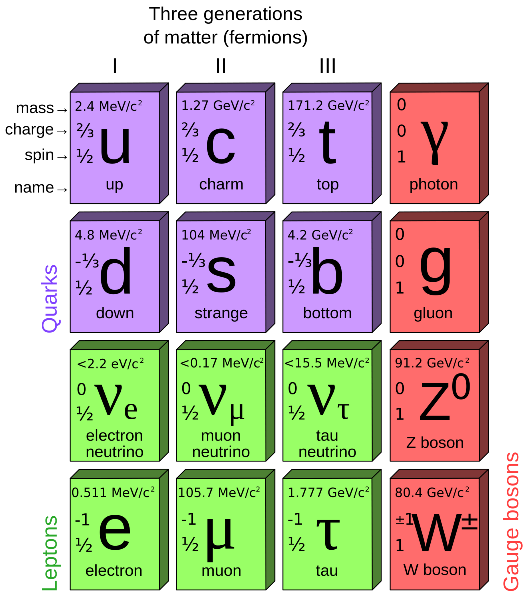

Figure 2.1.: Elementary particles and gauge bosons of the Standard Model together with their mass, charge and spin. The quarks are in shown purple, the leptons in green and the gauge bosons in red. Picture taken from [Wiki13].

from this symmetry can be grouped into an octet with spin and parity $J^P = \frac{1}{2}^+$ (Fig. 2.2 left), and the ground state mesons form a nonet with $J^P = 0^-$ (Fig. 2.2 right). Due to the mass differences of the hadrons the SU(3) is not a perfect symmetry, and it is broken in nature.

All baryons with at least one strange quark are called **hyperons**. Since the strong interaction conserves strangeness, the production of hyperons via the strong interaction requires an additional particle with an anti-strange quark (anti-hyperon or meson). This mechanism is called ”associated strangeness production”. In contrast to the fast production of hyperons ($\approx 10^{-23}$ s) in nucleon-nucleon interactions, they decay mostly via the weak interaction. Therefore, they have a quite long lifetime, and their decay vertex is separated from the production point in the order of centimeters. This gives a clear signature of the reaction in a particle detector like the COSY-TOF detector. Additionally, the weak decay of the hyperons breaks parity conservation. This can be used to determine their polarization (see Section 2.3).

A calculation of the hyperon production with perturbative QCD is not possible for the energy regime presented in this thesis. The coupling constant of the strong interaction is in the order of one, and thus the hadronic degrees of freedom become more relevant than the quark-gluon degrees of freedom. The appropriate theoretical models are described in the next section.

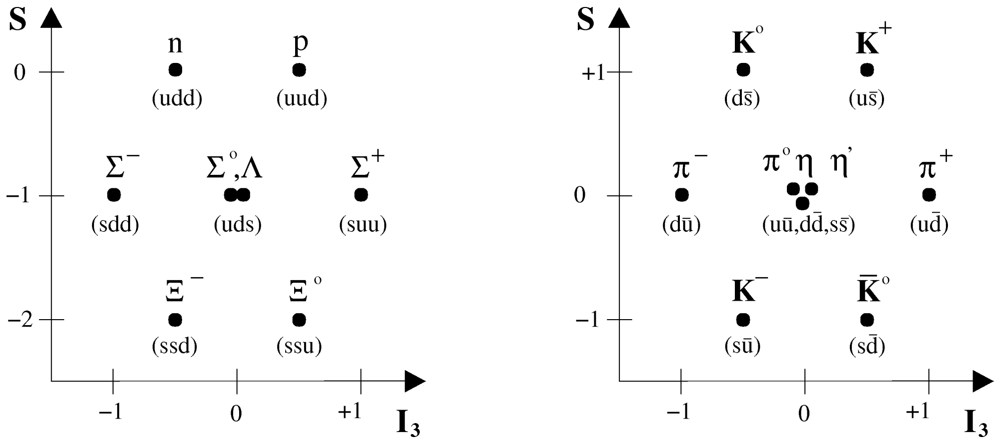

Figure 2.2.: Illustration of the ground state SU(3) symmetry ensembles for baryons and mesons sorted according to strangeness S and the isospin component I_3. Left: Baryon octet ($J^P = \frac{1}{2}^+$). Right: Meson nonet ($J^P = 0^-$) [Fri02].

2.2. Associated Strangeness Production: Theoretical Models and Data

The mechanism of associated strangeness production is mostly described by theoretical models using meson exchange diagrams. These can be split into two groups: One group of the models use a simple pion and/or kaon type exchange, and the other group takes explicitly resonance contributions into account. Nevertheless, there exist some quark models, which use the quark-gluon degrees of freedom in a phenomenological approach.

Since the results of a measurement of the reaction $pp \to pK\Lambda$ are shown in this thesis, the theoretical predictions presented here focus on this channel. However, most of the models consider the general reaction $pp \to NKY$. For further details of the commonly used models see also [Fri02, Schr03, Piz07].

2.2.1. Meson Exchange Models

In the meson exchange model the simplest processes are t-channel pion or kaon exchange. Their diagrams are shown in Figure 2.3. For both cases the total cross section of the reaction can be calculated by integrating the differential cross section over the available phase space [Sib98b, Sib98c],

$$\sigma = \int \mathrm{d}t\mathrm{d}s_1 \frac{\mathrm{d}^2\sigma}{\mathrm{d}t\mathrm{d}s_1} = \frac{1}{2^9\pi^3 q^2 s} \int \mathrm{d}t\mathrm{d}s_1 \frac{q_K}{\sqrt{s_1}} \left|M(t,s_1)\right|^2 . \tag{2.1}$$

Here, s is the square of the CMS energy, q is the incident proton momentum in the CMS, t is the squared four-momentum transfer carried by the exchanged meson, s_1 is

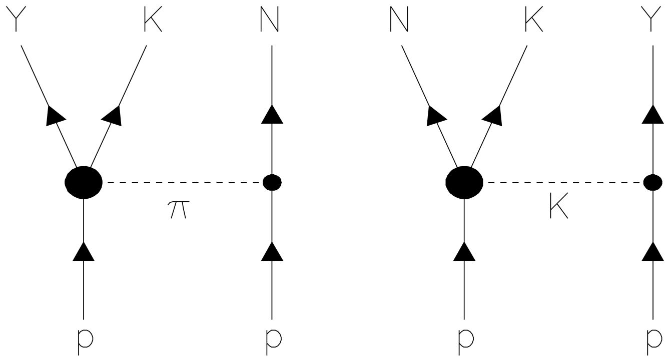

Figure 2.3.: Diagrams for pion exchange (left) and kaon exchange (right) for meson exchange models [Sib00].

the squared invariant mass of the $K\Lambda$ system for pion exchange or the Kp system for kaon exchange. q_K is the kaon momentum in the corresponding mass frame ($K\Lambda$ or Kp). $M(t, s_1)$ is the amplitude of the reaction.

The amplitude $M(t, s_1)$ is in general given for the meson X by

$$|M(t,s_1)|^2 = g^2_{pX1} F^2(t) t D^2(t) \left|A_{pX\to 23}(s_1)\right|^2 \tag{2.2}$$

defining the $2 \to 2$ vertex in the diagram as $pX \to 23$. $g_{pX1} = g_{pp\pi}$ or $g_{p\Lambda K}$ is the coupling constant at the $pp\pi$ or $p\Lambda K$ vertex. To take into account the off-shell nature of the exchanged mesons, the monopole form factors $F(t)$ are used, which are described by a cutoff mass. $D(t)$ is the meson propagator defined usually as $D(t) = 1/(t - m^2_X)$. The amplitude $A_{pX\to 23}(s_1)$ is deduced from the total cross section of the elementary $pX \to 23$ reaction, and thus it gives

$$\begin{aligned} \left|A_{p\pi\to K\Lambda}(s_1)\right|^2 &= 4\pi s_1 \frac{q_\pi}{q_K} \sigma_{p\pi\to K\Lambda}(s_1) && (2.3)\\ \left|A_{pK\to pK}(s_1)\right|^2 &= 4\pi s_1 \sigma_{pK\to pK}(s_1). && (2.4) \end{aligned}$$

q_π and q_K are the momenta of the exchanged pion and produced kaon in the $K\Lambda$ frame. The corresponding values cancel out for $A_{pK\to pK}$. The total cross sections are given by the experimental data for the reactions (on-shell). In this way resonance contributions for the pion exchange enter implicitly into the model. In case of resonance models this contributions are calculated explicitly.

For the pion exchange the coupling constant $g_{pp\pi}$ and the cutoff mass for the form factor are determined well by different models (for example from the Bonn model [Mac87, Mac89]) from the high amount of available data of pion production in pp interactions. In contrast, the experimental data for the determination of $A_{pK\to pK}$ is poor. Therefore, some models are depending on the cutoff value for the kaon monopole form factor, or the $g_{p\Lambda K}$ coupling constant is fitted. Nevertheless, the ratio $g_{pp\pi}/g_{p\Lambda K}$

is given by SU(3) symmetry (see [Sib05]) or SU(6) symmetry (see [Sib98c]). In addition, the relative phase of the pion and kaon exchange amplitudes is not fixed. Thus, interference effects between the exchange mechanism could influence the cross sections, and some models take this into account.

From previous measurements of the $pp \to pK\Lambda$ reaction it turned out that the implementation of $p\Lambda$ final state interaction (FSI) is necessary to describe the data close to threshold. This is done usually by multiplying the reaction amplitude $M(t, s_1)$ with the FSI amplitude. Therefore, the final state interaction is treated independently from the other amplitudes. A detailed introduction to FSI and its parametrization is given in Section 2.4.

The first description of the $pp \to pK\Lambda$ reaction with an pion-kaon exchange model is from Ferrari [Fer60]. This model adds up the pion and kaon exchange incoherently. In contrast, the models from Laget [Lag91] and Sibirtsev et al. [Sib95, Sib98c, Sib00] add the exchanges coherently. The difference in this models is the treatment of the $A_{p\pi\to K\Lambda}$ and $A_{pK\to pK}$ amplitudes. Laget takes them off-shell while Sibirtsev uses on-shell amplitudes. The parameters of both models are fit to bubble chamber measurements from [Fla84]. Both models describe the data well in the energy region of the bubble chamber data, and the $pp \to pK\Lambda$ reaction is dominated by kaon exchange. However, the total cross section data close to threshold [C1196, C1198a, CTOF98a] is underestimated substantially by the models. Therefore, Sibirtsev includes $p\Lambda$-FSI and the improved model describe the data well as it is seen in Figure 2.4 by the solid line. The data shown is from [C1196, C1198a, CTOF98a] (circles) and [Fla84] (squares) with the calculations presented in [Sib00].

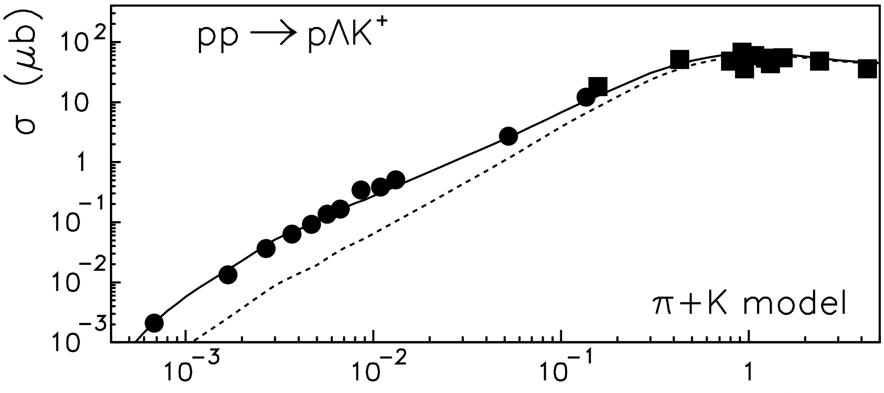

Figure 2.4.: Total cross section of the $pp \to pK\Lambda$ reaction versus the excess energy ϵ with the model calculations from Sibirtsev et al. (see [Sib00] and references therein) with $p\Lambda$-FSI (solid line) and without $p\Lambda$-FSI (dashed line). The data shown is from experiments at the COSY accelerator (circles [C1196, C1198a, CTOF98a]) and bubble chambers (squares [Fla84]). Picture taken from [Sib00].

Another model is from the Juelich theory group [Gas00, Gas01] which exploits the interference of pion and kaon exchange further. An additional feature of this model is the implementation of the $\Sigma N \to \Lambda N$ conversion due to the strong ΣN final state interaction. This conversion leads to an enhancement of the $p\Lambda$ invariant mass spectrum at the ΣN threshold (cusp effect). This is observed in inclusive $pp \to KX$ reactions [Sie94] as well as in exclusive reactions as $K^-d \to p\Lambda\pi^-$ [Tan69] and $pp \to pK\Lambda$ [CTOF10b, CTOF13a]. The calculations of this model predicts for the total cross section a dominant kaon exchange in the Λ production, regardless of assumed interferences, and therefore the reaction $pp \to pK\Lambda$ is insensitive to determine interference terms. This result coincides with the model calculations from Sibirtsev [Sib00] and Laget [Lag91].

2.2.2. Resonance Models

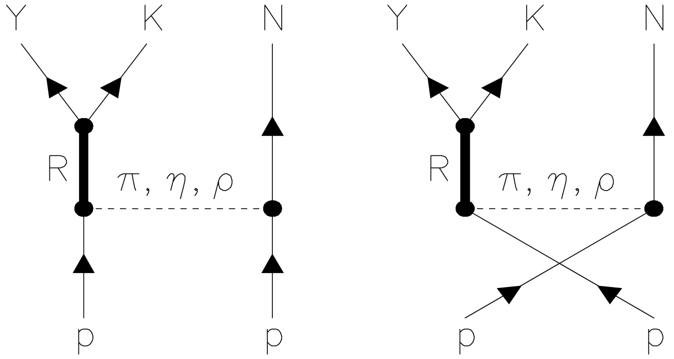

Figure 2.5.: Diagrams for a resonance model with π, η and ρ meson exchange and N^* resonances. Picture taken from [Sib00].

As already mentioned, the resonance models take the amplitudes of N^* resonances explicitly into account. For the model of Tshushima et al. [Tsu97, Tsu99] the corresponding diagrams are shown in Figure 2.5. The exchange mesons are in this model not only pions, but also η and ρ mesons. Mesons with strangeness are not used. The considered N^* resonances are $N^*(1650)$, $N^*(1710)$ and $N^*(1720)$, because they have a significant coupling to the $K\Lambda$ channel, and they are reasonable for the energy range of the data fitted. The reaction amplitude is expressed by [Tsu97]

$$\begin{aligned} M(pp \to pK^+\Lambda) &= M(\pi, N(1650)) + M(\pi, N(1710)) + M(\pi, N(1720)) + \\ &+ M(\eta, N(1710)) + M(\eta, N(1720)) + \\ &+ M(\rho, N(1710)) + M(\rho, N(1720)) + \text{exchange} \end{aligned} \tag{2.5}$$

neglecting interference terms. The coupling constants and cutoff masses for the resonance contributions are determined from measured $\pi p \to K\Lambda$ data and the branching

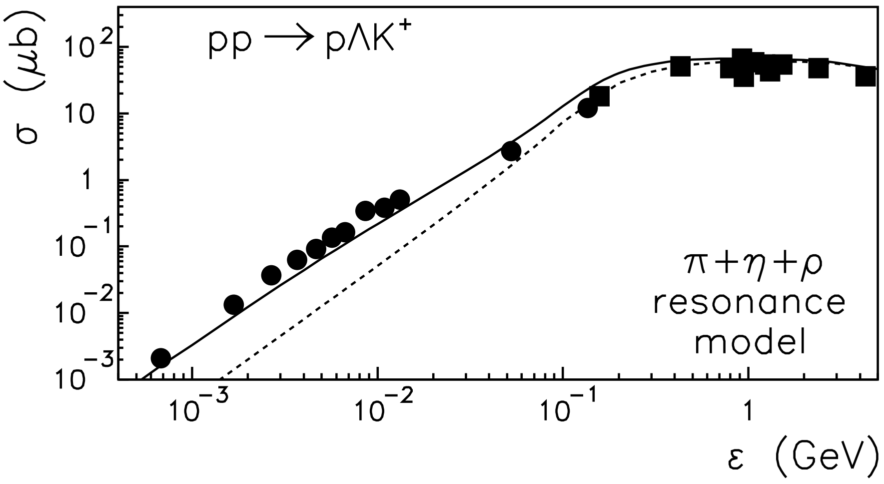

Figure 2.6.: Total cross section of the $pp \to pK\Lambda$ reaction versus the excess energy ϵ within the resonance model calculations from Tsushima et al. (see [Sib00] and references therein) with $p\Lambda$-FSI (solid line) and without $p\Lambda$-FSI (dashed line). The data shown is from experiments at the COSY accelerator (circles [C1196, C1198a, CTOF98a]) and bubble chambers (squares [Fla84]). Picture taken from [Sib00].

ratios of the resonances. The results of the model for the total cross section dependent on the excess energy ϵ is shown as the dashed line in Figure 2.6, together with the measured data from [C1196, C1198a, CTOF98a] (circles) and [Fla84] (squares).

Fitting the model to the bubble chamber data shows that the data close to threshold is underestimated by the resonance model. When including the $p\Lambda$ final state interaction into the model, the description is much better (solid line in Figure 2.6). Therefore, the implementation of the $p\Lambda$ final state interaction is necessary for the data close to threshold. The same result was obtained by the meson exchange models. Another result from the resonance model is the description of the $pp \to pK\Lambda$ reaction close to threshold with a domimant pion exchange including the excitation of the $N^*(1650)$ resonance. For high excess energies the exchange of the ρ meson dominates [Tsu99, Sib99].

In contrast to the resonance model from Tsushima, the model from Shyam [Shy99, Shy01] takes the interference between the resonance amplitudes into account. Beside the exchange of π, η and ρ mesons, the model includes additionally the exchange of the σ meson. The considered N^* resonances are the same as in the Tsushima model. Shyam implements the final state interaction of all particles in his model ($K\Lambda$, pK and $p\Lambda$ FSI). Although the meson-baryon FSI is very weak compared to the $p\Lambda$ final state interaction, it can have a strong influence via interference effects. The parameters for the meson-baryon FSI are taken from an effective Lagrangian model analysis by Feuster and Mosel [Feu98], and the $p\Lambda$ FSI parameters are taken from the Bonn-Jülich group [Reu94]. Within the model, the $pp \to pK\Lambda$ reaction close to threshold can be mainly described by a pion exchange with the excitation of the $N^*(1650)$ resonance. For higher beam momenta ($p_{\mathrm{beam}} > 3.3\,\mathrm{GeV}/c$) the contribution of the $N^*(1710)$ resonance is larger than the one from the $N^*(1650)$ resonance.

A similar behavior is seen in the Dalitz plot analysis of the COSY-TOF measurements at different beam momenta [CTOF10b]. The obtained Dalitz plots for the beam momenta $2.95\,\mathrm{GeV}/c$, $3.2\,\mathrm{GeV}/c$ and $3.3\,\mathrm{GeV}/c$ are shown in Figure 2.7 (upper row). The contributions of N^* resonances are extracted by a fit of the Dalitz plots with a resonance model from Sibirtsev [Sib02]. These fits are shown in the middle row of Figure 2.7. The contribution of the $N^*(1650)$ resonance and the sum of the $N^*(1710)$ and $N^*(1720)$ resonance contributions as a function of the beam momentum are shown in the lower plot of Figure 2.7. The strength of the contributions varies strongly with the beam momentum. As in the model calculations from Shyam, the contribution of the $N^*(1650)$ resonance decreases for higher beam momenta, whereas the contribution of the $N^*(1710)$ and $N^*(1720)$ are increasing.

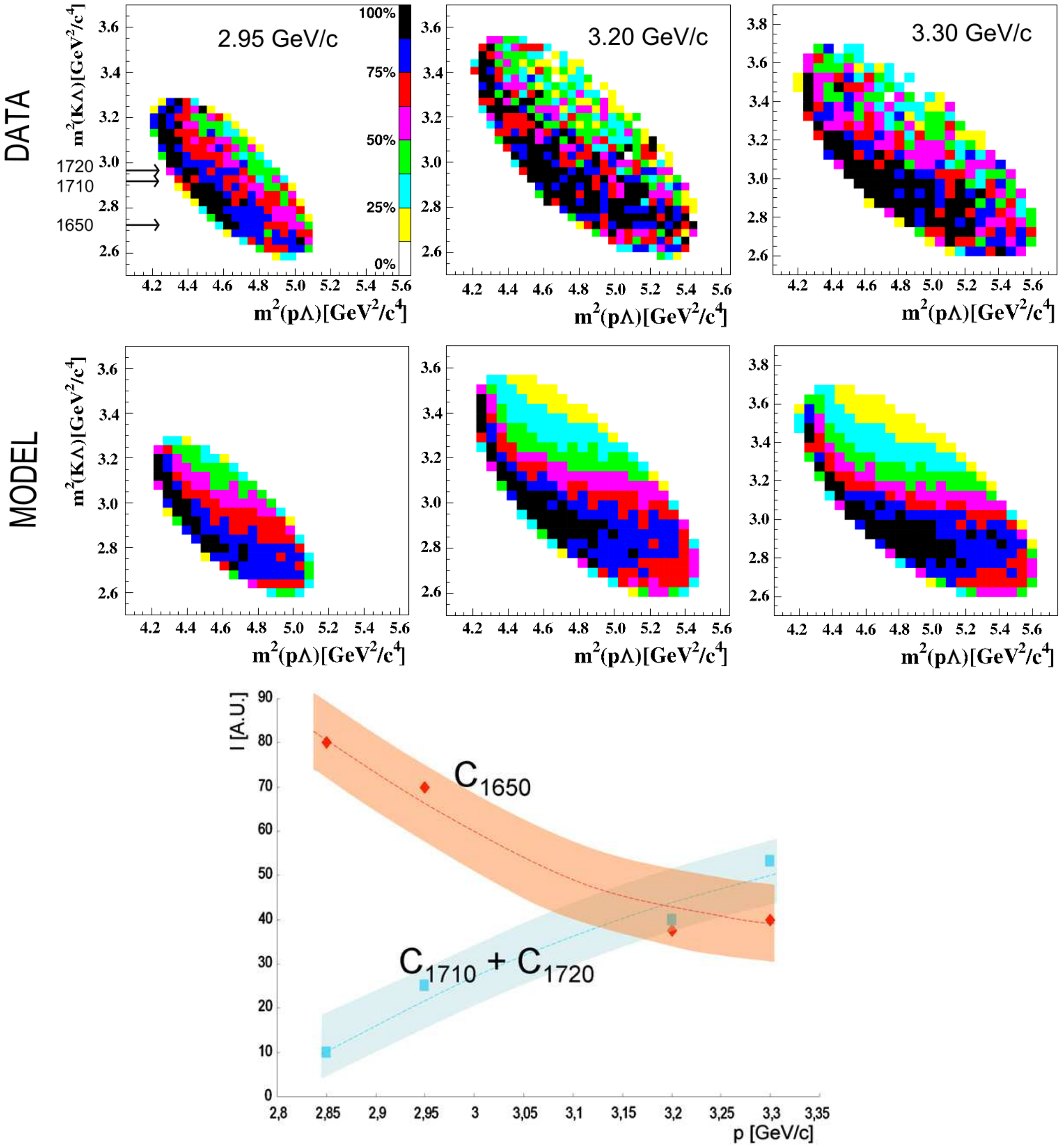

Figure 2.7.: Upper: Dalitz plots of the reaction $pp \rightarrow pK\Lambda$ measured with the COSY-TOF detector at the beam momenta 2.95 GeV/c (left), 3.2 GeV/c (middle) and 3.3 GeV/c (right). The Breit-Wigner masses of the considered N^* resonances are indicated by the arrows. **Middle:** Model fits of the measured Dalitz plots with a resonance model from Sibirtsev [Sib02]. **Lower:** Contributions of the $N^*(1650)$ resonance and the sum of the $N^*(1710)$ and $N^*(1720)$ resonances, obtained by a fit of the Dalitz plots, as a function of the beam momentum. For comparison the values at $p_{\mathrm{beam}} = 2.85$ GeV/c are added from [CTOF06a]. All pictures are taken from [CTOF10b].

2.2.3. Quark Model

Beside the various meson exchange and resonance models, Dillig and Kleefeld introduce a quark-gluon model for the $pp \rightarrow pKY$ reaction close to threshold [Kle96]. In this model the large momentum transfer of the incoming protons is shared by a two-gluon exchange between the interacting constituent quarks (see Figure 2.8 left). The interchanged quark lines guarantee colorless particles in the final state with the right flavor content.

The results of the model calculation for the total cross section is shown in Figure 2.8 (right) together with data from bubble chamber measurements [Fla84]. The data can be described qualitatively by the model but the result is strongly dependent on the scaling parameter Λ. Furthermore, N^* resonances are not implemented in the model. They could be described by a three-gluon exchange (see [Fri02] on page 27: "... Drei-Gluon-Austausch ..., mit dem auch die Resonanzen berücksichtigt werden können. [Dil02][3].")

When comparing all theoretical models the examination of the total cross section data alone can not clearly distinguish between the different models. To obtain a better picture of the reaction mechanism differential and polarization observables have to be taken into account. The Dalitz plot and the differential cross sections measured with the COSY-TOF detector indicate a strong influence of N^* resonances and $p\Lambda$ final state interaction [CTOF10b] with less contribution from strange meson exchange. Up to now the measured polarization observables have not been studied within these model approaches.

---

[3] Dillig, Private communication, Erlangen, 2002.

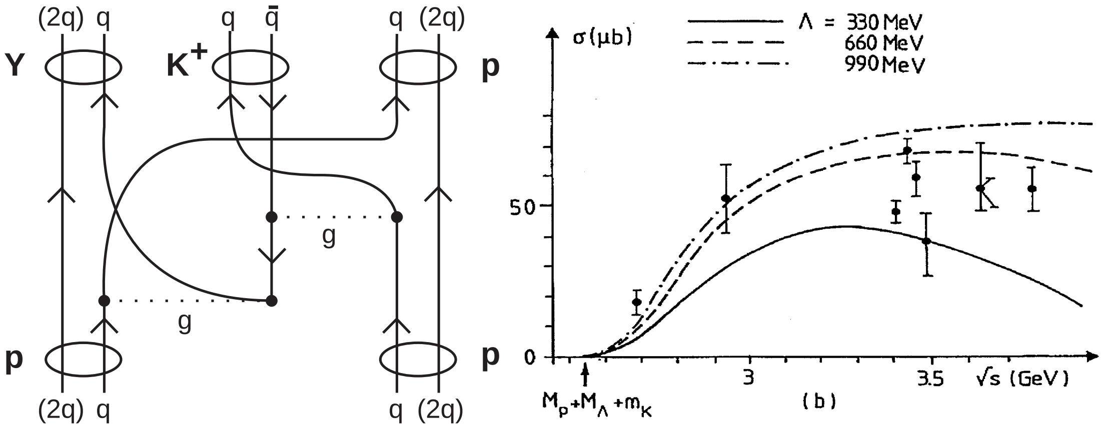

Figure 2.8.: Left: Quark-gluon interaction diagram of the $pp \to pKY$ reaction in the quark-gluon model from Dillig and Kleefeld [Kle96]. **Right:** The energy dependence of the total cross section for the $pp \to pK\Lambda$ reaction calculated with the quark-gluon model from Dillig and Kleefeld [Kle96] for different values of the scale parameter Λ. The data shown is from [Fla84]. Pictures are taken from [Kle96].

2.3. Λ Polarization

Λ polarization produced with an unpolarized proton beam was first seen in high energy proton-beryllium interactions [Bun76]. It was found that the Λ is polarized along the axis

$$\vec{n} = \vec{p}_{\text{beam}} \times \vec{p}_{\Lambda} \tag{2.6}$$

and that the polarization is *negative* with respect to this axis. The surprising result of this measurement was later confirmed by many other experiments with unpolarized beams and/or targets. The parity violating Λ decay allows to measure the polarization through the angular distribution of one of the decay particles. The angular distribution is given by

$$\frac{\mathrm{d}\sigma}{\mathrm{d}\cos\theta_p^{**}} = \sigma_0(1 + \alpha P_\Lambda \cos\theta_p^{**}) \tag{2.7}$$

with the angle θ_p^{**} between the decay proton and the $\vec{n}$ axis in the Λ reference frame and the weak asymmetry parameter $\alpha = 0.642 \pm 0.013$ [PDG2012]. The asymmetry parameter is correlated with the interference term of the S-wave and P-wave amplitudes of the Λ decay. Due to the parity violation of the decay α is not zero and the polarization can be measured. Therefore, the Λ decay is self-analyzing.

The Λ polarization is studied by the kinematic variables x_F (scaling or Feynman variable), $p_T(\Lambda)$ (transverse momentum) and $\cos(\theta_\Lambda^{\text{CMS}})$ (cosine of the scattering angle in CMS). The scaling variable is the longitudinal momentum of the Λ expressed as a fraction of the maximum kinematical allowed value. If x_F is positive the Λ is more correlated with the beam proton while if x_F is negative it is more correlated with the target proton. Many inclusive measurements were performed with $x_F > 0$ and the results can be summarized as follows (for details and references see [Sof99] and Section 1.1.2 in [Piz07]):

- The polarization is almost independent of beam momenta from 6 GeV/c to 2 TeV/c
- The polarization is almost independent of the target type
- For $p_T(\Lambda)$ below 1 GeV/c the magnitude of the polarization increases linearly with $p_T(\Lambda)$ and the slope increases with x_F
- For $p_T(\Lambda)$ above 1 GeV/c the magnitude of the polarization is independent of $p_T(\Lambda)$ and increases linearly with x_F

An exclusive measurement of the polarization in the region $x_F < 0$ was performed at 27.5 GeV/c beam momentum in the $pp \to pK^+\Lambda(\pi^+\pi^-)^n$ reaction with $n = 1 - 4$ by Felix et al. [Fel96, Fel99]. The authors pointed out that the Λ polarization in pp collisions is antisymmetric in x_F due to the rotational invariance. Because their detector has uniform acceptance in x_F they combined the data sets from $x_F < 0$ and $x_F > 0$ by multiplying the $\cos(\theta_p^{**})$ distribution by the sign of x_F. They concluded from their results, that the mechanism for the creation of the polarization is independent of the Λ production mechanism, since the measured behavior of the Λ polarization is the same for the studied reactions.

The study of the Λ polarization in the $pp \to pK\Lambda$ reaction has been done with the COSY-TOF detector at the beam momenta 2.75 GeV/c [Met98, Piz07], 2.85 GeV/c [Fri02], 2.95 GeV/c [Schr03, Piz07, Roe11] and 3.2 GeV/c [Schr03]. The obtained values for the polarization are consistent within the error bars with the measurements at much higher energies.

However, the theoretical explanation of the observed polarization and its dependence on the Λ transverse momentum $p_T(\Lambda)$ and the scaling variable x_F is rather unclear [Sof99]. One simple explanation can be given with the Lund semi-classical fragmentation model [And79]. It uses semi-classical arguments for the creation of the Λ polarization. The incident proton is treated as an ud diquark singlet system with an additional single u quark. After the collision, the diquark continues forward with unchanged flavor and spin and a one-dimensional color field or string is stretched between the diquark and the remnants of the collision. From this field the $s\bar{s}$ pair is created and the ud system picks up the s quark to form the Λ. Therefore, the spin of the Λ hyperon is determined purely by the s quark. Since part of the transverse momentum of the Λ is provided by the s quark and the quarks have a non zero mass, the $s\bar{s}$ pair has orbital momentum. This is compensated by the spin of the $s\bar{s}$ pair. Thus, the s quark has a non zero spin and that is transferred to the Λ. As an result of this consideration the Λ polarization has to be negative and increases with transverse momentum $p_T(\Lambda)$. Although, most of the data fits to this explanation nevertheless the dependence on x_F can not be explained [Piz07].

The meson exchange model from Laget is the only exchange model so far which make a prediction for the dependence of the Λ polarization on the transverse momentum. This prediction is shown in Figure 2.9. For a coupled pion and kaon exchange the polarization should exhibit an enhancement at $p_T(\Lambda) = 0.1\,\mathrm{GeV}/c$ and drop down to increased negative values for higher transverse momenta. For a pure kaon exchange the polarization dependence is quite flat and positive. Unfortunately, none of these predictions could be confirmed by measurements due to the lack of data precision in this momentum region.

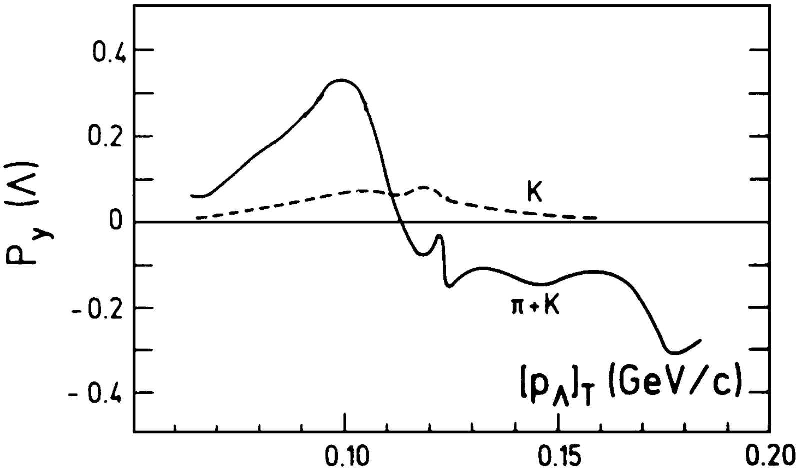

Figure 2.9.: Calculation from Laget [Lag91] for the dependence of the Λ polarization on the transverse momentum $p_T(\Lambda)$ for a pure kaon exchange (dashed line) and a combined kaon and pion exchange (solid line) in a meson exchange model.

2.4. Scattering Length and $p\Lambda$ Final State Interaction

2.4.1. Partial Wave Expansion and Scattering Length

The theoretical models show the necessity to implement $p\Lambda$ final state interaction into the description of the $pp \to pK\Lambda$ reaction to match the measured data. This interaction is an elastic scattering process of the two baryons after their creation. Since the momentum transfer between these baryons is small, the scattering can not be calculated by perturbative QCD[4]. The usual formalism to describe the scattering is a partial wave expansion of the outgoing spherical wave produced by the scattering of an incoming plane wave at a short range potential with radius r (see for instance [Mes67, Mah09]).

---

[4] Within the framework of Lattice QCD direct calculations are performed [Bea12, Bea13a, Bea13b].

Assuming spinless particles and the direction of the incoming plane wave is the z-axis, the outgoing wave $\Psi_s(r)$ is far away from the scattering region a superposition of the incoming wave and the scattered one, thus

$$\Psi_s(r) \simeq e^{ikz} + f(\theta)\frac{e^{ikr}}{r}. \tag{2.8}$$

k is the wave number and $f(\theta)$ is the scattering amplitude dependent on the scattering angle θ. $\Psi_s(r)$ is a solution of the Schroedinger equation. In the partial wave expansion the scattering amplitude is a sum of the partial waves amplitudes $f_l(k)$

$$f(\theta) = \sum_{l=0}^{\infty}(2l+1)f_l(k)P_l(\cos\theta). \tag{2.9}$$

$P_l(\cos\theta)$ are the Legendre polynomials. The partial wave amplitudes $f_l(k)$ are defined through the phase shifts $\delta_l(k)$ of the scattering via

$$f_l(k) = \frac{e^{2i\delta_l(k)} - 1}{2ik} = \frac{e^{i\delta_l(k)}}{k}\sin\delta_l(k) = \frac{1}{k\cot\delta_l(k) - ik}. \tag{2.10}$$

From the scattering amplitude the differential cross section can be calculated

$$\frac{\mathrm{d}\sigma}{\mathrm{d}\Omega} = |f(\theta)|^2 = \sum_{l=0}^{\infty}(2l+1)\,|f_l(k)|^2 = \sum_{l=0}^{\infty}(2l+1)\frac{\sin^2\delta_l(k)}{k^2}. \tag{2.11}$$

The total cross section can be obtained by integrating Equation 2.11 over the solid angle. Due to angular momentum conservation each angular momentum component scatters independently. Therefore, the total cross section can be written as a sum of “partial wave cross sections”

$$\sigma_{\text{tot}} = \sum_{l=0}^{\infty}\sigma_l(k) = \sum_{l=0}^{\infty}4\pi(2l+1)\frac{\sin^2\delta_l(k)}{k^2}. \tag{2.12}$$

For low momentum transfer or low energy scattering ($kr \ll 1$) only the first partial wave amplitudes are nonzero. In the limit $k \to 0$ the scattering is purely defined by the S-wave amplitude ($l = 0$) and this limit is defined as

$$\lim_{k\to 0} f_0(k) = -a \Longleftrightarrow \lim_{k\to 0}\frac{1}{k\cot\delta_l(k)} = -a. \tag{2.13}$$

The parameter a is called the scattering length. It parametrizes all zero energy scattering completely. Therefore, every potential with the same scattering length has the same zero energy scattering properties. The total cross section in the low energy limit is

$$\lim_{k\to 0}\sigma_{\text{tot}} = \lim_{k\to 0}\frac{4\pi}{k^2}\sin^2\delta_0(k) = 4\pi a^2. \tag{2.14}$$

If the two scattered particles have spin like the $p\Lambda$ system, each spin configuration has its own scattering potential and thus a different scattering length. The $p\Lambda$ system can be either in spin singlet or spin triplet configuration with the corresponding spin singlet scattering length a_s and spin triplet scattering length a_t. The extraction of the spin triplet scattering length is possible from the $p\Lambda$ FSI in the $pp \to pK\Lambda$ reaction. The theoretical method used here is described in Section 2.4.3.

2.4.2. $p\Lambda$ Scattering: Data and Models

Through SU(3) flavor symmetry the $p\Lambda$ interaction can be connected to the NN scattering. The NN scattering is precisely known because of the large amount of available data. Unfortunately, the available data for $p\Lambda$ scattering is scarce due to the technical difficulties in providing a high quality Λ beam. Direct $\Lambda p \to \Lambda p$ elastic scattering experiments at low energies were done at CERN [Sec68, Ale68, Kad71]. The scattering parameters are deduced from the measured energy dependence of the total cross section with the effective range approximation of the S-wave phase shifts:

$$k \cot \delta_{s,t} \simeq -\frac{1}{a_{s,t}} + \frac{1}{2} k r_{s,t}^2 \ . \tag{2.15}$$

$\delta_{s,t}$ are the S-wave phase shifts for spin singlet and triplet scattering and $a_{s,t}$ are the corresponding scattering lengths. $r_{s,t}$ are the effective ranges for the spin states. The total cross section from this approximation is [Gol64]

$$\sigma_{\Lambda p \to \Lambda p} \simeq \frac{1}{4}\sigma_s + \frac{3}{4}\sigma_t = \frac{\pi}{k^2 + \left(\frac{-1}{a_s} + \frac{1}{2}kr_s^2\right)^2} + \frac{3\pi}{k^2 + \left(\frac{-1}{a_t} + \frac{1}{2}kr_t^2\right)^2} \tag{2.16}$$

with the separated terms for singlet and triplet scattering. k is the center of mass momentum of the Λp system. With a likelihood fit Alexander et al. [Ale68] determine the value s for the scattering length to be $a_s = -1.8^{+2.3}_{-4.2}$ fm and $a_t = -1.6^{+1.1}_{-0.8}$ fm with highly correlated errors[5]. Obviously, this result suffers from the large errors.

Within the theoretical models a scattering potential is constructed, and the corresponding scattering amplitude is fitted to the total and differential cross sections[6]. From the potentials the values for scattering length and effective range are obtained. Examples for such models are quark based models (see [Fuj07]), meson exchange models and chiral effective field theory ChEFT. The later two are explained in more detail in the next paragraphs.

In the meson exchange model the interaction is produced by the exchange of different mesons between the Λ and the proton. Due to the scarce scattering data the coupling constants are mostly obtained by assuming SU(3) symmetry. The SU(3) breaking is included through the mass splitting of the particles. Examples of such models are the Nijmegen Model NSC97f [Rij99] or the Jülich Model Jülich 04 [Hai05].

---

[5] The error of the values has been taken from [Gas04].

[6] The modelling and fitting is usually done for all hyperon-nucleon channels.

The chiral effective field theory approach for hadron-hadron interactions is based on an idea from Weinberg [Wei90, Wei91][7]. The important feature is the underlying power counting which orders the Feynman graphs in leading order (LO), next to leading order (NLO) and so on. This allows one to improve the calculations systematically when going to higher orders. The Jülich theory group applied this method for YN interactions and the results are published for LO in [Pol06] and for NLO in [Hai13]. Besides the exchange parameters, the potentials in ChEFT contain so-called low-energy constants (LECs) which parameterize short distance properties and must be determined by a fit to the data. Since the amount of data is limited, some relations between the constants are used exploiting SU(3) symmetry. Nevertheless, the number of free parameters is increased.

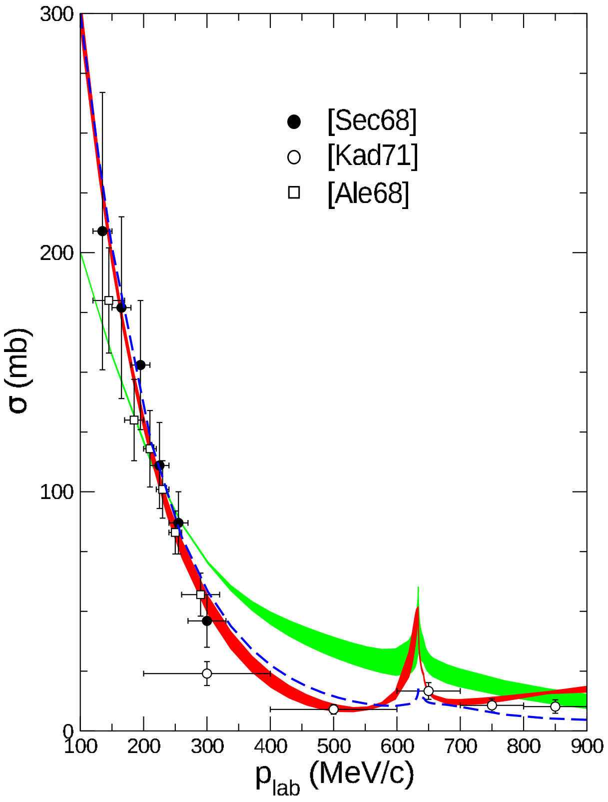

Figure 2.10.: Data and different model predictions for the $p\Lambda$ elastic scattering. The green and red band show the result from chiral effective theory calculations in leading order and next to leading order, respectively. The dashed blue line is the result from meson exchange model calculations of [Hai05]. Picture taken from [Hai13].

---

[7] For recent reviews of the application of chiral effective theory on nuclear forces and NN interactions see [Epe09, Mac11].

Model	a_s [fm]	a_t [fm]
LO [Pol06]	-1.91	-1.23
NLO [Hai13]	-2.91	-1.54
Jülich 04 [Hai05]	-2.56	-1.67
NSC97f [Rij99]	-2.60	-1.72

Table 2.1.: Predictions for $p\Lambda$ singlet and triplet scattering length from different theoretical calculations. All values are taken from [Hai13].

In Figure 2.10 the results of the LO and NLO calculations for the total cross section are shown together with the experimental data and the result from [Hai05]. As expected the NLO calculation (red band) delivers a better description of the data than the LO calculation (green band). The dashed blue line stems from the calculation in a meson exchange approach [Hai05]. Table 2.1 summarizes the results of the calculations for the spin singlet and triplet scattering length from the different models. In all cases the singlet scattering length is larger than the triplet one. The constraint of all models is the reproduction of the hypertriton binding energy. The hypertriton is a bound state of two nucleons and the Λ. Therefore, the strength of the S-wave scattering lengths are correlated to the Λ separation energy. All models shown in Table 2.1 predict a bound hypertriton with a binding energy in agreement with the measured value [Jur73].

Another, very promising way, is the extraction of the scattering length from final state interactions in strangeness transfer and associated strangeness production reactions. This is explained in the next section for the $pp \to pK\Lambda$ reaction.

2.4.3. Extraction of the $p\Lambda$ Scattering Length from $p\Lambda$ FSI

Two different methods are proposed for the extraction of the $p\Lambda$ scattering length from exclusive measurements of the $pp \to pK\Lambda$ reaction. One uses the parametrization of the differential cross section by an inverse Jost function [Hin04] while the other method derives an integral representation of the scattering length from the differential cross section with a dispersion integral approach [Gas04, Gas05].

2.4.3.1. Inverse Jost Function Approach

Due to the large momentum transfer between the initial and final baryons in the $pp \to pK\Lambda$ reaction, the range of the production mechanism is much smaller than the range of the final state interaction. Thus, the energy dependence of the reaction amplitude is given dominantly by the FSI amplitude and the production amplitude is nearly constant. This approximation was proposed by Watson and Migdal [Wat52, Mig55, Gol64, Gil64]. The reaction amplitude is

$$M \simeq M \times A_{\mathrm{FSI}}(k). \tag{2.17}$$

k is the center of mass momentum of the $p\Lambda$ system. Taking the inverse Jost function [Jos47, Jos52] the FSI amplitude A_{FSI} is approximated by

$$A_{\mathrm{FSI}}(k) = \frac{k - i\beta}{k + i\alpha}. \tag{2.18}$$

The parameters α and β are related to the scattering length a and the effective range r of the S-wave scattering by

$$\alpha = \frac{1}{r}\left(1 - \sqrt{1 - \frac{2r}{a}}\right) \ , \ \beta = \frac{1}{r}\left(1 + \sqrt{1 - \frac{2r}{a}}\right). \tag{2.19}$$

For the double differential cross section the contributions of spin singlet and triplet states of the $p\Lambda$ system can be added incoherently since close to the production threshold a transition from singlet to triplet is not allowed. With the spin statistical weights the double differential cross section can be written as [Hin04]

$$\begin{aligned} \frac{\mathrm{d}^2\sigma}{\mathrm{d}\Omega_K \mathrm{d}m_{p\Lambda}} &= \Phi_3 \cdot |\tilde{M}|^2 |\tilde{A}_{\mathrm{FSI}}|^2 = \\ &= \Phi_3 \left[\frac{1}{4}|M_s|^2 \frac{k^2 + \beta_s^2}{k^2 + \alpha_s^2} + \frac{3}{4}|M_t|^2 \frac{k^2 + \beta_t^2}{k^2 + \alpha_t^2}\right]. \end{aligned} \tag{2.20}$$

Φ_3 is the three-body phase space distribution function. $|M_s|$ and $|M_t|$ are the singlet and triplet production matrix elements, respectively. The parameters α_s, β_s, α_t and β_t are the potential parameters for the singlet and triplet scattering which are correlated to the singlet and triplet scattering lengths through Equation 2.19. This method was used by the COSY-11 collaboration [C1198b] and the HIRES collaboration [HIR10] in the analysis of their measurements, but only the later one obtained values for the spin resolved scattering lengths, namely $a_s = -2.43^{+0.16}_{-0.25}\,\mathrm{fm}$ and $a_t = -1.56^{+0.19}_{-0.22}\,\mathrm{fm}$.

For a further description of the implementation of the FSI with the Jost function approach into meson exchange models and its predictions see [Sib05].

2.4.3.2. Dispersion Integral Approach

The other method through a dispersion integral is used in the analysis of the COSY-TOF data [Roe11, CTOF13b]. The great advantages of the method described in [Gas04, Gas05] are the known theoretical uncertainty of 0.3 fm for the extraction of the scattering length, and the possibility to extract the spin resolved scattering length using the information of the kaon analyzing power. The dispersion integral approach relates the scattering length to the integral over the double differential cross section, hence its shape, by

$$\begin{aligned} a_{s,t} = & \lim_{m^2 \to m_0^2} \frac{1}{2\pi}\left(\frac{m_\Lambda + m_p}{\sqrt{m_\Lambda m_p}}\right) \mathbf{P}\int_{m_0^2}^{m_{\max}^2} \mathrm{d}m'^2 \sqrt{\frac{m_{\max}^2 - m^2}{m_{\max}^2 - m'^2}} \\ \times & \frac{1}{\sqrt{m'^2 - m_0^2} \cdot (m'^2 - m^2)} \log\left\{\frac{1}{p'}\left(\frac{\mathrm{d}^2\sigma_{s,t}}{\mathrm{d}m'^2 \mathrm{d}t}\right)\right\} \end{aligned} \tag{2.21}$$

with $m_0 = m_\Lambda + m_p$. $\mathbf{P}$ denotes that the Cauchy principal integral has to be applied. p' is the two-body phase space factor of the $p\Lambda$ system, thus the internal center of mass momentum of the $p\Lambda$ system. In [Gas04] it is shown that it is sufficient to use invariant masses up to $m_{\max} = m_0 + 40\,\mathrm{MeV}/c^2$ to achieve the theoretical uncertainty of 0.3 fm for the determination of the scattering length.

As it is described in Section 2.3 in [Roe11] the absolute normalization of the measured cross section is irrelevant for the determination of the scattering length. If the differential cross section is multiplied by an arbitrary number N, the logarithmic terms in Equation 2.21 becomes

$$\log\left\{N \cdot \frac{1}{p'}\left(\frac{\mathrm{d}^2\sigma}{\mathrm{d}m'^2\mathrm{d}t}\right)\right\} = \log\{N\} + \log\left\{s\frac{1}{p'}\left(\frac{\mathrm{d}^2\sigma}{\mathrm{d}m'^2\mathrm{d}t}\right)\right\}. \tag{2.22}$$

In [Gas04] it is shown that the integral of Equation 2.21 is zero for a constant in the integrand, thus the term $\log\{N\}$ vanishes. This feature is used in the analysis in the way that the absolute normalization of the spectrum is irrelevant (see Chapter 8).

The extraction of the spin triplet scattering length utilizes the kaon analyzing power together with the allowed partial wave combinations. In the basis system, used here, the proton and Λ are composed to the system $\{p\Lambda\}$ with internal momentum ($L'_{p\Lambda}$) and corresponding spin. The kaon is described by the relative angular momentum (l'_K) to the $\{p\Lambda\}$ system. Thus, the reaction can be expressed by $pp \to \{p\Lambda\}\,K$. The initial proton-proton state is described by the total angular momentum J, the angular momentum L and the spin S. In the reaction the total angular momentum and parity is conserved. Taking partial waves up to $L'_{p\Lambda} = 1$ and $l'_K = 2$ with the limit of $J = 2$, the combinations in Table 2.2 are allowed for the $pp \to \{p\Lambda\}\,K$ reaction. The partial wave combinations are given in the Rosenfeld notation [Ros54] and are sorted according to the final state angular momenta. If the $p\Lambda$ system is in S-wave ($L'_{p\Lambda} = 0$), it must have spin triplet configuration for kaons in P-wave.

The analyzing power of the kaon is given in terms of the differential cross section and associated Legendre polynomials P_l^m of degree l and order m by (adapted from [Bla85, Han04])

$$A_N(\cos\theta_K^*)\frac{\mathrm{d}\sigma}{\mathrm{d}\cos\theta_K^*} = \alpha P_1^1(\cos\theta_K^*) + \beta P_2^1(\cos\theta_K^*). \tag{2.23}$$

θ_K^* is the kaon scattering angle in the center of mass frame. From the analysis of data collected at 2.95 GeV/c [Roe11, CTOF13b], it turned out that high order terms of the Legendre polynomials are negligible for the further analysis[8]. Therefore, the parameter α is related to the interference of the S-wave and P-wave amplitudes of the kaon, and β results from the interference of the S-wave and D-wave amplitudes. As it is shown above, kaons in P-wave leads to the spin triplet configuration of the $p\Lambda$ system if it is in

---

[8] High order terms correspond to partial waves of the kaon higher than $l > 2$. They are strongly suppressed since the maximum momentum of the kaon in the CMS is $p_{K,\max}^{\mathrm{CMS}} \approx 323\,\mathrm{MeV}/c$ at 2.7 GeV/c beam momentum.

Class ($L'_{p\Lambda} l'_K$)	Initial State $^{2S+1}L_J$	Final State	$p\Lambda$ spin state
Ss	$^3P_0$	$^1S_0 s_0$	singlet
	$^3P_1$	$^3S_1 s_1$	triplet
Sp	$^1S_0$	$^3S_1 p_0$	triplet
	$^1D_2$	$^3S_1 p_2$	triplet
Sd	$^3P_1$	$^3S_1 d_1$	triplet
	$^3P_2$	$^1S_0 d_2$	singlet
	$^3F_2$	$^1S_0 d_2$	singlet
Ps	$^1S_0$	$^3P_0 s_0$	triplet
	$^1D_2$	$^3P_2 s_2$	triplet
Pp	$^3P_{0,1,2}$	$^1P_1 p_{0,1,2}$	singlet
	$^3F_2$	$^1P_1 p_2$	singlet
	$^3P_{0,1}$	$^3P_0 p_{0,1}$	triplet
	$^3P_{0,1,2}$	$^3P_1 p_{0,1,2}$	triplet
	$^3F_2$	$^3P_1 p_2$	triplet
	$^3P_{1,2}$	$^3P_2 p_{1,2}$	triplet
	$^3F_2$	$^3P_2 p_2$	triplet
Pd	$^1S_0$	$^3P_2 d_0$	triplet
	$^1D_2$	$^3P_{0,1,2} d_2$	triplet
	$^1D_2$	$^1P_1 d_2$	singlet

Table 2.2.: Partial wave composition of the initial and final states in the process $pp \rightarrow \{p\Lambda\}\, K$ up to an angular momentum of $L'_{p\Lambda} = 1$ for the $p\Lambda$ system and $l'_K = 2$ for the kaon. Additionally, the total angular momentum is limited to $J = 2$. The spin state of the $p\Lambda$ system is also given. The Rosenfeld notation is used [Ros54].

S-wave. Then the parameter α is only sensitive to spin triplet amplitudes. This feature is used to determine the $p\Lambda$ spin triplet scattering length. In addition, β vanishes when Equation 2.23 is integrated over the full angular range (see [CTOF13b]). The parameters α and β are determined in bins of $p\Lambda$ invariant masses by the fit of the Legendre polynomials to the data as it is shown in Section 7.5.3. Specifically, Equation 2.23 becomes (see Equation 5 in [CTOF13b])

$$A_N(\cos\theta_K^*, m_{p\Lambda}) = \alpha(m_{p\Lambda})P_1^1(\cos\theta_K^*) + \beta(m_{p\Lambda})P_2^1(\cos\theta_K^*). \tag{2.24}$$

The obtained value $\alpha(m_{p\Lambda})$ is multiplied to the final state amplitude in order to get the spin triplet amplitude behaviour. The absolute normalization might be wrong but as it was shown by Equation 2.22 this does not matter for the scattering length extraction by the method from [Gas04].

Therefore, the following equation holds for the limit $m_{p\Lambda} < m_0 + 40\,\mathrm{MeV}/c^2$ when the $p\Lambda$ system is in S-wave:

$$|A_{\mathrm{FSI,t}}(m_{p\Lambda})|^2 = \alpha(m_{p\Lambda}) \cdot |\tilde{A}_{\mathrm{FSI}}(m_{p\Lambda})|^2. \tag{2.25}$$

$|\tilde{A}_{\mathrm{FSI}}(m_{p\Lambda})|^2$ and $|A_{\mathrm{FSI,t}}(m_{p\Lambda})|^2$ are the spin averaged and spin triplet amplitudes, respectively. The amplitudes are fit with an exponential function as it is described in the Appendix A in [Gas04] in general. The fit procedure has been slightly modified in this thesis in order to improve the fit convergence and stability. The complete procedure is in detail explained in the Section 8.1. The effective scattering length $\tilde{a}$ is determined by the fit of $|\tilde{A}_{\mathrm{FSI}}(m_{p\Lambda})|^2$ and the spin triplet scattering length a_t by the fit of $|A_{\mathrm{FSI,t}}(m_{p\Lambda})|^2$, respectively.

In [CTOF13b] $\tilde{a}$ and $\alpha(m_{p\Lambda})$ are determined for the COSY-TOF measurement of $pp \to pK\Lambda$ at $2.95\,\mathrm{GeV}/c$ beam momentum. For the effective scattering length the value $\tilde{a} = (-1.25 \pm 0.08_{\mathrm{stat.}} \pm 0.3_{\mathrm{theo.}})\,\mathrm{fm}$ is obtained with the statistical and theoretical uncertainty. Additionally, influences of N^* resonances to the extraction method are checked by applying the method to two separated regions of the Dalitz plot. It turned out that the resonances have a significant effect on the value for the scattering length. The induced variation is in the order of 1.20 fm [CTOF13b]. Thus, this is also checked in the analysis of the data presented here (see Section 8.3). Unfortunately, the parameter $\alpha(m_{p\Lambda})$ is compatible with zero for the mass range $m_{p\Lambda} < m_0 + 40\,\mathrm{MeV}/c^2$ within the given statistics of the measurement at $2.95\,\mathrm{GeV}/c$ beam momentum. Therefore, an extraction of the spin triplet scattering length was not possible for this measurement. Possible explanations for $\alpha \approx 0$ can be [Roe11]:

- Dominant spin singlet scattering for which P-wave kaons are forbidden.[9]
- The individual amplitudes which contribute to P-wave kaons are small.

---

[9] This is the explanation from the HIRES collaboration for their results of the spin resolved scattering lengths and production matrix elements presented in [HIR10].

- The individual amplitudes which contribute to P-wave kaons interfere destructively.
- ...

Through the analysis of measurements at different beam momenta the explanations can be distinguished, since the amplitudes are energy dependent. Thus, if a nonzero value for α is obtained at a different beam momentum, the first explanation is most likely excluded.

In Section 7.5.3 the results of the kaon analyzing power for the measurement presented in this thesis are shown. As it turns out, α is not zero and an extraction of the $p\Lambda$ spin triplet scattering length from the invariant $m_{p\Lambda}$ spectrum is possible. The result is given in Section 8.4 together with a discussion of systematical errors.

Research is so unpredictable. There are periods when nothing works and all your experiments are a disaster and all your hypotheses are wrong.

(Francis Collins)

3. Experimental Setup

In this chapter the COSY-TOF experiment is described which is located at one of the external beam lines of the COSY (**Co**oler **Sy**nchroton) accelerator at the research centre Juelich.

Special attention is giving to the Straw Tube Tracker (STT) as the most important sub-detector in COSY-TOF for the event reconstruction presented here. In addition, the experimental trigger and data aquisition conditions are described.

3.1. COSY Accelerator

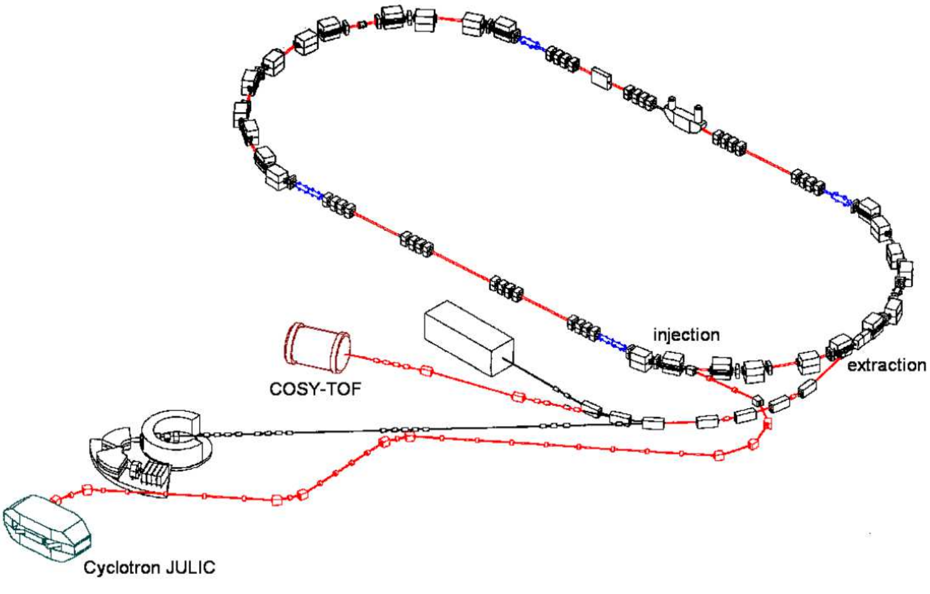

Figure 3.1.: Schematic view of the COSY accelerator facility with the JULIC cyclotron as injector and the external beam lines. The path of protons from the cyclotron to the COSY-TOF detector is highlighted in red (original from [Pau96], modified version from [Dzh12]).

The layout of the COSY facility is shown in Fig. 3.1. The highlighted red path marks the path of accelerated particles from the preaccelerator JULIC cyclotron via the COSY synchroton and storage ring to the COSY-TOF detector. It is possible to reach proton momenta up to 3.7 GeV/c inside the synchroton and up to 3.3 GeV/c at the external beam lines[1].

The source delivers unpolarized H^- ions with a current of about 100 μA or transversely polarized ions with a current of around 5 μA [Pra14] to the JULIC cyclotron which accelerates them to an energy of 40 MeV. After stripping of the electrons, the protons are injected into the COSY accelerator. This is an oval synchroton and storage ring with 184 m circumference where the protons can be accelerated to a beam momentum between 270 MeV/c and 3.7 GeV/c.

The beam is cooled with stochastic and electron cooling which leads to a momentum resolution of $\Delta p/p < 10^{-4}$ and a beam divergence < 2 mrad. After the cooling typically 5×10^{10} unpolarized or 3×10^9 polarized protons are stored in COSY [Pra14]. Via the ultra slow stochastic extraction method these are directed to the external beam lines and thus to the COSY-TOF experiment.

During the beam time in October 2011, COSY was operating with polarized protons ($P = (79.0 \pm 1.1)\%$ see Chapter 5.5) at a beam momentum of 2.7 GeV/c. The very high polarization compared to previous measurements was achieved through an additional stop in the acceleration process while crossing depolarization resonances [Lor13]. One extraction spill was 60 s long and the averaged extraction rate was around 6×10^6 protons per second. After each spill the spin of the beam was flipped to reduce systematic uncertainties in the determination of the polarization observables.

3.2. The COSY-TOF Detector

The COSY-TOF detector was developed in order to investigate associated strangeness production of hyperons close to the production threshold. The requirements are:

- Full geometrical reconstruction of all charged particles of the reaction,
- Reconstruction of the primary and secondary vertices,
- Reconstruction of the momenta through Time Of Flight (TOF) for additional kinematic information,
- High background rejection.

To fulfill all these requirements the COSY-TOF detector is built in a modular way. It is possible to change the detector length and the position of different sub-detectors. For

---

[1] It is also possible to accelerate deuterons but they are not used for hyperon production at the COSY-TOF experiment. Results from a measurement of $dp \to pp\pi^-$ with COSY-TOF can be found in [CTOF06b].

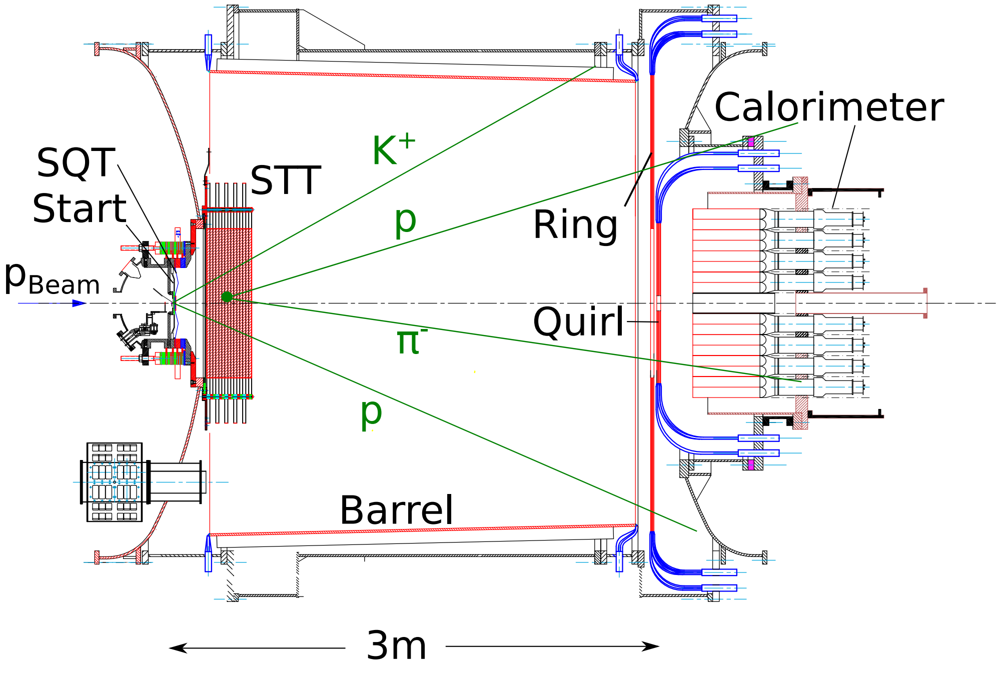

Figure 3.2.: Schematic drawing of the COSY-TOF detector including the different detector subsystems used during the 2011 measurement. The detected charged tracks of an example event of the $pp \to pK^+\Lambda \to pK^+(p\pi^-)$ reaction are drawn in green, and the decay vertex of the Λ is marked with a green point.

the measurement in 2011, the setup for hyperon production[2] was used. It is sketched in Figure 3.2 together with an example event of the $pp \to pK^+\Lambda \to pK^+(p\pi^-)$ reaction. In this setup the detector is a barrel-like vacuum tank with a length of about 3 m and a diameter of 3 m. The tank is evacuated to a residual pressure of $\leq 7 \times 10^{-4}$ mbar to minimize the rate of secondary interactions and multiple scattering. After passing a veto system the beam hits a liquid hydrogen target. The produced particles are then registered in different detector subsystems. These can be grouped into three different regions: start detector region, central straw tube tracker region and end detector region. The first one consists of the so called 'Starttorte', which is a set of plastic scintillators providing the start signal for the TOF measurement and trigger, and a silicon quirl detector (SQT) for precise track information near the primary vertex. The most important tracking system is the Straw Tube Tracker (STT), situated ≈ 25 cm downstream from the target. The end detector region consists of scintillators covering the full cyclindrical inner surface of the vacuum tank (Barrel detector) and the end cap (Quirl and Ring detector) and a calorimeter, both on the downstream end of the vacuum chamber.

---

[2] This setup has full phase space coverage for the $pp \to pK\Lambda$ reaction in the measured beam momentum range, but not necessarily for the production of Σ hyperons.

The scintillators provide the stop signal of the TOF measurement and also are used to generate a trigger signal.

In total, all these sub-detectors cover the full azimuthal range and a polar angular range from 2 ° to 60 °. That yields full phase space coverage in the center of mass reference frame. In addition, the tracking capabilities are excellent and allow for a separation of the Λ decay vertex from the primary one.

In the following sections the different detector components are explained in more detail.

3.2.1. The Veto System

To exclude reactions which occur in front of and outside of the target material, the beam must pass a veto system before hitting the target. The first part of the veto is two plates with apertures of 8 mm and 5 mm located 1 m and 0.5 m upstream of the target, respectively. The second part is a movable scintillator with five holes of different diameters (1.5 mm - 3.5 mm see also [Schr98]), located around 5 cm upstream of the target and the scintillator is also used to assist the beam focussing.

3.2.2. The Target

A hollow copper cylinder of 4 mm length and 6 mm diameter filled with liquid hydrogen is used as the target [Nak93, Jae94]. The entrance and exit window consists of about 1.5 μm thick heptan foil to have a minimum amount of beam-foil interactions and multiple scattering. Filled with liquid hydrogen, the pressure inside is 200 mbar and the proton areal density is 1.8×10^{22} protons/cm^2. The target is surrounded by high vacuum thus the foils are partly stretched and the effective target length is about 1 mm longer than the copper cylinder (see also Section 5.3).

3.2.3. Start Detector Region

The start detector region consists of the start counter so-called ‘Starttorte‘ and the Silicon Quirl Telescope (SQT).

The **start counter** consists of two 1 mm thick scintillator discs which are segmented in 12 wedge shaped pieces, each covers 30° azimuthal angle. The outer radius of each disc is 7.6 cm with a hole of 2 mm in the middle for the beam to pass the detector without interaction. The second disc is rotated by 15° around the beam axis with respect to the first one to get 24 coincidence regions with an azimuthal angular size of 15°. Positioned 2.2 cm behind the target, this counter provides the start signal for the time of flight measurement, and also measures the number of charged primary particles for the trigger.

The **silicon quirl telescope**[3] is a segmented silicon detector with a thickness of

---

[3] Technically it is not a telescope, because the detector consists only of one silicon disc. Originally, it was planned to install several identical discs, thus forming a telescope.

$300\,\mu$m and an outer radius of 3.5 cm. Like in the start counter a beam hole of 3 mm radius is in the center of the detector. It is positioned ≈ 2.5 cm downstream of the target. The silicon strip detector is segmented into 128 Archimedian spirals like the Quirl and Ring detector (see Figure 3.3) on each side of the detector. Each of the spirals covers an azimuthal angular range of π and has an identical amount of solid angle across an identical polar angle range. The rotational direction is counterclockwise for the upstream side and clockwise for the downstream side. This results in only one crossing point of a spiral of one side with any spiral of the other side. Each pixel produced by the overlap of a spiral on the front with one one the back subtends the same solid angle. Due to the high segmentation (128^2 pixels) the corresponding pixels have a high spatial resolution.

3.2.4. End Detector Region

The end detector region consists of the scintillating detectors Barrel, Ring and Quirl, which produce the stop signal of the TOF measurement and the charge multiplicity criterium for the trigger. A calorimeter is located behind them with a polar angle coverage from 1° to 10°. The calorimeter is only used for measurements with the short setup of the COSY-TOF detector and thus it will not explained in detail here.

The **Barrel detector** covers the complete cylindrical part of the inner surface of the vaccuum tank and consists of 96 scintillator bars, 15 mm thick and 2.853 m long. To avoid holes in the acceptance, the width of the bars reduces from 10.0 cm close to the target to 9.6 cm at the end cap while the radial distance decreases from 1.55 m to 1.48 m, respectively. The bars are read out from both ends to measure the polar angle from the time difference of the signals at opposite ends. It covers a polar angle range from 25° to 70°. The polar angle resolution is roughly 0.4° and the azimuthal angle resolution is $\sigma_\phi = 3.75°/\sqrt{12}$.

The **Quirl detector** consists of three layers of scintillators each 5 mm thick with different segmentation which are positioned at the inner part of the end cap, roughly 3 m downstream of the target. The outer radius of the active area is 58 cm with an inner hole for the beam of 4.2 cm radius, thus covering a polar angle range from 1° to 10°. The polar angle resolution is better than 0.24°. The first layer is structured in 48 wedge shaped slices like the start counter, resulting in an azimuthal resolution of $\sigma_\phi = 7.5°/\sqrt{12}$. The other two layers are structured in 24 Archimedian spirals each with one layer rotated in the clockwise direction and the other in the counterclockwise direction [Dah94]. The structure in the inner part can be seen in Figure 3.3.

The outer part of Figure 3.3 shows the **Ring detector**. The structure is similar to the Quirl detector with twice the number of elements per layer, hence the first one has 96 wedge-shaped pieces and the other two layers have 48 clockwise and 48 counterclockwise orientated spirals. Therefore, every slice of the Quirl detector is continued by two slices of the Ring detector. The inner radius of the Ring detector is 56.75 cm to have a small overlap area with the Quirl detector, which is positioned 10 cm behind the Quirl in beam direction. The outer radius is 154 cm giving a polar angle coverage of 10° to

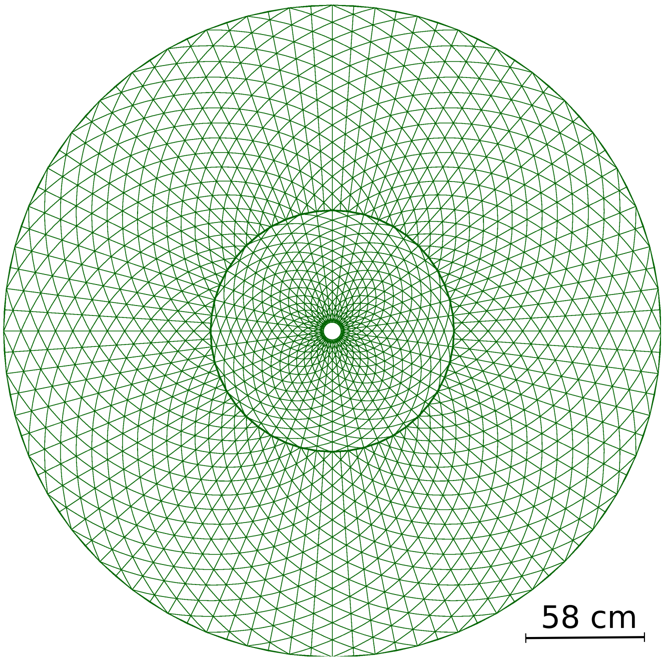

Figure 3.3.: Pixel structure of the Quirl and Ring detectors in the COSY-TOF end cap [Kra06].

26°. The polar angle resolution is better than 0.20°, and the azimuthal resolution is $\sigma_\phi = 3.75°/\sqrt{12}$.

3.3. The Straw Tube Tracker

The Straw Tube Tracker (STT) [Roe11, Dzh12, CTOF08] is the central tracking system of the COSY-TOF experiment, and gives the most precise information for track and vertex reconstruction. The achieved resolution for momentum and invariant mass of the $pK\Lambda$ final state is significantly better than from the time of flight measurement [Roe11]. Therefore, only the data from the STT were used in the analysis presented here.

The detector consists of 2704 straw tubes. Each straw tube is a cyclindrical mini-drift chamber with a single anode wire. A voltage is applied between the wire and the wall of the drift chamber. If a charged particle crosses the chamber it creates ionized clusters in the gas along its path. The resulting electrons and ions drift in the electric field between the wall and the wire. Close to the wire the electrons cause a cascade of ionization (avalanche region), because the high electric field is sufficiently strong there. The amplification of about $10^4 - 10^5$ is large enough to be read out. Through measurement of the time information of the signal the drift time of the electron

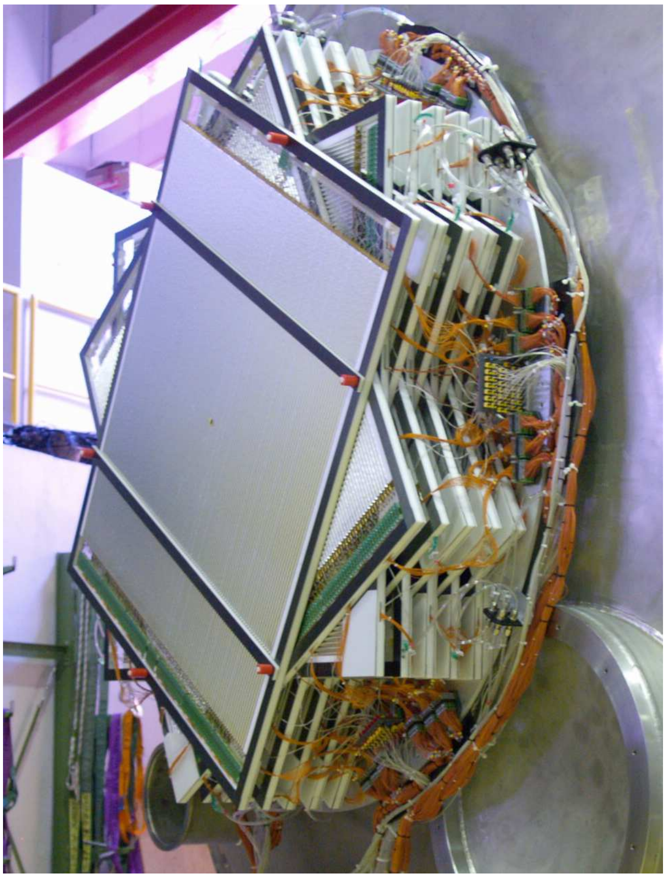

Figure 3.4.: The straw tube tracker during mounting in the COSY-TOF experiment.

from the closest cluster to the wire can be determined. This drift time corresponds to the minimum distance of the particle track to the wire (= isochrone radius). For that purpose a calibration is necessary relating the drift time to the isochrone radius (for details see Chapter 4). Precise track reconstruction is obtained by combining the distance information from all straw tubes in the STT.

The straw tubes of the STT are 105 cm long and their diameter is 1 cm. The walls are made of aluminized Mylar foil of 32 μm thickness. The anode is a 20 μm thick gold plated tungsten wire with a tension of 400 mN provided by the gas overpressure of 1.2 bar. Each wire is fixed by crimp pins at each end cap of the tube. The gas is a mixture of Ar and CO_2 with a ratio of 8:2. The high voltage between the anode and the wall is 1820 V with the wall at ground potential.

The straw tube tracker is shown in Figure 3.4 during the mounting process into the experiment. The straw tubes are organized in 13 double layers, which are rotated by an azimuthal angle of 60° counterclockwise with respect to the previous one. This is used to reconstruct the three dimensional tracks and to resolve ambiguities for hits from multiple tracks. The first double layer is arranged with the straws parallel to the x-axis of the global coordinate system of the analysis (see Chapter 4) and their electronics are in the positive x-direction. Three orientations of double layers exist, namely 0°, 60°, 120°, since each third double layer has the same straw tube orientation. The only difference is the position of the read out of the electronics. This alternation is important to average out different signal propagation time through the wire along the tubes of a track.

Each double layer consists of two layers, seperated by a distance of 8.8 mm along the beam direction. One layer is shifted by 5.05 mm normal to the beam direction to the other one to almost reach closely packed double layers. Additionally, it eliminates acceptance holes if one particle passes the tubes very close to the wall or in between two tubes. If this happens the track passes the tubes in the other layer close to the wire and any variation in efficiency and resolution is averaged out.

A beam hole is located with a diameter of 15 mm in the middle of each layer. For that purpose the 2 central straw tubes in each layer were replaced by 4 shorter straws with 51 cm length.

The full detector volume is around 230 l with a self stabilizing mechanical setup due to the overpressure in the straws. The total radiation length of the STT for all layers is on average $X/X_0 \sim 1\%$ [Roe11]. Thus, the material of the STT has only significant influence on the track reconstruction behind the STT, and therefore is of little importance for the current analysis.

3.4. Trigger and Data Aquisition

Compared to the previous measurements at COSY-TOF, the trigger conditions and data aquisition were modified for the 2011 beam time in order to enhance the rate of data taken and to partly circumvent a new problem with gaps in the start counter, which were observed for the first time in a measurement with the STT in 2010 (see Section 6.3.3 in [Roe11]). In general, the change in charge multiplity from 2 to 4 in the $pp \to pK\Lambda$ reaction is taken into account for the trigger, therefore the standard trigger (t11pkl) demands two hits in the 'Starttorte' from the primary proton and kaon and four or more hits in the whole end detector (Quirl, Ring and Barrel). Upper limits for the multiplicities are not applied in order to avoid losing events because of noisy detector channels or pile up or event mixing. For the measurement at 2.7 GeV/c the trigger condition was changed to at least 1 hit in the start counter in coincidence with 4 or more in the end detector. This improves the triggering of $pK\Lambda$ events, when one primary particle goes through the gaps in the inner part of the start counter, and therefore generates no signal for the trigger.

For the determination of the beam polarization, $pp \to pp$ elastic scattering events were triggered in addition to the $pK\Lambda$ events. This trigger was modified to require at least one hit in the start counter and 2 hits in the end detector. Since the cross section of elastic scattering is about four orders of magnitudes higher than for hyperon production, the elastic trigger (t10pp) is scaled down by a ratio of 1:100. That means that one of hundred elastic triggered events is read out by the DAQ system. For dedicated runs with pure elastic events without the t11pkl trigger the ratio was 1:1. Table 3.1 summarizes the trigger conditions and ratios.

name	reaction	hit conditions	ratio
t11pkl	$pp \to pK\Lambda$	≥ 1 start & ≥ 4 stop	1:1
t10pp	$pp \to pp$ elastic	≥ 1 start & ≥ 2 stop	1:100

Table 3.1.: Summary of trigger conditions and trigger ratios.

The data rate is limited by the dead time of the electronics in the read out system, which varies for different digitizing modules. The signals of all scintillators are digitized with ADC and TDC modules located in FastBus Crates [FB]. The read out of a FastBus crate has a total dead time of around 300 μs. The corresponding VME crate [VME] for the SQT read out has a similar dead time. Dedicated TDC electronics[4] were developed for the straw tube tracker with a much lower dead time of the full system of about $10 - 20\,\mu$s. The dead time of the FastBus crate determines the dead time of the whole DAQ system since all crates are read out in parallel. Therefore, taking only the data of the STT reduces the dead time by a factor of about 20 and accordingly increases the recorded event rate[5]. Due to the fact that the beam current is not randomly distributed but has a time structure in the millisecond range the effective event rate increases by about a factor of 3.

For roughly 90% of the data presented here the DAQ system was set in the mode of only collecting data from the STT. During the rest of the beam time all information was saved for checks and calibration purposes. An analysis of the data taken with and without the read out of the FastBus and VME modules shows no significant deviation in the observables.

---

[4] for a description of the electronics see Chapter 4 in [Uca06].

[5] The typical trigger rate is 3000 per second with a fractional deadtime of 75 % for the read out with the FastBus crates and a fractional deadtime of 25 % for the read out of the STT alone [Rod14].

An algorithm must be seen to be believed.

(Donald Knuth)

4. Event Reconstruction and STT Calibration

This chapter consists of two parts. First the event reconstruction is described with the individual tasks of track finding and fitting, vertex finding and fitting, $pK\Lambda$ geometrical reconstruction and finally kinematic fitting. The reconstruction software was already developed for former COSY-TOF measurements and is described in more detail in [Roe11]. Hence, only the important steps and features and some small modifications for the STT calibration are explained here. The second part of the chapter explains the different steps in the calibration procedure of the straw tube tracker. It starts from corrections of the raw TDC spectra and the relation of drift times to isochrone radius to the geometrical alignment and resolution of the straws.

4.1. Analysis Procedure

The analysis software for the reconstruction of the $pK\Lambda$ events from the isochrone radii informations of the STT was developed by R. Castelijns [Cas06] and improved by M. Röder [Roe11]. Therefore, only small modifications were needed here mainly for the calibration steps. The analysis routine is based on the programming language C++ combined with the package MINUIT [MINUIT] for least square fitting and the analysis framework ROOT [ROOT] for storing results from the different analysis steps. The complete package is linked as a library (tofStrawlib) to the main software tof++ [CTOF06c], which steers the input of the data and the setup of the geometrical information of the detectors. In addition, it converts TDC information to the corresponding times and isochrone radii with calibration files. However, the reconstruction of the $pp \to pK\Lambda$ reaction is only done with the straw tube tracker since the data from the other sub detectors was not available in 90% of the data at 2.7 GeV/c due to the modifications in the DAQ system to enhance the read out speed (see Section 3.4).

Without time of flight information, the $pK\Lambda$ event is kinematically determined by the event geometry. TOF measurements can in principle reduce further physical background, in particular from the $pp \to pK\Sigma^0$ reaction, which can not be separated purely by geometry. Nevertheless, the contribution of this background channel is neglibly small at 2.7 GeV/c, as shown in Section 6.3.3. In addition, as shown in [Roe11], the momentum resolution of the primary particles from the reconstruction with the STT alone is better than from TOF. Therefore, disregarding the time of flight information does not worsen the resolution but gives a much larger event sample. This was confirmed by comparing data taken with and without TOF information.

In the following, the different steps of the analysis routine are described.

4.1.1. Global Coordinate System

The global coordinate system for the event reconstruction is defined as an right-handed system with the origin in the target center. The beam direction correspond to the z-axis while the y-axis points upwards. Consequently, the x-axis points to the left when looking in beam direction. The spin of the beam protons is aligned parallel to the y-axis.

4.1.2. Track Finder and Fitter

The first step of the analysis routine is finding tracks from the isochrone radius information of the straw hits. This is done individually for each of the three rotational directions (u with rotation angles 0° and 180°, v with 60° and 240° and w with 120° and 300°) of the STT double layers producing two-dimensional tracks each. These are then combined to form three-dimensional tracks. In Figure 4.1 (top) the straw hits of a $pK\Lambda$ event candidate from data are shown for each of the three orientations. The axis u' v' and w' are perpendicular to the beam axis (z-axis) and the straw axis in each orientation (u, v and w). By blue lines possible tracks of charged particles are marked. The plots below show a zoom into the red marked areas of the top plots. Here the straw radii (large circles) and the isochrone radii (smaller circles) are visible for each hit. As seen in Figure 4.1, the two-dimensional tracks for a given orientation are obtained as a common tangent to the isochrones of their assigned hits. Therefore, tracks and their hits can be determined by the Hough Transformation method [Hou62, Dud72]. In this method tangents to all straw hits are determined and parametrized by an angle ϕ and the distance D to the origin, which is taken as the geometrical center of the STT. In Figure 4.2 the connection between the tangents (shown by the dashed lines) and the parameters is shown. It can be calculated as follows

$$D = a\sin(\phi) - z'\cos(\phi) \tag{4.1}$$

with a beeing u', v' or w' depending on the orientation and z' as the difference between z and the center of the STT. Parameter D is limited to the range $-40\,\mathrm{cm}$ to $40\,\mathrm{cm}$ by the straw geometry while ϕ is restricted to an interval of π to have an unique transformation from $a - z$ to $D - \phi$ coordinates. To avoid a reconstruction of tracks of δ electrons or from noise hits ϕ is further restricted in the intervall [0.3,2.8] radians, since such tracks are nearly parallel to the u', v' or w' axis, thus resulting in an angle of ϕ close to 0° or 180°.

In the Hough space, each hit emerges as a sinusoidal curve. After transforming all hits the curves intersect in a common point. Figure 4.3 shows the Hough space histograms for each of the three orientations for the hits in Fig. 4.1. The common

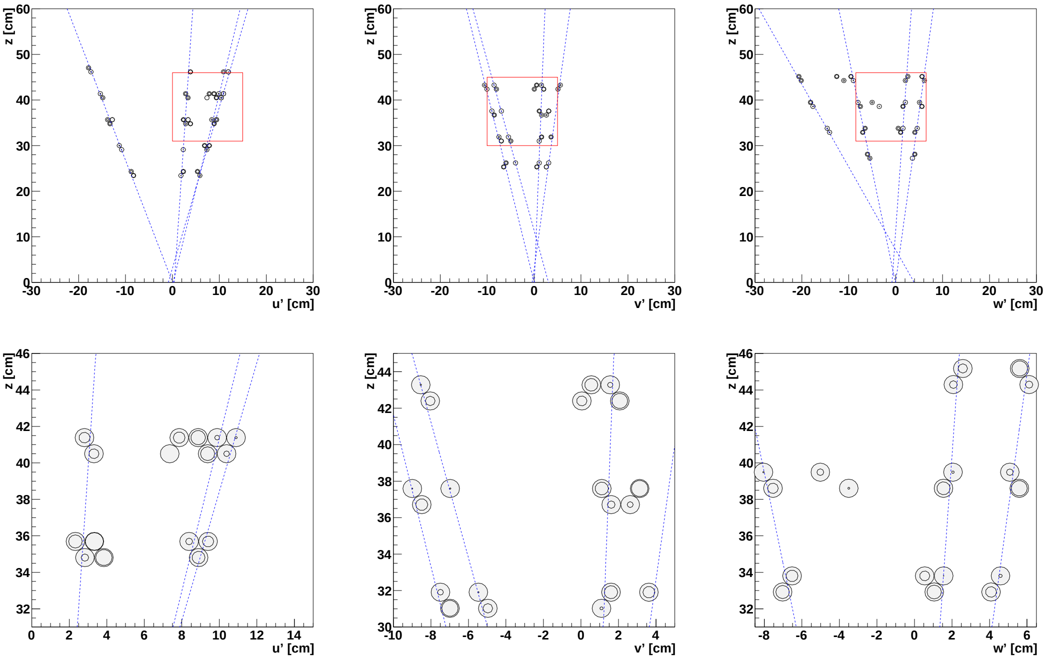

Figure 4.1.: Upper row: All straw hits with the corresponding isochrone radii for one $pK\Lambda$ event candidate. The axis u' v' and w' are perpendicular to the straw axis in each orientation (u, v, w) and the z-axis (beam direction). The dashed blue lines mark possible tracks to guide the eye. The regions marked in red are shown enlarged in the lower plots.

intersection points emerge as local maxima in the plots. They are marked with a red point in Fig. 4.3. In the left plot two red points are nearly on top of each other since two two-dimensional tracks are close together in this orientation. From the intersection points the track parameters and assigned hits are deduced in a loop from the highest maximum to the smaller one. In this iterative procedure, assigned hits are removed from the histogram to find the next highest maximum. A lower threshold for the height of a maximum is applied to reduce ghost tracks. After finding all possible tracks their parameters are optimized by a least square minimization of the track to isochrone distance with MINUIT [MINUIT]. If tracks share hits, the tracks with the poorer reduced χ^2 are removed from the next analysis steps. This also resolves ambiguities when several maxima have the same height, otherwise forming several possible tracks. Since the Hough space is a binned two-dimensional accumulator, the number of bins for D and ϕ are free parameters which need to be optimized for the track finding and event reconstruction (see Section 4.1.6).

After finding and fitting the two-dimensional tracks, they are combined to three-dimensional tracks. Since each two-dimensional track defines a plane, the intersection

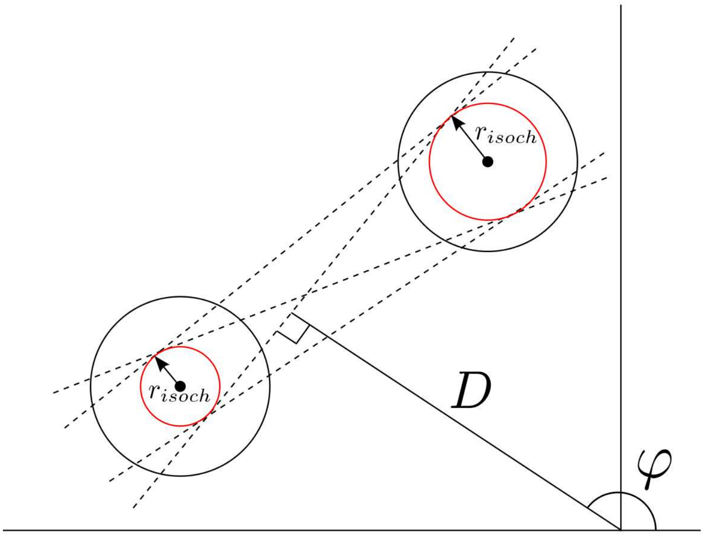

Figure 4.2.: Illustration of the correlation between the Hough space parameters D and ϕ to the isochrone radius. Taken from ([Dzh12]).

of two tracks from different orientations gives a three-dimensional track candidate if the planes are not parallel. The combined information of all three orientations is used to find out which tracks belong to the same particle track. For that purpose the two-dimensional tracks are combined to triplets. A triplet consists of a two-dimensional track of each rotational orientation. If n_u, n_v and n_w are the number of two-dimensional tracks in one rotational orientation, the number of triplets is $n_u \cdot n_v \cdot n_w$. For each triplet the three-dimensional track is calculated by averaging over all pairwise intersections of the two-dimensional tracks. Afterwards, the χ^2 values are determined for each triplet or rather its three-dimensional track by

$$\chi^2_{\mathrm{T}} = \sum_{i=1}^{N} \frac{(|d_3(\vec{p}, \vec{g}, \vec{w_i}, \vec{o_i})| - r_i)^2}{\sigma_i^2} \tag{4.2}$$

with the track to wire distance d_3 calculated by

$$d_3(\vec{p}, \vec{g}, \vec{w_i}, \vec{o_i}) = \frac{\vec{g} \times \vec{o_i}}{|\vec{g} \times \vec{o_i}|} \cdot (\vec{p} - \vec{w_i}). \tag{4.3}$$

$\vec{w_i}$ is the wire position of the ith straw hit and $\vec{o_i}$ is the corresponding orientation. The values for r_i, isochrone radius for hit i, and σ_i, the spatial resolution, are given by the calibration (see Section 4.2). The tracks are parametrized by a space point $\vec{p}$ and a direction $\vec{g}$.

The three-dimensional track with the best reduced χ^2 value is taken, and all other triplets are removed if they include one of the two-dimensional tracks. This is repeated

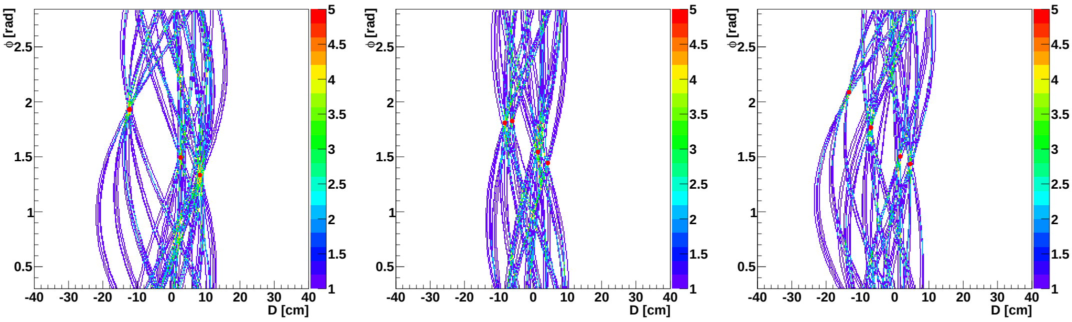

Figure 4.3.: Hough space for the three rotational orientations (left: $u' \widehat{=} 0°$, center: $v' \widehat{=} 60°$, right: $w' \widehat{=} 120°$) with the hits from Fig. 4.1. The red points mark regions with the four local maxima, corresponding to the four tracks. In the left plot two marks are nearly on top of each other, since two tracks are close together.

iteratively with the other tracks until no three-dimensional track with $\chi^2/\mathrm{NDF} < 5$ remains.

If some tracks could not be grouped into a triplet because one two-dimensional track in one of the three orientations is undetected, the remaining two-dimensional tracks are combined into a three-dimensional track and the third orientation is scanned for not assigned hits which fulfill the track parameters. The number of such hits is taken as a criterion for additional three-dimensional tracks as a combination of only two two-dimensional tracks (for details see Section 4.1.1 in [Roe11]).

After finding the three-dimensional tracks, the value of Equation 4.2 is minimized for each tracks with MINUIT [MINUIT]. Two additional corrections are performed afterwards. The first one accounts for hits which are assigned to the tracks accidentally because of the binning of the Hough space, e.g. hits from δ-electrons. To remove these hits an outlier test is conducted. For each track the mean value of the residuals is calculated. The hit is discarded from the track, and the track is refitted if the residual from a hit deviates by more than five times the resolution from the mean value. This is done iteratively for all hits starting from the one with the biggest deviation. The second correction removes hits which are assigned to two or more tracks. This can happen if two tracks are close together in one orientation like the blue and green track in orientation u' in Figure 4.4. For the following analysis shared hits are not allowed.

In Figure 4.4 the fitted three-dimensional tracks are shown in each orientation (u', v' and w') for the same event shown in Figure 4.1 and 4.3. The marked areas from the first row are shown enlarged in the second row, respectively. The color code indicates different tracks with the assigned hits in the same color. Black hits are not used for the fitting because of shared hits or outliers or noise.

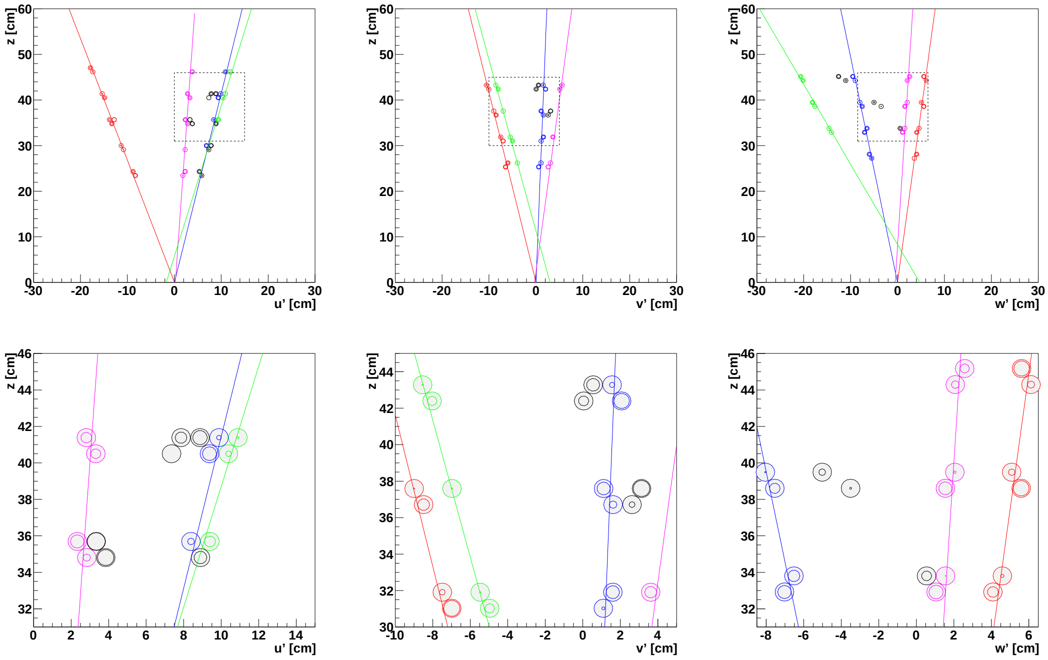

Figure 4.4.: Upper row: Three dimensional tracks with their assigned hits shown in each orientation u', v' and w'. Black colored hits are not used for the fitting (i.e. shared hits or outliers). The black marked regions are shown enlarged in the plots in the lower row.

4.1.3. Vertex Finder and Fitter

In the next step of the analysis pairs of tracks are combined to find vertices (for details see Section 4.2 in [Roe11]). This is done independently from the reactions, therefore the $pp \to pp$ reaction gives one vertex and the $pp \to pK\Lambda$ reaction two separated vertices (a primary and a secondary vertex). For all pairs of tracks the vertex is calculated as the point of closest approach from one track to the other. The determined vertices are sorted by the minimum distance from the corresponding tracks. Starting at the vertex with the smallest minimum distance, all other vertices with the same tracks are removed. This is done iteratively until all vertices have unique assigned tracks.

Afterwards the tracks are fitted again by calculating a combined χ^2 for both tracks taking the constraint of the common vertex into account.

4.1.4. $pK\Lambda$ Finder and Geometrical Fit

If two separate vertices are found, the $pp \to pK\Lambda$ reaction is fitted purely by geometry before a kinematic fit is performed. An addtional constraint for the geometrical fit exists without the kinematics because the Λ decay plane must contain the primary vertex. In total 13 parameters are necessary to describe the event: three parameters each for the location of the primary and secondary vertices. The two tracks from the primary vertex each have two parameters describing the direction of the tracks. The same holds for the tracks of the secondary vertex but with the Λ track calculated by the difference of the primary to secondary vertex $\vec{\Lambda} = (\vec{s} - \vec{p})/(|\vec{s} - \vec{p}|)$ and the angle ϕ between the decay products the directions of one secondary track can be calculated directly. This reflects the constraint of the Λ decay plane. If the directions of the secondary particles are $\vec{g}_{s1}$ and $\vec{g}_{s2}$ then $\vec{g}_{s2}$ is calculated by the rotation of $\vec{g}_{s1}$ by ϕ around the normal of the decay plane: $\vec{g}_{s2} = R(\phi, \vec{n}_\Lambda) \cdot \vec{g}_{s1}$.

Therefore, the 13 parameters are: $p_x, p_y, p_z, \vec{g}_{p1}, \vec{g}_{p2}, s_x, s_y, s_z, \vec{g}_{s1}, \phi$. The event is fitted with MINUIT by minimizing the sum of the χ^2 values of the four tracks

$$\begin{aligned} \chi^2_{\mathrm{G}} &= \chi^2_{\mathrm{T}}(\vec{p}, \vec{g}_{p1}, \mathbf{w}_1, \mathbf{o}_1, \mathbf{r}_1, \boldsymbol{\sigma}_1) + \chi^2_{\mathrm{T}}(\vec{p}, \vec{g}_{p2}, \mathbf{w}_2, \mathbf{o}_2, \mathbf{r}_2, \boldsymbol{\sigma}_2) \\ &+ \chi^2_{\mathrm{T}}(\vec{s}, \vec{g}_{s1}, \mathbf{w}_3, \mathbf{o}_3, \mathbf{r}_3, \boldsymbol{\sigma}_3) + \chi^2_{\mathrm{T}}(\vec{s}, R(\phi, \vec{n}_\Lambda) \cdot \vec{g}_{s1}, \mathbf{w}_4, \boldsymbol{o}_4, \mathbf{r}_4, \sigma_4). \end{aligned} \tag{4.4}$$

The $\mathbf{w}_i$ and $\mathbf{o}_i$ values are the wire positions and orientations of each hit for the individual tracks and the $\mathbf{r}_i$ and $\boldsymbol{\sigma}_i$ the isochrone radius and resolution values, respectively.

If the geometrical fit does not converge, χ^2_{G} is set to -1 and the kinematic fit is not applied. In the other case the fit values are taken as the start parameters for the kinematic fit described in the next section.

4.1.5. $pK\Lambda$ Kinematic Fitter

The last step of the event reconstruction is the application of a kinematic fit to the events after the geometric fit. For that purpose momentum and energy conservation is imposed and the masses of all particles are used as input parameters. The masses of the decay particles can be assigned directly because the decay proton has a higher mass than the pion thus it always has the lower angle relative to the Λ particle. For the primary particles the masses can not be deduced purely by geometry because it is unclear which prompt track is the proton or kaon. Therefore, both possibilities are used in the kinematic fit and the only one with the better χ^2 value is considered for the further analysis.

The $pp \to pK\Lambda$ reaction is divided into three $1 \to 2$ particle reactions to simply the calculation and parametrization of the event. The three sub-reactions are

- $\mathbf{pp} \to [\mathbf{p}\boldsymbol{\Lambda}]\mathbf{K}$ is parametrized with the primary vertex $\vec{p}$, the $p\Lambda$ invariant mass $m_{p\Lambda}$ and the direction of the kaon in the CM frame given by the angles $\cos(\theta^*_K)$ and ϕ^*_K (six parameters in total)
- $[\mathbf{p}\boldsymbol{\Lambda}] \to \mathbf{p}\boldsymbol{\Lambda}$ is parametrized by the direction of the proton in the $p\Lambda$ rest frame given by the angles $\cos(\theta^{**}_p)$ and ϕ^{**}_p (two parameters in total)
- $\boldsymbol{\Lambda} \to \mathbf{p}\pi$ is parametrized by the Λ flight length s_Λ and the direction of the decay pion in the Λ rest frame given by the angles $\cos(\theta^{***}_\pi)$ and ϕ^{***}_π (three parameters in total)

The secondary vertex can be calculated by $\vec{s} = \vec{p} + s_\Lambda \cdot \vec{p_\Lambda} / |\vec{p_\Lambda}|$. Given the total energy $\sqrt{s}$ and the masses of all particles and mass subsystems the magnitudes of the momentum vector of every particle can be determined in the corresponding rest frame by

$$|\vec{p}_1| = |\vec{p}_2| = \frac{\sqrt{(M^2 - (m_1 + m_2)^2) \cdot (M^2 - (m_1 - m_2)^2)}}{2M} \tag{4.5}$$

taking the relevant values for M, m_1 and m_2. Finally, the four-vectors of all particles can be calculated by Lorentz transformations. Therefore, the event kinematics can be described solely by the 11 parameters: $\vec{p}, \cos(\theta^*_K), \phi^*_K, m_{p\Lambda}, \cos(\theta^{**}_p), \phi^{**}_p, s_\Lambda, \cos(\theta^{***}_\pi), \phi^{***}_\pi$. There are two fewer parameters then for the geometric fit because of the constraints imposed by momentum conservation at the vertices.

The minimization uses different sets of start values which are determined by leaving out different measured values for the particles in order to obtain energy and momentum conservation. They would be violated by using only the values from the geometrical fit (for details see Section 4.4.2 in [Roe11]). The value for the invariant mass is limited to the allowed physical region from $m_p + m_\Lambda \leq m_{p\Lambda} \leq m_{p\Lambda,\mathrm{max}}$ in the fitting procedure to circumvent problems in the calculation with Equation 4.5.

The fit is done by minimizing the target function

$$\begin{aligned} \chi^2_\mathrm{K} &= \chi^2_\mathrm{T}(\vec{p}, \vec{g}_p, \mathbf{w}_p, \mathbf{o}_p, \mathbf{r}_p, \boldsymbol{\sigma}_p) + \chi^2_\mathrm{T}(\vec{p}, \vec{g}_K, \mathbf{w}_K, \mathbf{o}_K, \mathbf{r}_K, \boldsymbol{\sigma}_K) \\ &+ \chi^2_\mathrm{T}(\vec{s}, \vec{g}_{p(\Lambda)}, \mathbf{w}_{p(\Lambda)}, \mathbf{o}_{p(\Lambda)}, \mathbf{r}_{p(\Lambda)}, \boldsymbol{\sigma}_{p(\Lambda)}) + \chi^2_\mathrm{T}(\vec{s}, \vec{g}_\pi, \mathbf{w}_\pi, \mathbf{o}_\pi, \mathbf{r}_\pi, \boldsymbol{\sigma}_\pi) \end{aligned} \tag{4.6}$$

with the χ^2 values of the tracks assigned to the measured particles (primary proton p and kaon K and Λ decay particles $p(\Lambda)$ and π).

Figure 4.5 shows the event after the kinematic fit from the previous figures in each of the rotational orientations u', v' and w' . The yellow points marks the primary and secondary vertex positions. Therefore, the red and blue lines show the tracks of the primary particles while the violet and green lines the tracks of the decay particles. The black dotted line shows the Λ track. From this one can deduce that the violet line corresponds to the decay proton and the green line to the pion since the pion must have a higher angle relative to the Λ particle. The lower plots show an expanded region from the primary to the secondary vertex.

4.1.6. Hough Binning

As mentioned in Section 4.1.2, the event reconstruction is sensitive to both the bin size of the Hough space and the threshold to find a peak. If the binning is too coarse, tracks close to each other can not be reconstructed and thus the overall reconstruction efficiency drops. On the other hand if the binning is too high the computational time for the analysis increases and the hits of a track are distributed in more than one bin reducing the height of the peak, and thus the efficiency to find it. Additionally, the threshold value to find the peaks in the Hough space must be adjusted accordingly to the binning.

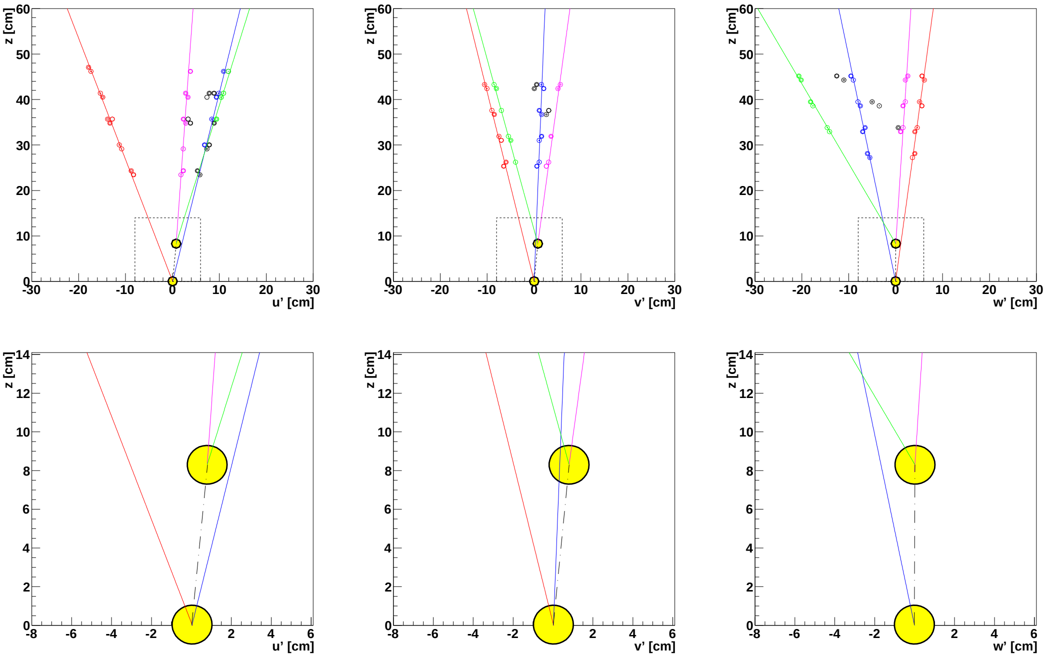

Figure 4.5.: Tracks of a $pK\Lambda$ event after the kinematic fit shown in each orientation u', v' and w'. The yellow points mark the primary and secondary vertices. The black dotted line shows the track of the Λ. The green and violet tracks correspond to the decay particles while the red and blue lines show the primary particles proton and kaon. The black marked regions are shown enlarged in the plots in the lower row.

Therefore, the dependence of the reconstruction efficiency on the computational time was performed with a dedicated data run. Since the software package does not allow to dynamically change the binning, only some values for the binning were studied. The reference value for the binning is $(D, \phi) = (200, 160)$ with a threshold of 4. This was used in the previous COSY-TOF $pp \to pK\Lambda$ analysis with the STT [Roe12], and it was determined to be a good "working point" for the $pp \to pK_s\Sigma^+$ analysis (Section 5.2.2 in [Dzh12]). Thus, the values for efficiency and computational time are given relative to the values for the working point. For the $pK\Lambda$ events the selection criteria described in Chapter 6 are used and one full run was analyzed. The computational time was determined with the first 2000 events of the same run to avoid systematic errors from additional usage of the analysis computer. The results from this study are shown in Table 4.1.

The table shows an increase of the efficiency for a finer Hough binning. The relative efficiency is relatively constant for a binning finer than $(500, 400)$. However, the computational time grows rapidly. When comparing the settings 1. and 4. with 5. and 6., it follows that the threshold value should be set accordingly to the binning. Otherwise

Setting	D bins	ϕ bins	threshold	relative efficiency	relative computational time
1.	200	160	4	1	1
2.	100	80	4	0.71	0.63
3.	200	160	6	0.59	0.60
4.	200	160	3	1.10	1.14
5.	300	200	4	0.98	1.45
6.	300	200	3	1.19	1.59
7.	400	300	3	1.24	2.48
8.	500	400	3	1.28	3.45
9.	600	500	3	1.28	4.74

Table 4.1.: Relative efficiency and computational time for different binning of the Hough space and the threshold condition for a maximum therein.

it overcompensates the positive effect of the finer binning. The settings for the values should be chosen such, that the relative efficiency is high and the relative computational time as low as possible. Therefore, the parameters from setting 7 $(400, 300, 3)$ are taken for the analysis of the data presented in this thesis. This results in a improvement of the reconstruction efficiency by roughly 25% compared to the previous settings.

4.2. Calibration of STT

The main aim of the calibration is to find the correlation between the measured TDC (Time to Digital Converter) time and the minimum distance of the particle track to the wire (= isochrone radius). Afterwards the mean resolution for each double layer is determined. The resolution is directly used as the weight of a hit in the reconstruction procedure. An improved resolution allows for better track separation in the Hough space because finer binning can be used. Several effects reduce the overall resolution and most of these are corrected in the calibration. This includes corrections to the raw TDC spectra such as a selection on the first hit and TDC offset corrections of the individual electronic modules. Additionally, the limited precision of the geometrical alignment of the STT reduces the resolution. The alignment is determined and corrected from data after the isochrone calibration.

In the next sections first the corrections on the raw TDC spectra are shown and explained. Second the track to wire calibration is shown followed by the geometrical alignment. Finally, the spatial resolution of each double layer is determined. Further details of the procedures are given in [Roe11, Dzh12, Jow12, Jow13a, Jow13b, Jow14].

4.2.1. Basic Corrections

When a charged particle crossing a straw it ionizes the gas inside. The ionization signal is recorded and its leading and tailing edges are stored as a TDC value. The start time of the time measurement is given by the start detector of COSY-TOF. The TDC value is related to the real time by $t = TDC \times 0.09259\,\mathrm{ns}$ where TDC corresponds to the channel and the conversion factor is given by the electronics. Before the time to isochrone radius correlation is determined some corrections are applied.

A charged track generally creates several clusters along its path through a straw, which all can be recorded but the main information is contained in the first cluster closest to the wire. Therefore, the TDC values related to the leading and trailing edges of a signal are sorted and the highest value in a given interval (corresponding to the allowed time region where a ionization can be) is taken. This value is equivalent to the smallest drift time hence to the closest cluster to the wire. Thus, all other values are neglected in the calibration and analysis later. Furthermore, the width is limited to $> 5\,\mathrm{ns}$ to suppress noise from the electronics (for details see [Jow14]).

The last correction of the time spectra is the correction of time offsets from the electronics. This is done individually for each straw by fitting the falling edge of the time spectrum with the convolution of the error function and a constant, taking noise into account (see also Chapter 6.2 in [Voigt09] and [Jow13b]). The fit determines the turning point of the spectrum and the width. Then the spectrum is corrected in such a way that the turning point is shifted to a common arbitrary time value of 780 ns. Applying the offset corrections[1] to all straws, the overall spread of the turning points reduces from $\sigma \approx 2\,\mathrm{ns}$ to $\sigma \approx 0.2\,\mathrm{ns}$ [Jow14].

In Figure 4.6 (left) the resulting time spectrum for double layer 7 is shown including all described corrections for the raw spectrum. Because the time signal is measured in a common stop mode large time values correspond to a short drift time (ionization close to the wire) and small time values to long drift times (ionization close to the wall of the straw). The width of the right slope of the spectrum is about 2.5 ns. Therefore, the right side cut off is chosen to be 785 ns (turning point $+ 2 \times$ width). Therefore, a drift time of 0 ns corresponds to a time value of 785 ns. The resulting drift time spectrum from the time spectrum is shown in the right plot in Figure 4.6. The tail part on the left side of the time spectrum in Figure 4.6 stems from improper recognition of the closest cluster to the wire and event mixing. Since only $\sim 1\%$ of the hits are in this region, they are neglected in the analysis. Therefore, the time values of a hit should be in the range of 645 ns to 785 ns and other time values are cut away giving a drift time interval of 0 ns to 140 ns. In the next section the determination of the correlation between drift time and isochrone radius is described.

---

[1] The values to correct straws with a very small number of entries are determined by a linear interpolation between the surrounding straws.

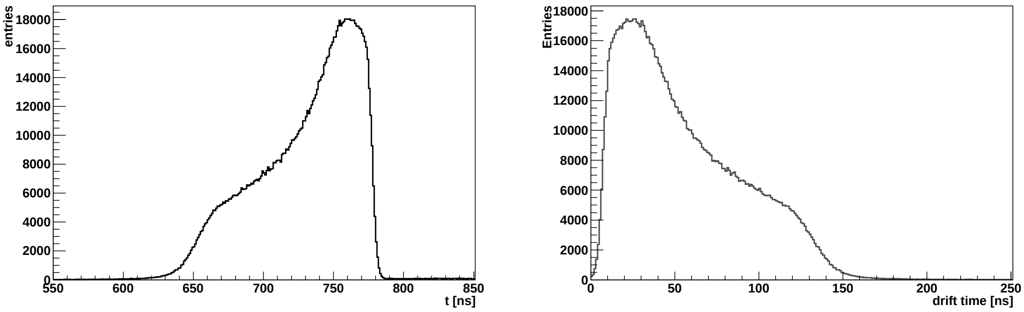

Figure 4.6.: Stop time spectrum for the STT double layer 7 after applying the basic corrections (left). Drift time spectrum for the same double layer (right).

4.2.2. Track to Wire Calibration

The determination of the correlation between the drift time and the isochrone radius is done in two steps each using a different method. The first method is called the "self calibrating" method and it calculates the general shape of the drift time to isochrone radius curve. Its result is improved afterwards with the "distance to track" method by taking into account reconstructed tracks.

In the **"self calibrating"** method it is assumed that the straws are homogeneously illuminated by the tracks and the detection efficiency is constant over the whole straw diameter [Roe11, Dzh12]. Thus, the following relation for the density of hits as a function of radius can be constructed:

$$\frac{\mathrm{d}N}{\mathrm{d}r} = \frac{N_{\mathrm{tot}}}{R}, \tag{4.7}$$

with the straw radius $R = 5\,\mathrm{mm}$ and the total number of entries N_{tot} in the time spectrum. This can be related to the drift time as follows:

$$\frac{\mathrm{d}N}{\mathrm{d}t} = \frac{\mathrm{d}N}{\mathrm{d}r}\frac{\mathrm{d}r}{\mathrm{d}t} = \frac{N_{\mathrm{tot}}}{R} v_{\mathrm{drift}}(t). \tag{4.8}$$

Integration of Equation 4.8 gives:

$$r(t_{\mathrm{i}}) = \int_{t_0}^{t_{\mathrm{i}}} \mathrm{d}t v_{\mathrm{drift}}(t) = R\frac{\sum_i N_i}{N_{\mathrm{tot}}}, \tag{4.9}$$

with N_i being the number of events in the time interval between t_0 and t_{i}. t_0 corresponds to the shortest drift time. To take into account inefficiencies in the straw tube in the avalanche region near the anode wire Equation 4.9 was modified to

$$r(t_{\mathrm{i}}) = (R - R_{\mathrm{wire}})\frac{\sum_i N_i}{N_{\mathrm{tot}}} + R_{\mathrm{avalanche}}, \tag{4.10}$$

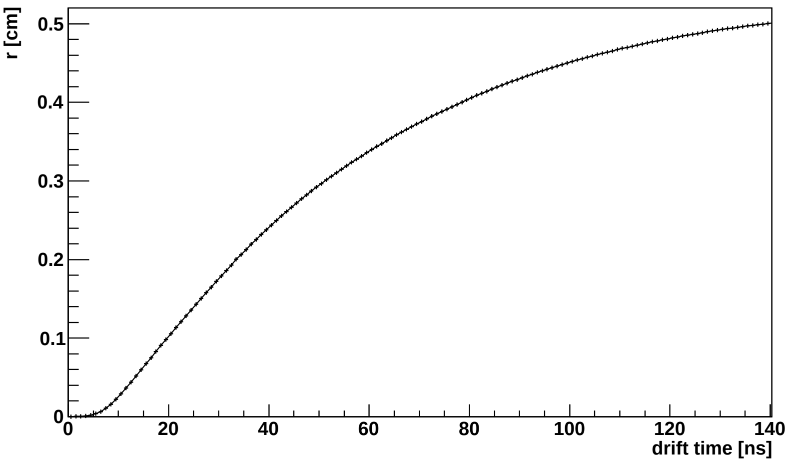

Figure 4.7.: Drift time to isochrone radius curve determined by the self calibrating method for double layer 7.

with $R_{\mathrm{wire}} = 0.01\,\mathrm{mm}$ and $R_{\mathrm{avalanche}} = 0.02\,\mathrm{mm}$. For the calculation of $r(t_{\mathrm{i}})$ the drift time spectrum is divided into 140 bins, each with width of 1 ns. Then Equation 4.10 is evaluated for each double layer, and t_{i} is the center value of a bin. The resulting drift time to radius curve is shown in Figure 4.7. Since all straws in the double layers have the same structure, the resulting $r(t)$ curve should be the same for all double layers. Unfortunately, they differ slightly from each other due to differences in the electronics (amplification and sensitivity). But the curves can be arranged into three groups (1,2,3,4), (5,11,12,13) and (6,7,8,9,10). For each group the same $r(t)$ curve will be used for the further analysis (for details see [Jow14]).

Tracks with at least 18 hits are reconstructed and fitted using the $r(t)$ curves. From these tracks the track to wire distances for the hits are calculated. The correlation of the calculated distance with the known drift time is shown in Figure 4.8. The two branches of the plot result from the ambiguity of a track being on the left or right side of the wire. This is the basis of the **"distance to track"** method. This is an iterative procedure where the most probable correlation of drift time to isochrone radius is calculated from Figure 4.8 (for details see [Jow14]), and the resulting $r(t)$ curve is then used in the track reconstruction. Afterwards the correlation is calculated again and the tracks are reconstructed. The procedure is stopped when the distribution of the track residual mean values is close to zero within the errors for all double layers. The track residuals are the difference of the track to wire distance from a fitted track and the isochrone radius predicted by the used $r(t)$ curve. On the left side of Figure 4.9 the track residual distribution versus drift times is shown for double layer 7 after five iteration steps. On the right side the same distribution is plotted versus the isochrone radius calculated from the $r(t)$ curve.

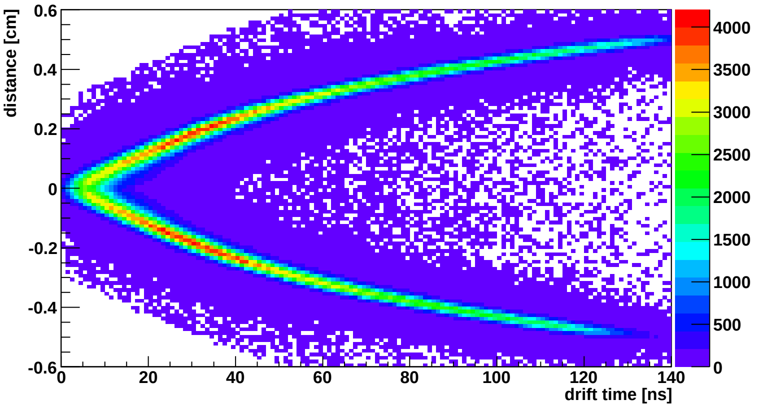

Figure 4.8.: Correlation of the drift time versus the track to wire distance for double layer 7.

To determine the mean and sigma value of the distribution each x-bin is projected on the y-axis and fitted with a Gaussian function. The deviation of the mean value reflects the quality of the calibration step of the distance to track method while the sigma value of the Gaussian fit determines the spatial resolution of the double layer. It turned out that after 5 steps of the distance to track method the mean values of all double layers are distributed around zero. The $r(t)$ curve for double layer 7 is shown in Figure 4.10. To improve the calibration further, the correct geometrical position of all double layers has to be taken into account. Therefore, the geometry calibration is explained next.

4.2.3. Geometry Calibration of the Double Layers

The positions of each straw tube in a double layer is known very precisely due to the compact setup in a double layer and the self supporting structure. Therefore, only errors in the alignment of the double layers is taken into account. In general this can be translations and rotations around all three axis. Since the layers are close together along the beam direction, rotation corrections around the x- and y-axis as well as shifts in beam direction and along the wire are neglected. Therefore, the resulting corrections applied are a shift perpendicular to the beam direction and the wire (y' direction) and a rotation around the beam axis. The details of the geometrical corrections can be found in [Roe11, Jow13b, Jow14], thus only the important feature are described here. "Unbiased" tracks are reconstructed to determine the corrections. In this context unbiased means that the corresponding hits of a track in a double layer under consideration are removed and the track is refitted. The track to wire distances for the corresponding double layer are then calculated from the refitted tracks.

Any shift in the y' direction emerges as a difference between the mean values of the track to wire distances for the two wings in the distance to drift time plot (see Figure

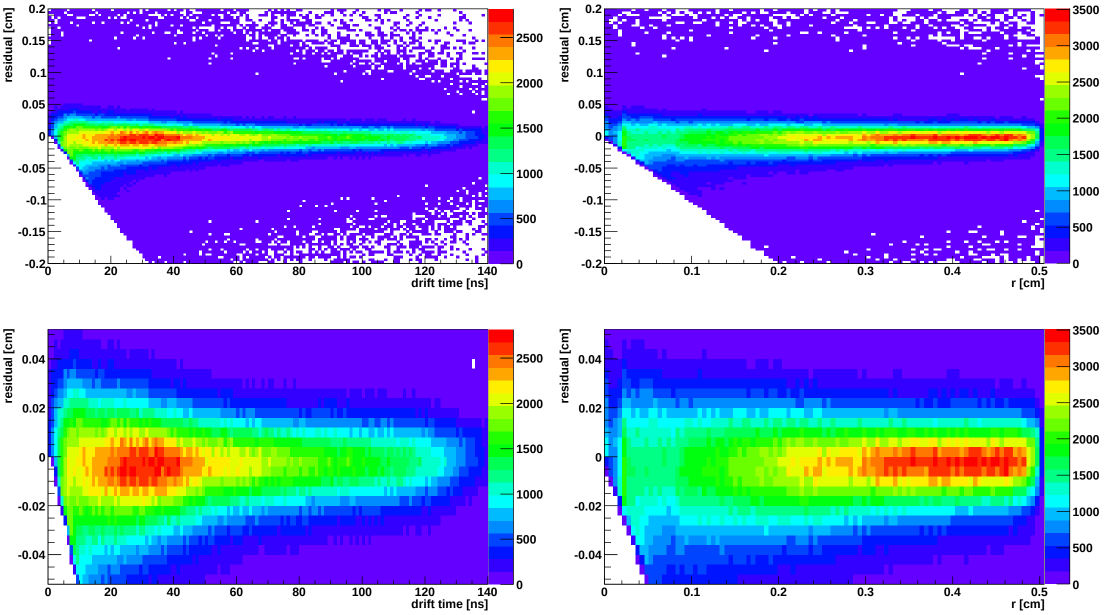

Figure 4.9.: Left: Track residuals plotted versus the drift time for double layer 7 after five iterations of the distance to track method. **Right:** Track residuals plotted versus isochrone radius calculated from the $r(t)$ curve for double layer 7 for the same iteration step. The area of the upper plots from $-0.05\,\text{cm}$ to $0.05\,\text{cm}$ of the y-axis is shown enlarged in the lower plots.

4.8) because a systematic misalignment gives higher distance values on one side of the wire and lower values on the other side. In an iterative procedure the differences of the mean values are determined and the double layer with highest shift is corrected for the next iteration until the shifts of all double layers are below $50\,\mu\text{m}$.

For the rotation correction the residuals of the "unbiased" tracks are plotted as a function of the position along the wire. Now rotation misalignments emerge as a rotation of the mean residual values around the straw middle point. The mean values are determined by the residual distribution fitted with a Gaussian function for narrow bins of the length along the wire. The rotation correction angle is given by the slope of the resulting linear dependence between the mean value and the position along the wire. The rotation corrections are applied iteratively starting from the double layer with the largest angle until the deviations are smaller than 0.5 mrad.

After applying all geometry corrections the track to wire calibration has been repeated and the final $r(t)$ curves and resolutions are determined for each double layer.

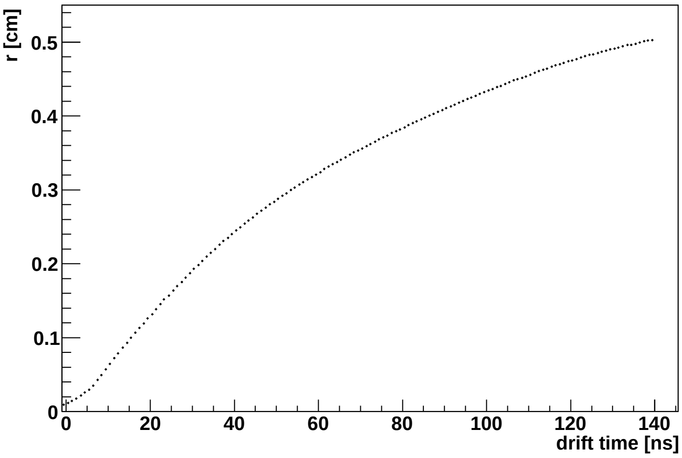

Figure 4.10.: Drift time to isochrone radius curve for double layer 7 determined by the distance to track method after 5 iterations. The range from 0 to 10 ns is extrapolated by a Gaussian function.

4.2.4. Spatial Resolution of the STT Double Layers

The spatial resolution of each double layer is determined using the track residual to drift time spectrum (see Figure 4.9 left). In the range from 15 ns to 140 ns the y-projections of each x-bin is fitted with a Gaussian function. Its width (σ) corresponds to the spatial resolution for the drift time value of the x-bin. With the $r(t)$ curve the isochrone radius is calculated for each drift time. Figure 4.11 shows the resulting resolution to isochrone radius distribution for double layer 7. As expected the resolution improves from the wire to the wall. The deviations close to the wire arise from the asymmetric distributions in the projections of the residuals where the Gaussian function does not describe the data properly anymore. Therefore, the resolution distribution is fitted with a second order polynomial from 0.1 cm to 0.5 cm. This is shown as the red function in Figure 4.11. For each double layer the function is determined, and it is used to calculate the weight of a straw tube hit with the corresponding isochrone radius for the χ^2 fits in the analysis procedure. No significant difference in the shapes of the curves for each double layer is observed. Therefore, the corrections to the time spectra and geometry are done with a similar quality for each double layer.

For a more quantative comparison, the σ values at a radius of 0.25 cm are summarized in Table 4.2 for all double layers. In addition, the values from the previous calibration in [Dzh12] are also given.

With the new calibration the resolution is improved for most of the double layers by about 10 μm. The averaged value over all double layers is 137 μm (compare with 146 μm from [Dzh12]). The fluctuations of the resolution of each double layer around this mean

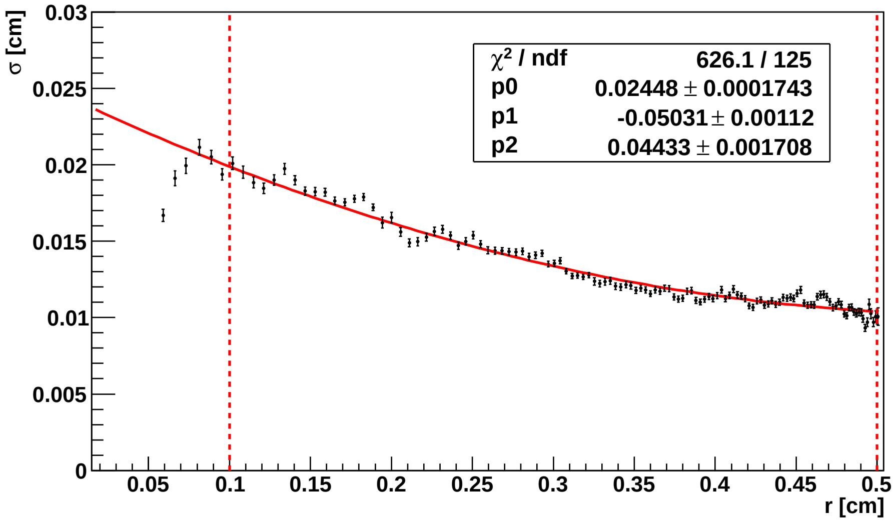

Figure 4.11.: Resolution of double layer 7 as a function of the isochrone radius. The dashed red lines mark the range of the fit with a polynomial function of second order shown in red.

double layer	1	2	3	4	5	6	7	8	9	19	11	12	13
$\sigma_{0.25\,\mathrm{cm}}[\mu\mathrm{m}]$	136	143	125	136	136	145	152	151	135	137	134	118	132
σ [Dzh12]	140	142	136	146	160	146	164	161	146	141	144	135	139

Table 4.2.: Spatial resolution for each double layer at an isochrone radius of 0.25 cm. The results from [Dzh12] are shown for comparison.

value is similar for both calibrations, hence the new calibration should not include new systematic errors compared to the last one. Furthermore, there is no indication for a systematic change of the resolution of the first and last group of double layers in comparison with the middle double layers. This could happen if the quality of the track parameters is different between an interpolation from outer double layers to the inner ones compared to an extrapolation from the inner double layers to the outer ones.

In contrast to previous Monte Carlo simulations the position resolution is implemented separately for each double layer taking into account the corresponding resolution curves. This gives an adequate description of the data. The results of the simulations can be found in Chapter 6.

Ein Merkmal eines guten Detektors ist die Möglichkeit der Rekonstruktion des einlaufenden Strahls.

(Kurt Kilian)

5. $\vec{p}p \to pp$ Analysis and Beam Properties

The analysis of the elastic scattering process $\vec{p}p \to pp$ is applied to determine the beam polarization with the known analyzing power from the partial wave analysis SAID [SAID]. In addition, the reaction is used to determine properties of the incoming beam beside its polarization and the target position relative to the straw tube tracker through the distribution of the elastic vertices.

5.1. $pp \to pp$ Selection and Reconstruction

The first step in selecting elastic scattered events is the condition imposed by the elastic trigger (see Section 3.4). Furthermore, the reconstructed event must have two tracks and one vertex. If this is fulfilled the kinematics of the elastic scattering can be calculated from the geometrical information after the vertex fit (see Section 4.1.3).

Momentum conservation at the pp elastic scattering vertex is $\vec{p}_{\mathrm{beam}} = \vec{p}_1 + \vec{p}_2$ because the target is at rest. $|\vec{p}_{\mathrm{beam}}| = 2700\,\mathrm{MeV}/c$ is the beam momentum for the measurement presented in this thesis, and $\vec{p}_1$ and $\vec{p}_2$ are the momenta of the two outgoing protons. The polar angle to the beam direction of each outgoing proton is known from the geometry, and it is

$$\theta_{1,2} = \arccos\left(\frac{\vec{p}_{\mathrm{beam}}}{|\vec{p}_{\mathrm{beam}}|} \cdot \frac{\vec{p}_{1,2}}{|\vec{p}_{1,2}|}\right). \tag{5.1}$$

The momenta of the outgoing protons are chosen in the way that $\theta_1 < \theta_2$ is valid for all events. With the polar angles the longitudinal and transversal momenta can be calculated by

$$p_\perp = |\vec{p}_{\mathrm{beam}}| \cdot \frac{\tan(\theta_1)\cdot\tan(\theta_2)}{\tan(\theta_1)+\tan(\theta_2)} \tag{5.2}$$

$$p_{\parallel\,1,2} = \frac{p_\perp}{\tan(\theta_{1,2})}. \tag{5.3}$$

The absolute value of the proton momenta is

$$|\vec{p}_{1,2}| = \sqrt{p_\perp^2 + p_{\parallel\,1,2}^2}\,. \tag{5.4}$$

Figure 5.1 shows the $p_\perp$ versus $p_\parallel$ distribution for the elastic triggered events reconstructed with two tracks and one vertex. The distribution has to be symmetric around

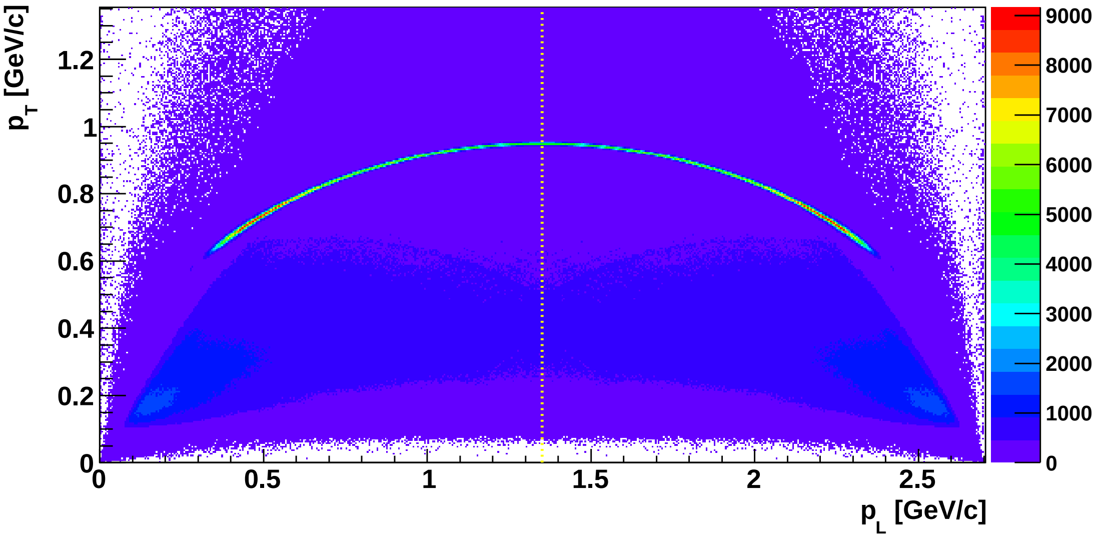

Figure 5.1.: $p_\perp$ versus $p_{||}$ distribution for the elastic triggered two track events. The momenta are calculated by Equation 5.2 and 5.3. The $pp \to pp$ elastic events appear in the enhanced ellipse over a large background. The dotted yellow line marks the symmetry axis of the event topology. Right of the line are the protons with the smaller scattering angle θ_1 and left of the line are the protons with the larger scattering angle θ_2.

the yellow dotted line at $p_{\text{beam}}/2$ because the momentum information of both protons is plotted. Thus, right of the line are all protons with the smaller scattering angle θ_1 and right of the line the protons with the scattering angle θ_2. An enhanced ellipse is visible above a large smooth background. The $pp \to pp$ elastic events lay inside this ellipse. Enhancements due to other types of two tracks events such as $pp \to d\pi^+$ are not visible. The background stems mostly from pion production reactions with three particles in the final state with one neutral particle[1] i.e. $pp \to pp\pi^0$. Therefore, two additional constraints are applied for the event selection (see also Section 6.2 in [Roe11] and Section 6.1 in [Dzh12]).

Assuming the proton mass, the four vectors of the two final state particles are obtained. Thus, the missing four vector P_{miss} is defined by

$$P_{\text{miss}} \equiv P_{\text{beam}} + P_{\text{target}} - P_1 - P_2. \tag{5.5}$$

Since the momentum conservation is used in the determination of the final state vectors, the missing four vector is $P_{\text{miss}} = (E_{\text{miss}}, 0, 0, 0)^T$. The missing energy E_{miss} could deviate from zero because the tracks could be reconstructed imprecisely or the event

---

[1] Neutral particles can not be seen directly by the straw tube tracker.

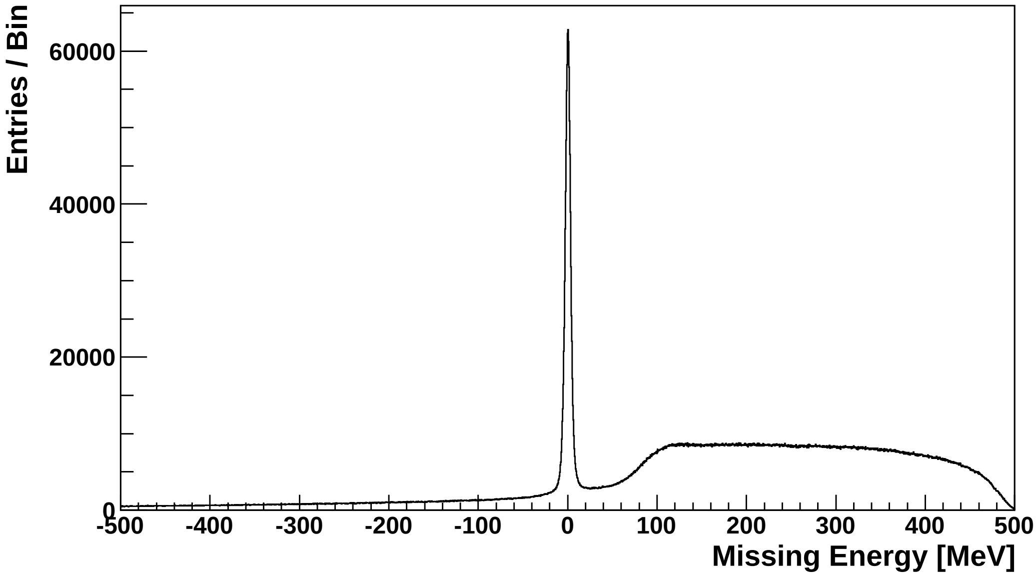

Figure 5.2.: Missing energy distribution for the elastic triggered two track events. The peak around zero stems from $pp \to pp$ elastic events.

does not stem from the $pp \to pp$ reaction. Therefore, E_{miss} is used as one additional constraint for the event selection. Its distribution is shown in Figure 5.2 for all events already plotted in Figure 5.1. The peak can be fitted with a Gaussian with a standard deviation of $\sigma_{\mathrm{miss}} \approx 3.2\,\mathrm{MeV}$.

The other constraint is the coplanarity of the events. For a $2 \to 2$ process in a fixed target experiment the vectors $\vec{p}_1$ and $\vec{p}_2$ span a plane that must contain the beam direction. Thus, the normal vector of the plane is orthogonal to the beam direction and the cosine of the angle α between the normal vector and the beam momentum is zero. The cosine C is calculated by

$$C \equiv \cos(\alpha) = \left(\frac{\vec{p}_1}{|\vec{p}_1|} \times \frac{\vec{p}_2}{|\vec{p}_2|} \right) \cdot \frac{\vec{p}_{\mathrm{beam}}}{|\vec{p}_{\mathrm{beam}}|}. \tag{5.6}$$

Here C is a quality criterium of the coplanarity of the events. Its distribution is shown in Figure 5.3. The two track events which are coplanar appear as a peak around zero. The width of the peak reflects the measurement precision. The correction of the beam direction is included (see Section 5.2). The width of the peak is determined to be $\sigma_C \approx 0.002$ from a Gaussian fit.

In Figure 5.4 the events from Figure 5.1 are shown with the constraint on the coplanarity $|C| \leq 0.005$. The background is highly suppressed compared to the previous figure. Besides the pp elastic elliptical band (marked with the dashed white line in the

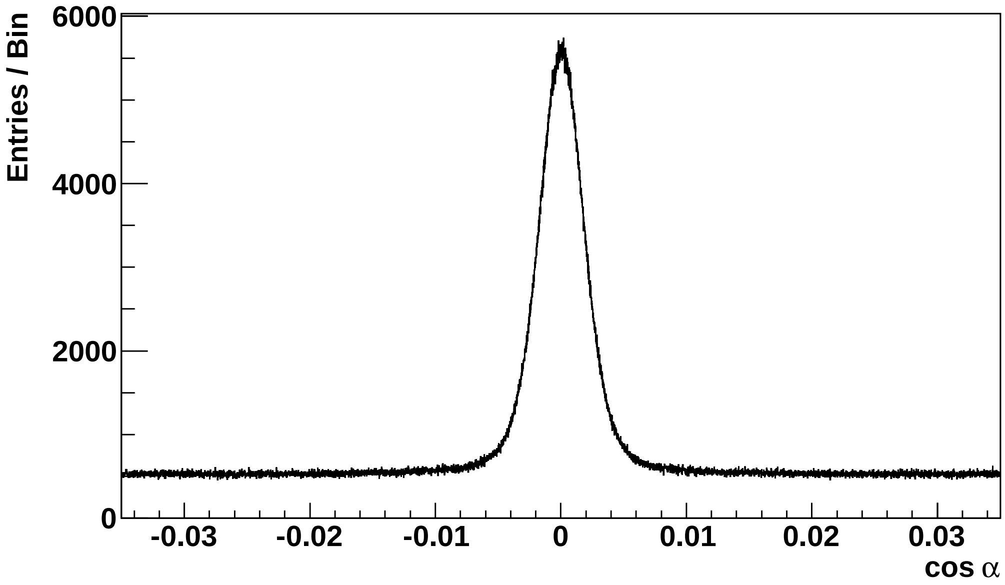

Figure 5.3.: Coplanarity C distribution for the elastic triggered two track events. The peak around zero stems from coplanar two track events.

lower plot) two additional bands are visible. These bands correspond to the $pp \rightarrow d\pi^+$ reaction, which fulfills the coplanarity condition, too. Since the deuteron and the pion have different mass, the particles lie on two separated kinematical ellipses. The one with higher longitudinal momentum belongs to the deuteron and the other one to the pion. The expected curve is shown with the dashed red lines in the lower plot of Figure 5.4 for the pion and the deuteron, respectively.

The coplanarity and missing energy constraints are correlated. This is visible in Figure 5.5 where the distribution of coplanarity versus missing energy is shown as a two-dimensional plot (upper part) and a three-dimensional plot (lower part). The pp elastic events are distributed in the peak around zero. Analog to [Roe11], an elliptical constraint around the peak is used for the selection of the elastic events. The constraint is given by

$$\sqrt{\left(\frac{C}{0.005}\right)^2 + \left(\frac{E_{\text{miss}}}{8\,\text{MeV}}\right)^2} \leq 1 \tag{5.7}$$

which is indicated through the white dashed line in the upper part of Figure 5.5. The individual constraints for the coplanarity and missing energy are $2.5\,\sigma$ of the peaks in the individual distributions (Figure 5.2 and 5.3). In the three-dimensional plot of the coplanarity versus missing energy distribution the number of bins has been decreased for both axis by a factor of two for better visibility. In addition, the color code is changed. The obtained sample consists of about 2.8 million $\vec{p}p \to pp$ elastic scattered events, which are used for the further analysis.

To estimate the fraction of background events, the number of events in the peak is compared with the number of events in a wider area assuming a constant background contribution (see Section 6.2 in [Roe11]). The wider area is spaned from $|C| \in [0.01, 0.02]$ and $|E_{\mathrm{miss}}| \in [16\,\mathrm{MeV}, 38\,\mathrm{MeV}]$ with $5\,\sigma$ as the lower value and $10\,\sigma$ as the upper value. The number of events in the wider area is corrected for the surface area ratio to the peak area to obtain the number of background events N_{bg}. The background fraction is

$$\frac{N_{\mathrm{bg}}}{N_{\mathrm{peak}}} = (3.75 \pm 0.0099) \times 10^{-3}. \tag{5.8}$$

This background fraction is considered to be sufficiently small, so that it is neglected in the further analysis of the elastic events.

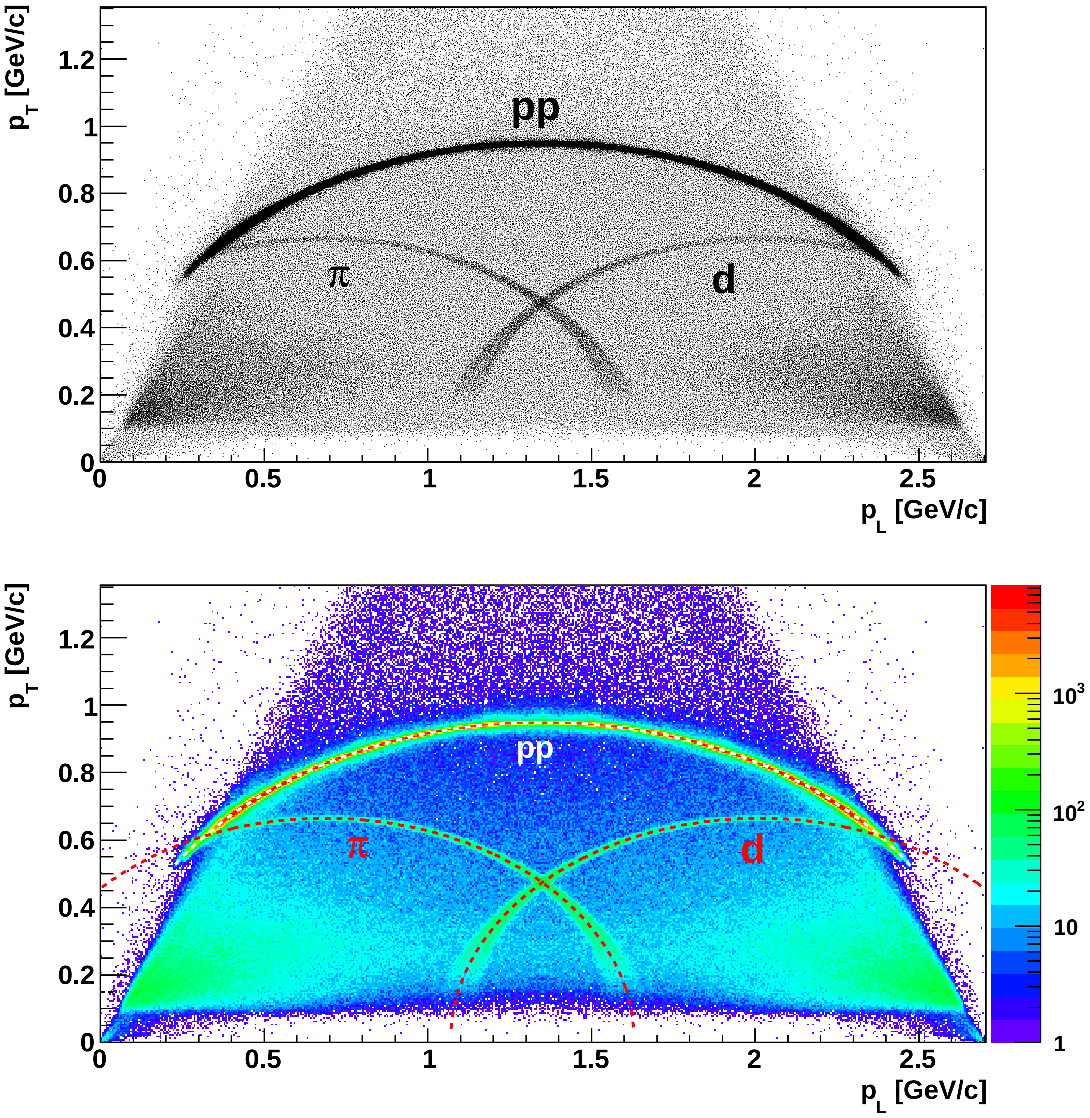

Figure 5.4.: $p_\perp$ versus $p_\parallel$ distribution for the elastic triggered two track events with a restriction on coplanarity $|C| \leq 0.005$ as a scatter plot (upper) and a colored plot with logarithmic z-axis (lower). The momenta are calculated by Equation 5.2 and 5.3. The pp elastic events lie in the symmetric elliptical band marked with the white dashed line in the lower plot. The $d\pi^+$ events emerge as two elliptical bands since the particles have different masses marked with the red dashed lines.

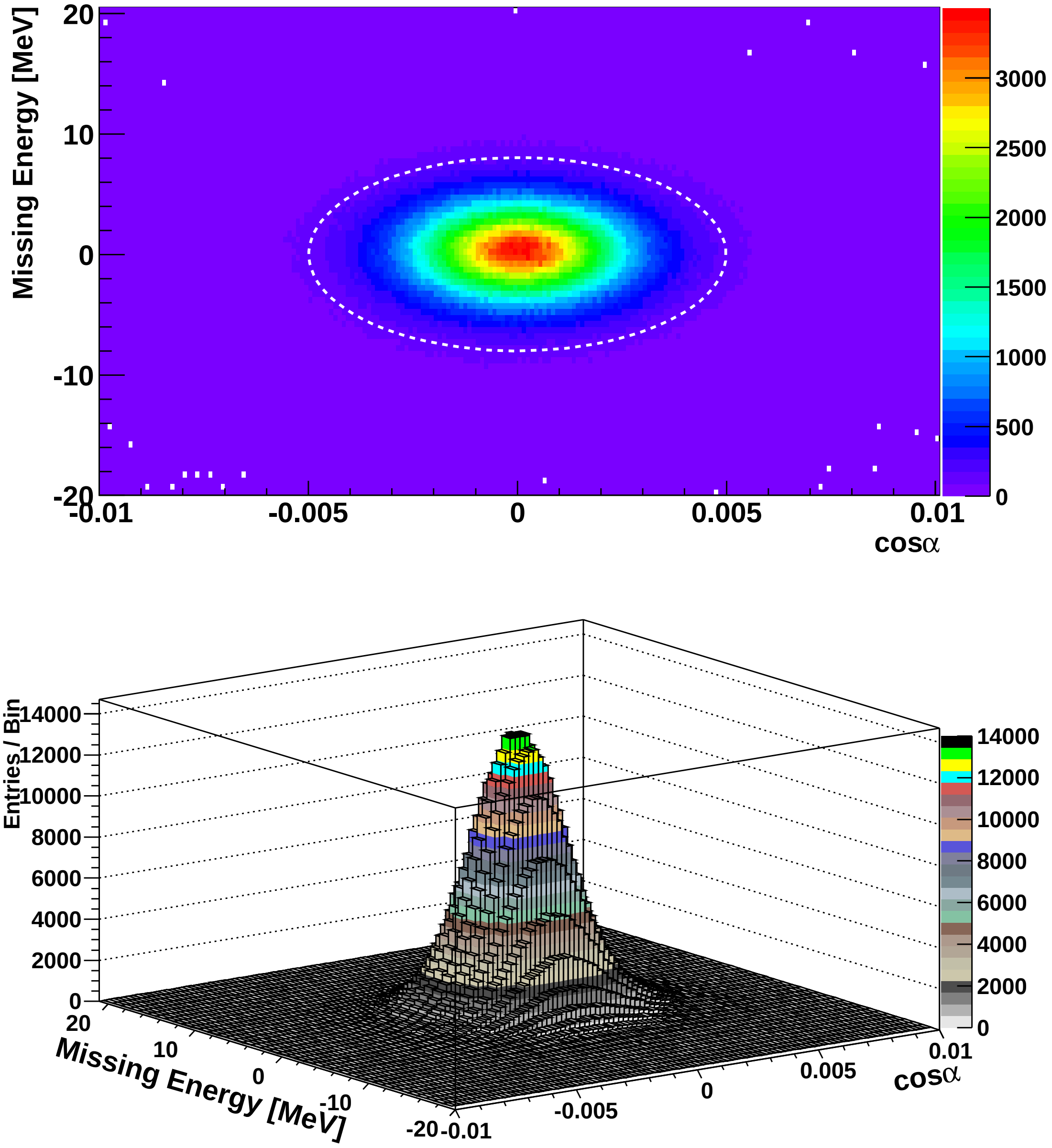

Figure 5.5.: Coplanarity versus missing energy distribution as a two-dimensional plot (upper) and a three-dimensional plot (lower). The dashed white line elllipse in the upper part marks the constraint from Equation 5.7 for the *pp* elastic selection. In the lower part the binning and the color scheme is changed for better visibility. The peak contains the *pp* elastic events.

5.2. Beam Direction and Correction

The beam direction $\vec{p}_{\text{beam}}$ is an important information for the kinematic fit of the $pK\Lambda$ events as well as for the calculation of the coplanarity constraint. In the analysis the beam direction defines the z-axis of the global coordinate system, which corresponds to the z-axis of the straw tube tracker in the ideal case. The ideal beam direction is $\vec{p}_{\text{beam,id}} = (0,0,1)^T$, as it is implemented in the Monte Carlo simulations. This direction corresponds to the horizontal axis from the target to the beam dump. Since the beam is perpendicular to the normal vector of the pp elastic scattering plane $\hat{n} = \hat{p}_1 \times \hat{p}_2$, the scalar product of the beam direction and the normal vector should be equally distributed around zero for all azimuthal angles of the normal vector $\phi_{\hat{n}}$ [2]. In the previous analyses [Roe11, Dzh12] it is demonstrated that this is not the case for these measurements.

For the data presented in this thesis a similar behavior is observed. Figure 5.6 shows the deviation of the normal directions in a cyclindrical coordinate system defined by the azimuthal angle $\phi_{\hat{n}}$. The top of the cylinder corresponds to $\phi_{\hat{n}} = 0$. The ideal beam direction (z-axis) coincides with the horizontal cyclinder axis. It is visible that the normal distributions are not perpendicular to the z-axis for all azimuthal angles[3]. The reasons could be a misalignment of the STT relative to the ideal beam direction, or a tilt of the real beam direction during the measurement to the ideal one, which is assumed in the analysis first, or a combination of both effects.

Assuming the STT has no misalignment, the real beam direction during the measurement can be obtained by the same distribution as in Figure 5.6 in a two-dimensional illustration. This is shown in the upper plot in Figure 5.7. The mean value for each azimuthal angle bin is given by the black marks, which are fitted with a cosine function according to

$$f(\phi_{\hat{n}}) = -\sin(\theta_{\text{beam}}) \cdot \cos(\phi_{\hat{n}} - \phi_{\text{beam}}) \tag{5.9}$$

to obtain the real beam direction parametrized with the polar angle θ_{beam} and azimuthal angle ϕ_{beam}. The angle θ_{beam} corresponds to the tilt angle between the real beam and the assumed ideal beam direction. From the fit the values $\theta_{\text{beam}} = (4.03 \pm 0.02)\,\text{mrad}$ and $\phi_{\text{beam}} = (2.234 \pm 0.003)\,\text{rad}$ are obtained.

From the necessity that the beam hits the beam dump, which is $\approx 13\,\text{m}$ behind the target, it is concluded in [Roe11] that the tilt angle of the beam to the ideal beam direction has to be less than 1 mrad. Thus, the observed deviation includes a tilt of the straw tube tracker compared to the horizontal axis from the target to the beam dump. In [Roe11] the value for the polar angle θ_{beam} was determined to be 3.69 mrad. Therefore, the value $\theta_{\text{beam}} = (4.03 \pm 0.02)\,\text{mrad}$ is composed of the STT tilt angle and the beam tilt angle. Assuming the obtained value from [Roe11] stems merely from the straw tube tracker misalignment, the tilt angle for the beam is $(0.34 \pm 0.02)\,\text{mrad}$ which is well below the maximum allowed value. Since the analysis is purely done by the STT

---

[2] This corresponds to the azimuthal angle of the pp elastic scattering plane.

[3] The non uniform distribution around $\phi_{\hat{n}}$ of the maxima is due to the asymmetric azimuthal angular distributions in the acceptance limit for the pp elastic scattering. This is explained in Section 5.4.

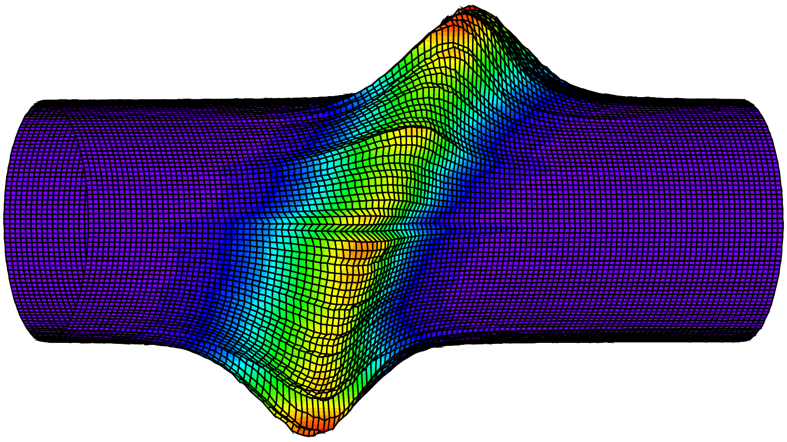

Figure 5.6.: Distribution of the scalar product of the normal vector on the *pp* elastic scattering plane and the ideal beam direction for the azimuthal angle of the normal vector in a cylindrical coordinate system. The cylinder axis corresponds to the z-axis (ideal beam direction). The top of the cylinder is in the direction of $\phi = 0$.

the corrections from the fit can be either applied to the beam direction or the STT or both. For simplification a correction of the STT tilt is omitted and the correction is applied only on the beam direction in the further analysis, hence defining a new z-axis of the global coordinate system .

Figure 5.7 (lower plot) shows the scalar product of the normal vector and the corrected beam direction dependent on the azimuthal angles $\phi_{\hat{n}}$. It is visible that all deviations observed in the upper plot have been vanished. The corrected behavior is used in the *pp* elastic event selection shown in Section 5.1 since the projection of the spectrum to the y-axis yields the coplanarity spectrum from Figure 5.3.

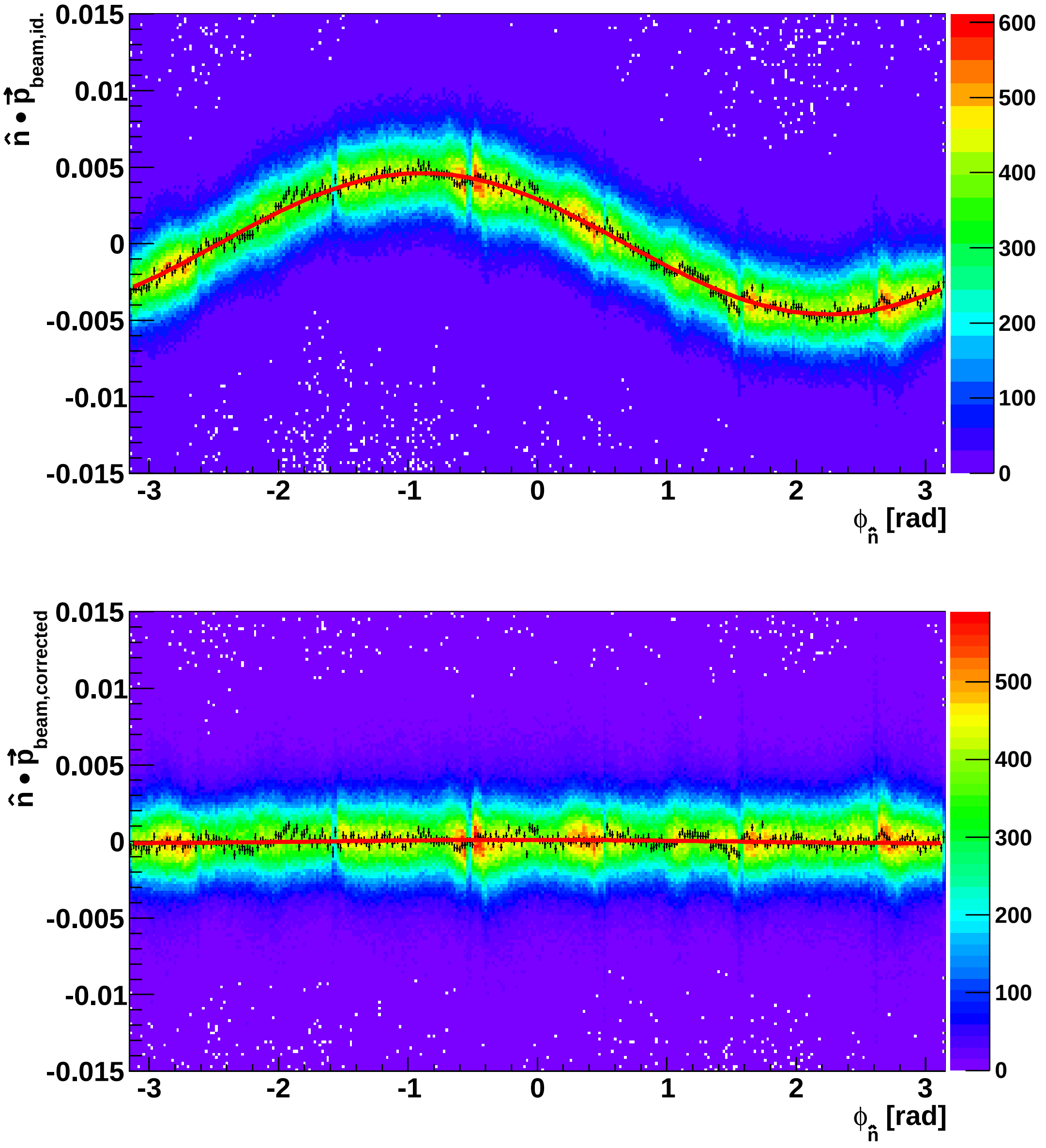

Figure 5.7.: Distribution of the scalar product of the normal vector on the *pp* elastic scattering plane and the beam vector versus the azimuthal angle of the normal vector $\phi_{\hat{n}}$ for the uncorrected beam direction (upper) and the corrected beam direction (lower). The black marks correspond to the mean value for each azimuthal angle, and the red line shows the fit of the beam direction according to Equation 5.9.

5.3. Vertex Distribution

The vertex distributions of the *pp* elastic scattered events are a tool to study the precision of the vertex reconstruction under the experimental conditions and the positioning of the target relative to the detector geometry. The width of the vertex distributions in x- and y-direction are a convolution of the beam size and the vertex reconstruction precision. In the z-direction the width of the vertex distribution is a convolution of the target length and the reconstruction precision.

In Figure 5.8 (left) the vertex distribution is shown projected on the x-y plane. The distribution is slightly shifted in the x-direction due to a misalignment from the target position relative to the straw tube tracker, which is not corrected for the analysis presented in this thesis. This has no influence on the results since the vertex is independently determined in the analysis, and a constraint on the primary vertex is not applied. Comparing the dimension of the interaction region (circle with approximately 0.1 cm radius) with the size of the target cell ($r = 0.3\,\mathrm{cm}$), the beam-target interaction takes place completely inside the target without touching the cell walls. The width of the distributions is wider for the x-axis than for the y-axis. To determine the widths, the distribution is projected on both axis and fitted with a Gaussian function. This is shown in Figure 5.9 for the x-axis (left) and the y-axis (right). The mean values of the fit define the center of the beam to be ($-0.0194\,\mathrm{cm}, -0.0034\,\mathrm{cm}$). The widths are $\sigma_\mathrm{x} = 736\,\mu\mathrm{m}$ for the x-axis and $\sigma_\mathrm{y} = 468\,\mu\mathrm{m}$ for the y-axis, respectively. This results have a large difference for x and y and deviate significantly from the values from [Roe11]: $558\,\mu\mathrm{m}$ for the x-axis and $559\,\mu\mathrm{m}$ for the y-axis. The reason is most likely a different focus of the beam at the target compared to the measurement from [Roe11].

The vertex distribution projected on the z-x plane is shown in Figure 5.8 in the right plot. The interaction takes place in the whole target cell in z-direction. The z-position is shifted due to misalignment of the distance between the target and the straw tube tracker. The distribution projected on the z-axis is shown in Figure 5.10. It can be described by a convolution of a box function, representing the target cell dimensions in the z-direction, and a Gaussian, representing the smearing of the edges due to the finite vertex resolution neglecting the curvature of the target foils. The fit is shown as the red line in Figure 5.10. It is parametrized by the height (p0), the width of the Gaussian (p1), the center of the target in z-direction (p2) and the target length (p3). The fit range is limited to the range $[-0.6\,\mathrm{cm}, -0.1\,\mathrm{cm}]$ to exclude the outside tails, which might stem from multiple scattering.

For the center of the target the value $-2.55\,\mathrm{mm}$ is obtained, which is indicted by the dashed green line in Figure 5.10. Thus, the distance from the target to the STT is larger than assumed in the reconstructed data presented in this thesis. As for the deviation in the x- and y-direction, the deviation in z does not influence the results, but it can be corrected in a further analysis. The length of the target cell is determined to be $l = 4.84\,\mathrm{mm}$. The calculated boarders of the target are shown with the blue dashed lines in Figure 5.10. Compared to size of the target cell of about 4 mm this is an enlargement of $\approx 0.84\,\mathrm{mm}$. As it is shown in Figure 6.8 in [Roe11] the foils at the

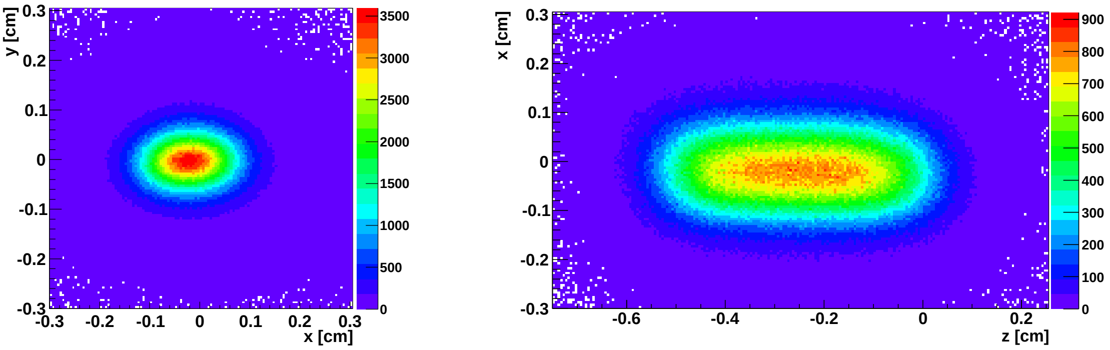

Figure 5.8.: Vertex distributions of the *pp* elastic scattered events projected in the x-y plane (left) and z-x plane (right).

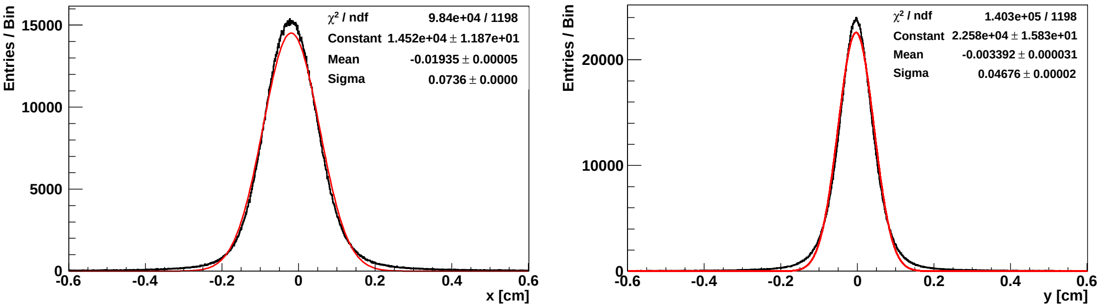

Figure 5.9.: Vertex distributions of the *pp* elastic scattered events for the x-axis (left) and the y-axis (right). Both distributions are fitted with a Gaussian function to obtain the beam spot.

edges of the target cell are extended by the working pressure of 200 mbar inside. The prolongation of the target through the foils at both ends is about 0.5 mm each. Thus, the obtained target length is in agreement with the physical length of the target plus the extensions of the foils from the overpressure. The width of the Gaussian, representing the smearing of the edges, is $\sigma_z = 795\,\mu$m.

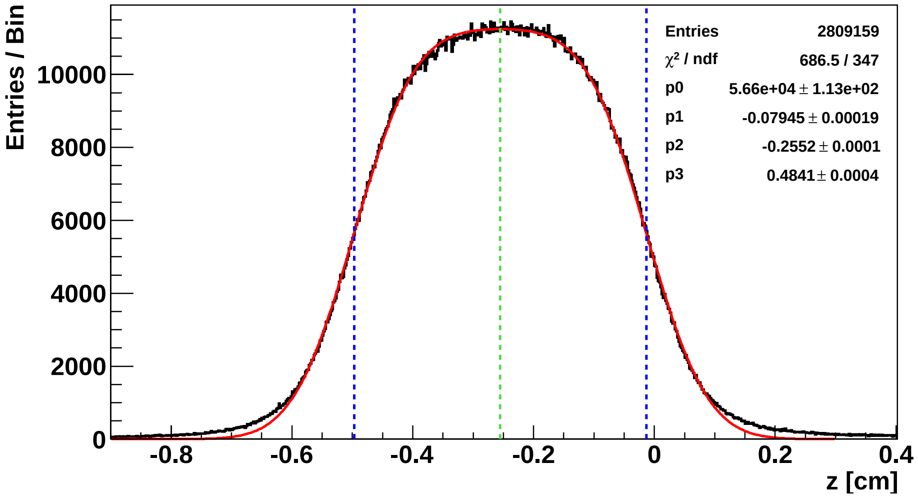

Figure 5.10.: Vertex distribution of the *pp* elastic scattered events projected on the z-axis fitted with a convolution of a Gaussian and a box function in the range $[-0.6\,\text{cm}, -0.1\,\text{cm}]$. The fit parameters p0, p1, p2 and p3 correspond to the height of the convolution function, the width of the Gaussian, the center of the target and the length of the target in z-direction. The green dashed line indicates the center of the target in z-direction, and the blue dashed lines show the boarders of the target from the fit.

5.4. *pp* Elastic Acceptance Limit

As it is already visible in the Figures 5.1 and 5.4, the *pp* elastic scattered events can not be measured for the full polar angular range since for small scattered angles of one proton, the other proton exceeds the angular range of the straw tube tracker. Therefore, such an event can not be reconstructed and only a part of the polar angular range can be used to determine the beam polarization (see next section). To illustrate the limits of the acceptance, the distribution of the polar angle in the center of mass system (θ_p^{CMS}) as a function of the azimuthal angle for the proton with the smaller scattering angle (p_1) is shown in Figure 5.11.

Below a polar angle of 52° (red line in Figure 5.11) a strong variation over ϕ is observed. It is a reflection of the varying efficiency for the reconstruction of the second proton, since it passes the straw tube tracker in the areas where only double layers of two rotational directions overlap[4]. The STT geometry is sketched in Figure 5.12, and the areas where double layers from two rotational directions overlap are shown in red. In total, there are twelve of these areas, thus 12 peaks are expected in Figure 5.11 with

---

[4] The track reconstruction is not possible in the areas without an overlapping of straws with different rotational orientation (yellow marked areas in Figure 5.12).

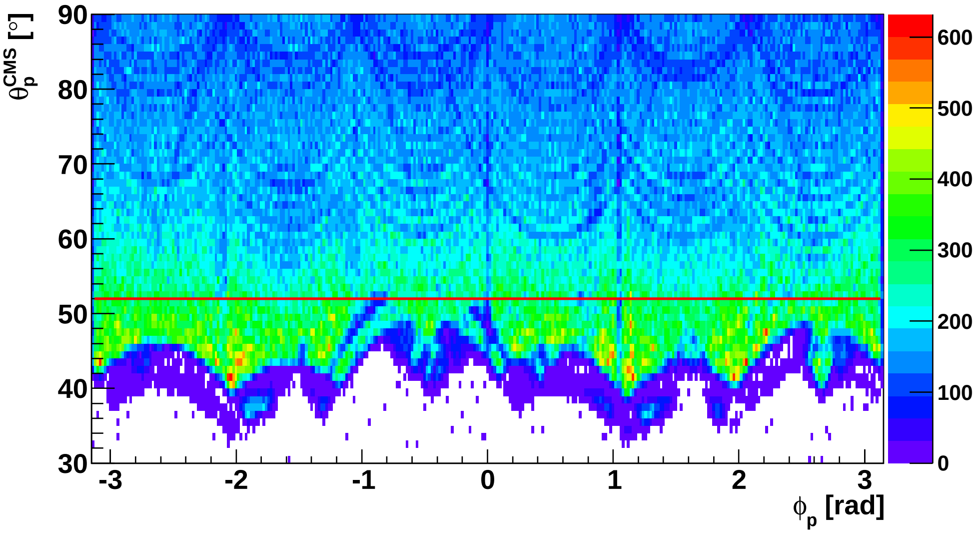

Figure 5.11.: The distribution of the polar angle θ_p^{CMS} in the center of mass system as a function of the azimuthal angle ϕ is shown for the elastic scattered proton with the smaller scattering angle. Only events above the red line are used for the determination of the beam polarization. The structures below the red line are acceptance holes due to detector inefficiencies.

a repetition of $30° \approx 0.53\,\mathrm{rad}$. Some of the peaks can be seen in the figure for instance at 1.1 rad, 2 rad and 2.6 rad. However, not all of them are visible due to additional inefficiencies of the straws (see STT hit map in Figure 6.9) or insufficient triggering of the pp elastic scattered events by the other sub-detectors in COSY-TOF. Nevertheless, the structures have a π-symmetry in ϕ due to the coplanarity of the elastic events. For the determination of the beam polarization (see next section) the constraint $\theta_p^{\mathrm{CMS}} > 52°$ is applied on the data to avoid systematical errors from the areas with a nonuniform ϕ distribution. A similar constraint was applied in the analysis from [Roe11].

Additionally, small substructures for higher polar angles are visible in Figure 5.11. The arc like shapes stem probably from inefficient overlapping groups of straws, since no other sub-detector in COSY-TOF has this shape. The thin sparsely populated areas with constant ϕ for example at $\phi \sim 0\,\mathrm{rad}$ and $\phi \sim 1\,\mathrm{rad}$ originate from wedge-shaped ring detector elements with lower efficiency.

In Figure 5.13 the azimuthal angular distribution of the proton with the smaller scattering angle is shown with and without the constraint on the polar angle $\theta_p^{\mathrm{CMS}} > 52°$ (red and black, respectively). For some ϕ values gaps can be seen due to some ring elements with lower efficiency. The gaps have a π-symmetry due to the coplanarity of the elastic scattered protons. After applying the constraint on the polar angle, the distribution gets relatively flat (red).

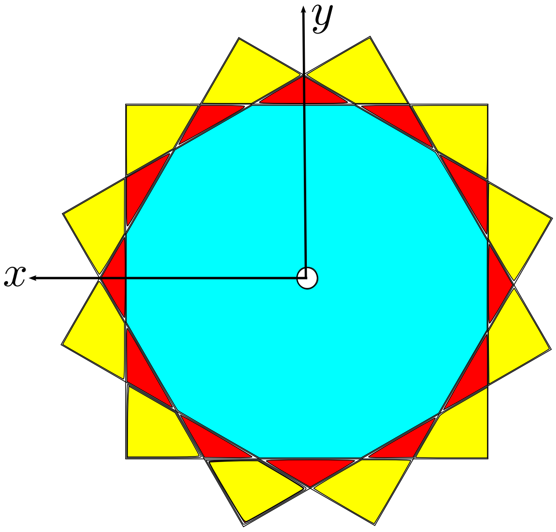

Figure 5.12.: Sketch of the straw tube tracker geometry with the three rotational directions of the double layers. The areas with an overlapping of three rotational directions are marked in blue, with two rotational directions in red and without an overlapping of different orientations in yellow.

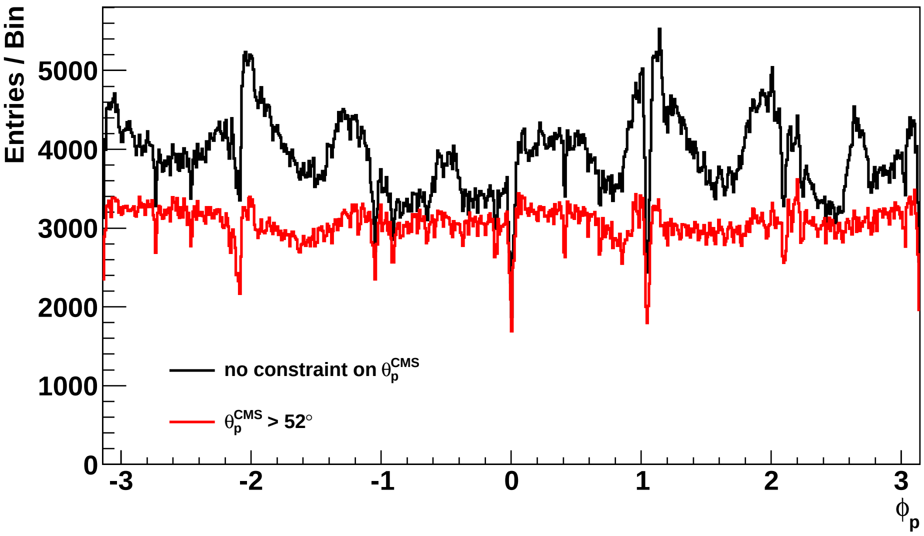

Figure 5.13.: Azimuthal angular distribution for the elastic scattered proton with the smaller scattering angle. For the red distribution the constraint $\theta_p^{\mathrm{CMS}} > 52°$ is applied.

5.5. Beam Polarization

The averaged polarization for both spin directions is determined utilizing the left-right azimuthal asymmetry $\epsilon_{LR}(\theta_{\mathrm{p}}^{\mathrm{CMS}}, \phi)$ and the known analyzing power $A(\theta_{\mathrm{p}}^{\mathrm{CMS}})$ from the partial wave analysis SAID [SAID]. It is defined by (see [Roe11, Dzh12])

$$p_B = \frac{\epsilon_{LR}(\theta_p^{\mathrm{CMS}}, \phi)}{\cos(\phi) \cdot A(\theta_p^{\mathrm{CMS}})}. \tag{5.10}$$

The asymmetry can be determined from the count rates according to (see [Ohl73])

$$\epsilon_{LR}(\theta_p^{\mathrm{CMS}}, \phi) = \frac{L(\theta_p^{\mathrm{CMS}}, \phi) - R(\theta_p^{\mathrm{CMS}}, \phi)}{L(\theta_p^{\mathrm{CMS}}, \phi) + R(\theta_p^{\mathrm{CMS}}, \phi)} \text{ for } \phi \in \left[-\frac{\pi}{2}, \frac{\pi}{2}\right] \tag{5.11}$$

with

$$L(\theta_p^{\mathrm{CMS}}, \phi)) = \sqrt{N^+(\phi) \cdot N^-(\phi + \pi)} \tag{5.12}$$

$$\text{and} \quad R(\theta_p^{\mathrm{CMS}}, \phi) = \sqrt{N^+(\phi + \pi) \cdot N^-(\phi)} \;. \tag{5.13}$$

$N^{\pm}(\phi)$ are the number of events for the azimuthal angle ϕ with a spin up (+) or spin down (−) polarized beam, respectively. The usage of all four count rates in the determination of the asymmetry cancels out systematic effects from an azimuthal asymmetric detector acceptance to first order.

For the beam polarization determination only data with a scattering angle of $\theta_p^{\mathrm{CMS}} \geq 52°$ have been used, to avoid the range with lower acceptance and asymmetric azimuthal angular distributions (see Section 5.4). For angles between 52° and 80° bins with a width of 4° are used. The range from 80° to 90° is divided into two bins with 5° width, because the analyzing power is approximately half the size compared to the other bins. To obtain a measurable asymmetry the number of events per bin are increased by broadening the bins.

For each scattering angle bin the asymmetry $\epsilon_{LR}(\theta_p^{\mathrm{CMS}}, \phi)$ is divided into eight ϕ-bins in the range $[-\pi/2, \pi/2]$. In Figure 5.14 the azimuthal asymmetry for the scattering angle range $\theta_p^{\mathrm{CMS}} \in [52°, 56°]$ is shown. Since for a fixed θ-bin the asymmetry becomes

$$\frac{\epsilon_{LR}(\theta_p^{\mathrm{CMS}}, \phi)}{\cos(\phi)} = \bar{\epsilon}(\theta_p^{\mathrm{CMS}}) = \text{const.}, \tag{5.14}$$

the obtained asymmetry is fitted with $\bar{\epsilon} \cdot \cos(\phi)$. For the scattering angle range shown in Figure 5.14 the averaged asymmetry is $\bar{\epsilon} = 0.102 \pm 0.003$. The beam polarization for this bin is determined by dividing the asymmetry with the analyzing power taken from SAID.

In Figure 5.15 the beam polarization is shown for each individual scattering angle bin. The distribution is fitted with a constant function, giving the beam polarization averaged over all asymmetry to be $p_B = (79.0 \pm 1.1)\,\%$. The polarization in the previous

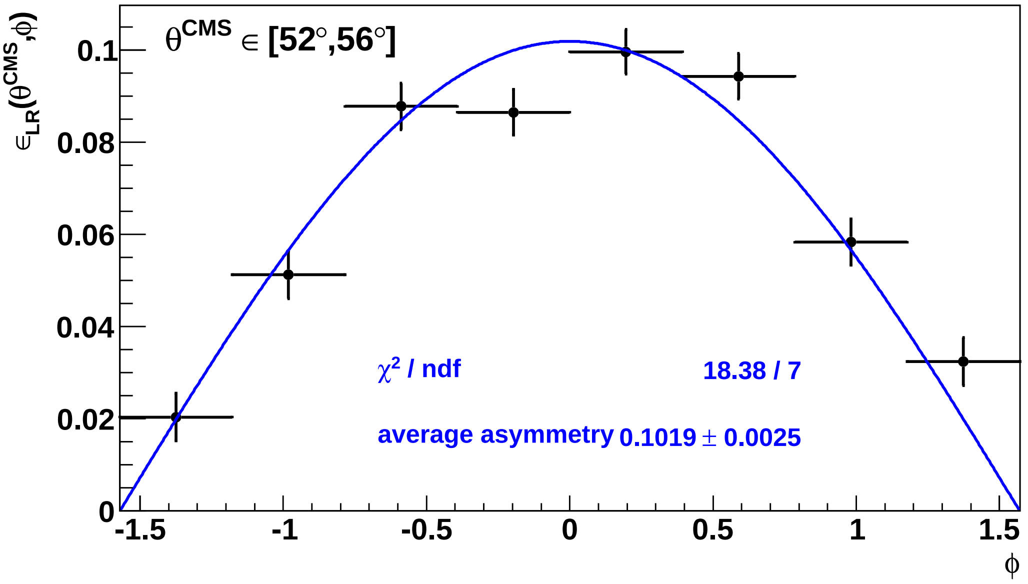

Figure 5.14.: The azimuthal asymmetry $\epsilon_{LR}(\theta_p^{\mathrm{CMS}}, \phi)$ for the elastic scattered proton in the range $\theta_p^{\mathrm{CMS}} \in [52°, 56°]$ is shown. The blue line shows the fit with $\bar{\epsilon} \cdot \cos(\phi)$.

COSY-TOF measurement was $p_B = (61.0 \pm 1.7)\,\%$ [Roe11]. The improvement of the polarization by 18 percentage points has two reasons: First the beam momentum was higher in the previous measurement, hence more depolarization resonances have to be crossed during the acceleration of the beam. Second, the acceleration process in the actual measurement includes an additional stop while crossing the most important depolarization resonances in contrast to the previous measurement [Lor13].

With the determined beam polarization the analyzing power can be calculated by inverting Equation 5.10. The result is compared with the prediction from SAID. This is shown in Figure 5.16. As expected the SAID prediction fits in the measured values, since they are calculated from the prediction binwise.

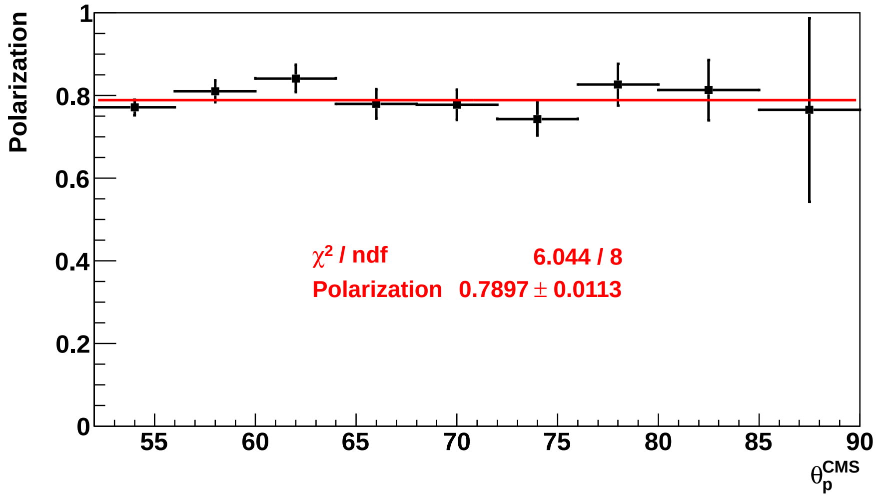

Figure 5.15.: Beam polarization p_b as a function of the proton elastic scattering angle in the center of mass system θ_p^{CMS} for the measurement presented in this thesis. From the fit with a constant (red) the beam polarization is determined.

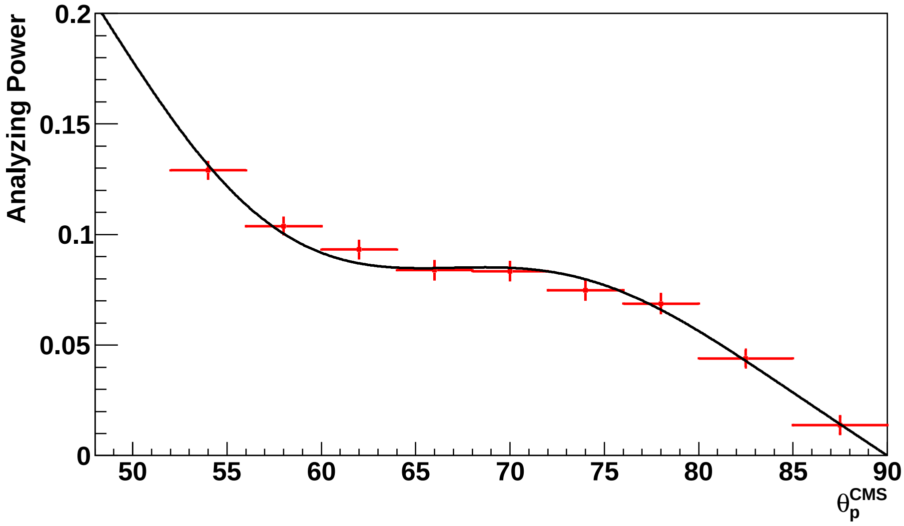

Figure 5.16.: Analyzing power as a function of the proton elastic scattering angle in the center of mass system θ_p^{CMS} for the measurement presented in this thesis (red) together with the prediction from SAID (black). The analyzing power is determined by employing the averaged beam polarization on the measured asymmetry.

It is a capital mistake to theorize before one has data.

(*Arthur Conan Doyle*)

6. Data Selection and Monte Carlo Studies

In this chapter the selection criteria for events of the $pp \to pK\Lambda$ reactions are described. In addition, the results of Monte Carlo simulations for the $pp \to pK\Lambda$ and $pp \to pK\Sigma$ reaction are shown. They are performed to study the resolution and efficiency of the event reconstruction of the $pK\Lambda$ events as well as the background fraction from the $pK\Sigma$ events.

6.1. $pp \to pK\Lambda$ Event Selection

As in previous analyses of COSY-TOF data, three criteria are used to select the $pK\Lambda$ events (see e.g. Chapter 7 in [Roe11]): A selection on the reduced $\chi^2_{\mathrm{K}}/\mathrm{NDF}$ of the kinematic fit, the Λ decay length (s_Λ) and the angle between the Λ and its decay proton.

The selection on $\chi^2_{\mathrm{K}}/\mathrm{NDF}$ enforces that events fulfill the required kinematics. The dominant background process stems from the reaction $pp \to pK\Sigma^0 \to pK\Lambda\gamma$ which has the same event topology. This reaction can not be suppressed by a further constraint on the Λ decay length since the Σ^0 has a lifetime of 10^{-20} s which is much shorter compared to the Λ. Therefore, the Σ^0 decay vertex can not be separated from the primary vertex, and the $pK\Sigma^0$ events are only separated through the χ^2 constraint. In Figure 6.1 the s_Λ distribution is shown with a logarithmic scale for events with $\chi^2_{\mathrm{K}}/\mathrm{NDF} < 50$ (black) and $\chi^2_{\mathrm{K}}/\mathrm{NDF} < 5$ (red). For both samples a large peak is visible at values $s_\Lambda < 0.1\,\mathrm{cm}$. The peak stems from processes with a misinterpreted decay vertex very close to the target. This is probably due to reactions with four primary particles for which one or two are imprecisely reconstructed, and thus they fake a secondary vertex close to the target. In the region up to $s_\Lambda \sim 3\,\mathrm{cm}$ a shoulder is visible for the red distribution. This could be due to multiple scattering of particles in the start detector or the SQT, and therefore the secondary vertex position is misidentified by $pK\Lambda$ events or other four track events. Additionally, hadronic interactions in these detector parts can generate false secondary vertices (see also Figure 6.20 in [Dzh12]).

Because an independent distribution of the background processes is not available, the optimal values for the decay length and $\chi^2_{\mathrm{K}}/\mathrm{NDF}$ constraint can not be determined straightforward. To determine a suitable value the method described in Section 7.2 in [Roe11] is applied. For a given $\chi^2_{\mathrm{K}}/\mathrm{NDF}$ constraint i, the decay length distribution is fitted in the range from 0.5 cm to 20 cm with two exponential functions. The range is limited to fit only the shoulder and the rest of the distribution. The upper limit is

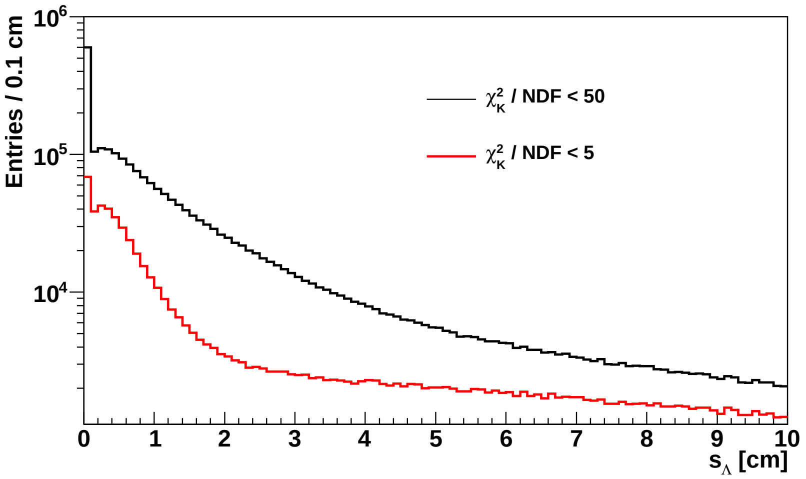

Figure 6.1.: Λ decay length s_Λ distribution for two selections of $\chi^2_{\mathrm{K}}/\mathrm{NDF}$.

choosen to avoid the drop of reconstruction efficiency when the Λ decays inside the straw tube tracker. The two exponential functions are *expbg* which models the background, and *expsignal* corresponding to the expected distribution for s_Λ. In the range $s_\Lambda > 5\,\mathrm{cm}$ the background is negligible hence the distribution is characterized by *expsignal*. The range from 0.5 cm to 1.5 cm on the other hand is dominated by background, and thus the function *expbg* should describe the distribution well there. In Figure 6.2 the combined fit (black) is shown together with the individual contributions from *expsignal* (red) and *expbg* (blue) for the constraint $\chi^2_{\mathrm{K}}/\mathrm{NDF} < 5$. From the individual contributions of the combined fit the number of signal events S_i and background events B_i can be calculated for a given $\chi^2_{\mathrm{K}}/\mathrm{NDF}$ constraint i and s_Λ-constraint t_s by

$$S_i(t_s) = \int_{t_s}^{20\,\mathrm{cm}} \mathrm{d}s_\Lambda\, expsignal(s_\Lambda) \qquad \text{and} \qquad B_i(t_s) = \int_{t_s}^{20\,\mathrm{cm}} \mathrm{d}s_\Lambda\, expbg(s_\Lambda). \tag{6.1}$$

In general, the optimal value for t_s for each value of i can be calculated by the significance $S_i/\sqrt{B_i}$. However, there is still a constant amount of $pp \to pK\Sigma^0 \to pK\Lambda\gamma$ background events in the distribution which can not be eliminated due to the nearly identical decay length distribution of the Σ^0. The fraction x of these events is known to be less than 1% (see Section 6.3.3). Therefore, the figure of merit (FoM) for a given value of i and t_s is (see also Section 7.2 in [Roe11]):

$$\mathrm{FoM}(i, t_s) = \frac{(1 - 0.01) \cdot S_i(t_s)}{\sqrt{B_i(t_s) + 0.01 \cdot S_i(t_s)}} \tag{6.2}$$

In Figure 6.3 (left) the results of the figure of merit are shown for different values of the constraints i (x-axis) and t_s (y-axis). The maximum values of the FoM in the figure are in the range of $5 < i < 7$ and $3\,\mathrm{cm} < t_s < 4.5\,\mathrm{cm}$. However, the constraint on the

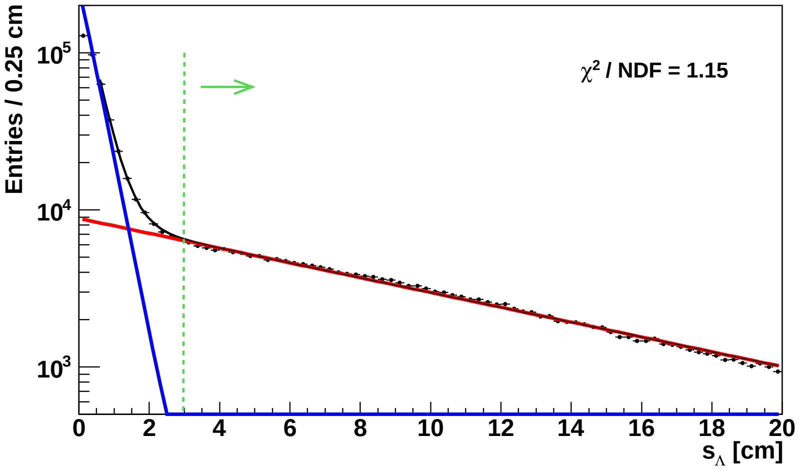

Figure 6.2.: Λ decay length distribution for events with $\chi^2_{\mathrm{K}}/\mathrm{NDF} < 5$. The data are fitted with the sum of two exponential functions (black with $\chi^2/\mathrm{NDF} = 1.15$). The exponential function for the signal is shown in red. The function in blue models the background of events with faked secondary vertices in the range $s_\Lambda > 0.1\,\mathrm{cm}$. The dashed green line marks the value of the decay length constraint applied later and the selection region is indicated with the green arrow. Note the logarithmic scale on the y-axis.

decay length should be as low as possible to maximize the resulting statistics. Thus, the constraint $t_s = 3\,\mathrm{cm}$ is used (indicated by the green line in Figure 6.2) since it is the smallest value in the maximum area of the figure of merit. From the projection of the two-dimensional FoM distribution for $t_s = 3\,\mathrm{cm}$ on the x-axis, the χ^2 constraint is determined from the maximum. The projection is shown in 6.3 (right) together with the selected constraint $\chi^2_{\mathrm{K}}/\mathrm{NDF} < 5$ which is marked with the dashed green line in Figure 6.3 (right). Thus, the first two selections

$$\chi^2_{\mathrm{K}}/\mathrm{NDF} < 5 \tag{6.3}$$

$$s_\Lambda > 3\,\mathrm{cm}. \tag{6.4}$$

are applied for the $pK\Lambda$ event selection. These are marked by the black lines in the Figures 6.3 (left) and by the green line in 6.2 and 6.3 (right).

Finally, Figure 6.4 shows the two-dimensional distribution for both criteria $\chi^2_{\mathrm{K}}/\mathrm{NDF}$ and s_Λ of the $pK\Lambda$ event candidates after the kinematic fit. The dashed violet lines and arrows indicate the region of events which are tagged as $pK\Lambda$ events in the further analysis taking the constraints from the Equations 6.3 and 6.4 into account.

The final criterium is a constraint on the angle between the Λ and its decay proton in the laboratory reference frame. This also reduces background contributions from

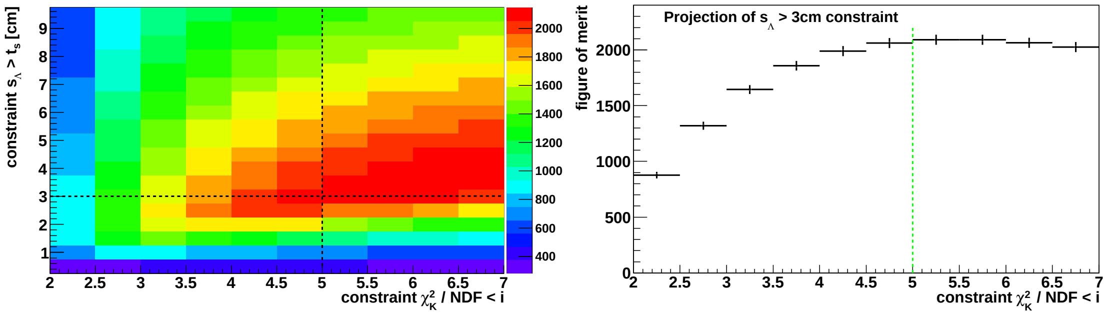

Figure 6.3.: Left: The figure of merit calculated with Equation 6.2 for different values of the constraints i and t_s. The dashed black lines marks the choosen i and t_s values for the event selection. **Right:** Projection of the $s_\Lambda > t_s = 3\,\text{cm}$ bin from the left plot with the choosen $\chi^2_\text{K}/\text{NDF} < i$ constraint marked by the dashed green line.

events with four primary particles where one particle is not precisely reconstructed and fakes a decay vertex with one other track. Such a track is then identified as the decay proton but it has an angle close to zero relative to the Λ direction. Therefore, this background should be visible as an enhancement at small relative angles in comparision to Monte Carlo simulations. In Figure 6.5 the distribution of the angle is shown for data (black) and Monte Carlo (red) scaled to the same height after applying the cuts from Equations 6.3 and 6.4. As expected, the data at angles below around 1° exhibit a small enhancement compared to the Monte Carlo distribution. Above an angle of around 2° both distributions match, thus the selection criterium for the angle is

$$\angle(\Lambda, p(\Lambda \to p\pi)) > 2^\circ. \tag{6.5}$$

This is indicated with the blue line and arrow in Figure 6.5.

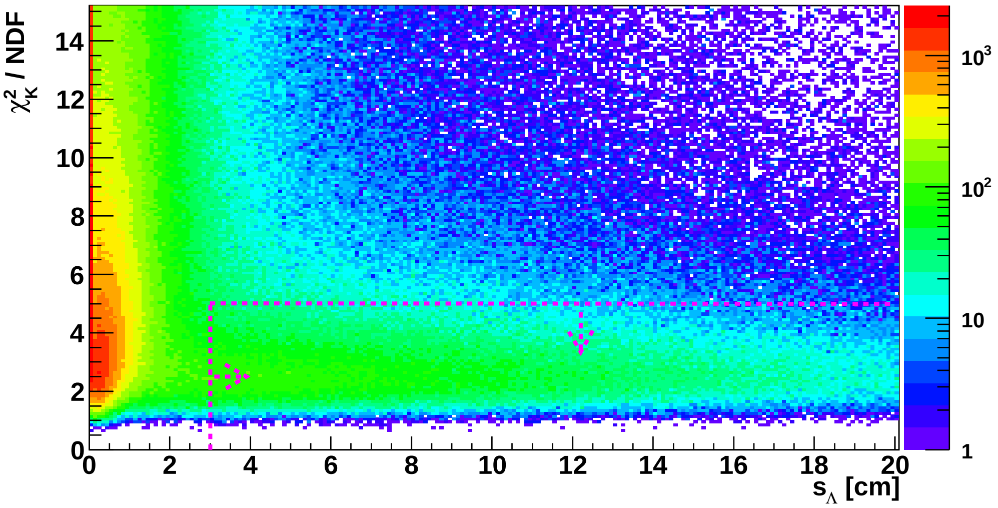

Figure 6.4.: Distribution of χ^2_{K}/NDF versus Λ decay length s_Λ for all $pK\Lambda$ event candidates of the data, which pass the kinematic fit. The dashed violet lines and arrows indicate the region from which events are accepted. The color code is in a logarithmic scale.

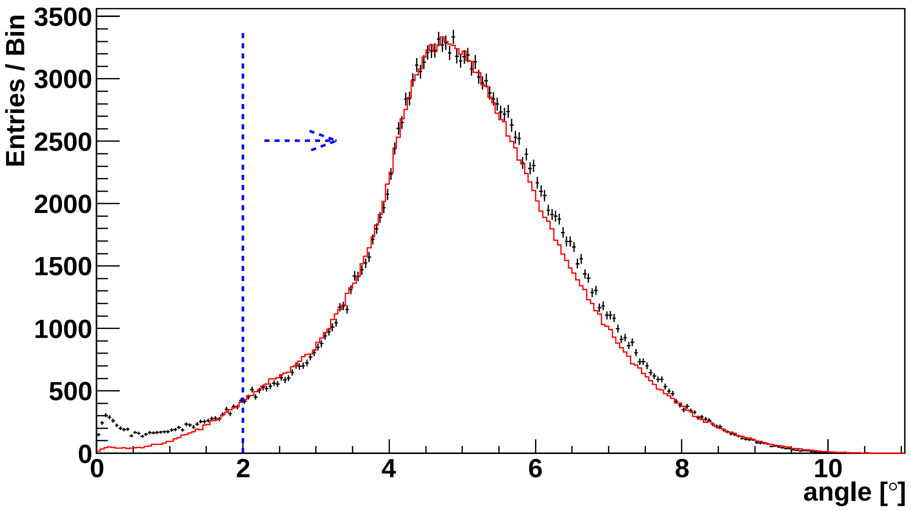

Figure 6.5.: Distribution of the angle between the Λ and its decay proton for the data (black) and Monte Carlo (red), scaled to the same height. The blue line and arrow marks the accepted region to reduce additional background at small angles.

6.2. $pp \to pK\Lambda$ Data Quality and Statistics

The Λ lifetime distribution and the missing energy distribution at the primary vertex from the geometrical fit[1] are examined to check the selection criteria. The lifetime or proper time cT can be calculated from the decay length via

$$cT = s_\Lambda \cdot \frac{m_\Lambda}{|\vec{p}_\Lambda|} = s_\Lambda \cdot \frac{1}{\beta\gamma} \tag{6.6}$$

for each event. At 2.7 GeV/c beam momentum the minimum and maximum value for $\beta\gamma$ are $\beta\gamma_{\mathrm{min}} = 0.58$ and $\beta\gamma_{\mathrm{max}} = 1.58$. With the selection criterium for the decay length $s_\Lambda > 3\,\mathrm{cm}$ the proper time distribution must drop for values of cT smaller than $3\,\mathrm{cm} \cdot \frac{1}{\beta\gamma_{\mathrm{min}}} = 5.16\,\mathrm{cm}$, reflecting the constraint on the decay length. This is indicated with the dashed green line in both plots in Figure 6.6. The left plot shows the acceptance and reconstruction efficiency from MC simulations for the proper time. Around $cT = 18.4\,\mathrm{cm}$ the efficiency starts to drop. This corresponds to a decay length of $s_\Lambda \approx 29\,\mathrm{cm} = 18.4\,\mathrm{cm} \cdot \beta\gamma_{\mathrm{max}}$ where the Λ already decays inside the straw tube tracker resulting in a decreased number of available straws for the reconstruction of the secondary tracks.

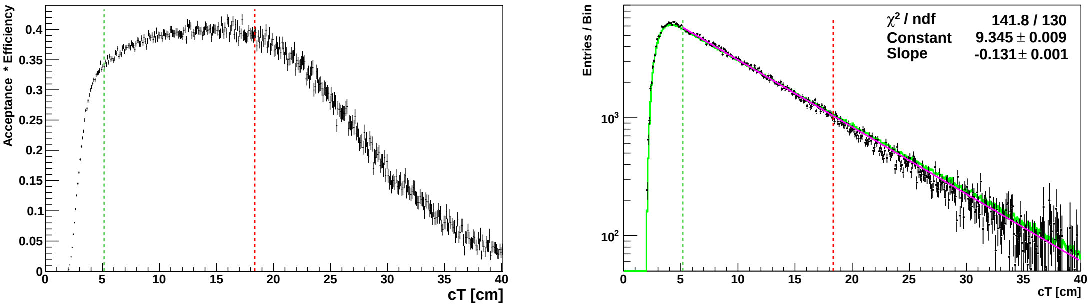

Figure 6.6.: Left: Acceptance and reconstruction efficiency for the proper time distribution. The dashed green line marks the drop from the decay length cut modified through $\beta\gamma$. The dashed red line marks the drop of the efficiency due to Λ decays inside the straw tube tracker. **Right:** Data corrected for acceptance and reconstruction efficiency (black) and phase space distribution from Monte Carlo (green). The red line is an exponential fit to the data. The dashed lines are the same as in the left plot, and they show the range of the fit.

The right plot in Figure 6.6 shows the proper time distribution of the data corrected for acceptance and reconstruction efficiency (black) together with the expectation from a phase space distribution (green). The dashed lines are the same as in the left plot and now show the limits of the fit by an exponential function (red). The mean lifetime

---

[1] The missing energy must be zero after the kinematic fit, thus the value before the fit is used.

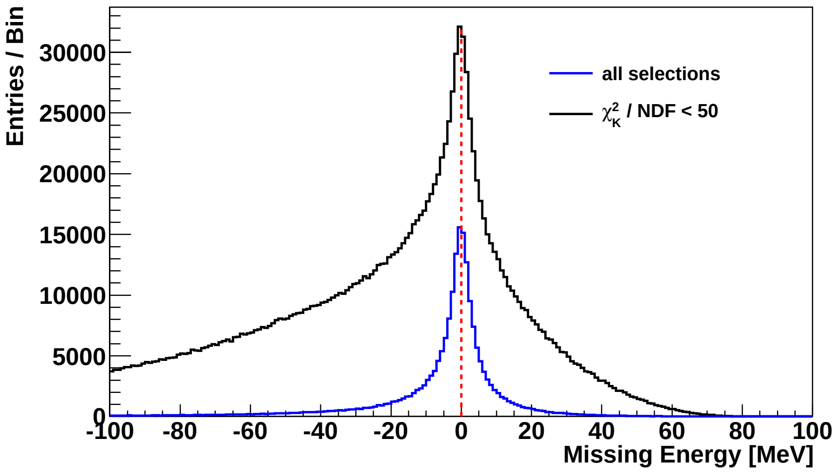

Figure 6.7.: Missing Energy distribution at the primary vertex before the kinematic fit. All events with $\chi^2_\mathrm{K}/\mathrm{NDF} < 50$ are shown together with the events after all selection criteria (blue).

of the Λ is obtained as the inverse of the slope parameter of the function. Therefore, the measured mean liftime is $c\tau = (7.63 \pm 0.06)\,\mathrm{cm}$, which is within 2σ in agreement with the literature value of $c\tau_\Lambda = (7.89 \pm 0.06)\,\mathrm{cm}$ [PDG2012].

The other quantity to check the selection criteria for the $pK\Lambda$ events is the missing energy distribution at the primary vertex from the geometrical fit. This is shown in Figure 6.7 for all events with a $\chi^2_\mathrm{K}/\mathrm{NDF} < 50$ (black) and for the events applying the three selection constraints (blue). The events with the constraint $\chi^2_\mathrm{K}/\mathrm{NDF} < 50$ stems from a preselection of the $pK\Lambda$ events. The background is strongly reduced for the blue curve in comparision to the black curve, and it becomes a symmetric distribution around zero (dashed red line). The background reaction $pp \to pK\Sigma^0 \to pK\Lambda\gamma$ can not be observed directly in the plot as an extra peak. Therefore, the number of $pK\Sigma^0$ events in the distribution has to be examined by Monte Carlo simulation as described in Section 6.3.3.

Finally, the blue distribution contains 207,219 events which are used for the further analysis. Figure 6.8 shows the number of $pK\Lambda$ events for each individual “run”. A “run” is a data file with constant experimental parameters and corresponds usually to a measurement time of 20 - 30 minutes. The run number counts the data files from the first measurement of the COSY-TOF experiment on. Thus, the run numbers for the measurement presented here are in the range from 12720 to 14255. Runs without any events are runs for calibration issues, with pp elastic trigger or they were stopped during the measurement due to problems. The range around run number 14000 was a different measurement, thus not considered in this analysis. The average number of events per run is 170 with some outliers where the beam intensity changed. The

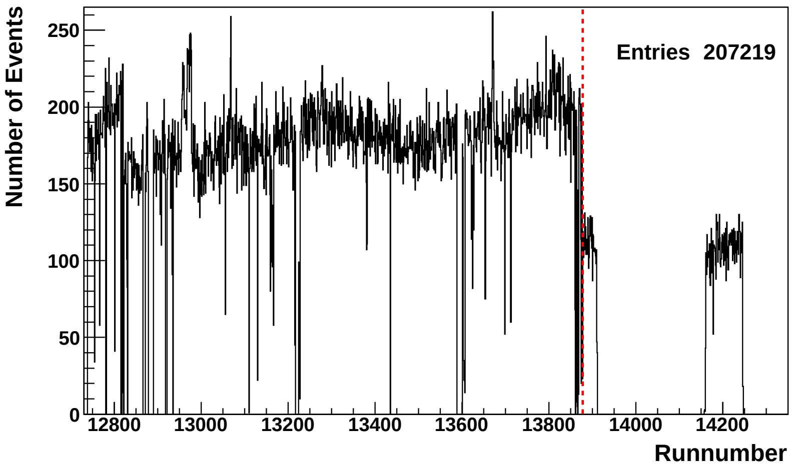

Figure 6.8.: Number of $pK\Lambda$ events as a function of the run number. The run number counts the data files stored on hard disc from the first measurement of the COSY-TOF experiment on. Only the runs of the measurement of the $pp \to pK\Lambda$ reaction at 2.7 GeV/c beam momentum is shown. The dashed red line indicates the change of the trigger setup as described in Section 3.4. Left of the line the data with the improved t11pkl trigger without FB crates read out, and right of the line the control sample with the former trigger with FB read out.

dashed red line marks the border of the data with the two different trigger setups. The improved t11pkl trigger without the read out of the FastBus crates was used for the data files left of the dashed red line as described in Section 3.4, and right of the line the former trigger was used with a read out of the FastBus crates. The increase of the number of events by a factor of up to two mentioned above is visible.

6.3. Monte Carlo Studies

Monte Carlo simulations were performed for the $pp \to pK\Lambda$ and $pp \to pK\Sigma^0$ reactions in order to estimate the background contribution, to optimize the constraint on the reduced χ^2 of the kinematic fit and to determine acceptance and reconstruction efficiency corrections as well as momentum and mass resolutions for the $pp \to pK\Lambda$ reaction. The simulation is based on the detector configuration including all relevant details, and the performance was set to be as close as possible to the measurement conditions. The software which is used for the simulations is based on the CERN package GEANT 3.2.1 [GEANT]. Since the analysis of the data is done here purely with the straw tube tracker the Monte Carlo program was modified to include the different resolutions of the STT double layers to obtain a more realistic detector response.

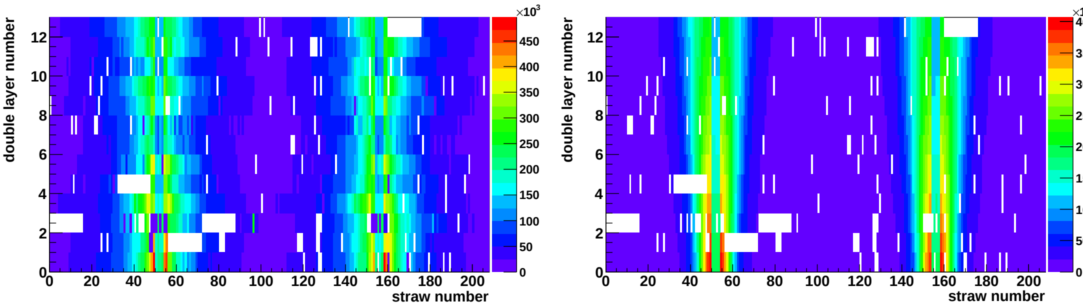

Figure 6.9.: Hit map of the straw tube tracker for $pK\Lambda$ events from data (left) and from MC simulation (right).

6.3.1. Simulation Methods

In the first step of the simulation the parameters for the particles like momenta and decay vertices are generated randomly. The process produces pure s-wave phase space. The beam is assumed to have a radius of 0.3 mm and a divergence of 1.4 mrad. The target is implemented as a cylinder of 4 mm length and 6 mm diameter. Afterwards the particles are transported through the detector and their interaction with the detector material is calculated. Multiple scattering and hadronic interactions are considered for all particles. The energy loss of a particle in the detector volume is digitized into signals (ADC and/or TDC) which are saved in files equivalent to the measured data. These files are processed in the same way as the data with the analysis program tof++ [CTOF06c].

The geometry of the COSY-TOF detector is implemented with the same parameters as for real data. Additionally, the efficiencies of the detector components are simulated according to parameters extracted from data. As an example the hit map for the STT is shown in Figure 6.9 for data (left) and from simulation (right). The horizontal axis correspond to the straw number in each plane while the vertical axis shows the different double layer planes. In a given double layer the straws from 104 to 207 are downstream of the straws 0 to 103. The straws $50-53$ and $154-157$ are the central straws with half length for the beam hole, thus they have roughly only half the number of counts as the surrounding straws. The five large regions without any hits are groups of 16 straws each. These inefficiencies could be explained by problems in the electronic read out, since the straws are grouped into 16-channel units there. Other inefficient regions could be due to mechanical damage of the straw or electronical problems.

The generated isochrone radius from a particle interacting with the STT in the simulation is randomly smeared with the resolution function determined by the calibration procedure (see Section 4.2.4). To gain a realistic detector response this is done with individual resolution curves per double layer.

In the next section the results for the simulations of the $pp \to pK\Lambda$ and $pp \to pK\Sigma^0$ are presented.

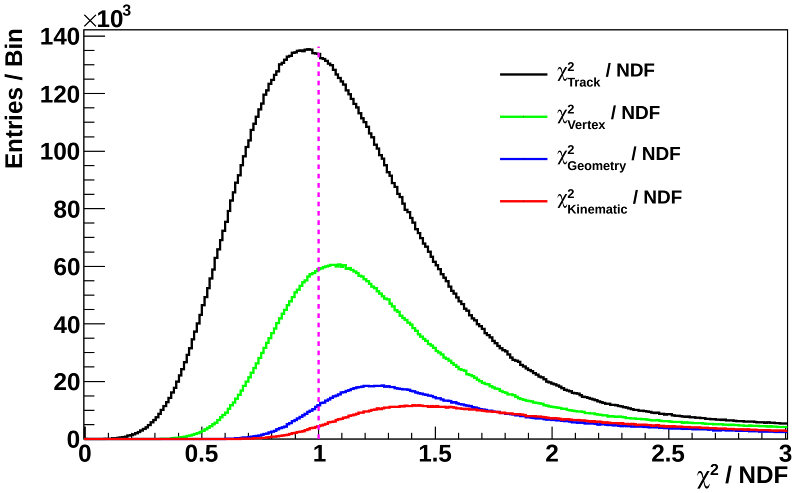

Figure 6.10.: Reduced χ^2 distribution for the different steps in the reconstruction procedure: Track fit (black), vertex fit (green), geometry fit (blue) and kinematic fit (red). The dashed violet line marks the expectation value of $\chi^2/\mathrm{NDF} = 1$.

6.3.2. $pp \to pK\Lambda$ Simulation Results

Five million $pp \to pK\Lambda \to pK\{p\pi^-\}$ events were simulated to determine the reconstruction efficiency and acceptance and to obtain the resolution for the vertices, momenta and invariant masses. The $\Lambda \to n\pi^0$ decay is not simulated because it can not be measured by COSY-TOF. Therefore, all determined efficiencies are multiplied by the branching ratio of the charged decay channel $\mathrm{BR}(\Lambda \to p\pi^-) = 0.64$ [PDG2012] for the corrections applied to the data.

6.3.2.1. Efficiency and Acceptance Correction

From the simulation the reduced χ^2 distributions are investigated for the different steps of the reconstruction procedure. These are shown in Figure 6.10 with the resulting histograms from the track fit (χ^2_T, black), the vertex fit (χ^2_V, green), the geometry fit (χ^2_G, blue) and the kinematic fit (χ^2_K, red). The expectation value $\chi^2/\mathrm{NDF} = 1$ is shown as the dashed violet line. Only the χ^2 distribution after the track fit is roughly centered around this value. The other histograms increasingly deviate from the expectation value due to the effect of multiple scattering of the particles. The planarity condition that the Λ decay plane must contain the primary vertex in the geometry and kinematic fit is strongly influenced by multiple scattering. Additionally, the finite beam divergence effects the determination of the χ^2_K value, thus the kinematic fit distribution deviates more from the expectation value than the geometry distribution. Nevertheless, the χ^2 distributions are similar to the ones determined at 2.95 GeV/c beam momentum (see Figure 4.3 in [Roe11]), hence the quality of the analysis presented here is similar to the

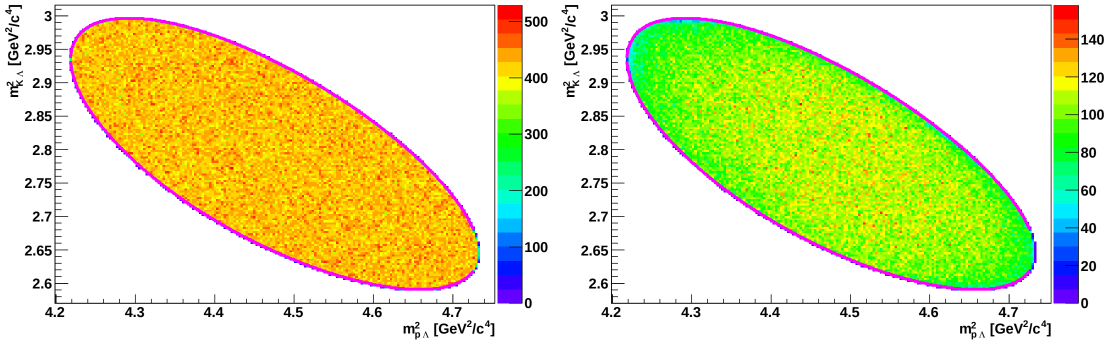

Figure 6.11.: Dalitz plot of the generated $pK\Lambda$ events from Monte Carlo simulation (left) and reconstructed events (right). The violet lines mark the kinematical limits.

previous one.

To demonstrate the full phase space coverage of the COSY-TOF detector the generated and reconstructed Dalitz plot of the $pK\Lambda$ events is shown in Figure 6.11 on the left and right plot, respectively. The reconstructed Dalitz plot covers the full phase space and is nearly flat. Therefore, the combined reconstruction efficiency and acceptance correction is almost constant over the available phase space.

After applying the three selection criteria for the $pp \to pK\Lambda$ reaction for the simulated data the combined reconstruction efficiency (RE) and acceptance correction (AC) for the $pp \to pK\Lambda \to pK\,\{p\pi^-\}$ reaction is

$$(\mathrm{RE}\cdot\mathrm{AC})_{\mathrm{K}} = \frac{N_{reco}}{N_{gen}} = (24.0 \pm 0.02)\,\%. \tag{6.7}$$

The quoted error is the statistical error. This value has to be multiplied with the branching ratio 0.64 to obtain the combined reconstruction efficiency and acceptance correction for the $pp \to pK\Lambda$ reaction of $(\mathrm{RE}\cdot\mathrm{AC})_{\mathrm{K,tot}} = (15.4 \pm 0.01)\,\%$.

6.3.2.2. Detector Resolution

To study the detector resolution the selection criteria used for the data analysis are applied to the reconstructed Monte Carlo events. The difference between the reconstructed and the generated values gives the resolution. Figure 6.12 shows the resolution of the primary vertex (left column) and the Λ decay vertex (right column) for each of the three axes x (upper), y (middle) and z (lower). Each distribution has been fitted with a Gaussian function (red) to describe the peak region since the tails, which might caused by the multiple scattering, have a non Gaussian shape. The σ values of the fit is shown for each distribution and summarized in Table 6.1.

Vertex Type	σ_x [μm]	σ_y [μm]	σ_z [μm]
Primary vertex	511	426	1650
Λ vertex	580	465	2380

Table 6.1.: Resolution for each spatial direction of the primary vertex and the Λ decay vertex from Monte Carlo simulation.

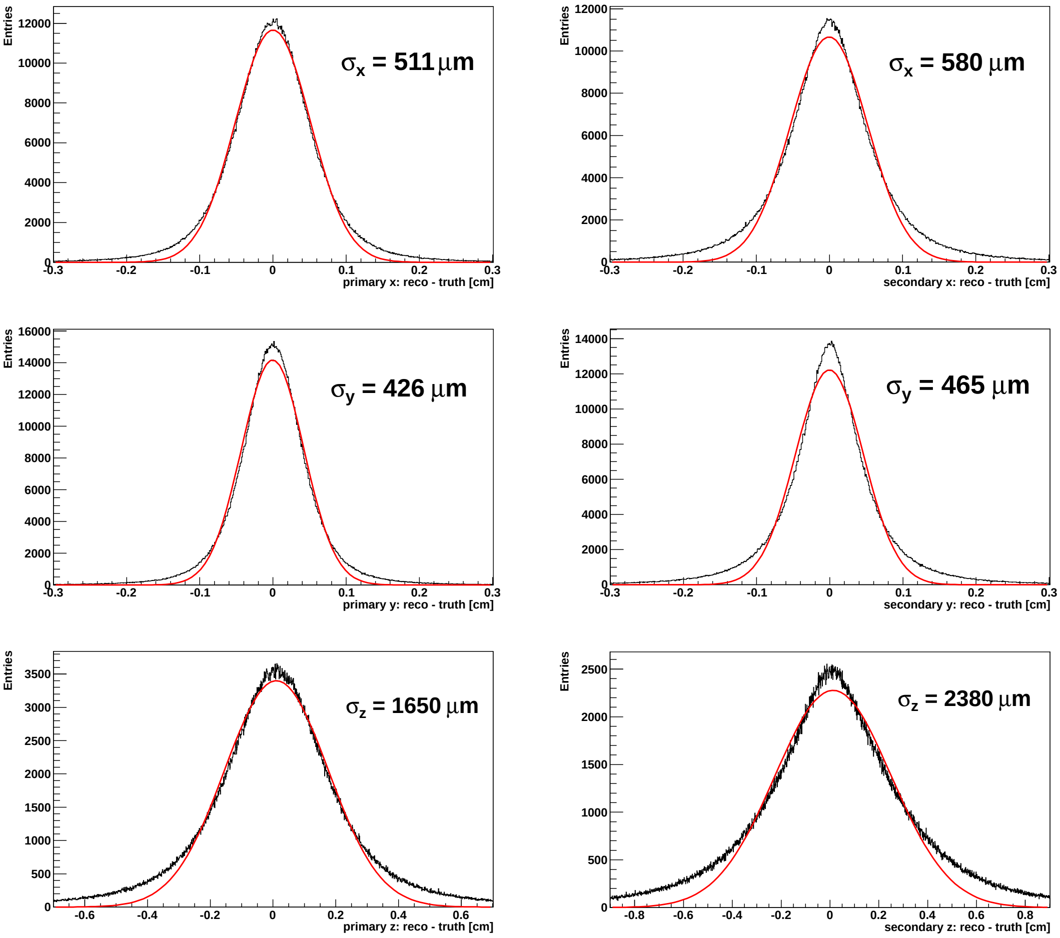

Figure 6.12.: Resolution of primary vertex (left column) and Λ decay vertex (right column) for the three directions x (upper), y (middle) and z (lower). The red curves show a Gaussian fit to describe the peak region. Note that the z-components have a different scale compared to the others.

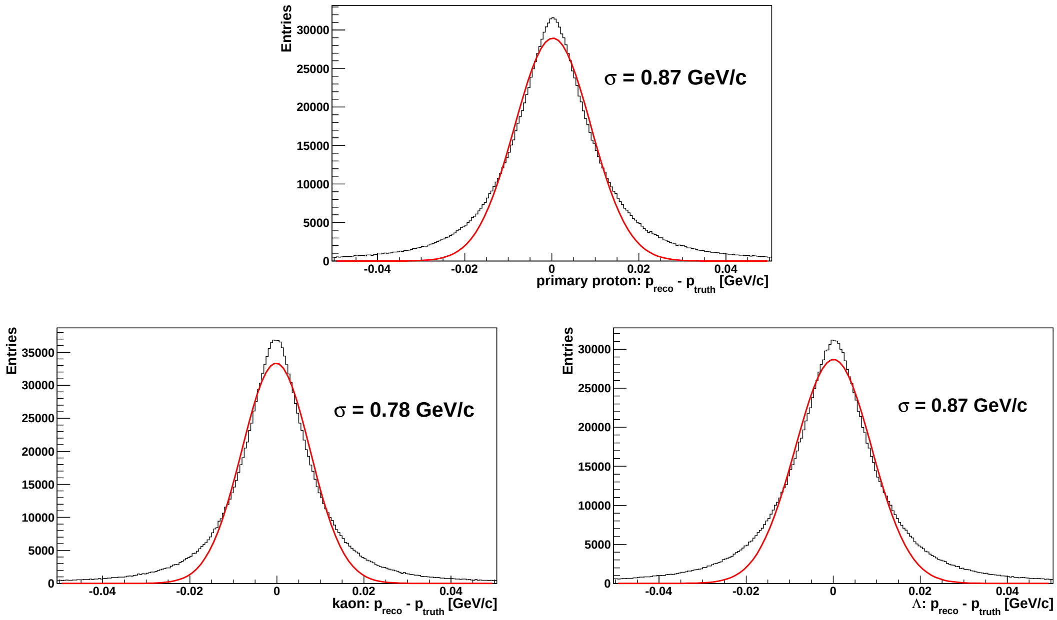

Figure 6.13.: Momentum resolution $|\vec{p}_{\text{reco}}| - |\vec{p}_{\text{truth}}|$ of the final state particles of the $pp \to pK\Lambda$ reaction. These are proton (upper), kaon (lower left) and Λ (lower right). The red lines show a Gaussian fit to describe the peak region properly. The σ values from the fit are given.

In all cases the peaks are distributed around zero, thus the reconstruction of the vertex has no systematic deviation in any direction. Because the reconstruction of the secondary vertex is done with the primary vertex and the Λ decay length, its resolutions can be not better than the resolution of the primary vertex. Since most of the tracks have small polar angle, the resolution for the z-component is about a factor three to four worse than the resolution of the orthogonal axis.

The momentum resolution is determined by $|\vec{p}_{\text{reco}}| - |\vec{p}_{\text{truth}}|$ for the final state particles of the reaction after the kinematic fit. The results are shown in Figure 6.13 for the proton (upper), kaon (lower left) and Λ (lower right) together with a Gaussian fit to describe the peak region. All distributions are peaked around zero but they have non Gaussian tails from multiple scattering. The momentum resolution is similar for all particles. This is expected after the kinematic fit since any inaccuracies in the momentum reconstruction should be equally distributed for all particles.

For the determination of the $p\Lambda$ scattering length (see Chapter 8) it is important to know the $p\Lambda$ invariant mass resolution because it is an input parameter for the fit of the $m_{p\Lambda}$ spectrum. In the former analysis [Roe11] the mass resolution was determined for the full data set. But the distribution of the mass difference $m_{p\Lambda}^{\text{reco}} - m_{p\Lambda}^{\text{truth}}$ over the generated value $m_{p\Lambda}^{\text{truth}}$ (Figure 6.14 left) shows that it has to be done for every mass bin separatly. The eye-like structure in Figure 6.14 (left) is due to the kinematic

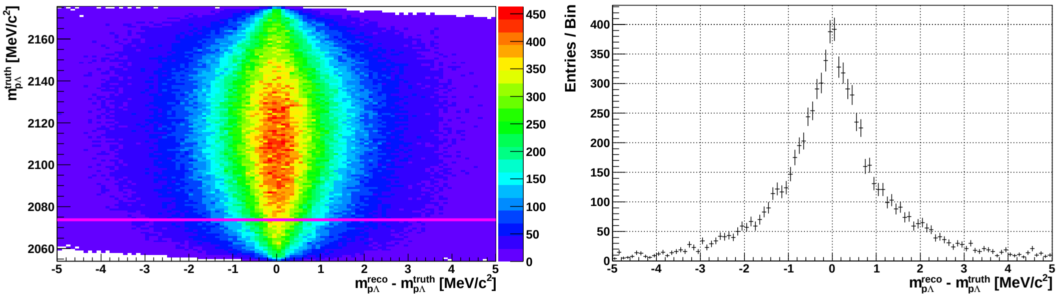

Figure 6.14.: Left: Invariant mass difference $m_{p\Lambda}^{\mathrm{reco}} - m_{p\Lambda}^{\mathrm{truth}}$ versus $m_{p\Lambda}^{\mathrm{truth}}$ determined by Monte Carlo simulations. The structure observed is a result of the kinematic fit. **Right:** Projection of the y-bin indicated by the violet line in the left plot onto the x-axis.

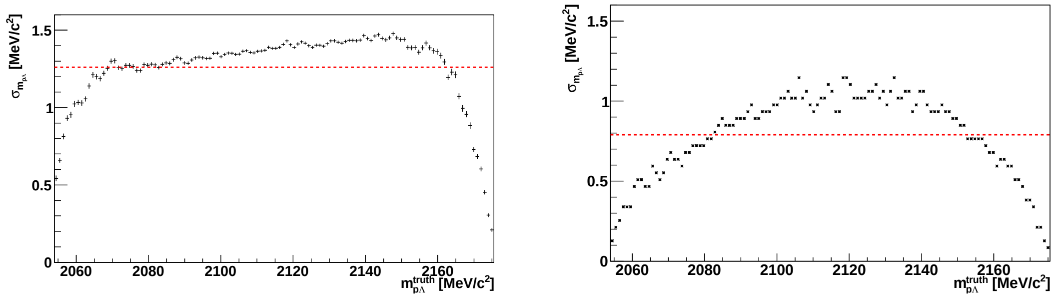

Figure 6.15.: Left: Mass resolution σ_m over $m_{p\Lambda}^{\mathrm{truth}}$ determined by a Gaussian fit of the projections shown in Fig. 6.14 right. **Right:** Mass resolution σ_m over $m_{p\Lambda}^{\mathrm{truth}}$ determined by FWHM of the projections shown in Fig. 6.14 right. The dashed red line marks the averaged value for both distributions.

fit which pushes the mass value at the kinematical boarders into the allowed range, thus improving the resolution for $m_{p\Lambda}^{\mathrm{truth}}$ values close to 2054 MeV/c^2 and 2175 MeV/c^2. Therefore, the resolution is determined as a function of $m_{p\Lambda}^{\mathrm{truth}}$ by taking the projection on the x-axis for every y-bin. Figure 6.14 (right) shows as an example this projection at the bin which is marked with the violet line in the left part of the figure. The mass resolution σ_{m} is determined from the projections by a Gaussian fit and by the FWHM value of the distribution. Both methods are used since the distribution has non Gaussian tails. Therefore, a Gaussian fit of the whole range does not describe the peak properly while the FWHM methods does not take into account the tails properly. Nevertheless, the result of the Gaussian fit gives an upper limit of the mass resolution while the FWHM method gives a lower limit.

The result for both methods is shown in Figure 6.15 (fit method on the left plot and the FWHM method on the right plot). The resolution distributions have a similar shape for both methods. The resolution is improved at the borders of the spectrum and is roughly constant for the middle values. The result from the FWHM yields a better resolution than the fit method as expected. For the fit method the rise of the resolution from the limits of the spectrum to the middle is faster than for the FWHM method. The dashed red lines shows the averaged value for the mass resolutions. They are $\sigma_{\mathrm{m}} = (1.26 \pm 0.24)\,\mathrm{MeV}/c^2$ for the fit method and $\sigma_{\mathrm{m}} = (0.79 \pm 0.26)\,\mathrm{MeV}/c^2$ for the FWHM method. Both values are below the required invariant mass resolution $\sigma_{\mathrm{m}} = 5\,\mathrm{MeV}/c^2$ for the spin triplet extraction method [Gas04]. The averaged mass resolution $\sigma_{\mathrm{m}} = 1.1\,\mathrm{MeV}/c^2$ determined in [Roe11] by the FWHM method is inside the limits of the two methods. For the determination of the effective scattering length in Chapter 8 the result from the fit method is used. Additionally, the mass resolution is determined with the fit method for a $5\,\mathrm{MeV}/c^2$ bin width of $m_{p\Lambda}$, and the result is employed in the extraction of the spin triplet scattering length presented in Chapter 8.

6.3.3. $pp \to pK\Sigma^0$ Background

As already mentioned the $pp \to pK\Sigma^0$ reaction is the dominant background channel, since the $\Sigma^0 \to \Lambda\gamma$ decay is indistinguishable from the directly produced Λ[2], and therefore the decay length distributions are similar. Only the constraint on $\chi^2_{\mathrm{K}}/\mathrm{NDF}$ of the kinematic fit could suppress the Σ^0 channel. A Monte Carlo sample of two million $pp \to pK\Sigma^0 \to pK\Lambda\gamma \to pK\,\{p\pi^-\}\,\gamma$ was analyzed in order to calculate the surviving percentage of the background channel in the data. All parameters are set to the same values as for the $pK\Lambda$ analysis.

To determine the surviving percentage of the $pK\Sigma^0$ background in the data, the ratio of total cross section and combined reconstruction efficiency and acceptance has to be determined. Applying the three selection criteria (see Section 6.1) on the simulated $pp \to pK\Sigma^0$ data, the combined reconstruction efficiency and acceptance is $(5.8 \pm 0.02)\,\%$. For the $pK\Lambda$ reaction this is $(24.0 \pm 0.02)\,\%$ (see Section 6.3.2.1).

The excess energy for the $pp \to pK\Sigma^0$ reaction at $2.7\,\mathrm{GeV}/c$ beam momentum is $\epsilon \approx 45\,\mathrm{MeV}$. According to [C1104, CTOF10a] the excitation function of the total cross section can be described by a pure phase space dependence with $\sigma_{\Sigma^0}(\epsilon) = A \cdot \epsilon^2$ and $A = (0.150 \pm 0.008) \cdot 10^{-3}\mu\mathrm{b}/\mathrm{MeV}^2$. Therefore, the total cross section at $2.7\,\mathrm{GeV}/c$ is estimated to be $\sigma_{\mathrm{tot}}(pp \to pK\Sigma^0) = (0.3 \pm 0.02)\,\mu\mathrm{b}$. With the interpolated total cross section for $pp \to pK\Lambda$ (see Section 7.1) the ratio becomes

$$\frac{\sigma_{\mathrm{tot}}(pp \to pK\Lambda)}{\sigma_{\mathrm{tot}}(pp \to pK\Sigma^0)} = 33.3 \pm 5.2. \tag{6.8}$$

Taking into account the ratio of the combined reconstruction efficiency and acceptance for both channels, the admixture of $pK\Sigma^0$ background is $(0.73 \pm 0.11)\,\%$. The error is dominated by the uncertainty of the cross section ratio. The background is lower than

---

[2] The photon leaves the detector undetected.

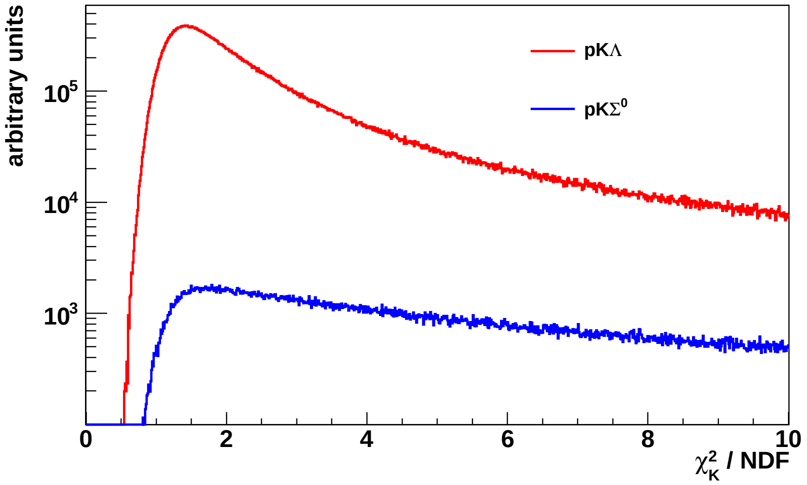

Figure 6.16.: Monte Carlo distributions of χ^2_{K}/NDF for the reactions $pp \to pK\Lambda$ (red) and $pp \to pK\Sigma^0$ (blue) corrected with the total cross section ratio from Equation 6.8 and the ratio of simulated Monte Carlo events. Note the logarithmic scale on the y-axis.

a conservative upper limit of 1%, and thus is neglected in the following. In addition, this can be seen in Figure 6.16 where the χ^2_{K}/NDF distributions of the reconstructed $pp \to pK\Lambda$ and $pp \to pK\Sigma^0$ Monte Carlo events are shown in red and blue corrected for the total cross section ratio and the different number of simulated events (five million to two million). In both cases the distributions peak at $\chi^2_{\mathrm{K}}/\mathrm{NDF} \approx 1.5$ but the peak height for the $pK\Lambda$ events is about a factor two hundred higher than for the $pK\Sigma^0$ events which have a much wider χ^2_{K}/NDF distribution.

The $pK\Sigma^0$ background exhibits a surprising kaon angular distribution in the CMS. The distribution is shown in Figure 6.17 and is strongly peaked in the range $\cos(\theta_K^{\mathrm{CMS}}) \in [-1, -0.9]$. In fact, roughly 30% of the reconstructed events lie in this range. Therefore, the $pK\Sigma^0$ background could be visible in the kaon angular distribution of the analyzed data, if the determined upper limit is wrong. As it turns out, no peak at $\cos(\theta_K^{\mathrm{CMS}}) = -1$ is visible in data (see Section 7.3.1).

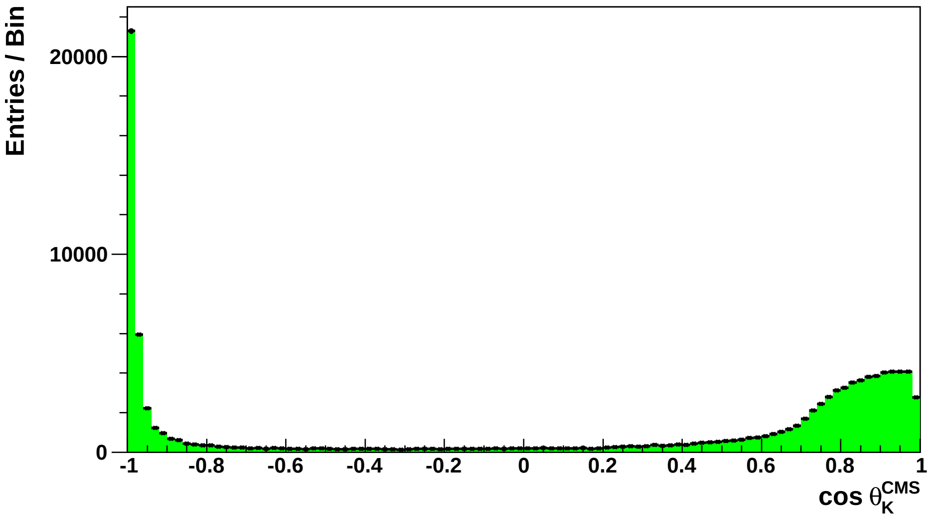

Figure 6.17.: Kaon angular distribution in the CMS for the reconstructed $pp \to pK\Sigma^0$ MC sample.

Theories come and go, but fundamental data
always remain the same.

(Mary Leakey)

7. Results for the $\vec{p}p \to pK\Lambda$ Reaction

In this chapter the results for the data collected at a beam momentum of 2.7 GeV/c will be shown. This includes the Dalitz plot and its projections, the angular distributions, the Λ polarization and the analyzing power for the final state particles. For the determination of the $p\Lambda$ scattering length from the $p\Lambda$ invariant mass see Chapter 8.

7.1. Interpolated Total Cross Section

In Figure 7.1 the total cross section for the $pp \to pK\Lambda$ reaction is shown as a function of the excess energy. The green line marks the excess energy $\epsilon = 122\,\mathrm{MeV}$ corresponding to 2.7 GeV/c beam momentum. For this analysis the total cross section is interpolated between the data values at 2.68 GeV/c ($\sigma_{\mathrm{tot}} = (8.6 \pm 0.6)\,\mu\mathrm{b}$) from [CTOF06a] and at 2.75 GeV/c ($\sigma_{\mathrm{tot}} = (12.0 \pm 0.4)\,\mu\mathrm{b}$) from [CTOF98a] with a pure phase space dependence, hence $\sigma_{\mathrm{tot}} = A \cdot \epsilon^2$.

The result is $\sigma_{\mathrm{tot}} \sim (10.0 \pm 0.7)\,\mu\mathrm{b}$ taking into account the error from the measurement at 2.68 GeV/c and at 2.75 GeV/c. The determination method has a systematic uncertainty from the interpolation function because a realistic description of the total cross section dependence on the excess energy must include $p\Lambda$ final state interaction (FSI). Such a function is shown as the black line in Figure 7.1 taking a parametrization of Fäldt and Wilkin [Fae97] into account. It is estimated, that the systematic error from the parametrization is of the same order as the statistical error from the 2.68 GeV/c measurement. Therefore, the total cross section is interpolated to be $\sigma_{\mathrm{tot}} \sim (10.0 \pm 0.7_{\mathrm{stat.}} \pm 0.7_{\mathrm{sys.}})\,\mu\mathrm{b}$.

For the normalisation of the differential distributions the total cross section is taken to be $\sigma = 10.0\,\mu\mathrm{b}$.

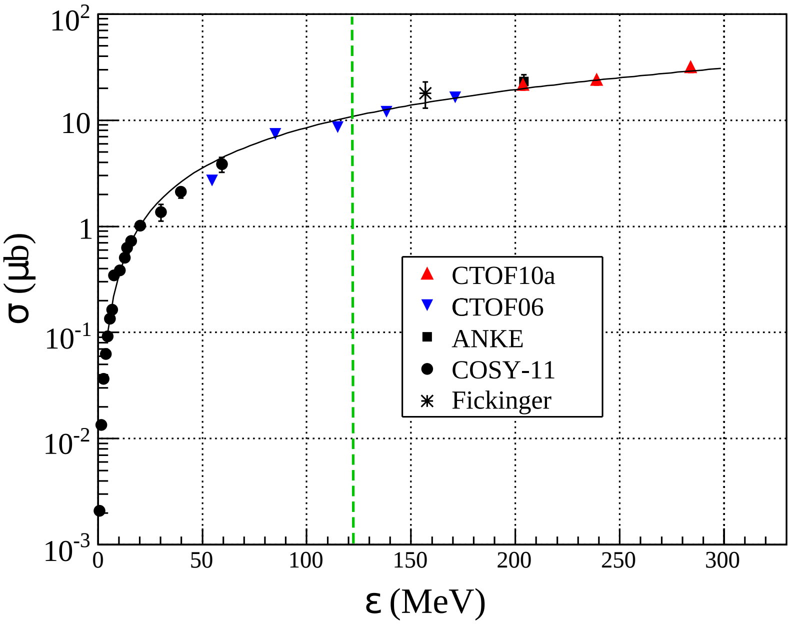

Figure 7.1.: Total cross section of the reaction $pp \to pK\Lambda$ for excess energies $\epsilon \leq$ 300 MeV taken from [CTOF10a]. The data shown are from COSY-TOF [CTOF10a, CTOF06a] (red and blue triangles), COSY-11 [C1197, C1198a, C1199, C1104] (black circles), ANKE [Val07] (black square) and Fickinger [Fic62] (black cross). The dashed green line marks the excess energy for the measurement at 2.7 GeV/c presented in this thesis. The black line corresponds to a parametrization of the total cross section by phase space and $p\Lambda$ final state interaction proposed by Fäldt and Wilkin in [Fae97].

7.2. Dalitz Plot and Invariant Mass Distributions

7.2.1. Dalitz Plot and Projections

The Dalitz plot [Dal53] is usually shown as a two dimensional plot of two invariant mass squared subsystems. For a pure phase space distribution the Dalitz plot would be uniformly filled. It is possible to draw three different Dalitz plots for the $pp \to pK\Lambda$ reaction, each with a different combination of two invariant masses on the x and y-axes. After the kinematic fit these Dalitz plots, corrected by acceptance and reconstruction efficiency, are shown in Figure 7.2 in the left column. The combinations for the mass systems are from upper to lower: $m^2_{p\Lambda}$ versus $m^2_{K\Lambda}$, $m^2_{p\Lambda}$ versus m^2_{pK} and $m^2_{p\Lambda}$ versus $m^2_{K\Lambda}$. The violet lines mark the allowed kinematical region.

The invariant mass squared distributions can be obtained by projecting the Dalitz plot to the corresponding axis. The distributions are shown on the right column in Figure 7.2 together with the acceptance and reconstruction efficiency correction from Monte Carlo simulation below each plot.

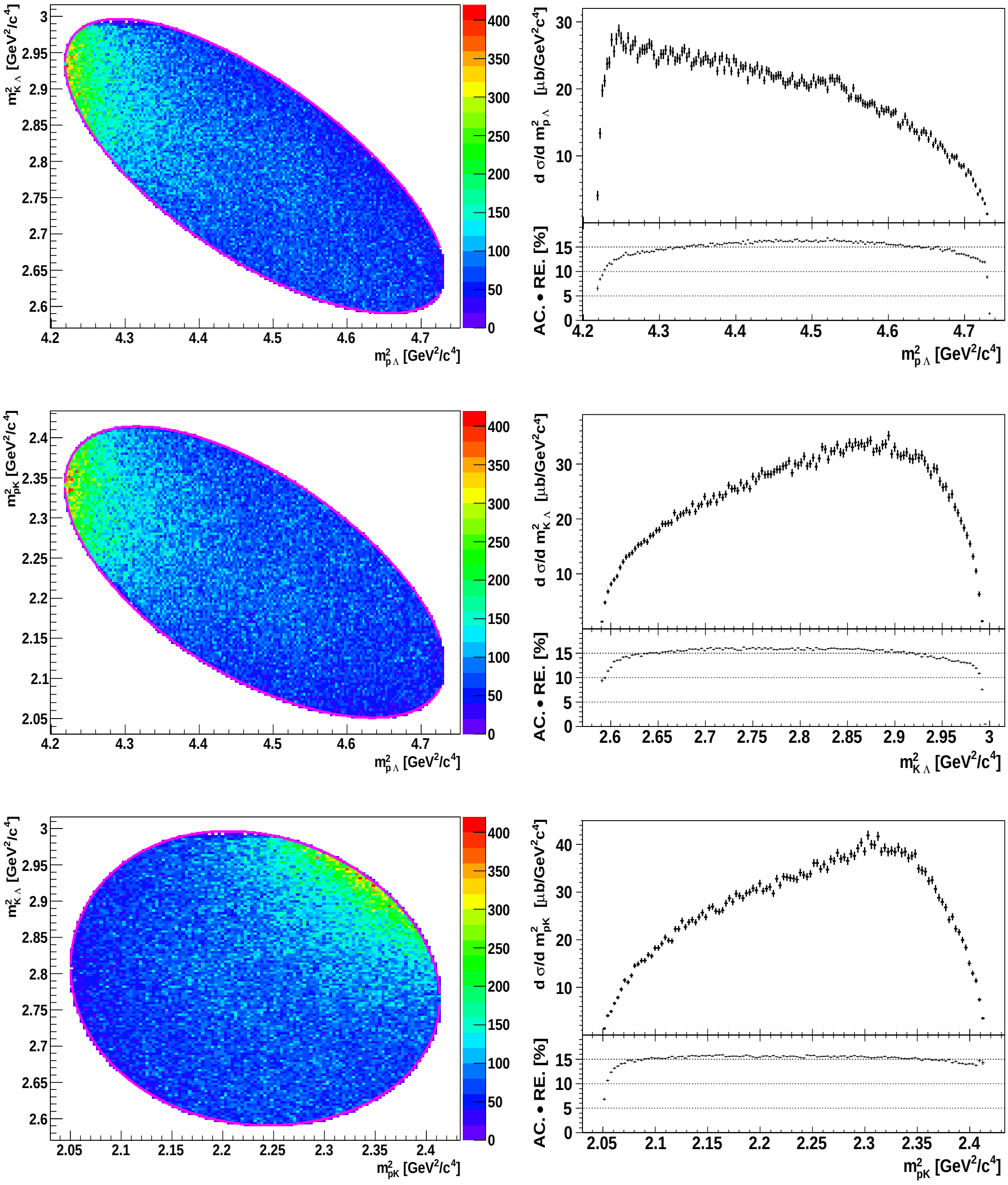

Figure 7.2.: Dalitz plot for different combinations of the invariant mass subsystems: $m^2_{p\Lambda}$ versus $m^2_{K\Lambda}$ (upper), $m^2_{p\Lambda}$ versus m^2_{pK} (middle) and $m^2_{p\Lambda}$ versus $m^2_{K\Lambda}$ (lower). The violet lines mark the allowed kinematical region. On the right side the projections on each mass subsystem is shown normalized to a total cross section of 10 μb with the correction for acceptance and reconstruction efficiency from Monte Carlo simulation below each plot: $m^2_{p\Lambda}$ invariant mass (upper), $m^2_{K\Lambda}$ invariant mass (middle) and m^2_{pK} invariant mass (lower).

From previous measurements [CTOF98a, CTOF10a] the influences of the processes in the production mechanism (N^* resonances, $p\Lambda$ final state interaction and $N\Sigma$ cusp effect) are directly visible in the Dalitz plot with the axes $m^2_{p\Lambda}$ and $m^2_{K\Lambda}$. The other illustrations exhibit only structures from kinematical reflections. Therefore, the acceptance and efficiency corrected Dalitz plot with the $m^2_{p\Lambda}$ mass subsystem on the x-axis and the $m^2_{K\Lambda}$ mass subsystem on the y-axis is again plotted in Figure 7.3.

The Dalitz plot clearly deviates from uniformly distributed phase space for low $p\Lambda$ masses due to the $p\Lambda$ final state interaction. The peak position (mass) of possible N^* resonances are drawn as the dashed brown line (N^*-1650) and the dashed black line (N^*-1720) but there is no obvious enhancement from them along the $m^2_{K\Lambda}$ mass. This is explainable since these resonances are more than 100 MeV wide. Thus, they extend over the whole Dalitz plot. But a partial wave analysis or a fit of amplitude models[1] can be used to extract the resonance contributions. In addition, the red and violet dashed lines show the $p\Sigma^0$ and $n\Sigma^+$ thresholds, respectively. This is the position of the coupled channel effect enhancement observed in measurements at higher beam momenta at COSY-TOF [CTOF10b, CTOF13a]. It is pratically not visible in the Dalitz plot for the measurement at 2.7 GeV/c beam momentum.

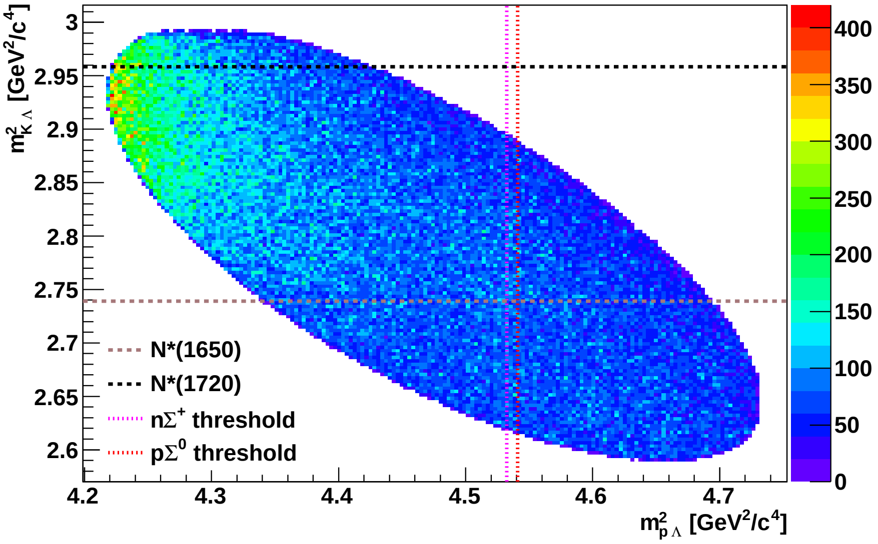

Figure 7.3.: Acceptance and reconstruction efficiency corrected Dalitz plot for the kinematically fitted 2.7 GeV/c data. The brown and black dashed lines mark the peak position (mass) of the resonances $N^*(1650)$ and $N^*(1720)$, respectively. The red and violet dashed lines show the $p\Sigma^0$ and $n\Sigma^+$ threshold, respectively.

---

[1] for instance the ISOBAR model from A.Sibirtsev [Sib02], which was used in former COSY-TOF publications and theses [CTOF10b, Fri02, Schr03].

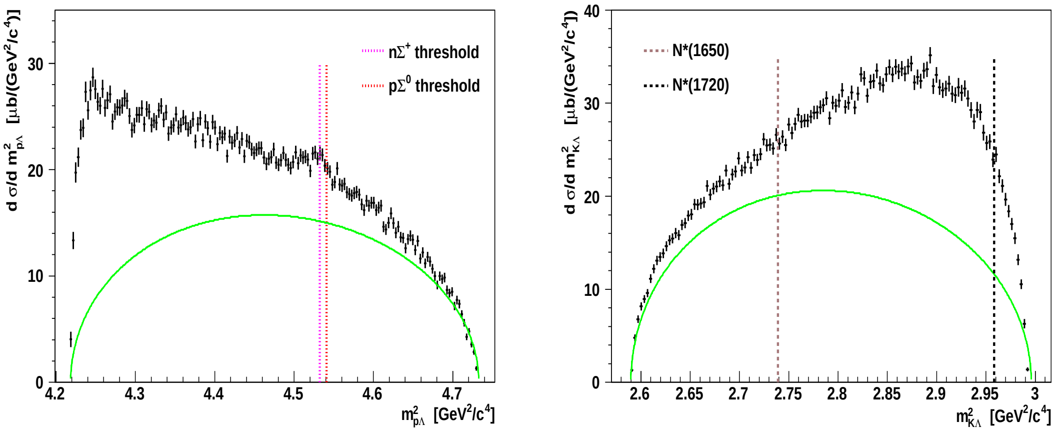

Figure 7.4.: Projections on the $m^2_{p\Lambda}$ axis (left) and $m^2_{K\Lambda}$ axis (right) of the Dalitz plot shown in Figure 7.3. In both spectra the green line denotes a phase space distribution scaled to fit the data at the end without the $p\Lambda$-FSI enhancement. The dashed lines are the same as in Figure 7.3.

In Figure 7.4 the projections of the Dalitz plot on both axis is shown together with the phase space distribution (green line), scaled in a way that it fits the data at the region without the $p\Lambda$-FSI enhancement. The green line denotes the maximal allowed phase space contribution in both spectra, assuming the cross section to be an incoherent sum of phase space, resonance contributions, $N\Sigma$ enhancement and $p\Lambda$-FSI.

In the projection to the $m^2_{p\Lambda}$ axis (Fig. 7.4 left) the enhancement at low invariant masses results from the final state interaction. In contrast to the Dalitz plot, an additional enhancement is visible at the $N\Sigma$ thresholds marked by the red and violet dashed lines. It is small compared to measurements at higher beam momenta (see [Roe11, Jow14]). The projection on the $m^2_{K\Lambda}$ axis (Fig. 7.4 right) shows no separate enhancement. The brown and black dashed lines mark the peak value of N^* resonances which are more than 100 MeV wide, and therefore are not visible as single peaks. The kinematic reflection of the $p\Lambda$ final state interaction enhances the $m^2_{K\Lambda}$ distribution in the range from $2.8\,\mathrm{GeV}^2/c^4$ to $2.98\,\mathrm{GeV}^2/c^4$.

7.2.2. Dalitz Plot of different $\cos\theta^{p\Lambda}_{pK}$ Ranges

For the determination of the $p\Lambda$ scattering length and the influence of N^* resonances on this variable, the Dalitz plot is separated into different ranges of the helicity angle $\cos\theta^{p\Lambda}_{pK}$ (for an explanation of the angle see Section 7.3). The data is split into four ranges which are shown in Figure 7.5: $\cos\theta^{p\Lambda}_{pK} > 0.5$ (upper left), $0 < \cos\theta^{p\Lambda}_{pK} < 0.5$ (upper right), $-0.5 < \cos\theta^{p\Lambda}_{pK} < 0$ (lower left) and $\cos\theta^{p\Lambda}_{pK} < -0.5$ (lower right). This

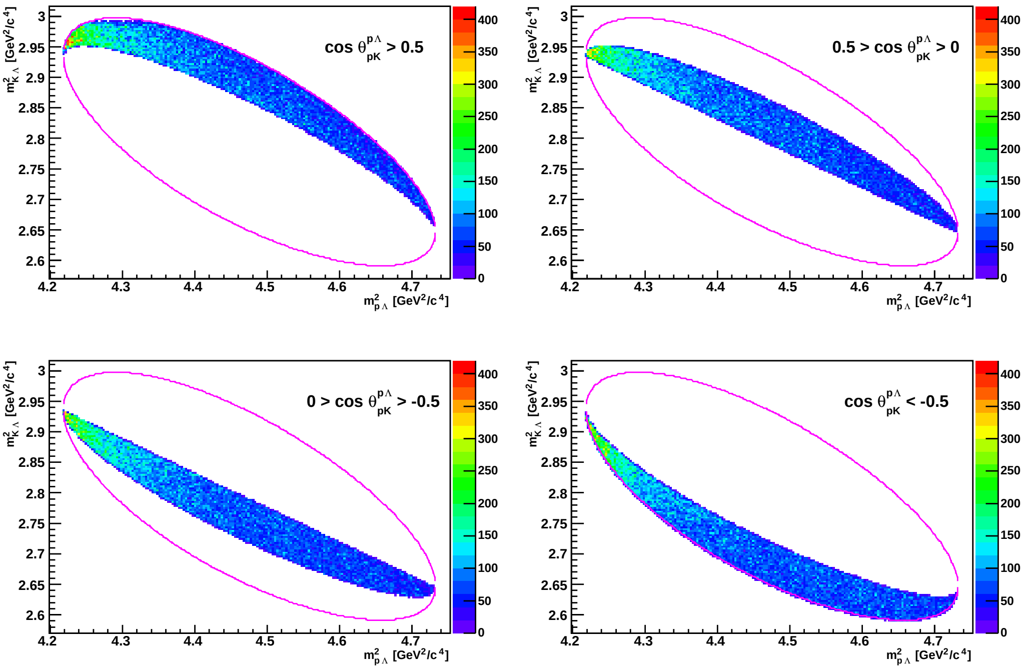

Figure 7.5.: Acceptance and reconstruction efficiency corrected Dalitz plot of the kinematical fitted data presented in this thesis for different $\cos\theta_{pK}^{p\Lambda}$ ranges in order to determine the influence of N^* resonances on the $p\Lambda$ final state interaction (see Section 8.3). The violet lines show the kinematical limits.

separation corresponds to splitting the total $m^2_{K\Lambda}$ range for a given $m^2_{p\Lambda}$ value into four equal parts. Therefore, the phase space distribution of each part contains exactly 1/4 of the total phase space and its functional description is the same [Kil13]. By comparing the invariant mass distribution of the various parts, any influence of N^* resonances on the $m_{p\Lambda}$ spectrum is directly visible. In addition, a systematic error on the extraction of the scattering length for the different data sets due to a different phase space behavior is excluded (see Section 8.3). The corresponding invariant mass distributions are shown in the next section.

7.2.3. $m_{p\Lambda}$ Invariant Mass Distributions

In Figure 7.6 the $p\Lambda$ invariant mass distribution corrected for acceptance and reconstruction efficiency is shown normalized to a total cross section of 10 μb. The large enhancement at low invariant masses is due to the $p\Lambda$-FSI. It is fitted in Section 8.2 to determine the $p\Lambda$ effective scattering length. The small enhancement at an invariant mass of about 2130 MeV/c^2 stems from the $N\Sigma$ coupled channel effect already seen in the Dalitz plot projection in the left plot in Figure 7.4. The invariant mass distribution

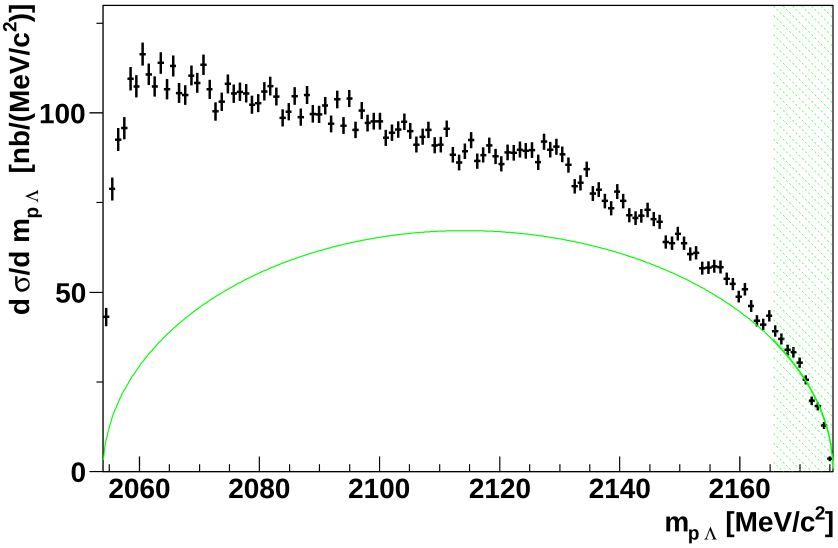

Figure 7.6.: Acceptance and reconstruction efficiency corrected $m_{p\Lambda}$ invariant mass distribution normalized to a total cross section of 10 μb. The green line shows a fit of the phase space distribution in the green shaded area ($m_{p\Lambda} > 2165\,\mathrm{MeV}/c^2$), where the FSI and $N\Sigma$ enhancements are taken to be negligible.

is fitted with the phase space distribution (green line) in the green shaded area where the $p\Lambda$-FSI and $N\Sigma$ enhancement are negligible. Thus, this phase space distribution indicates the maximum expected phase space contribution to the total cross section, assuming an incoherent sum of phase space, resonance contributions, $N\Sigma$ enhancement and $p\Lambda$ final state interaction.

As explained in the previous section the data is separated into different ranges of the helicity angle $\cos\theta_{pK}^{p\Lambda}$ to study the influence of N^* resonances on the invariant mass spectrum. The results for the invariant mass distributions are shown in Figure 7.7: $\cos\theta_{pK}^{p\Lambda} > 0.5$ (upper left), $0 < \cos\theta_{pK}^{p\Lambda} < 0.5$ (upper right), $-0.5 < \cos\theta_{pK}^{p\Lambda} < 0$ (lower left) and $\cos\theta_{pK}^{p\Lambda} < -0.5$ (lower right). The green line in each plot corresponds to the phase space distribution of Figure 7.6 divided by four because the phase space distribution for each helicity angle range is 1/4 of the total phase space. In all plots the enhancement at the $N\Sigma$ thresholds is not observed significantly.

From the number of events in each distribution the relative total cross section can be calculated assuming a total cross section of 10 μb for the complete data. The numbers are 43479 events for the upper left plot, 56194 events for the upper right plot, 57262 events for the lower left plot and 50284 for the lower right plot. This gives a total cross section fraction of $\sigma = (2.098 \pm 0.011)\,\mu$b, $\sigma = (2.712 \pm 0.013)\,\mu$b, $\sigma = (2.763 \pm 0.013)\,\mu$b and $\sigma = (2.427 \pm 0.012)\,\mu$b for the four helicity angle ranges, respectively. Thereby, only

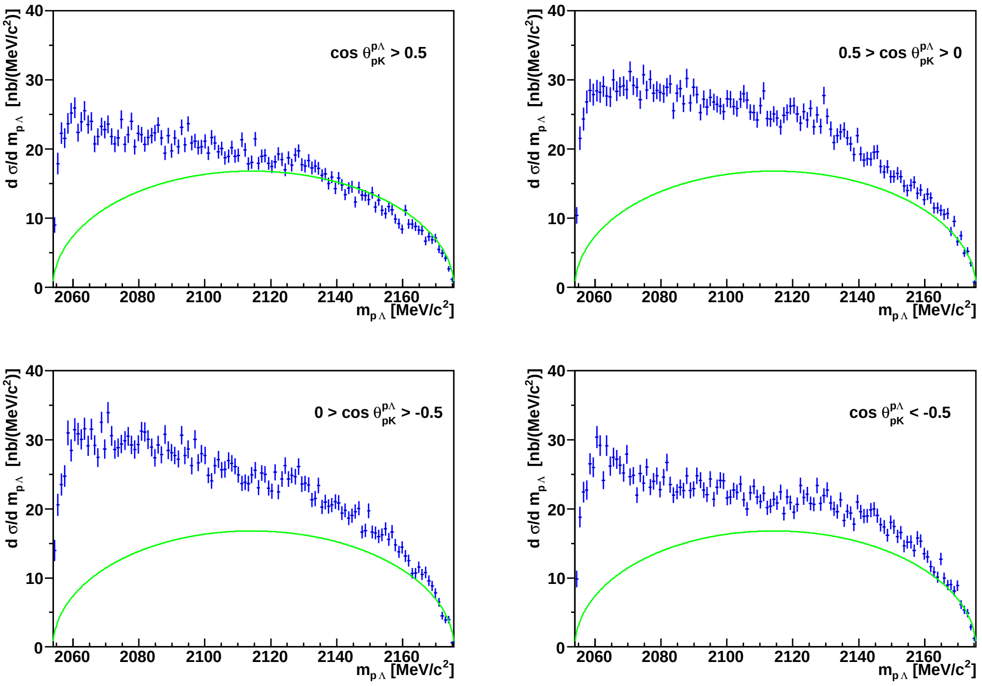

Figure 7.7.: Acceptance and reconstruction efficiency corrected $m_{p\Lambda}$ invariant mass distributions for different $\cos\theta^{p\Lambda}_{pK}$ ranges. The green line corresponds to the phase space fit of the total invariant mass spectrum (see Figure 7.6) divided by four.

the statistical error from the number of events is computed and not the systematic error from the total cross section normalization.

The invariant mass distribution for $\cos\theta^{p\Lambda}_{pK} > 0.5$ follows the phase space expectation for invariant masses $m_{p\Lambda} > 2135\,\mathrm{MeV}/c^2$, whereas the distributions of the other helicity ranges match only with the phase space distribution for $m_{p\Lambda} > 2165\,\mathrm{MeV}/c^2$ corresponding to the phase space fit range of Figure 7.6. This deviation is connected to a larger influence of the kinematical reflection of the N^*-1650 MeV resonance in the ranges $\cos\theta^{p\Lambda}_{pK} < 0.5$.

For comparison the invariant mass distributions of Figure 7.7 are divided by their phase space distributions and plotted together in Figure 7.8. Again the deviation of the distributions with $\cos\theta^{p\Lambda}_{pK} < 0.5$ from the distributions with $\cos\theta^{p\Lambda}_{pK} > 0.5$ in the range $m_{p\Lambda} > 2135\,\mathrm{MeV}/c^2$ is visible. Furthermore, there is an indication of different shapes of the $p\Lambda$-FSI enhancement for the helicity angle ranges. This results in different values for the $p\Lambda$ effective scattering length as shown in Section 8.3. The reason might be an influence of the N^*-1720 MeV resonance. Nevertheless, the effect is significantly weaker than in the $pp \to pK\Lambda$ measurement at 2.95 GeV/c beam momentum [CTOF13b].

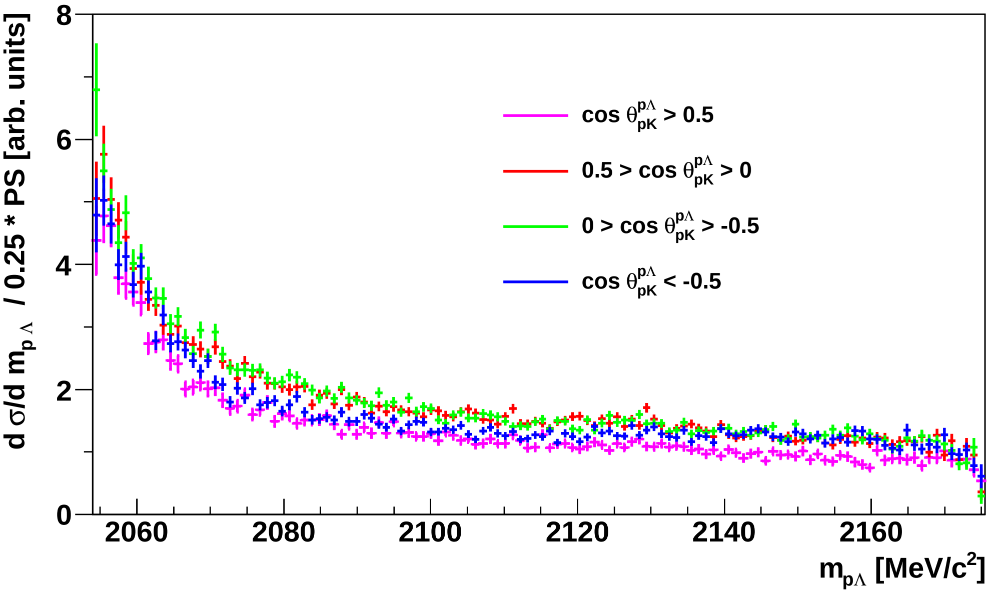

Figure 7.8.: The $m_{p\Lambda}$ invariant mass distributions for different $\cos\theta^{p\Lambda}_{pK}$ ranges shown in Figure 7.7 divided by their phase space distributions (green lines in Figure 7.7).

7.3. Angular Distributions

In the following section the angular distributions in different reference frames will be shown. Beside the distributions of the final state particles in the overall center of mass system, the angular distributions in the three different two particle mass subsystems ($p\Lambda$, $K\Lambda$ and pK) are shown.

The mass subsystem $R12$ is defined by the following condition (for further details see [Byc00])

$$\vec{p}_1 + \vec{p}_2 = \vec{p}_B + \vec{p}_T - \vec{p}_3 = 0.$$

The vectors $\vec{p}_B$, $\vec{p}_T$ and $\vec{p}_3$ define the production plane. $\vec{p}_B$ and $\vec{p}_T$ are the beam and target vector, respectively. To calculate the relative orientation of one of the subsystem vectors (for instance $\vec{p}_2$) the selection of a polar axis can be either $\vec{p}_B$ or $\vec{p}_3$.

The choice of $\vec{p}_B$ defines the so called Gottfried-Jackson frame [Got64] and the corresponding angle is called (Gottfried)-Jackson angle. Analogously, the choice of $\vec{p}_3$ is called the helicity frame and helicity angle. Especially the Gottfried-Jackson angles describe kinematical observables, which are not directly accessible with the Dalitz plot, whereas the helicity angles are special projections of the Dalitz plot and do not contain further information.

7.3.1. Center of Mass System

In Figure 7.9 the acceptance corrected angular distributions in the CMS for the three final state particles are shown: Kaon (upper), Λ (middle) and proton (lower). All distributions are normalized to a total cross section of $10\,\mu$b. The acceptance and reconstruction efficiency correction (AC $\cdot$ RE) from Monte Carlo simulation is depicted below each distribution.

Since the entrance channel of the reaction consists of identical particles the distributions should be symmetric with respect to $\cos\theta^{\mathrm{CMS}} = 0$. This is fulfilled for all spectra in the range $\cos\theta^{CMS} \in [-0.85, 0.85]$. The deviations at the boarders of the distributions arise possibly from an incorrect acceptance correction at these angles. Since the scattering length is determined by the acceptance and reconstruction efficiency corrected $p\Lambda$ invariant mass distribution, it is necessary to check if the improper description of the angular distributions in the simulation influence the correction for the invariant mass.

For that purpose the acceptance and reconstruction efficiency corrected $p\Lambda$ invariant mass distributions are determined for the two constraints $\cos\theta_K^{\mathrm{CMS}} < 0.9$ and $|\cos\theta_p^{\mathrm{CMS}}| < 0.95$. In Figure 7.10 (upper) these distributions are shown in red and blue, respectively, within the limit of the fitting procedure for the extraction of the scattering length. The distributions have a similar shape as the unconstrained invariant mass distribution (black in Figure 7.10). For a better visualization the unconstrained distribution is divided individually through the constrained distributions. The results are shown in the lower plot in Figure 7.10 in red for $\cos\theta_K^{\mathrm{CMS}} < 0.9$ (scaled for better visibility) and blue for $|\cos\theta_p^{\mathrm{CMS}}| < 0.95$. The black dashed lines show a fit with a constant to both results. Comparing with this fit, there might be a small bias to higher values for the lower part of the distributions and smaller values for the upper part in both distributions. But all differences lie within the error bars. Therefore, it is assumed that the improper acceptance correction in the angular distribution have no significant effect on the $p\Lambda$ scattering length from the invariant mass spectrum.

The angular distribution of the kaon exhibits no enhancement in the range $\cos(\theta_K^{\mathrm{CMS}}) \geq -0.9$, where the background of the $pp \rightarrow pK\Sigma^0$ reaction is expected (see Section 6.3.3). Thus, a higher amount of this background than expected can be excluded.

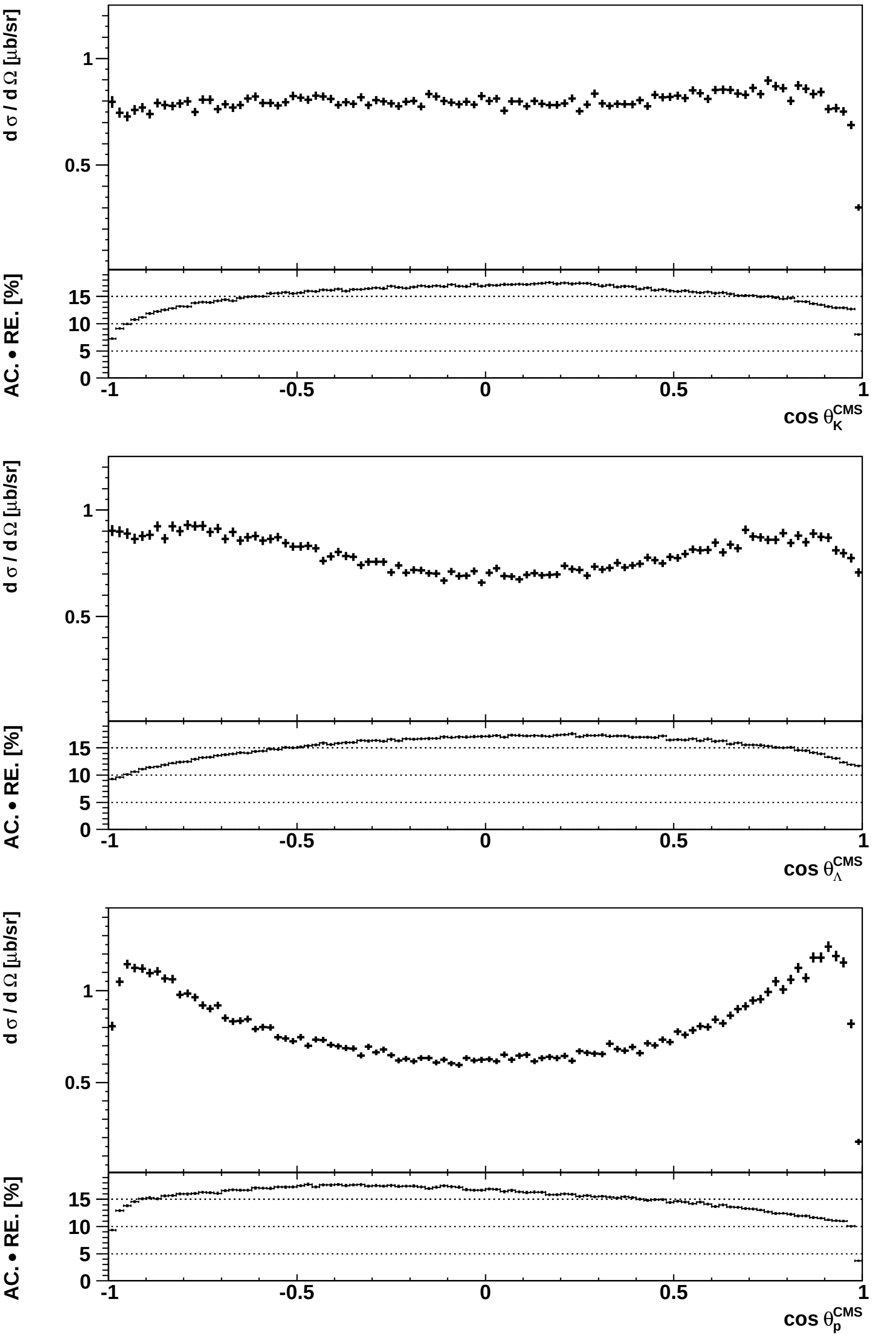

Figure 7.9.: Angular distributions in the overall CMS for each of the final state particles kaon (upper), Λ (middle) and proton (lower). The distributions are normalized to a total cross section of 10 μb. The acceptance and reconstruction efficiency correction (AC · RE) from Monte Carlo simulation is shown below each distribution.

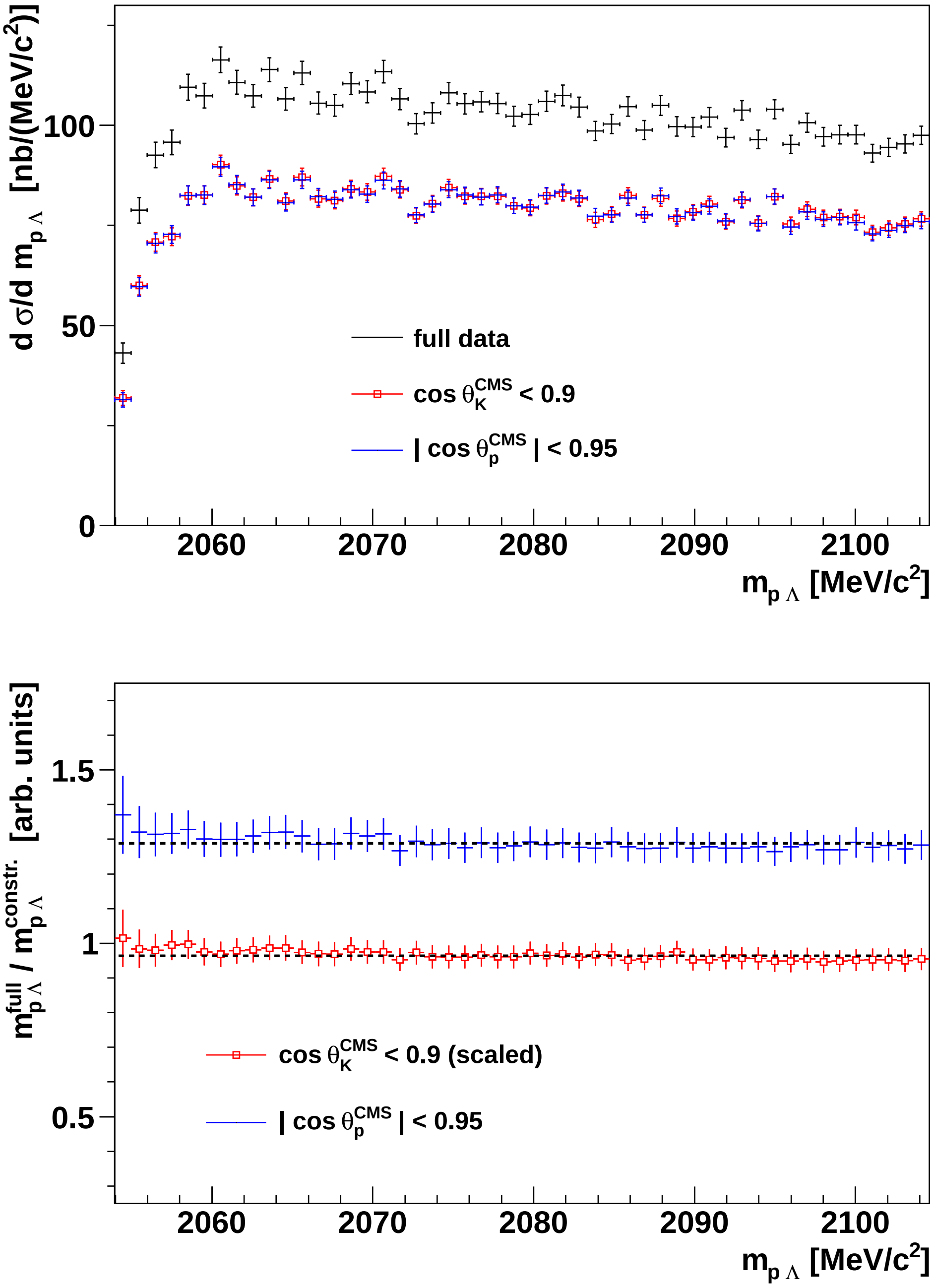

Figure 7.10.: Upper: $p\Lambda$ invariant mass distributions for the full data and the constraints $\cos(\theta_K^{\mathrm{CMS}}) < 0.9$ (red) and $|\cos(\theta_p^{\mathrm{CMS}})| < 0.95$ (blue) within the limits of the fitting procedure for the extraction of the scattering length. **Lower:** Divided invariant mass distributions for the same constraints. The red distributions is scaled by 0.75 for better visibility. The black dashed lines show a fit with a constant to both distributions.

7.3.2. Gottfried-Jackson Frame

The angular distributions in the Gottfried-Jackson frame contain information about the relative angular momenta in the two particle mass subsystems. This information is not directly accessible through the Dalitz plot or the CMS distributions. If resonances are contributing to the production of the two particles of the reference frame considered, the distribution of the corresponding Jackson angles reflects the angular momenta of the resonances. As it is pointed out in [Sib05] and [CTOF10a], an analysis of the distributions allows the relative contributions of the resonances to be extracted.

In Figure 7.11 the acceptance corrected angular distributions in the three different Gottfried-Jackson frames are shown. All distributions are normalized to a total cross section of $10\,\mu$b. The acceptance and reconstruction efficiency correction (AC · RE) from Monte Carlo simulation is depicted below each distribution. From the upper to the lower plot the distribution of the proton in the $p\Lambda$ system ($\theta_p^{p\Lambda}$), the kaon in the $K\Lambda$ system ($\theta_K^{K\Lambda}$) and the kaon in the Kp system (θ_K^{Kp}) are shown. All distributions are nearly symmetric around $\cos(\theta) = 0$. This is surprising, since the distributions of the Jackson angles are not in general symmetric, because the entrance channel in the subsystems does not consists of identical particles.

The distribution in the $p\Lambda$ Jackson frame looks similar to the proton and Λ CMS distributions. This was already observed in measurements of the $pp \to pK\Lambda$ reaction with COSY-TOF at higher beam momenta. The results, shown in [CTOF10a], are interpreted as a maximum angular momentum of $L \leq 2$ in the $p\Lambda$ system and a connection with the CMS distributions of the proton and Λ through kinematics. Because the kaon and the Λ have a large mass difference, the $p\Lambda$ Jackson frame is a good representation of the center of mass system, and thus giving similar distributions.

Since the N^* resonances decay into kaon and Λ, the angular distribution in the corresponding Jackson frame should exhibit contributions of the involved resonances. The $\cos\theta_K^{K\Lambda}$ distribution is rather flat with some deviations for forward and backward directions. This hints to a dominant S-wave in the $K\Lambda$ system, which can be explained by a dominant contribution of the resonance $S_{11}(1650\,\mathrm{MeV})$ with $L = 0$ or a weak influence of resonances to the production mechanism. However, the result of the Dalitz plot analysis [CTOF10b] from other COSY-TOF measurements show clear evidence for the first explanation.

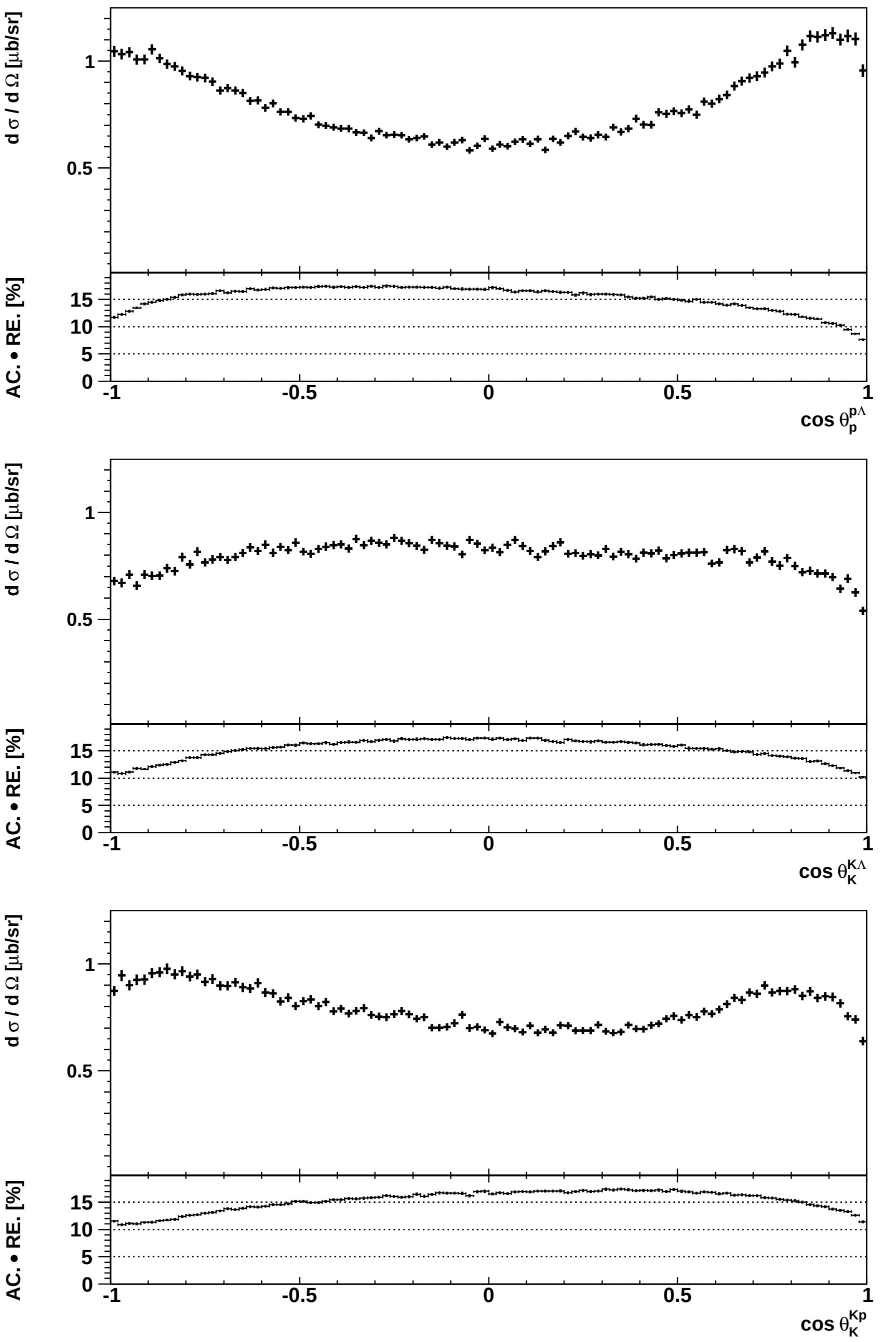

Figure 7.11.: Angular distributions in the Jackson frames for each of the two particle mass subsystems (upper: Proton in the $p\Lambda$ system, middle: Kaon in the $K\Lambda$ system, lower: Kaon in the Kp system). The distributions are normalized to a total cross section of $10\,\mu$b. The acceptance and reconstruction efficiency correction (AC $\cdot$ RE) from Monte Carlo simulation is shown below each distribution.

If the dominant production mechanism is a π exchange with intermediate N^* resonances, the distribution in the Kp Jackson frame should be isotropic, since the proton and the kaon in the final state are not coming from the same vertex in the diagrams of meson-exchange models (see Figure 2.3 in Chapter 2). Additionally, the Kp scattering in the kaon exchange process is dominated by S-wave, which produces an isotropic distribution in the Jackson frame [Sib05]. Nevertheless, the obtained distribution in the lower plot of Figure 7.11 shows some asymmetries connected with influences of higher angular momenta. This can be interpreted as an important role of kaon exchange with higher partial waves in the production mechanism or a similar kinematic correlation with the CMS distributions as for the $p\Lambda$ Jackson angle. However, the first explanation is in contradiction to the results from [CTOF10b], and thus the second explanation is more probable.

7.3.3. Helicity Frame

As mentioned above, the helicity angles are a special projection of the Dalitz plot. Thus, structures in the helicity angles are correlated with the structures in the Dalitz plot. The $p\Lambda$ final state interaction enhancement should be visibile in the $K\Lambda$ helicity frame at angles close to $\cos^{K\Lambda}_{p\Lambda} = 1$ and in the pK helicity frame at angles close to $\cos^{pK}_{K\Lambda} = -1$ [CTOF10a].

In Figure 7.11 the acceptance corrected angular distributions in the three different helicity frames are shown. All distributions are normalized to a total cross section of $10\,\mu$b. The acceptance and reconstruction efficiency correction (AC $\cdot$ RE) from Monte Carlo simulation is depicted below each distribution. From the upper to the lower plot the pK helicity angle in the $p\Lambda$ system ($\theta^{p\Lambda}_{pK}$), the $p\Lambda$ helicity angle in the $K\Lambda$ system ($\theta^{K\Lambda}_{p\Lambda}$) and the $K\Lambda$ helicity angle in the pK system ($\theta^{pK}_{K\Lambda}$) are shown.

As expected, the distributions show an enhancement near the angles $\cos^{K\Lambda}_{p\Lambda} = 1$ and $\cos^{pK}_{K\Lambda} = -1$ due to the $p\Lambda$-FSI. In addition, the remaining part of the distributions deviates from isotropy. This hints to contributions of resonances in the production of the final state particles, as it can be seen in the invariant mass distributions for helicty angle constraints in Figure 7.8. However, to draw further conclusions a partial wave analysis has to be performed e.g. in the framework of the Bonn-Gatchina group [Ani07a], which was already applied to hyperon photoproduction data (see [Sar05] and [Ani07b]).

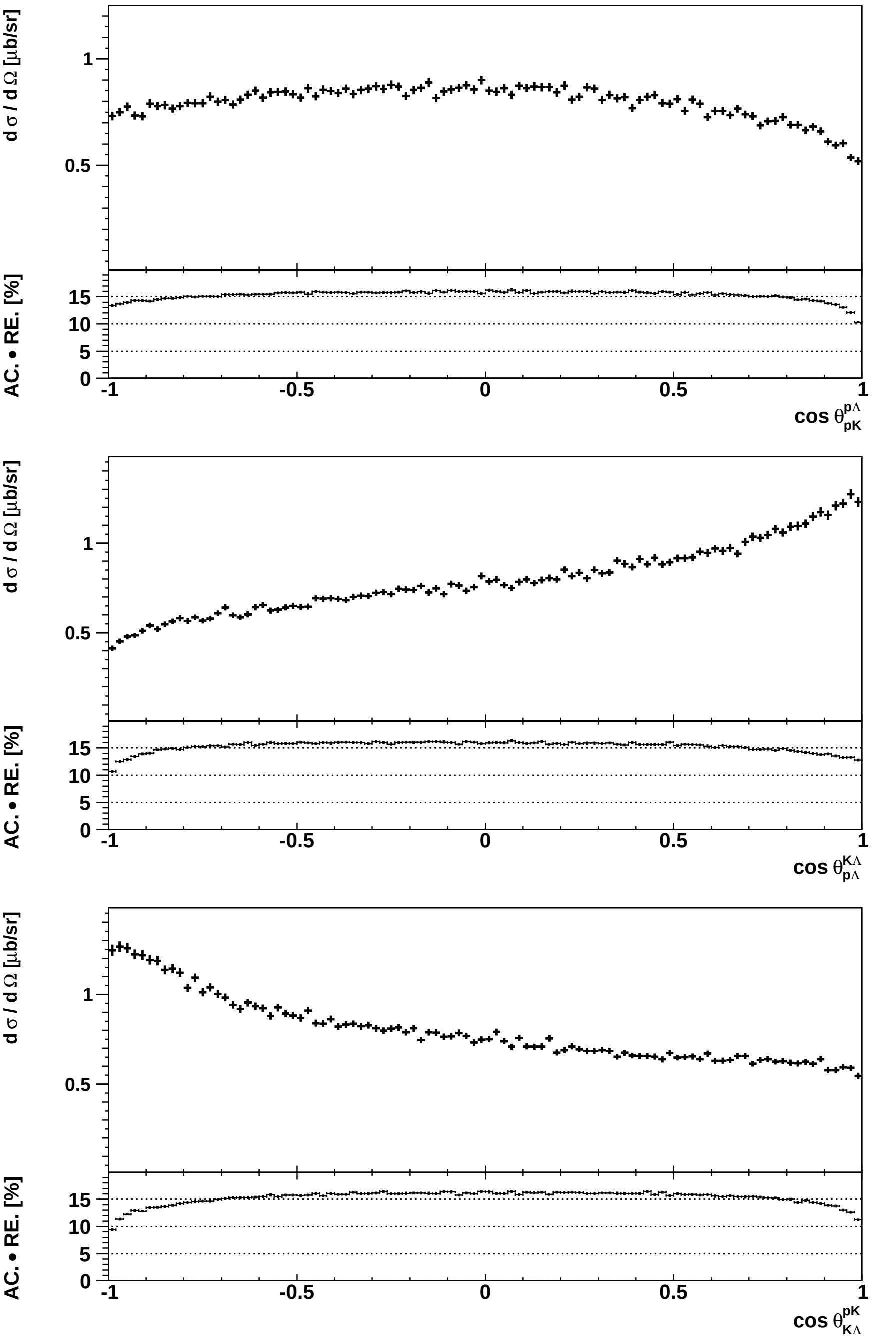

Figure 7.12.: Angular distributions in the helicity frames for each of the two particle mass subsystems (upper: Proton to kaon angle in the $p\Lambda$ system, middle: Proton to Λ angle in the $K\Lambda$ system, lower: Kaon to Λ angle in the pK system). The distributions are normalized to a total cross section of $10\,\mu$b. The acceptance and reconstruction efficiency correction (AC · RE) from Monte Carlo simulation is shown below each distribution.

7.4. Λ Polarization

The Λ polarization P_Λ is determined by the distribution of the angle of the decay proton with respect to the quantization axis $\vec{n}$ of the polarization. This is the axis perpendicular to the beam and the Λ plane (see Section 2.3). If k_n is the cosine of the angle between the decay proton in the Λ rest frame and the $\vec{n}$ axis, the polarization can be determined by the "Weighted Sum Method" according to [Kin02] and [Bes79] as

$$P_\Lambda = \frac{1}{\alpha}\frac{< k_n >}{< k_n^2 >} = \frac{1}{\alpha}\frac{\sum_{i=0}^{N} k_{n,i}}{\sum_{i=0}^{N} k_{n,i}^2} \tag{7.1}$$

for N events. $\alpha = 0.642 \pm 0.013$ [PDG2012] is the weak decay asymmetry parameter. The necessary condition for the method is a 180° symmetric acceptance around $\vec{n}$ which is given in the COSY-TOF experiment. The error is calculated via [Fri02]

$$\Delta P_\Lambda = \frac{1}{\alpha}\frac{1}{\sqrt{\sum_{i=0}^{N} k_{n,i}^2}}. \tag{7.2}$$

It is possible to calculated the Λ polarization with other methods as the Up-Down-Integral method. This will give similar results within the error bars as shown in [Roe11] and [Piz07].

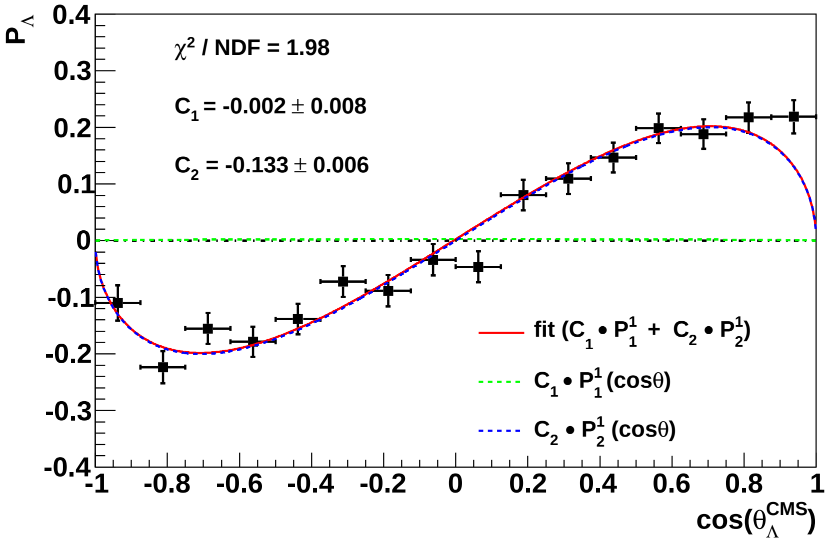

Figure 7.13.: Λ polarization P_Λ as a function of $\cos(\theta_\Lambda^{\mathrm{CMS}})$. The data are fitted with the sum of the two associated Legendre polynomials $P_1^1(\cos\theta)$ and $P_2^1(\cos\theta)$ (red line with $\chi^2/\mathrm{NDF} = 1.98$). The individual contributions of the Legendre polynomials P_1^1 and P_2^1 are shown with the dashed green and blue lines, respectively.

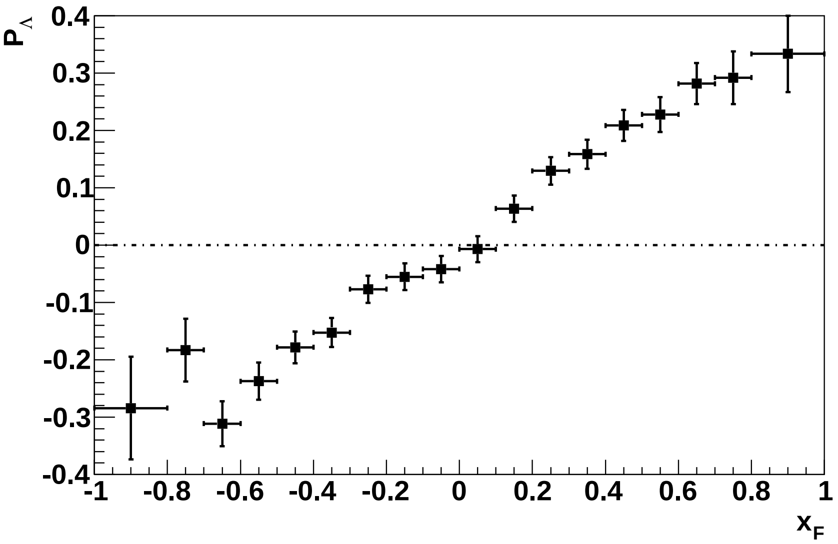

Figure 7.14.: Λ polarization P_Λ as a function of the scaling variable $x_F = \frac{p_{||}^{\mathrm{CMS}}}{p_{||\mathrm{max}}^{\mathrm{CMS}}}(\Lambda)$.

In Figure 7.13 the results for P_Λ as a function of $\cos(\theta_\Lambda^{\mathrm{CMS}})$ is shown determined by Equation 7.1. For $\cos(\theta_\Lambda^{\mathrm{CMS}}) = \pm 1$ the polarization has to be 0 because the normal vector on the beam-Λ plane is not defined there, since the beam is parallel or anti parallel to the Λ direction. Therefore, an angle with respect to the quantization axis can not be obtained clearly. The polarization changes its sign from negative values for the scattering in backward direction to positive values in forward direction with the maximum absolute value being $|P_\Lambda| \approx 0.2$.

The polarization is fitted with the sum of associated Legendre polynomials with the order $m = 1$ for vector polarization. The first two are $P_1^1(\cos\theta) = -\sin\theta$ and $P_2^1(\cos\theta) = -3\cos\theta\sin\theta$, which are zero for $\cos(\theta_\Lambda^{\mathrm{CMS}}) = \pm 1$. The complete fit result is shown by the red line in Figure 7.13, and the individual contributions of the polynomials P_1^1 and P_2^1 are shown by the green dashed and blue dashed lines, respectively. As it turned out, the behavior of the polarization can be described by P_2^1, and the contribution of P_1^1 is neglible small.

The same trend is observed in Figure 7.14, where the Λ polarization as a function of the scaling variable $x_F = p_{||}^{\mathrm{CMS}}/p_{||\mathrm{max}}^{\mathrm{CMS}}(\Lambda)$ is shown. For values $x_F < 0$ the polarization is negative and for $x_F > 0$ it is positive. The polarization is 0 for $x_F = \pm 1$ because of the same reasons as for $\cos(\theta_\Lambda^{\mathrm{CMS}}) = \pm 1$. In contrast to the distribution dependent on the scattering angle, the polarization reaches maximum values of around ± 0.3.

P_Λ as a function of the transverse momentum in the center of mass system p_T is shown in Figure 7.15. The kinematical limit at $2.7\,\mathrm{GeV}/c$ is marked by the violet dashed line in the figure. The polarization is compatible with zero in the whole momentum range.

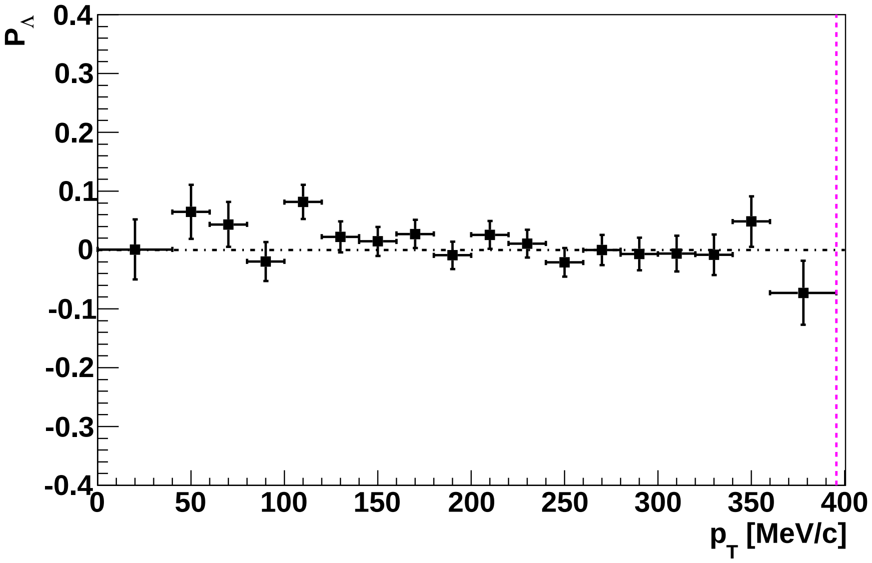

Figure 7.15.: Λ polarization P_Λ as a function of the transverse momentum $p_T(\Lambda)$. The horizontal violet line marks the kinematical limit of p_T at 2.7 GeV/c beam momentum.

This is expected for a detector with an uniform acceptance in x_F since the Λ polarization is antisymmetric in x_F [Fel96]. Therefore, the polarization is determined as a function of p_T for the two constraints $x_F > 0$ and $x_F < 0$, separately.

The results are shown in Figure 7.16 in red and blue. The same absolute values are seen for both ranges of x_F.

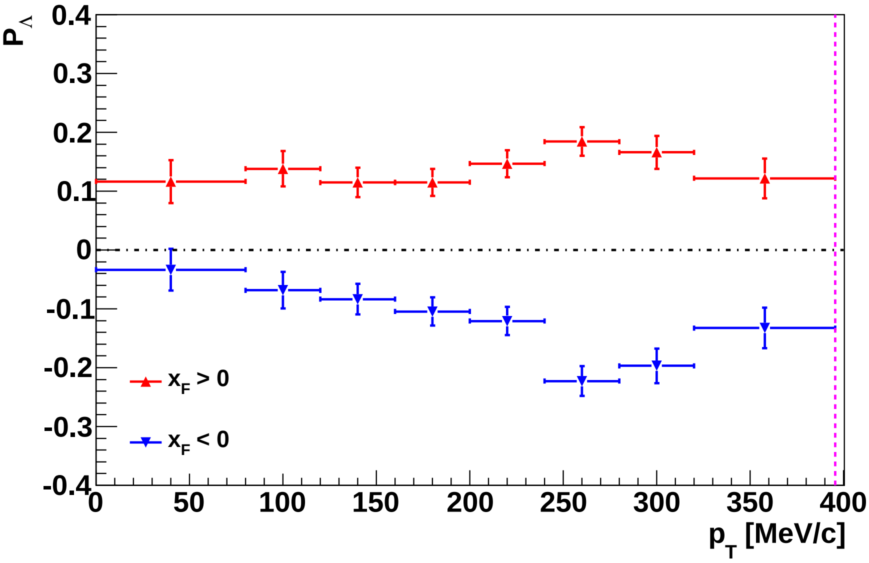

Figure 7.16.: Λ polarization P_Λ as a function of the transverse momentum $p_T(\Lambda)$ for $x_F > 0$ (red) and $x_F < 0$ (blue). The horizontal violet line marks the kinematical limit of p_T at $2.7\,\mathrm{GeV}/c$ beam momentum.

7.5. Analyzing Power

The analyzing power for each primary particle is determined in an analog way as the beam polarization, but now taken into account the left-right azimuthal asymmetry and the determined beam polarization p_B (see Chapter 5). Therefore, the analyzing power can be calculated according to

$$A_N(\cos\theta_X^{\mathrm{CMS}}) = \frac{\epsilon_{LR}(\cos(\theta_X^{\mathrm{CMS}}),\phi)}{\cos(\phi)\cdot p_B} \tag{7.3}$$

with $X = p, K, \Lambda$ being the particle of interest. ϵ_{LR} is the left-right azimuthal asymmetry given by Equation 5.11 as for the pp elastic scattering. The results for the analyzing power as a function of $\cos(\theta_X^{\mathrm{CMS}})$ are shown next. For $\cos(\theta_X^{\mathrm{CMS}}) = \pm 1$ the analyzing power has to be zero since the ϕ angle is not defined there, thus the asymmetry ϵ_{LR} is zero. The analyzing powers are fitted with the sum of the associated Legendre polynomials $P_1^1(\cos\theta) = -\sin\theta$ and $P_2^1(\cos\theta) = -3\cos\theta\sin\theta$. These are the polynomials with the order $m = 1$ for vector analyzing power and the lowest angular momentum. The fit parameters α and β are the magnitudes of the individual P_l^m contributions. In case of the kaon analyzing power the parameter α is used for the extraction of the $p\Lambda$ spin triplet scattering length (see Section 8.4).

A comparison of these results with COSY-TOF measurements at different beam momenta is given in Section 9.2.

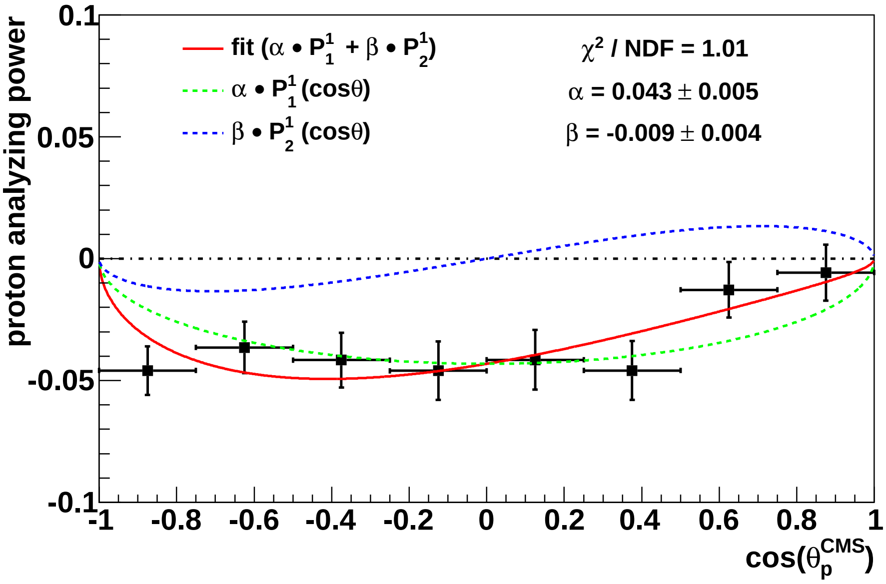

Figure 7.17.: Proton analyzing power as a function of $\cos(\theta_p^{\text{CMS}})$. The red line shows the fit with a sum of the two associated Legendre polynomials P_1^1 and P_2^1. The individual contributions of the polynomials are shown by the green dashed and blue dashed lines, respectively.

7.5.1. Proton Analyzing Power

In Figure 7.17 the proton analyzing power as a function of $\cos(\theta_p^{\text{CMS}})$ is shown for the full event sample. For the region $-1 < \cos(\theta_p^{\text{CMS}}) < 0.5$ the analyzing power is almost constant with a value of about -0.05. For the forward scattered protons the analyzing power reaches zero. The fit with the sum of the Legendre polynomials (red line) gives a very good description of the data with a reduced χ^2 of 1.01. The inclusion of Legendre polynomials with higher l, such as P_3^1 or P_4^1 does not improve the reduced χ^2. The individual contributions of the corresponding polynomials P_1^1 and P_2^1 are shown by the green dashed and blue dashed lines.

7.5.2. Λ Analyzing Power

In Figure 7.18 the Λ analyzing power as a function of $\cos(\theta_\Lambda^{\text{CMS}})$ is shown for the full event sample. In the whole range the analyzing power is negative. From negative cosine of scattering angle to positive values the analyzing power decreases to a minimum of ≈ -0.1. The fit with the sum of the Legendre polynomials (red line) describes the data with a reduced χ^2 of 2.69. The individual contributions of the corresponding polynomials P_1^1 and P_2^1 are shown by the green dashed and blue dashed line. Including

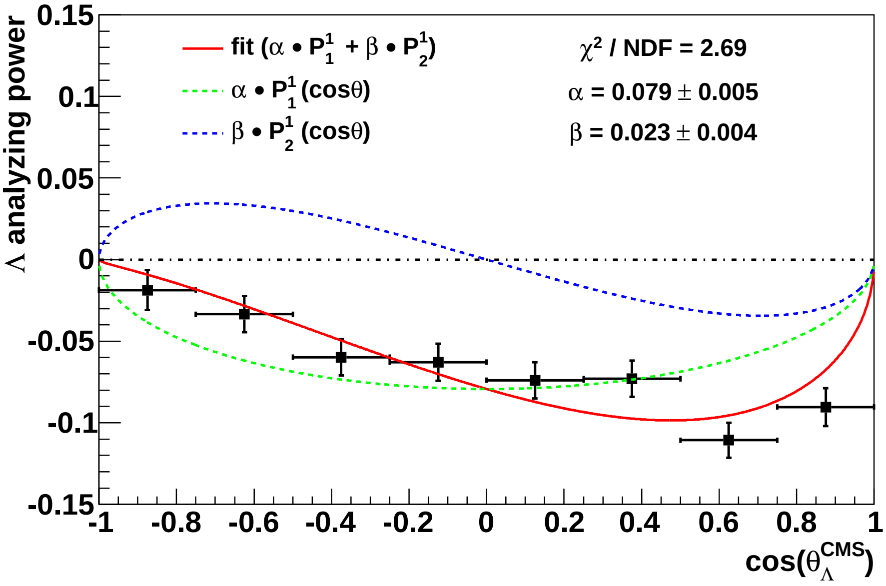

Figure 7.18.: Λ analyzing power as a function of $\cos(\theta_\Lambda^{\mathrm{CMS}})$. The red line shows the fit with a sum of the two associated Legendre polynomials P_1^1 and P_2^1. The individual contributions of the polynomials are shown by the green dashed and blue dashed lines, respectively.

associated Legendre polynomials with higher angular momentum in the fit improves the χ^2 value slightly. The result of the fit including the associated Legendre polynomial P_3^1 is shown in Section 9.2.2 where the comparison with the COSY-TOF measurement at 2.95 GeV/c is shown. The Λ analyzing power as a function of x_F and p_T is shown in Appendix A.

7.5.3. Kaon Analyzing Power

In Figure 7.19 the kaon analyzing power as a function of $\cos(\theta_K^{\mathrm{CMS}})$ for the full event sample is shown. It is positive in the whole scattering range with a maximum value of about 0.2. The fit with the sum of the Legendre polynomials (red line) describes the data with a reduced χ^2 of 2.14. Including associated Legendre polynomials with higher l in the fit does not improve the χ^2 value. The individual contributions of the corresponding polynomials P_1^1 and P_2^1 are shown by the green dashed and blue dashed line. From the measurements at 2.95 GeV/c beam momentum [Roe11, Jow14] the values α and β has been determined by the same fitting procedure. The results from these measurements and the data shown in Figure 7.19 are summarized in Table 7.1. The α value coincides for the different measurements, while the β value deviates significantly between the measurements at 2.7 GeV/c and 2.95 GeV/c. This can be explained by a

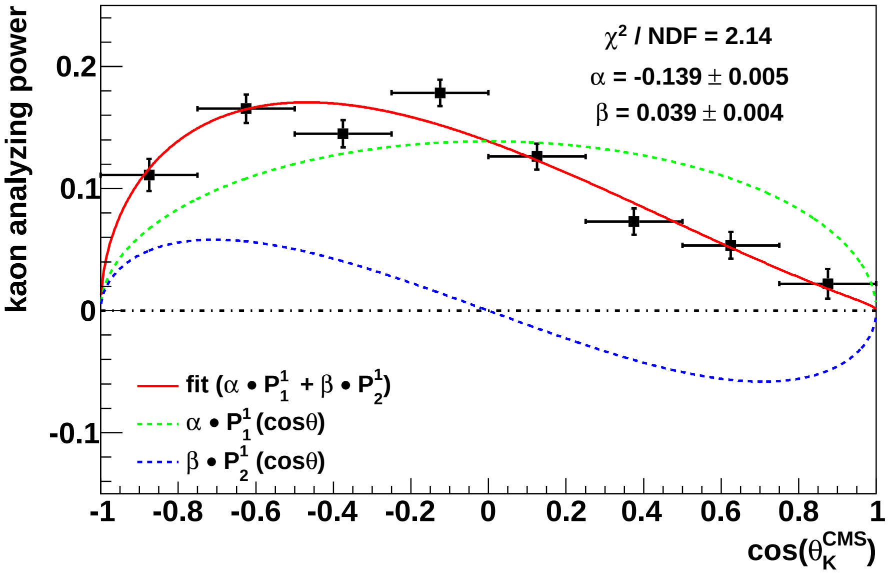

Figure 7.19.: Kaon analyzing power as a function of $\cos(\theta_K^{\mathrm{CMS}})$ for the full event sample. The red line shows the fit with a sum of the two associated Legendre polynomials P_1^1 and P_2^1. The individual contributions of the polynomials are shown by the green dashed and blue dashed lines, respectively.

reduced amount of kaons in D-wave for 2.7 GeV/c. Therefore, the magnitude of the S+D wave interference term β is decreased, but the S+P wave interference term α is not influenced.

To extract the $p\Lambda$ spin triplet scattering length the dependence of the analyzing power on the $m_{p\Lambda}$ invariant mass has to be determined, especially in a range of $m_{p\Lambda} \leq m_\Lambda + m_p + 40\,\mathrm{MeV}/c^2$. This constraint enforces the internal orbital momentum of the $p\Lambda$ system to be $l = 0$, which is a necessary condition for applying the extraction procedure of the scattering length (see Section 2.4 and Chapter 8). For this analysis the $p\Lambda$ invariant mass is binned in 5 MeV/c^2 steps. For the first bin the obtained kaon

Beam momentum	α	β
2.7 GeV/c	-0.139 ± 0.005	0.039 ± 0.004
2.95 GeV/c [Roe11]	-0.145 ± 0.013	0.065 ± 0.010
2.95 GeV/c [Jow14] (preliminary)	-0.137 ± 0.006	0.059 ± 0.004

Table 7.1.: Values for α and β from the fit of the kaon analyzing power for the measurements at 2.95 GeV/c ([Roe11] and [Jow14]) and 2.7 GeV/c.

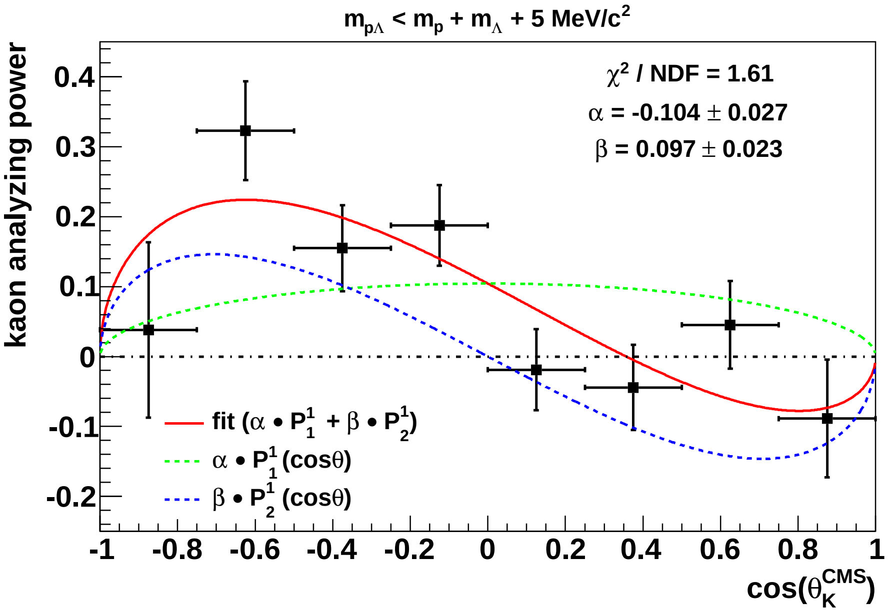

Figure 7.20.: Kaon analyzing power as a function of $\cos(\theta_K^{\mathrm{CMS}})$ for the events with the constraint $m_{p\Lambda} < m_p + m_\Lambda + 5\,\mathrm{MeV}/c^2$. The red line shows the fit with a sum of the two associated Legendre polynomials P_1^1 and P_2^1. The individual contributions of the polynomials are shown by the green dashed and blue dashed lines, respectively.

analyzing power is shown in Figure 7.20 together with the fit of the associated Legendre polynomials. The obtained values for α and β deviate from zero by more than $4\,\sigma$. This is consistent with the expectation from [CTOF07], but opposite to the results obtained from the data at $2.95\,\mathrm{GeV}/c$ [CTOF13b], where a value of α compatible with zero has been obtained[2] for the invariant mass range $m_{p\Lambda} \leq m_\Lambda + m_p + 40\,\mathrm{MeV}/c^2$. Thus, a change of α at low $p\Lambda$ invariant mass with the beam momentum is observed. This could be connected to energy dependent wave amplitudes. Unfortunately, no theoretical model is available at the moment which describes this behavior.

The dependence of α and β on the $p\Lambda$ invariant mass is shown in Figure 7.21. For better visualization $-\alpha$ is shown in red. β is shown in blue. As expected, β vanishes for higher invariant masses since the kaon momentum becomes too low for D-wave contributions, and thus the S+D interference term becomes zero. This behavior is similar to the measurement at $2.95\,\mathrm{GeV}/c$ beam momentum. The α value is roughly constant at -0.14 for almost the whole invariant mass range. For high invariant masses it drops down to zero because the kaon momentum is even too low for P-wave contributions. The

---

[2] The preliminary results from [Jow14] gives $\alpha \approx -0.04 \pm 0.015$ for the first invariant mass bin. Thus, α is $2.7\,\sigma$ away from zero, but still $\sim 2\,\sigma$ lower in absolute value than the result from the data at $2.7\,\mathrm{GeV}/c$.

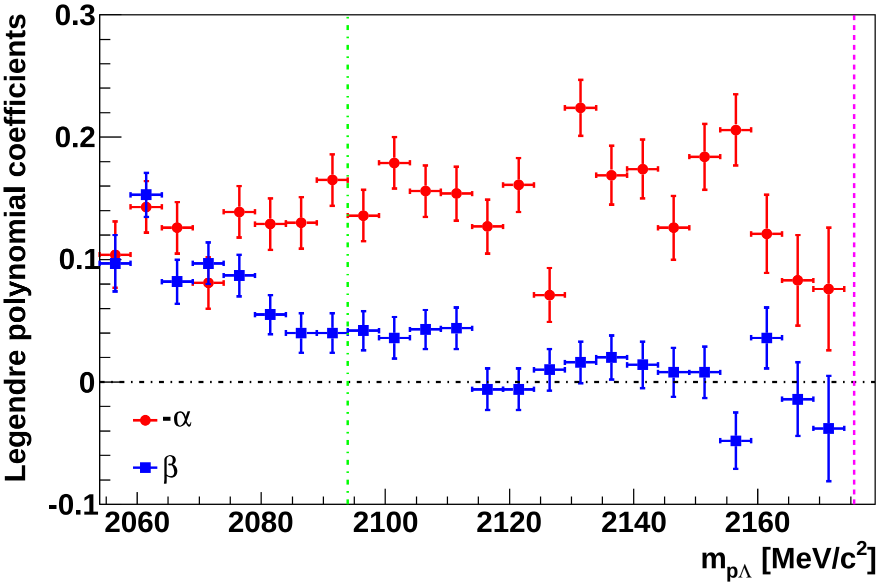

Figure 7.21.: Contributions of the associated Legendre polynomials P_1^1 (α, red) and P_2^1 (β, blue) to the kaon analyzing power as a function of the $p\Lambda$ invariant mass. $-\alpha$ is shown for better visualization. The kinematic limit at 2.7 GeV/c beam momentum is indicated by the dashed violet line. The dash dotted green line indicates the fit range for the determination of the $p\Lambda$ spin triplet scattering length.

dashed violet line indicates the kinematical limit for a beam momentum of 2.7 GeV/c. The important region for the determination of the $p\Lambda$ spin triplet scattering length is $m_{p\Lambda} \leq m_\Lambda + m_p + 40\,\mathrm{MeV}/c^2$. This limit is marked by the dash dotted green line in Figure 7.21. In this range α is clearly nonzero which allows the spin triplet scattering length to be extracted. Furthermore, a dominant spin singlet scattering can be excluded since spin singlet scattering forbids P-wave kaons, hence $\alpha \neq 0$.

The paradigm of physics - with its interplay of data, theory and prediction - is the most powerful in science.

(Geoffrey West)

8. Determination of the $p\Lambda$ Spin Triplet Scattering Length

In this chapter the method for the determination of the $p\Lambda$ spin triplet and effective scattering length is described first. Afterwards, the results for the effective scattering length for the full event sample and the sub samples for different ranges of the helicity angle $\cos^{p\Lambda}_{pK}$ are shown for further checks of influences from N^* resonances. Finally, the spin triplet scattering length is determined and systematic errors are discussed.

8.1. Description of the Fit Method

The fit method follows in general the proposed way in [Gas04, Roe11, CTOF13b]. Nevertheless, it is modified in some details to simplify and stabilize the fit procedure and convergence. As described in Section 2.4.3.2 and in [Gas04], it is possible to extract the $p\Lambda$ scattering length from the $p\Lambda$ FSI enhancement in the invariant mass distribution with a known theoretical precision of 0.3 fm. For that purpose the enhancement is parametrized by

$$\frac{\mathrm{d}\sigma}{\mathrm{d}m_{p\Lambda}} = C_{PS} \cdot PS(m_{p\Lambda}) \cdot |A_{\mathrm{FSI}}(m_{p\Lambda})|^2 = C_{PS} \cdot PS(m_{p\Lambda}) \cdot \exp\left[C_0 + \frac{C_1}{m^2_{p\Lambda} - C_2}\right]. \quad (8.1)$$

It is a modified version of the similar formula in [Gas04] (Equation A.1) or in [Roe11] (Equation 7.7), where C_1 and C_2 enter quadratically in the final state parametrization. The modification leads to one global minimum of the fit in comparison to the four before[1]. $PS(m_{p\Lambda})$ corresponds to the phase space distribution, and C_{PS} is the strength of the phase space.

The scattering length a is given by

$$a(C_1, C_2) = -\frac{1}{2} C_1 \sqrt{\left(\frac{m_0^2}{m_p m_\Lambda}\right) \cdot \frac{(m^2_{\mathrm{max}} - m_0^2)}{(m^2_{\mathrm{max}} - C_2) \cdot (m_0^2 - C_2)^3}} \hbar c. \quad (8.2)$$

m_p and m_Λ are the corresponding particle masses. $m_0 = m_p + m_\Lambda$ is the minimum $m_{p\Lambda}$ mass and $m_{\mathrm{max}} = m_0 + 40\,\mathrm{MeV}/c^2$ the limit of the dispersion integral from Equation 2.21 to achieve a systematic error of 0.3 fm from theory.

---

[1] It has been checked, that the fit with the former quadratic parametrization gives the same result for the scattering length as the modified one.

The implementation of the finite detector resolution $\sigma_m(m_{p\Lambda})$ for each invariant mass is done by folding Equation 8.1 with a corresponding Gaussian function. Therefore, the following function is fitted to the data

$$\frac{\mathrm{d}\sigma}{\mathrm{d}m_{p\Lambda}} = \int_{m_{p\Lambda}-5\sigma_m}^{m_{p\Lambda}+5\sigma_m} \mathrm{d}m'_{p\Lambda} \frac{C_{PS} \cdot PS(m'_{p\Lambda}) \cdot \left|A_{\mathrm{FSI}}(m'_{p\Lambda})\right|^2}{\sqrt{2\pi}\sigma_m} \cdot \exp\left[-\frac{(m_{p\Lambda} - m'_{p\Lambda})^2}{2\sigma_m^2}\right]. \tag{8.3}$$

It has four parameters: One for the strength of the phase space (C_{PS}) and three for the final state parametrization (C_0, C_1 and C_2). Since parameter C_0 can be absorbed by the phase space strength and vice versa, pure phase space was first fitted to the upper range of the invariant mass distribution[2] to determine a value for C_{PS}. This value has been fixed in the subsequent fit of the invariant mass distribution with the function from Equation 8.3. As it is shown in Section 2.4, a change in C_0 does not influence the result for the scattering length a.[3]

The error for the scattering length can not be calculated simply by Gaussian error propagation, since the parameters $C_{1,2}$ and C_0 are highly correlated and a does not depend on C_0. Therefore, the likelihood for the scattering length from the result of the fit has been taken. It can be approximated according to [Gas04, Roe11] by

$$L(\mathrm{data}, C_i) \approx \exp\left[-\frac{1}{2}\chi^2(C_0, C_1, C_2)\right] \tag{8.4}$$

with the χ^2 value for a given set of parameters C_i.

Thus, the likelihood probability for a value of the scattering length a is [Roe11]

$$L(a) = N \int\int\int \mathrm{d}C_0 \mathrm{d}C_1 \mathrm{d}C_2 \exp\left[-\frac{1}{2}\chi^2(C_0, C_1, C_2)\right] \delta(a - a'(C_1, C_2)) \tag{8.5}$$

The normalization constant N should be chosen such that $\int L(a)\mathrm{d}a = 1$, but an incorrect normalization does not influence the result for a. Thus, N was set to 1 in the calculation.

One integration of Equation 8.5 is calculated straight forward by a variable substitution from C_1 to a', which is followed by the integration over a' to eliminate the Delta function. The substitution gives

$$\mathrm{d}C_1 = \mathrm{d}a' \frac{-2}{\sqrt{\left(\frac{m_0^2}{m_p m_\Lambda}\right) \cdot \frac{(m_{\max}^2 - m_0^2)}{(m_{\max}^2 - C_2)\cdot(m_0^2 - C_2)^3}}\hbar c}. \tag{8.6}$$

After the substitution and the integration over a', the likelihood probability is

$$L(a) = N \int\int \mathrm{d}C_0 \mathrm{d}C_2 \frac{-2}{\sqrt{\ldots}\hbar c} \exp\left[-\frac{1}{2}\chi^2(C_0, C'(a, C_2), C_2)\right] \tag{8.7}$$

---

[2] The range of this fit is indicated by the green shaded areas in the figures later.

[3] This has been confirmed by fitting the data with different values of C_{PS}. There was no difference in the resulting scattering length a and the corresponding error.

with the term from Equation 8.6 $\sqrt{\ldots}$ and

$$C'(a, C_2) = \frac{-2a}{\sqrt{\ldots}\hbar c}. \tag{8.8}$$

The two dimensional integral of Equation 8.7 is calculated numerically with Monte Carlo integration methods from the GNU Scientific Library GSL [GSL]. The integration is done over a $\pm 3\sigma$ range of C_0 and C_2.

As described in [Roe11], the term $\chi^2(C_0, C'(a, C_2), C_2) = \chi^2(\vec{C})$ is approximated by a Taylor expansion up to second order around the results of the fit of the function from Equation 8.3. Assuming these are given by $\vec{f} = (f_0, f_1, f_2)$, the expansion is

$$\chi^2(\vec{C}) \approx \chi^2(\vec{f}) + \frac{1}{2}(\vec{C} - \vec{f})\, H_C(\vec{f})\, (\vec{C} - \vec{f})^T \tag{8.9}$$

with the Hessian matrix H_C. The first order term vanishes since

$$\nabla_C \cdot \chi^2(\vec{f}) = 0, \tag{8.10}$$

which is the condition for the fit minimum. The Hessian matrix is obtained from the software MINUIT [MINUIT], which is used for the fitting procedure. It is the inverse of the error matrix, and a parabolic χ^2 function around the fit minimum is assumed.

The resulting distribution of the likelihood probability for different values of a follows a Gaussian distribution. By fitting a Gaussian, its mean and sigma value give the result for a and the error Δa, including effects from the correlation of the fit parameters.

8.2. $p\Lambda$ Effective Scattering Length for Full Data Sample

In Figure 8.1 (upper plot) the $p\Lambda$ invariant mass distribution for the full event sample is shown. The final state parametrization function (red) is fitted in a range up to $m_{p\Lambda} = m_0 + 40\,\mathrm{MeV}/c^2$ with a reduced χ^2 of 1.69, which is indicated by the vertical red dashed line. Beyond this boarder the function is shown by the red dashed line. It describes quite well the rest of the distribution, besides the enhancement at the $N\Sigma$ threshold around $2130\,\mathrm{MeV}/c^2$. Additionally, the phase space expectation is fitted in the green shaded area. The invariant mass distribution as well as the FSI function divided through the fitted phase space distributions is shown in the lower plot of Figure 8.1. This is the visualization of the spin averaged final state interaction amplitude $\left|\tilde{A}_{\mathrm{FSI}}(m_{p\Lambda})\right|^2$. An exponential function describes the data in the relevant region nearly perfect. Therefore, the parametrization of the final state interaction amplitude with Equation 8.1 is reasonable.

The obtained parameters of the final state interaction fit are shown in the upper plot of Figure 8.1 in the caption. As already mentioned, the likelihood from these parameters is calculated in order to determine the value of the scattering length and its error, because the parameters are highly correlated. The obtained likelihood probability distribution as a function of the scattering length is shown in Figure 8.2.

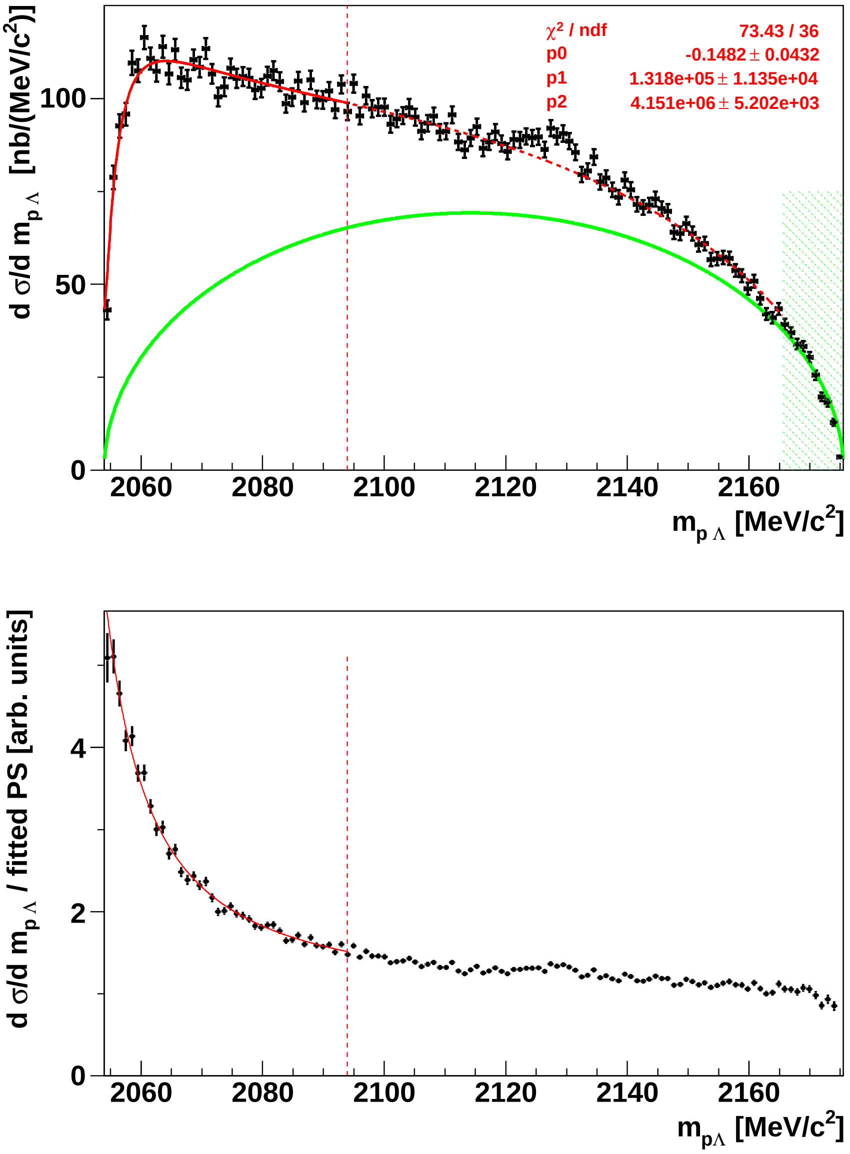

Figure 8.1.: Upper: $m_{p\Lambda}$ invariant mass distribution for the full event sample normalized to a total cross section of 10 μb fitted with phase space (green) and the final state parametrization function described by Equation 8.3 (red). The red dashed line marks the upper limit of the FSI fit, and the green shaded area marks the range of the phase space fit. The behavior of the FSI function extrapolated beyond the fit range is shown by the red dashed line. The parameters of the fit are given in the caption. **Lower:** $m_{p\Lambda}$ invariant mass distribution from the upper plot divided by the phase space function. The red line shows the final state fit of the upper plot divided by the phase space function. The vertical red dashed line marks the upper limit of the FSI fit.

The distribution is fitted with a Gaussian, which gives an effective scattering length of $\tilde{a} = (-1.233 \pm 0.014_{\text{stat.}} \pm 0.3_{\text{theo.}})\,\text{fm}$.

The small deviations of the likelihood distribution from a Gaussian might stem from the complicated involved numerical calculations from the scientific library GSL [GSL]. However, the theoretical uncertainty dominates the error of the scattering length. Further systematic errors are discussed in Section 8.5.

The weights of the spin singlet and spin triplet contributions to the effective scattering length are not known, when using the dispersion integral approach (see Section 2.4.3). Therefore, the determined effective scattering length can not be directly compared with the spin averaged scattering lengths from [C1198b] and [HIR10], since in these references the spin singlet and spin triplet contributions to the scattering length are assumed to be given by the spin statistical weights 1/4 and 3/4, respectively (see inverse Jost function approach in Section 2.4.3.1). Nevertheless, in [Gas04] the scattering length is extracted with the dispersion integral approach from unpolarized data from the inclusive reaction $pp \rightarrow K^+X$ measured at the SPES4 facility in Saclay [Sie94]. The obtained value is $\tilde{a} = (-1.5 \pm 0.15_{\text{stat.}} \pm 0.3_{\text{theo.}})\,\text{fm}$. This is compatible with the value determined in this thesis.

The result for the effective scattering length from the COSY-TOF measurement at $2.95\,\text{GeV}/c$ beam momentum is $\tilde{a} = (-1.25 \pm 0.08_{\text{stat.}} \pm 0.3_{\text{theo.}})\,\text{fm}$ [CTOF13b], which is consistent with the value obtained in this thesis. However, a systematic influence of N^* resonances on the extracted value was seen in [CTOF13b] by a study of the scattering length value for separated $m_{K\Lambda}$ regions of the Dalitz plot. The values for the separated regions are $\tilde{a}(m^2_{K\Lambda} < 3.176\,\text{GeV}^2/c^4) = (-0.86 \pm 0.06_{\text{stat.}} \pm 0.3_{\text{theo.}})\,\text{fm}$ and $\tilde{a}(m^2_{K\Lambda} > 3.176\,\text{GeV}^2/c^4) = (-2.06 \pm 0.16_{\text{stat.}} \pm 0.3_{\text{theo.}})\,\text{fm}$. Thus, the deviation of the effective scattering length due to N^* resonances is in the order of $1.2\,\text{fm}$. To check for such a deviation in the data from this thesis, a similar analysis is done. For that purpose, the event sample is split into four different ranges of the helicity angle $\cos\theta^{p\Lambda}_{pK}$ (for an explanation of the angle see Section 7.3). This corresponds to a separation of the Dalitz plot into four parts with the same phase space volume [Kil13]. For each part the $p\Lambda$ effective scattering length is determined. This is shown in the next section.

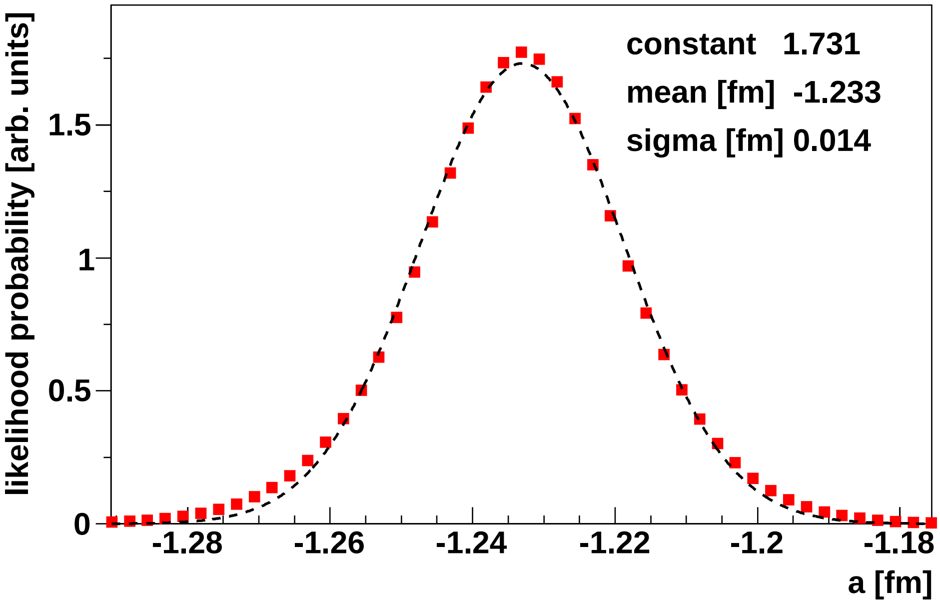

Figure 8.2.: The likelihood probability distribution for the full event sample for the determination of the $p\Lambda$ effective scattering length $\tilde{a}$ and its error. The mean value of the fitted Gaussian corresponds to the effective scattering length $\tilde{a}$, while the sigma value of the Gaussian corresponds to the scattering length error $\Delta\tilde{a}$.

8.3. $p\Lambda$ Effective Scattering Length for Different $\cos\theta_{pK}^{p\Lambda}$ Ranges

In Figure 8.3 the $p\Lambda$ invariant mass distributions are shown for different ranges of the helicity angle: $\cos\theta_{pK}^{p\Lambda} > 0.5$ (upper left), $0 < \cos\theta_{pK}^{p\Lambda} < 0.5$ (upper right), $-0.5 < \cos\theta_{pK}^{p\Lambda} < 0$ (lower left) and $\cos\theta_{pK}^{p\Lambda} < -0.5$ (lower right). Each of the distributions are fitted with phase space (green) and the FSI function (red) in the limit of the FSI fit $m_{p\Lambda} = m_0 + 40\,\mathrm{MeV}/c^2$, indicated by the vertical red dashed lines. The parameters of the final state interaction fits are shown in the captions, respectively. In Appendix C the invariant mass distributions divided by the phase space fits are shown, similar to the lower plot of Figure 8.1.

From the fitted FSI function, the likelihood probability is calculated for each invariant mass distribution. The results are shown in Figure 8.4. The obtained values for the effective scattering length $\tilde{a}$ and the error $\Delta\tilde{a}$ are summarized in Table 8.1.

Only the value for the range $\cos\theta_{pK}^{p\Lambda} < -0.5$ is in agreement with the value for the full data within $1\,\sigma$. Nevertheless, the maximum deviation of the effective scattering length for the different helicity angle ranges is in the order of 0.15 fm. Therefore, the influence

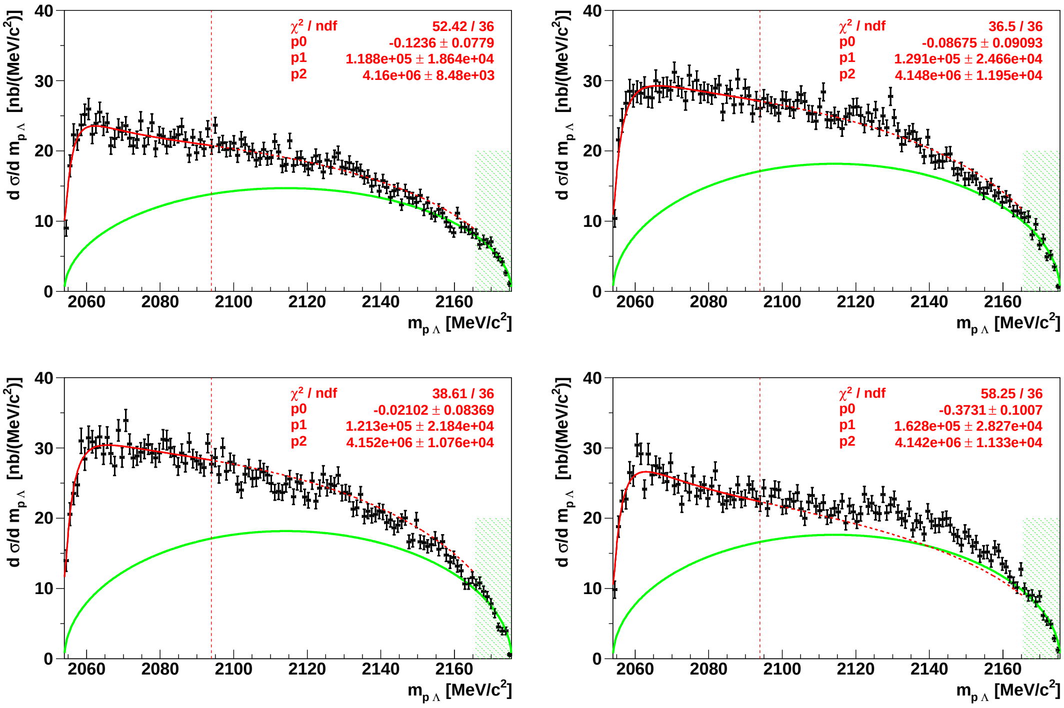

Figure 8.3.: $m_{p\Lambda}$ invariant mass distribution for different ranges of the helicity angle $\cos\theta_{pK}^{p\Lambda}$ fitted with phase space (green) and the final state parametrization function described by Equation 8.3 (red). The ranges for the plots are $\cos\theta_{pK}^{p\Lambda} > 0.5$ (upper left), $0 < \cos\theta_{pK}^{p\Lambda} < 0.5$ (upper right), $-0.5 < \cos\theta_{pK}^{p\Lambda} < 0$ (lower left) and $\cos\theta_{pK}^{p\Lambda} < -0.5$ (lower right). In each distribution the vertical red dashed line marks the upper limit of the FSI fit, and the green shaded area marks the range of the phase space fit. The behavior of the FSI function extrapolated beyond the fit range is shown by the red dashed line. The parameters of the fit are given in the caption.

of N^* resonances on the $p\Lambda$ final state interaction seems to be very weak compared to the measurement at 2.95 GeV/c beam momentum, where the deviations are in the order of 1.2 fm [CTOF13b].

The deviations in the ranges $\cos\theta_{pK}^{p\Lambda} > 0.5$ and $0 < \cos\theta_{pK}^{p\Lambda} < 0.5$ can be explained by an significant influence of the N^*-1720 MeV resonance, because its peak value is in these regions if a Breit-Wigner distribution is assumed (see additionally Figures 7.3 and 7.5).

However, combining the results of the upper and lower plots in Figure 8.3, the effective scattering lengths are $\tilde{a}(\cos\theta_{pK}^{p\Lambda} > 0) = (-1.273 \pm 0.023)\,\text{fm}$ and $\tilde{a}(\cos\theta_{pK}^{p\Lambda} < 0) = (-1.215 \pm 0.019)\,\text{fm}$. The first value is now nearly within $1\,\sigma$ to the result for the full data, reflecting again the very weak influence of the resonance compared to the

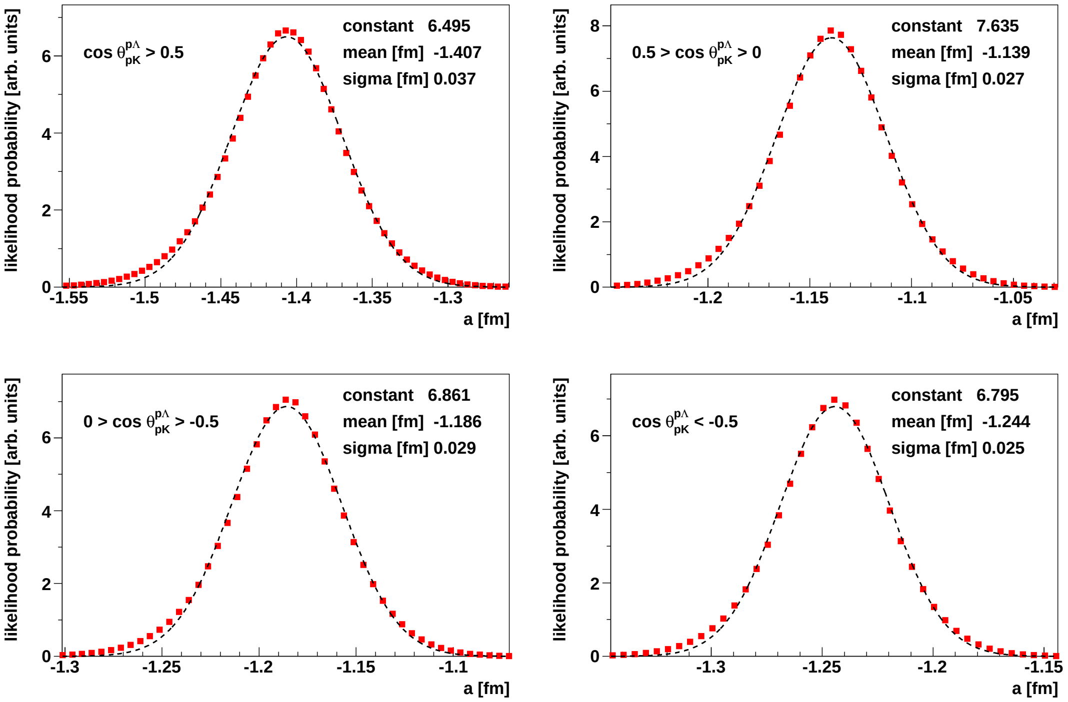

Figure 8.4.: Likelihood probability distribution for the FSI fit of the $m_{p\Lambda}$ invariant mass distributions in Figure 8.3. The $p\Lambda$ effective scattering length $\tilde{a}$ and its error $\Delta\tilde{a}$ correspond to the mean and sigma value of the Gaussian fit to the likelihood distribution.

measurement at 2.95 GeV/c beam momentum.

From this results the systematic error from the influence of N^* resonances is assumed to be maximal 0.1 fm.

$\cos\theta_{pK}^{p\Lambda}$ range	$\tilde{a}$ [fm]	$\Delta\tilde{a}$ [fm]
$\cos\theta_{pK}^{p\Lambda} > 0.5$	-1.407	0.037
$0 < \cos\theta_{pK}^{p\Lambda} < 0.5$	-1.139	0.027
$-0.5 < \cos\theta_{pK}^{p\Lambda} < 0$	-1.186	0.029
$\cos\theta_{pK}^{p\Lambda} < -0.5$	-1.244	0.025
full range	-1.233	0.014

Table 8.1.: $p\Lambda$ effective scattering length and its error for different ranges of the helicity angle $\cos\theta_{pK}^{p\Lambda}$ from the Gaussian fit of the likelihood distributions in Figure 8.4.

8.4. Extraction of the $p\Lambda$ Spin Triplet Scattering Length

As described in Section 2.4.3.2 by Equation 2.25, the contribution of the associated Legendre polynomial P_1^1 to the kaon analyzing power $\alpha(m_{p\Lambda})$ has to be multiplied to the spin averaged final state interaction amplitude $\left|\tilde{A}_{\text{FSI}}(m_{p\Lambda})\right|^2$ to determine the spin triplet scattering length from the spin triplet final state interaction amplitude $|A_{\text{FSI,t}}(m_{p\Lambda})|^2$. Since the $m_{p\Lambda}$ invariant mass distribution is proportional to phase space times the final state amplitude, as described by Equation 8.1, $\alpha(m_{p\Lambda})$ is multiplied bin wise to the invariant mass distribution. This gives a distribution proportional to phase space times $|A_{\text{FSI,t}}(m_{p\Lambda})|^2$, which is shown in Figure 8.5. This modified invariant mass distribution is again fitted with phase space (green) and the final state parametrization of Equation 8.1 (red). From the FSI fit, the spin triplet scattering length can be obtained in the same way as the effective one.

Due to the large error of the fit parameter C_2, the root term of the variable substitution for the likelihood probability calculation (Equation 8.6) is not defined for the full error range of C_2, even in a range of $\pm 1\sigma$. Thus, the likelihood has been set to zero, if the parameter reaches this undefined range in the calculation of the probability via Equation 8.7. Unfortunately, this induces a large deviation of the likelihood probability distribution, shown in Figure 8.6 from a Gaussian shape. Nevertheless, the distribution is fitted with a Gaussian for the right side and a mean value is determined. The error of the scattering length is calculated by the distance of the crossing points of the half maximum line (blue dashed) with the probability distribution and the mean value. These values are 0.58 fm for the left point and 0.37 fm for the right point. The systematic uncertainty from the used method is described in the next section. The values for σ are calculated with the usual relation between full width half maximum and sigma of a Gaussian. Thus, an asymmetric error for the spin triplet scattering length is obtained, reflecting the constraint of the undefined C_2 range. The result is $a_{\text{t}} = (-1.31^{+0.32}_{-0.49}{}_{\text{stat.}} \pm 0.3_{\text{theo.}})\,\text{fm}$.

This result is compatible with the recent theoretical prediction of NLO ChEFT calculations $a_{\text{t}} = -1.54\,\text{fm}$ [Hai13] within the error bars.

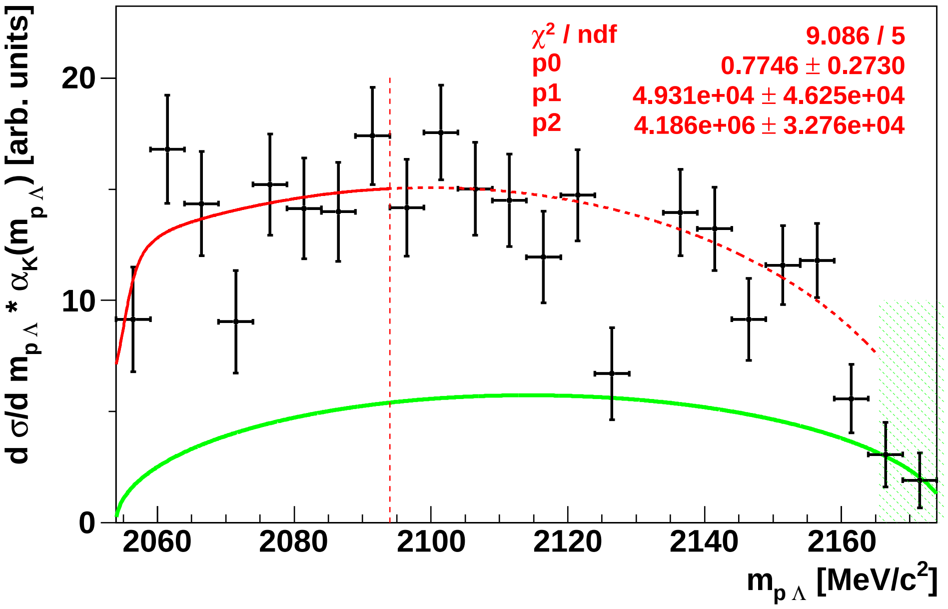

Figure 8.5.: $m_{p\Lambda}$ invariant mass distribution multiplied with the contribution of the Legendre polynomial P_1^1 to the kaon analyzing power ($\alpha_K(m_{p\Lambda})$) for each mass bin. The fits with phase space (green) and the final state parametrization function described by Equation 8.3 (red) are shown. The vertical red dashed line marks the upper limit of the FSI fit. The result of the fit are given in the caption.

Other experimental results for the $p\Lambda$ spin triplet scattering length a_t are

- $a_\mathrm{t} = (-1.6^{+1.1}_{-0.8})\,\mathrm{fm}$ (Λp elastic scattering) [Ale68],
- $a_\mathrm{t} = (-2.0 \pm 0.5)\,\mathrm{fm}$ ($K^- d \to \pi^- \Lambda p$ reaction at rest) [Tan69],
- $a_\mathrm{t} = (-1.56^{+0.19}_{-0.22}{}_\mathrm{stat.} \pm 0.4_\mathrm{theo.})\,\mathrm{fm}$ ($pp \to K^+ + (\Lambda p)$ inclusive measurement at $p_\mathrm{beam} = 2.735\,\mathrm{GeV}/c$) [HIR10].

These results coincide with the result from this thesis within $1\,\sigma$ error, but they are determined by the Jost function approach as described in Section 2.4. The value from [HIR10] is obtained by a combined six-parameter fit of the kaon missing mass spectrum from their measurement and the Λp elastic scattering data from [Ale68]. Additionally, the spin triplet scattering length from [Tan69] is used as a $1\,\sigma$ constraint in the fitting procedure of [HIR10]. Thus, the result from [HIR10] comprises the other measurements. However, another implication of [HIR10] is a dominant $p\Lambda$ spin singlet production process[4] at a similar beam momentum to the measurement presented in this thesis. This

---

[4] Their fit gives a spin triplet matrix element $|M_\mathrm{t}|^2 = (0.0^{+19}_{-0.0})\,\mathrm{b/sr}$ and a spin singlet matrix element

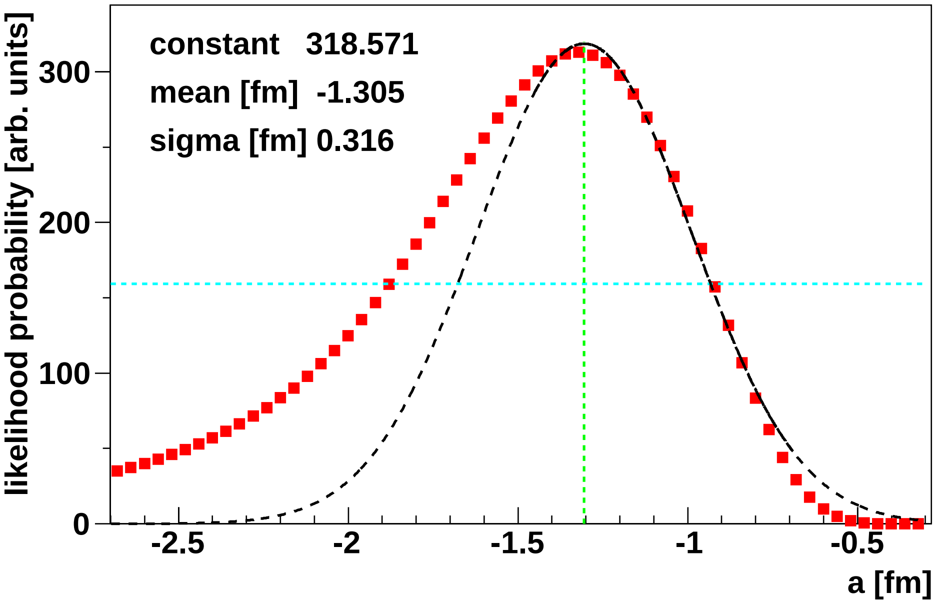

Figure 8.6.: The likelihood probability distribution for determination of the $p\Lambda$ spin triplet scattering length and its error. A Gaussian function is fitted to the right side of the spectrum and its parameters are given in the caption. The mean value is indicated by the green dashed line. The blue dashed line marks the half maximum of the Gaussian for the calculation of the asymmetric scattering length error by the crossing points of the half maximum line with the distribution.

is in contradiction to the observed contribution of the associated Legendre polynomial P_1^1 to the kaon analyzing power at 2.7 GeV/c beam momentum, which is proportional to spin triplet scattering. An explanation for the result from [HIR10] could be further systematic errors from N^* resonance contributions. These can not be directly studied by [HIR10] by a Dalitz plot analysis, since the $pp \to K^+ + (\Lambda p)$ reaction has been measured inclusively. By the exclusive measurement of the $pp \to pK\Lambda$ reaction with COSY-TOF, the influences of N^* resonances can be investigated due to the full phase space coverage of the detector (see previous section). Therefore, I am convinced, that the result for the $p\Lambda$ spin triplet scattering length presented in this thesis is more reliable than the other one. Furthermore, the dispersion integral method allows the extraction of the scattering length from the measured data without the use of other data as for instance the Λp elastic scattering data.

$|M_s|^2 = (111^{+8}_{-38})$ b/sr.

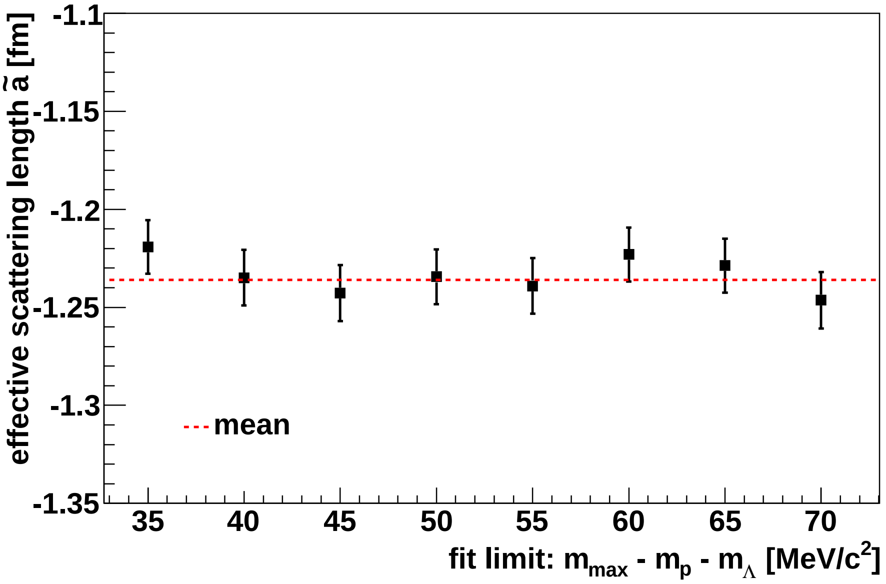

Figure 8.7.: Dependence of the determined effective scattering length $\tilde{a}$ on the limit of the FSI fit. The red dashed line marks the mean value.

8.5. Systematic Errors

Since the determination of the spin triplet $p\Lambda$ scattering length from the invariant mass distribution and the kaon analyzing power is quite complicated, several checks have been performed for systematic errors.

First, the limit of the FSI fit is varied from the usual value $40\,\mathrm{MeV}/c^2$ over threshold. This is done for the determination of the effective scattering length, because it is assumed that any observed deviation is similar for the determination of the spin triplet scattering length. In Figure 8.7 the effective scattering length $\tilde{a}$, obtained from the likelihood probability distribution, as a function of the fit limit is shown. The dashed red line marks the mean value (1.236 fm) for all points, which agrees well with the taken value for the effective scattering length at a fit limit of $40\,\mathrm{MeV}/c^2$ over threshold. Furthermore, no systematic effect of the fit limit on the extracted scattering length value is observed.

Another systematic error could stem from an improper acceptance correction of the $p\Lambda$ invariant mass distribution. This effect is assumed to be negligible, as it is shown in Section 7.3.1.

The influence of N^* resonances on the extracted values are shown in Section 8.3. The obtained systematic error is in the order of 0.1 fm.

The binning of the invariant mass distribution could change the extracted scattering length value. Thus, the scattering length extraction method is applied to the

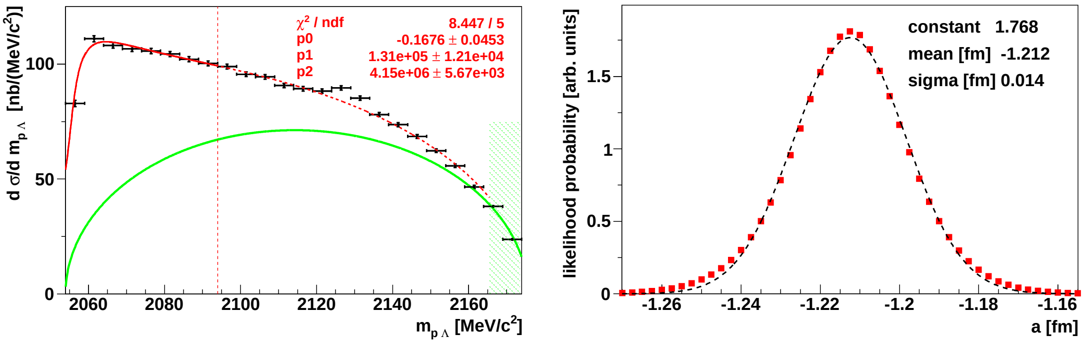

Figure 8.8.: Left: $m_{p\Lambda}$ invariant mass distribution for the full event sample with a $5\,\mathrm{MeV}/c^2$ binning normalized to a total cross section of $10\,\mu$b. For the description of the lines and parameters see Figure 8.1. **Right:** The likelihood probability distribution for the full event sample with the $5\,\mathrm{MeV}/c^2$ binning for the determination of $\tilde{a}$ and its error.

$p\Lambda$ invariant mass distribution with $5\,\mathrm{MeV}/c^2$ broad bins. This invariant mass distribution and the corresponding likelihood probability distribution of the fit are shown in Figure 8.8. The obtained effective scattering length with the $5\,\mathrm{MeV}/c^2$ binning is $\tilde{a} = (-1.212 \pm 0.014_{\mathrm{stat.}} \pm 0.3_{\mathrm{theo.}})\,\mathrm{fm}$. By comparing this values with the result from Section 8.2, a systematic error of 0.02 fm from the binning is assumed.

To check the influence of a wrongly determined beam polarization on the α parameter, α has been again evaluated for a beam polarization, which is 5 % lower than the correct value. The results for α for the correct and wrong beam polarization is shown in Figure 8.9 (left plot) as a function of the $p\Lambda$ invariant mass. All α values with the wrong polarization (blue, shifted by $m_{p\Lambda} = +2\,\mathrm{MeV}/c^2$ for better visibility) are systematically shifted to higher values compared to the correct ones (red). However, the ratio of the α values is almost constant at 95 % over the whole $p\Lambda$ invariant mass range. This is shown in the right plot of Figure 8.9. Therefore, a wrong beam polarization changes only the absolute height of the distribution in Figure 8.5 and not the shape. Thus, no systematic error is introduced in the determination of the spin triplet scattering length. Similar, different values for the up and down polarization have no significant effect on the kaon analyzing power. This is demonstrated in [Hau13].

The errors for the $p\Lambda$ spin triplet scattering length are determined by the crossing points of the half maximum line with the likelihood probability distribution. (see previous section). For this values a systematic uncertainty of 0.05 fm is assumed. This is the distance between two points of the likelihood probability distribution in Figure 8.6. Therefore, the corresponding systematic error for σ is assumed to be 0.04 fm.

An overview over the systematic errors can be found in Table 8.2. Taking the sum of the systematic errors, the results for the spin effective and spin triplet $p\Lambda$ scattering

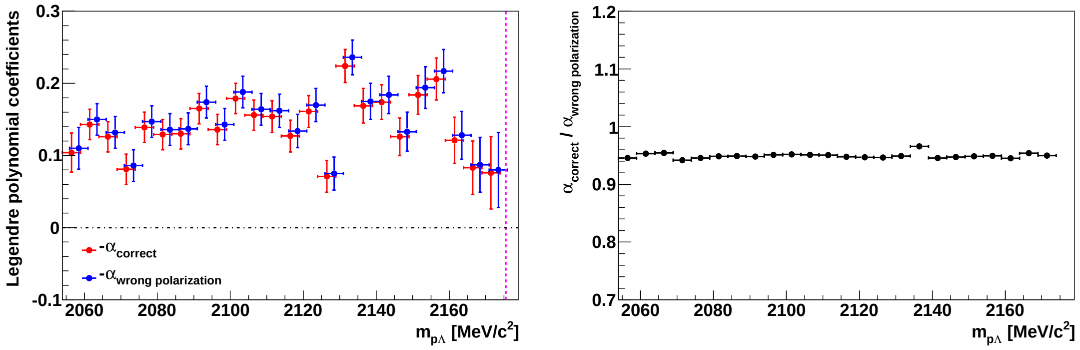

Figure 8.9.: **Left:** Contribution of the associated Legendre polynomial $P_1^1(\alpha)$ to the kaon analyzing power as a function of the $p\Lambda$ invariant mass for the correct beam polarization (red) and a wrong polarization, which is 5 % lower (blue). The blue points are shifted by $m_{p\Lambda} = +2\,\text{MeV}/c^2$ for better visibility. **Right:** Ratio of the two α values from the left plot as a function of the $p\Lambda$ invariant mass. The error bars are not shown, since the error bars of the spectra in the left plot are highly correlated due to the same underlying event sample.

length are

$$\begin{aligned}\tilde{a} &= (-1.233 \pm 0.014_{\text{stat.}} \pm 0.3_{\text{theo.}} \pm 0.12_{\text{syst.}})\,\text{fm}\\ a_{\text{t}} &= (-1.31^{+0.32}_{-0.49}{}_{\text{stat.}} \pm 0.3_{\text{theo.}} \pm 0.16_{\text{syst.}})\,\text{fm}.\end{aligned}$$

Systematic error	effective scattering length	spin triplet scattering length
Fit limit of the FSI fit	negligible	negligible
Improper acceptance correction	negligible	negligible
Influence of N^* resonances	0.1 fm	0.1 fm
Binning of the $m_{p\Lambda}$ distribution	0.02 fm	0.02 fm
Wrong beam polarization	negligible	negligible
Spin triplet error method	-	0.04 fm
Total (sum)	0.12 fm	0.16 fm

Table 8.2.: Overview of the considered systematic errors for the scattering length determination.

> A theory can be proved by experiment; but no path leads from experiment to the birth of a theory.
>
> *(Manfred Eigen)*

9. Comparison of Polarization Observables with other COSY-TOF Results

In this chapter, the results for the polarization observables are compared with COSY-TOF measurements of the $pp \to pK\Lambda$ reaction at different beam momenta. These observables are more sensitive to the features of the production mechanism than the unpolarized observables. Especially, changes in the behavior of the polarization observables with beam momentum can give a deeper understanding of the various contribution in the associated strangeness production. Unfortunately, no predictions from theoretical side for the polarization observables and their behavior at different beam momenta exist. Therefore, the results of this chapter are an experimental study, which can be used as input and constraints for further theoretical investigations of the associated strangeness production in the $pp \to pK\Lambda$ reaction, such as a partial wave analysis, which is currently in preparation within the framework of the Bonn-Gatchina group [Ani07a].

In the first part of the chapter a comparison of the Λ polarization results is shown with an unexpected result. The dependence of the Λ polarization on the beam momentum is further studied by fitting associated Legendre polynomials to previous COSY-TOF data in addition to the data from this thesis.

The second part of the chapter shows the comparison of the analyzing powers. For the proton and Λ analyzing power the results of fits with the sum of two or three associated Legendre polynomials are given. In the case of the kaon analyzing power the fit results are already given in Section 7.5.3.

9.1. Λ Polarization

In Figure 9.1, the result for the Λ polarization as a function of $\cos(\theta_\Lambda^{\mathrm{CMS}})$ is shown for COSY-TOF measurements at the beam momenta 2.7 GeV/c (black), 2.75 GeV/c [Piz07] (green) and 2.95 GeV/c [Roe11] (blue)[1]. The measurement at 2.95 GeV/c from [Roe11] has been done with the same COSY-TOF detector setup and the same event reconstruction program as the one presented in this thesis, while the measurement at

---

[1] Unfortunately, the Λ polarization can not be compared with the result from the COSY-TOF measurement at 2.68 GeV/c [Met98], because the polarization as a function of $\cos(\theta_\Lambda^{\mathrm{CMS}})$ was not determined there.

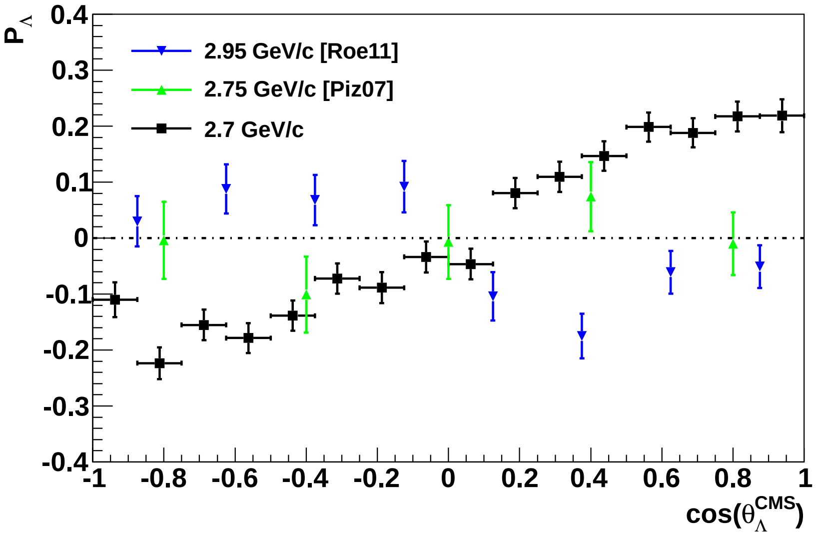

Figure 9.1.: Λ polarization P_Λ as a function of $\cos(\theta_\Lambda^{\mathrm{CMS}})$ from different COSY-TOF measurements. The data shown are measured at 2.7 GeV/c (this thesis, black), at 2.75 GeV/c beam momentum [Piz07] (green) and at 2.95 GeV/c beam momentum [Roe11] (blue).

2.75 GeV/c from [Piz07] has been done with the previous COSY-TOF setup without the straw tube tracker and a different reconstruction program.

Surprisingly, a large deviation of the Λ polarization measurements at the different beam momenta is observed. Comparing the measurements at 2.7 GeV/c and 2.95 GeV/c, the polarization changes the sign and the maximum value of the 2.7 GeV/c data is about twice the maximum value of the 2.95 GeV/c data. The measurement at 2.75 GeV/c follows more the behavior at 2.7 GeV/c, but the maximum value is much lower and within the error bars the result from this measurement is nearly compatible with zero.

To study the behavior of the Λ polarization, all available COSY-TOF results for the Λ polarization as a function of $\cos(\theta_\Lambda^{\mathrm{CMS}})$ has been fitted with the sum of the two associated Legendre polynomials P_1^1 and P_2^1 in the way as the results from this thesis shown in Figure 7.13. If there are more than one COSY-TOF measurement at the same beam momentum, the results of the one with the higher statistics is used. Therefore, the fitting is applied to the data from [Piz07] (2.75 GeV/c beam momentum), [Fri02] (2.85 GeV/c beam momentum), [Roe11] (2.95 GeV/c beam momentum) and [Schr03] (3.2 GeV/c beam momentum). The results of the fits and the data are shown in Figure 9.2 from the upper left plot to the lower right plot. The complete fit is shown in red in each plot, and the individual contributions of the polynomials P_1^1 and P_2^1 are shown by the green dashed and blue dashed curves, respectively.

The fit with the sum of the two associated Legendre polynomials describes the various

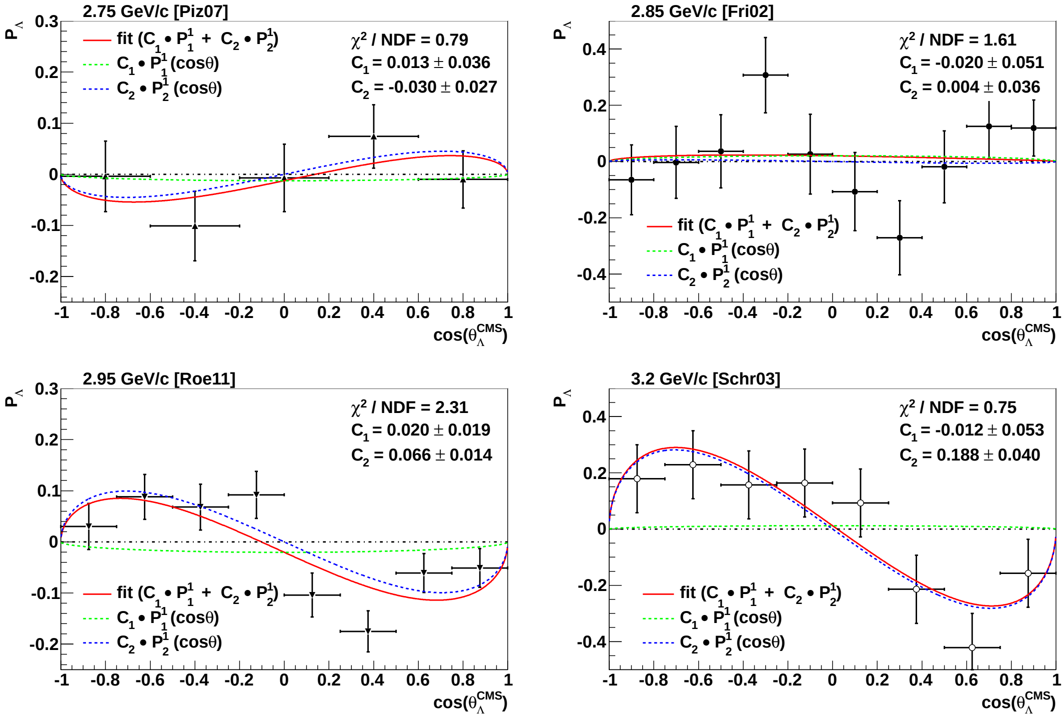

Figure 9.2.: Λ polarization P_Λ as a function of $\cos(\theta_\Lambda^{\mathrm{CMS}})$ for several COSY-TOF measurements. Each polarization is fitted with the sum of the two associated Legendre polynomials P_1^1 and P_2^1 shown in red. The individual contributions of the polynomials are shown by the green dashed and blue dashed curves, respectively. The fit results are given in the captions. The measurements are taken at 2.75 GeV/c beam momentum [Piz07] (upper left), at 2.85 GeV/c beam momentum [Fri02] (upper right), at 2.95 GeV/c beam momentum [Roe11] (lower left) and at 3.2 GeV/c beam momentum [Schr03] (lower right).

data quite well. The contribution of the associated Legendre polynom $P_1^1(C_1)$ is more or less compatible with zero in the $1\,\sigma$ range for each measurement. The contribution of $P_1^1(C_2)$ on the other hand changes steadily from -0.030 to 0.188 with increasing beam momentum. This linear increase of the C_2 value with beam momentum can clearly be observed in Figure 9.3, where the results for C_1 and C_2 from the fits are plotted as a function of the beam momentum including the result from this thesis at 2.7 GeV/c. In Table 9.1 the results of the fits are summarized for all measurements.

A theoretical interpretation of the observed behavior of the Λ polarization as a function of the beam momentum is still missing. Of interest might be that the values C_1 and C_2 are connected to partial wave amplitudes similar to the α and β values of the analyzing powers. In this picture the dependence of C_2 from the beam momentum can be interpreted as an increase of a corresponding partial wave interference with an

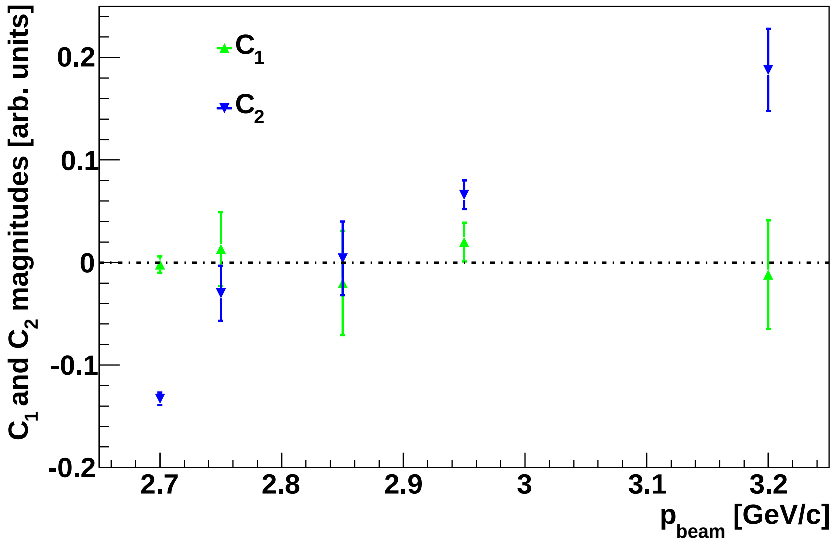

Figure 9.3.: C_1 and C_2 values from the fits of the Λ polarization measurements (this thesis and [Piz07, Fri02, Roe11, Schr03]) as a function of the beam momentum. The fits are shown in Figure 9.2 and Figure 7.13.

angular momentum of $l = 2$. This increase might be connected with the large difference of the $N\Sigma$ coupled channel enhancement in the $p\Lambda$ invariant mass distributions of the measurements at 2.7 GeV/c and 2.95 GeV/c (see Section 7.2.3 and [Roe11]).

Beam momentum	C_1	C_2	χ^2/NDF
2.70 GeV/c (see Fig. 7.13)	-0.002 ± 0.008	-0.133 ± 0.006	1.98
2.75 GeV/c [Piz07]	0.013 ± 0.036	-0.030 ± 0.027	0.79
2.85 GeV/c [Fri02]	-0.020 ± 0.051	0.004 ± 0.036	1.61
2.95 GeV/c [Roe11]	0.020 ± 0.019	0.066 ± 0.014	2.31
3.20 GeV/c [Schr03]	-0.012 ± 0.053	0.188 ± 0.040	0.75

Table 9.1.: Contributions of the associated Legendre polynomials P_1^1 (C_1) and P_2^1 (C_2) to the Λ polarization for measurements at different beam momenta. In addition, the reduced χ^2 values of the fits with the first two polynomials are given.

9.2. Analyzing Power

The results for the analyzing power of the three final state particles are already shown in Section 7.5. In this section they are compared with the results of the other COSY-TOF measurements at different beam momenta, which are [Piz07] (2.7 GeV/c beam momentum) and [Roe11, Jow14] (2.95 GeV/c beam momentum). However, some analyzing powers were not determined in these measurements, and hence in this case no data is available for the comparison.

9.2.1. Proton Analyzing Power

In Figure 9.4 the proton analyzing power as a function of $\cos(\theta_p^{\mathrm{CMS}})$ is shown for the measurements at 2.7 GeV/c from this thesis and at 2.95 GeV/c from [Jow14]. In [Piz07] and [Roe11], the proton analyzing power was not determined. In the figure the red points are shifted by $\cos(\theta_p^{\mathrm{CMS}}) = +0.0015$ for better visibility. Close to $\cos(\theta_p^{\mathrm{CMS}}) = -1$, the behavior of the analyzing power differs significantly, but for the rest of the scattering angle the analyzing power is nearly overlapping within the errors bars.

Additionally, the fit of the analyzing power with the sum of associated Legendre polynomials is compared. The result from this thesis can be well described by the sum of the two polynomials P_1^1 and P_2^1 with a reduced χ^2 of 1.01 (see Figure 7.17). The same has been done with the data from [Jow14] with a very poor fit with $\chi^2/\mathrm{NDF} = 10.12$ [Jow13b]. However, including the next order of the associated Legendre polynomials, P_3^1, improves the fit to $\chi^2/\mathrm{NDF} = 1.08$ [Jow14]. The results for the contribution of the individual polynomials from the fit are summarized in Table 9.2. In all cases, the contribution of $P_1^1(\alpha)$ is the dominant one. β is very small for the measurement at 2.7 GeV/c and compatible with zero for the measurement at 2.95. GeV/c. The value for γ is about half the size than α in absolute numbers.

These results can be explained by contributions from higher partial waves at the beam momentum of 2.95 GeV/c than at 2.7 GeV/c. This gives a significant contribution of the P_3^1 to the proton analyzing power.

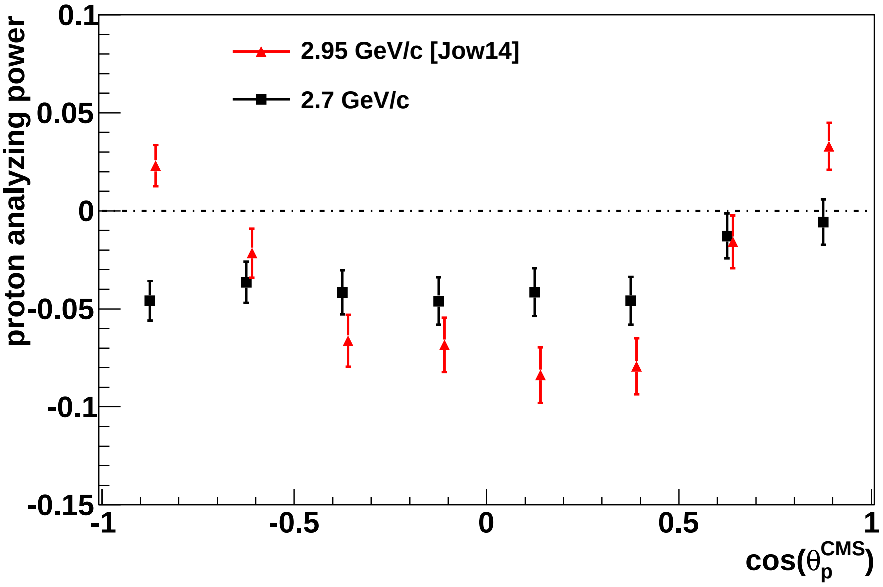

Figure 9.4.: Proton analyzing power as a function of $\cos(\theta_p^{\mathrm{CMS}})$ for two COSY-TOF measurements. The results shown are from this thesis (black) and for the data measured at 2.95 GeV/c beam momentum from [Jow14] (red). The red points are shifted by $\cos(\theta_p^{\mathrm{CMS}}) = +0.015$ for better visibility.

Beam momentum	α	β	γ	χ^2/NDF
2.7 GeV/c	0.043 ± 0.005	-0.009 ± 0.004	-	1.01
2.95 GeV/c [Jow14b]	0.049 ± 0.006	0.001 ± 0.004	-	10.12
2.95 GeV/c [Jow14]	0.054 ± 0.006	-0.001 ± 0.004	-0.026 ± 0.003	1.08

Table 9.2.: Contributions of the associated Legendre polynomials $\alpha(P_1^1)$, $\beta(P_2^1)$ and $\gamma(P_3^1)$ to the proton analyzing power from the fit of the data measured at 2.7 GeV/c (this thesis, see Figure 7.17) and at 2.95 GeV/c (from [Jow14] and [Jow14b]). In addition, the reduced χ^2 values of the fits are given.

9.2.2. Λ Analyzing Power

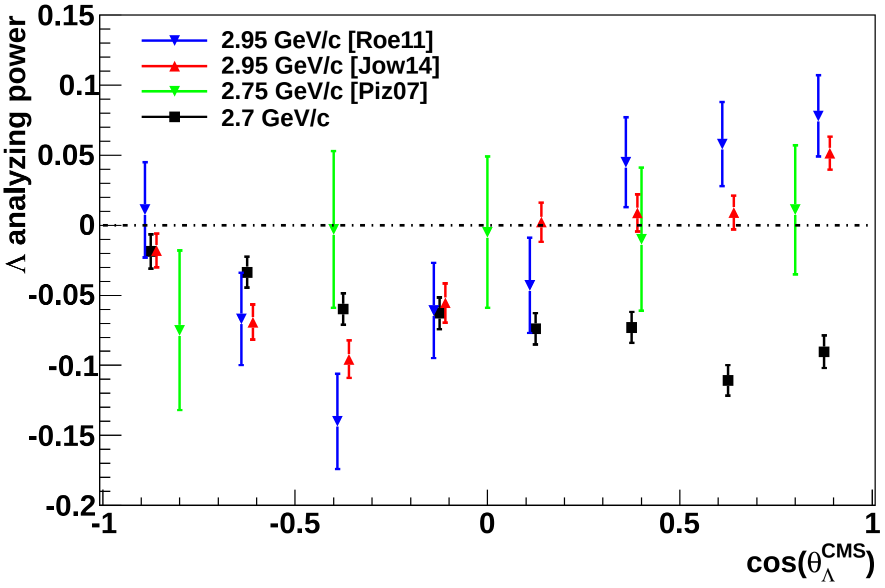

Figure 9.5.: Λ analyzing power as a function of $\cos(\theta_\Lambda^{\mathrm{CMS}})$ for different COSY-TOF measurements. The results are from this thesis (black), from the data measured at 2.75 GeV/c beam momentum from [Piz07] (green) and from the data measured at 2.95 GeV/c beam momentum from [Roe11] (blue) and [Jow14] (red). The red and blue points are shifted by $\cos(\theta_\Lambda^{\mathrm{CMS}}) = \pm 0.015$ from the black points for better visibility.

The comparison of the Λ analyzing power as a function of $\cos(\theta_\Lambda^{\mathrm{CMS}})$ for different COSY-TOF measurements is shown in Figure 9.5 with the results from this thesis (black), from [Piz07] (green), from [Roe11] (red) and from [Jow14] (blue). The red and blue points are shifted by $\cos(\theta_\Lambda^{\mathrm{CMS}}) = +0.0015$ and $\cos(\theta_\Lambda^{\mathrm{CMS}}) = -0.0015$ from the black points for better visibility.

As expected, the results of the two measurements at 2.95 GeV/c match within the errors bars. In addition, the results of all measurements are similar in the backward scattering range ($\cos(\theta_\Lambda^{\mathrm{CMS}}) < 0$). But in the forward scattering range ($\cos(\theta_\Lambda^{\mathrm{CMS}}) > 0$), the result for the Λ analyzing power from this thesis differs significantly from the other ones. Moreover, the sign is opposite to the measurements at 2.95 GeV/c.

In Section 7.5, the Λ analyzing power is already fitted with the sum of the two associated Legendre polynomials P_1^1 and P_2. This has been also done for result of the measurement at 2.95 GeV/c, which is shown by the red points in Figure 9.5 [Jow14b]. However, including the polynomial P_3^1 into the fit gives a better reduced χ^2 for both measurements. The analyzing power of this thesis, fitted with the three associated

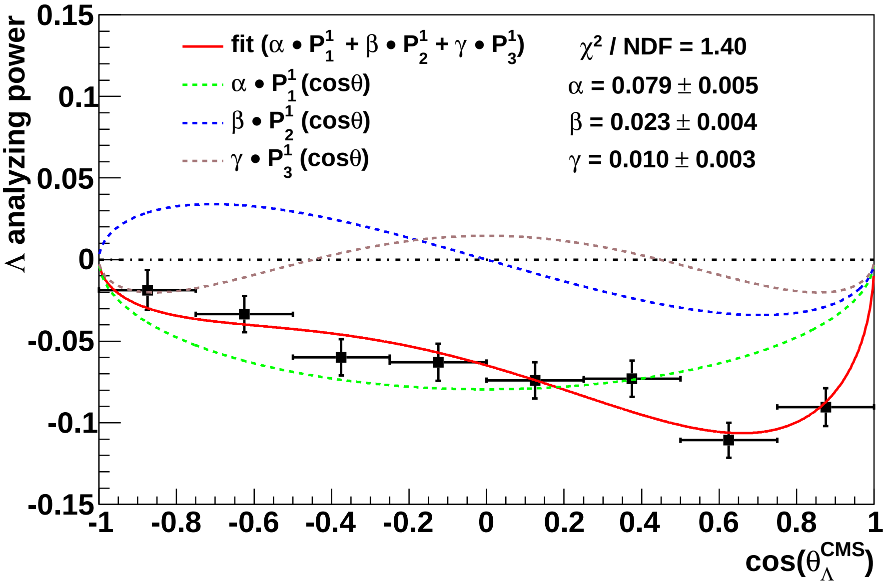

Figure 9.6.: Λ analyzing power at 2.7 GeV/c as a function of cos($\theta_\Lambda^{\mathrm{CMS}}$). The red line shows the fit with a sum of the three associated Legendre polynomials P_1^1, P_2 and P_3^1. The individual contributions of the polynomials are shown by the green dashed, blue dashed and brown dashed lines, respectively.

Legendre polynomials, is shown in Figure 9.6. The individual contributions of the polynomials are shown by the green dashed, blue dashed and brown dashed lines, respectively. The obtained values for the contributions are given in the caption. The similar figure from the fit of the measurement at 2.95 GeV/c can be found in [Jow14].

The obtained values for the contributions and the reduced χ^2 values from the different fits are given in Table 9.3. As expected, the result for α and β is not influenced by including P_3^1 into the fit. Therefore, the results of the two fits with the sum of three associated Legendre polynomials are compared.

α is reduced of about 60 % from this thesis to the measurement at 2.95 GeV/c. The sign of the parameters β and γ flips, and the absolute value of β changes by about 50 %. Most likely, these results and the strong dependence of the Λ polarization with beam momentum (see Section 9.1) have the same origin. As already mentioned above, one reason is a strong dependence of the Λ partial wave amplitudes with the beam momentum. Unfortunately, the data measured at 2.75 GeV/c from [Piz07] can not be used further for a fit of the associated Legendre polynomials due to the large errors bars.

Beam momentum	α	β	γ	χ^2/NDF
2.7 GeV/c	0.079 ± 0.005	0.023 ± 0.004	-	2.69
2.95 GeV/c [Jow14b]	0.030 ± 0.006	-0.034 ± 0.004	-	3.97
2.7 GeV/c	0.079 ± 0.005	0.023 ± 0.004	0.010 ± 0.003	1.40
2.95 GeV/c [Jow14]	0.032 ± 0.006	-0.034 ± 0.004	-0.009 ± 0.004	3.59

Table 9.3.: Contributions of the associated Legendre polynomials $\alpha(P_1^1)$, $\beta(P_2^1)$ and $\gamma(P_3^1)$ to the Λ analyzing power from the fits of the data measured at 2.7 GeV/c (this thesis, see Figure 7.18) and at 2.95 GeV/c (from [Jow14] and [Jow14b]). In addition, the reduced χ^2 values of the fits are given.

9.2.3. Kaon Analyzing Power

In Figure 9.7 the kaon analyzing power as a function of $\cos(\theta_p^{\mathrm{CMS}})$ is shown for the measurements at 2.7 GeV/c from this thesis (black), at 2.75 GeV/c [Piz07] and at 2.95 GeV/c from [Roe11] (blue) and [Jow14] (red). The result for 2.75 GeV/c is extracted as the mean value of the points plotted in Figure 33 in [CTOF07], which references to [Piz07] and a private communication with C. Pizzolotto, since in [Piz07] the kaon analyzing power is not shown. The red and blue points in Figure 9.7 are shifted by $\cos(\theta_K^{\mathrm{CMS}}) = \pm 0.015$ from the black points for better visibility.

The behavior of the analyzing power is similar for the two measurements at 2.95 GeV/c as expected. The result from this thesis deviates in the range $\cos(\theta_K^{\mathrm{CMS}}) > 0.5$ from the measurement from [Jow14]. As already explained in Section 7.5.3, the contribution of the asymmetric associated Legendre polynomial P_2^1 is lower for the measurement at 2.7 GeV/c due to a reduced amount of D-wave kaons[2]. Thus, the kaon analyzing power distribution is less asymmetric than at 2.95 GeV/c, which is compatible with the behavior in Figure 9.7. The data measured at 2.75 GeV/c follows the general trend of the analyzing power. There might be an indication of a deviation from the 2.7 GeV/c data in the range $\cos(\theta_K^{\mathrm{CMS}}) > 0.6$, but this is not significant due to the large error bars.

---

[2] The table with the results of the fits with the associated Legendre polynomials P_1^1 and P_2^1 can be found in Section 7.5.3 (see Table 7.1).

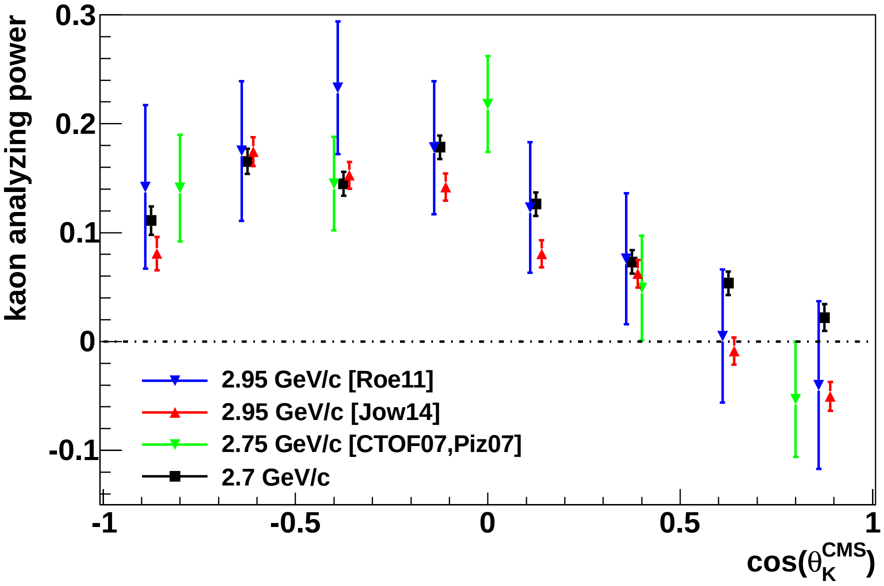

Figure 9.7.: Kaon analyzing power as a function of $\cos(\theta_K^{\mathrm{CMS}})$ for different COSY-TOF measurements. The results are from this thesis (black), from the data measured at 2.75 GeV/c beam momentum [Piz07] (green) and the data measured at 2.95 GeV/c beam momentum from [Roe11] (blue) and [Jow14] (red) and the data. The result for 2.75 GeV/c is extracted as the mean value of the points plotted in Figure 33 in [CTOF07], which references to [Piz07] and a private communication with C. Pizzolotto. The red and blue points are shifted by $\cos(\theta_K^{\mathrm{CMS}}) = \pm 0.015$ from the black points for better visibility.

10. Summary and Outlook

10.1. Summary

The $\vec{p}p \to pK\Lambda$ reaction was measured with the COSY-TOF detector with a polarized proton beam at a momentum of 2.7 GeV/c in 2011. The selected data sample consists of 207,219 events. This is so far the largest data sample for this beam momentum and for the COSY-TOF experiment. To obtain this amount of statistics, the data taking process was modified to reduce the dead time of the read out system. Most of the data were recorded only with the straw tube tracker. Therefore, in the analysis of this thesis the $pK\Lambda$ events are reconstructed by the STT alone.

After corrections on the rare TDC spectra of the straw tubes, the STT was calibrated double layer wise. Similar the geometrical alignment was corrected. The obtained spatial resolutions lie between 120 μm and 150 μm, which corresponds to an $\approx 25\,\%$ improvement to the previous calibration presented in [Roe11] due to more sophisticated routines for the calibration and geometrical alignment. In addition, the spatial resolutions have been implemented double layer wise in the Monte Carlo simulations to have a more adequate description of the detector.

Parameters of the reconstruction software were optimized for high reconstruction efficiency and low computational time. From Monte Carlo simulations the combined reconstruction efficiency and acceptance correction for the $pK\Lambda$ final state has been obtained to be $(15.4 \pm 0.01)\,\%$. The fraction of $\vec{p}p \to pK\Sigma^0$ background events was determined by Monte Carlo simulations. It was found to be $(0.73 \pm 0.11)\,\%$, and thus this background was neglected in the analysis.

The beam direction and polarization as well as target properties were determined by $\vec{p}p \to pp$ elastic scattered events, which were triggered and reconstructed in parallel to the $\vec{p}p \to pK\Lambda$ reaction. Similar to previous analyses ([Roe11, Dzh12]) a small tilt of the beam direction to the straw tube tracker was determined and corrected in the $pK\Lambda$ analysis. The polarization of the beam was extracted to be $(79.0 \pm 1.1)\,\%$, which is 18 percentage points higher than in the previous measurement at 2.95 GeV/c beam momentum [CTOF13b].

The analysis of the $pK\Lambda$ event sample focuses on the polarization observables and the extraction of the $p\Lambda$ effective and spin triplet scattering lengths from the shape of the $p\Lambda$ final state interaction, where for the determination of the spin triplet scattering length a new method [Gas04] was used the first time. In addition, the Dalitz plot and the angular distributions are examined. All these results are presented in Chapter 7 and Chapter 8.

The Dalitz plot contains no significant enhancement at the $N\Sigma$ thresholds as seen in other measurements at higher beam momenta due to a $p\Lambda - N\Sigma$ coupled channel effect (e.g. see [CTOF13a]). However, a small enhancement is visible in the projection on the $m_{p\Lambda}$ invariant mass. A theoretical explanation for the change of the strength of this enhancement with beam momentum is still missing.

A surprising result was obtained for the Λ polarization as a function of $\cos(\theta_\Lambda^{\mathrm{CMS}})$. Compared to the result from the COSY-TOF measurement at $2.95\,\mathrm{GeV}/c$ beam momentum the polarization flips its sign in the full $\cos(\theta_\Lambda^{\mathrm{CMS}})$ range. A detailed study has been done by fitting associated Legendre polynomials to the Λ polarization distribution of all available COSY-TOF data. It is found out from these fits that the contribution of the associated Legendre polynomial P_2^1 to the Λ polarization changes smoothly with beam momentum, and thus the polarization does the same. An easy explanation for this behavior can not be given. However, the results give important information for further theoretical investigations of the associated strangeness production.

The result for the $p\Lambda$ effective scattering length is $\tilde{a} = (-1.233 \pm 0.014_{\mathrm{stat.}} \pm 0.3_{\mathrm{theo.}} \pm 0.12_{\mathrm{syst.}})\,\mathrm{fm}$. This is compatible with the result from the measurement at $2.95\,\mathrm{GeV}/c$ [CTOF13b], but significantly smaller errors could be achieved in this thesis. The influence of N^* resonances on the scattering length has been studied by dividing the Dalitz plot and the invariant mass spectra in four parts with the same phase space volume. It is found out that the influence of the N^* resonances is weaker than in previous COSY-TOF measurement at $2.95\,\mathrm{GeV}/c$ [CTOF13b]. The systematic error of this influence on the extracted scattering length in this thesis is determined to be $0.1\,\mathrm{fm}$

The main goal of the thesis, namely the extraction of the $p\Lambda$ spin triplet scattering length from data, has been achieved. A requirement, fulfilled by the data, is that the contribution of the associated Legendre polynomial P_1^1 to the kaon analyzing power does not vanish for low $p\Lambda$ invariant masses. This behavior is again opposite to the measurement at $2.95\,\mathrm{GeV}/c$, where an extraction of the scattering length was not possible. The obtained result for the spin triplet scattering length is $a_{\mathrm{t}} = (-1.31^{+0.32}_{-0.49}{}_{\mathrm{stat.}} \pm 0.3_{\mathrm{theo.}} \pm 0.16_{\mathrm{syst.}})\,\mathrm{fm}$. The statistical error is not symmetric due to the complicated numerical calculations involved in the determination process (see Section 8.4).

10.2. Outlook

For a further analysis, the origins for the difference in the behavior of the polarization observables and the $p\Lambda - N\Sigma$ coupled channel effect between the measurements from this thesis and at $2.95\,\mathrm{GeV}/c$ have to be figured out by theoretical investigation. Such an investigation is a partial wave analysis, which is currently in preparation within the framework of the Bonn-Gatchina group [Ani07a]. This could lead to a deeper understanding of the associated strangeness production in the $pp \to pK\Lambda$ reaction. Another quantity which can be studied in this context is the spin transfer coefficient

D_{NN}, which can be extracted from the data by a new method for a full acceptance detector, as it is the COSY-TOF detector. This method is proposed in [Hau14]. In addition, the Dalitz plot can be analyzed in terms of a resonance model as it is shown in [CTOF10b].

Due to the large number of events, the analyzing powers and Λ polarization can be studied in more detail by applying an additional binning on kinematic variables as invariant masses or momenta. These is partly shown in [Jow14] with the newest COSY-TOF data measured at 2.95 GeV/c.

The successful extraction of the spin triplet scattering length with the dispersion integral method from [Gas04] could be possibly improved by a more sophisticated fit method with less numerical difficulties. The scattering length can also be determined by the Jost function approach, and the results of both methods can be compared directly.

A. Further Plots for the Λ Analyzing Power

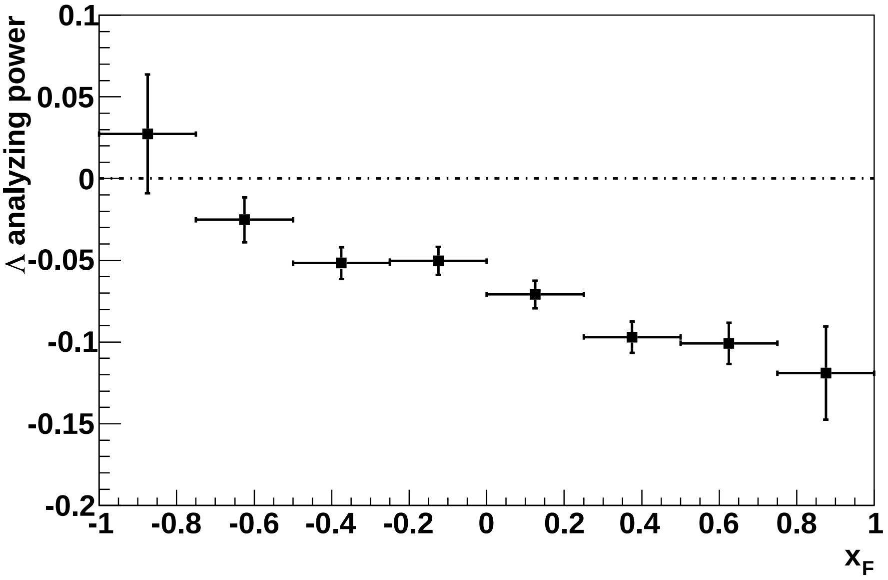

Figure A.1.: Λ analyzing power as a function of the scaling variable x_F.

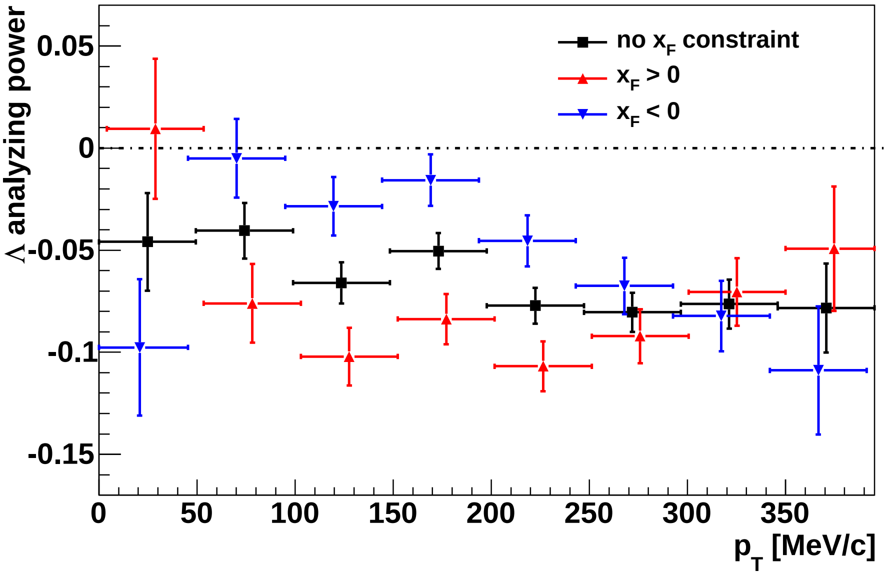

Figure A.2.: Λ analyzing power as a function of the transverse momentum $p_T(\Lambda)$ for the full data (black) and the constaints $x_F > 0$ (red) and $x_F < 0$ (blue). The red and blue points are shifted by $p_T = \pm 4\,\mathrm{MeV}/c$ for better visibility.

B. Data Tables

B.1. Beam Polarization

θ_p^{CMS}	p_B	Δp_B	θ_p^{CMS}	p_B	Δp_B	θ_p^{CMS}	p_B	Δp_B
54	0.772	0.019	66	0.780	0.036	78	0.827	0.051
48	0.810	0.027	70	0.778	0.037	82.5	0.814	0.073
62	0.842	0.033	74	0.744	0.041	87.5	0.765	0.222

Table B.1.: Beam polarization as a function of θ_p^{CMS}.

B.2. Analyzing Power pp Elastic Scattering

θ_p^{CMS}	A	ΔA	θ_p^{CMS}	A	ΔA	θ_p^{CMS}	A	ΔA
54	0.129	0.004	66	0.084	0.004	78	0.069	0.004
48	0.104	0.004	70	0.083	0.004	82.5	0.044	0.004
62	0.093	0.004	74	0.075	0.004	87.5	0.014	0.004

Table B.2.: Analyzing power from *pp* elastic scattering as a function of θ_p^{CMS}.

B.3. Data Tables for the $m_{p\Lambda}$ Invariant Mass Distributions

$m_{p\Lambda}\left[\frac{\mathrm{MeV}}{c^2}\right]$	$\frac{\mathrm{d}\sigma}{\mathrm{d}m}\left[\frac{\mathrm{nb}\,c^2}{\mathrm{MeV}}\right]$	Δ	$m_{p\Lambda}\left[\frac{\mathrm{MeV}}{c^2}\right]$	$\frac{\mathrm{d}\sigma}{\mathrm{d}m}\left[\frac{\mathrm{nb}\,c^2}{\mathrm{MeV}}\right]$	Δ	$m_{p\Lambda}\left[\frac{\mathrm{MeV}}{c^2}\right]$	$\frac{\mathrm{d}\sigma}{\mathrm{d}m}\left[\frac{\mathrm{nb}\,c^2}{\mathrm{MeV}}\right]$	Δ
2054.47	43.1	2.6	2094.99	104.0	2.4	2135.51	77.6	2.0
2055.48	78.8	3.2	2096.00	95.3	2.3	2136.52	78.6	2.0
2056.49	92.6	3.2	2097.01	100.7	2.4	2137.53	75.4	2.0
2057.51	95.8	3.0	2098.03	97.2	2.3	2138.55	73.4	2.0
2058.52	109.6	3.3	2099.04	97.7	2.3	2139.56	78.1	2.0
2059.53	107.4	3.1	2100.05	97.7	2.3	2140.57	75.4	2.0
2060.54	116.4	3.2	2101.06	93.1	2.2	2141.58	71.5	1.9
2061.56	110.8	3.0	2102.08	94.5	2.3	2142.60	70.7	1.9
2062.57	107.4	2.8	2103.09	95.4	2.3	2143.61	71.3	1.9
2063.58	113.9	2.9	2104.10	97.5	2.3	2144.62	73.0	2.0
2064.60	106.6	2.8	2105.12	95.0	2.2	2145.64	70.4	1.9
2065.61	113.1	2.9	2106.13	91.2	2.2	2146.65	69.7	1.9
2066.62	105.6	2.7	2107.14	93.4	2.2	2147.66	64.0	1.9
2067.64	105.0	2.7	2108.16	95.3	2.2	2148.68	63.7	1.8
2068.65	110.4	2.8	2109.17	91.0	2.2	2149.69	66.3	1.9
2069.66	108.4	2.7	2110.18	91.2	2.2	2150.70	63.7	1.9
2070.67	113.4	2.8	2111.19	95.6	2.3	2151.71	60.7	1.8
2071.69	106.6	2.7	2112.21	88.3	2.2	2152.73	61.0	1.8
2072.70	100.4	2.5	2113.22	86.2	2.1	2153.74	56.7	1.8
2073.71	103.1	2.6	2114.23	89.3	2.2	2154.75	56.9	1.8
2074.73	108.1	2.7	2115.25	92.4	2.2	2155.77	57.2	1.8
2075.74	105.4	2.6	2116.26	86.6	2.1	2156.78	57.0	1.8
2076.75	105.9	2.6	2117.27	88.3	2.1	2157.79	53.7	1.7
2077.77	105.5	2.6	2118.29	90.9	2.2	2158.81	52.3	1.7
2078.78	102.3	2.5	2119.30	87.9	2.1	2159.82	48.8	1.6
2079.79	102.8	2.5	2120.31	85.8	2.1	2160.83	50.9	1.7
2080.80	106.0	2.5	2121.32	88.9	2.2	2161.84	46.2	1.6
2081.82	107.5	2.6	2122.34	88.9	2.2	2162.86	42.0	1.5
2082.83	104.5	2.5	2123.35	89.8	2.2	2163.87	41.0	1.5
2083.84	98.6	2.4	2124.36	89.4	2.2	2164.88	43.4	1.6
2084.86	100.3	2.4	2125.38	89.6	2.2	2165.90	39.2	1.5
2085.87	104.7	2.8	2126.39	86.3	2.1	2166.91	37.0	1.5
2086.88	98.9	2.4	2127.40	92.0	2.2	2167.92	33.9	1.4
2087.90	105.0	2.5	2128.42	89.8	2.2	2168.94	33.3	1.4
2088.91	99.7	2.4	2129.43	90.6	2.2	2169.95	30.4	1.4
2089.92	99.6	2.4	2130.44	88.5	2.2	2170.96	25.6	1.3
2090.93	102.0	2.4	2131.45	85.5	2.1	2171.97	19.7	1.1
2091.95	97.0	2.3	2132.47	79.5	2.0	2172.99	18.2	1.1
2092.96	103.8	2.4	2133.48	80.5	2.1	2174.00	12.9	0.9
2093.97	96.5	2.3	2134.49	84.3	2.1	2175.01	3.6	0.6

Table B.3.: $p\Lambda$ invariant mass distribution for the full data.

$m_{p\Lambda}\left[\frac{\mathrm{MeV}}{c^2}\right]$	$\frac{\mathrm{d}\sigma}{\mathrm{d}m}\left[\frac{\mathrm{nb}\,c^2}{\mathrm{MeV}}\right]$	Δ	$m_{p\Lambda}\left[\frac{\mathrm{MeV}}{c^2}\right]$	$\frac{\mathrm{d}\sigma}{\mathrm{d}m}\left[\frac{\mathrm{nb}\,c^2}{\mathrm{MeV}}\right]$	Δ	$m_{p\Lambda}\left[\frac{\mathrm{MeV}}{c^2}\right]$	$\frac{\mathrm{d}\sigma}{\mathrm{d}m}\left[\frac{\mathrm{nb}\,c^2}{\mathrm{MeV}}\right]$	Δ
2054.47	9.0	1.1	2094.99	23.6	1.1	2135.51	16.2	0.9
2055.48	17.9	1.6	2096.00	20.9	1.1	2136.52	16.4	0.9
2056.49	22.3	1.6	2097.01	21.2	1.1	2137.53	15.0	0.9
2057.51	21.6	1.4	2098.03	20.2	1.0	2138.55	15.9	0.9
2058.52	23.7	1.5	2099.04	20.3	1.0	2139.56	14.3	0.8
2059.53	25.2	1.5	2100.05	21.1	1.1	2140.57	15.8	0.9
2060.54	25.9	1.5	2101.06	19.4	1.0	2141.58	14.8	0.9
2061.56	22.4	1.3	2102.08	21.7	1.1	2142.60	13.4	0.8
2062.57	23.9	1.4	2103.09	20.9	1.1	2143.61	14.3	0.9
2063.58	25.5	1.4	2104.10	19.6	1.0	2144.62	14.5	0.9
2064.60	23.5	1.3	2105.12	20.1	1.0	2145.64	12.3	0.8
2065.61	24.0	1.3	2106.13	18.7	1.0	2146.65	14.4	0.9
2066.62	20.7	1.2	2107.14	18.9	1.0	2147.66	13.3	0.8
2067.64	21.8	1.2	2108.16	20.2	1.0	2148.68	13.3	0.8
2068.65	23.2	1.3	2109.17	19.0	1.0	2149.69	12.7	0.8
2069.66	22.8	1.3	2110.18	19.1	1.0	2150.70	13.7	0.9
2070.67	23.6	1.3	2111.19	21.3	1.1	2151.71	11.6	0.8
2071.69	21.8	1.2	2112.21	19.9	1.0	2152.73	12.6	0.8
2072.70	20.7	1.2	2113.22	17.9	0.9	2153.74	11.1	0.8
2073.71	21.6	1.2	2114.23	18.1	1.0	2154.75	10.7	0.8
2074.73	24.3	1.3	2115.25	21.4	1.1	2155.77	11.7	0.8
2075.74	20.7	1.1	2116.26	17.9	0.9	2156.78	11.2	0.8
2076.75	22.1	1.2	2117.27	18.9	1.0	2157.79	9.9	0.7
2077.77	24.0	1.2	2118.29	19.0	1.0	2158.81	9.2	0.7
2078.78	20.3	1.1	2119.30	18.0	0.9	2159.82	8.4	0.7
2079.79	22.3	1.2	2120.31	17.4	0.9	2160.83	11.1	0.8
2080.80	22.1	1.1	2121.32	18.1	0.9	2161.84	9.1	0.7
2081.82	20.7	1.1	2122.34	19.3	1.0	2162.86	9.1	0.7
2082.83	21.7	1.1	2123.35	18.5	1.0	2163.87	8.8	0.7
2083.84	21.9	1.1	2124.36	17.0	0.9	2164.88	8.3	0.7
2084.86	22.3	1.2	2125.38	18.7	1.0	2165.90	8.2	0.7
2085.87	23.5	1.2	2126.39	17.7	0.9	2166.91	6.7	0.6
2086.88	21.6	1.1	2127.40	19.1	1.0	2167.92	7.3	0.7
2087.90	19.4	1.0	2128.42	19.7	1.0	2168.94	6.9	0.6
2088.91	21.9	1.1	2129.43	17.7	0.9	2169.95	7.1	0.7
2089.92	19.7	1.0	2130.44	17.6	0.9	2170.96	5.5	0.6
2090.93	21.6	1.1	2131.45	18.3	1.0	2171.97	4.9	0.5
2091.95	20.3	1.1	2132.47	17.3	0.9	2172.99	4.2	0.5
2092.96	23.2	1.1	2133.48	17.6	0.9	2174.00	2.6	0.4
2093.97	20.6	1.1	2134.49	17.2	0.9	2175.01	1.1	0.4

Table B.4.: $p\Lambda$ invariant mass distribution for $\cos\theta^{p\Lambda}_{pK} > 0.5$.

$m_{p\Lambda}\left[\frac{\mathrm{MeV}}{c^2}\right]$	$\frac{\mathrm{d}\sigma}{\mathrm{d}m}\left[\frac{\mathrm{nb}\,c^2}{\mathrm{MeV}}\right]$	Δ	$m_{p\Lambda}\left[\frac{\mathrm{MeV}}{c^2}\right]$	$\frac{\mathrm{d}\sigma}{\mathrm{d}m}\left[\frac{\mathrm{nb}\,c^2}{\mathrm{MeV}}\right]$	Δ	$m_{p\Lambda}\left[\frac{\mathrm{MeV}}{c^2}\right]$	$\frac{\mathrm{d}\sigma}{\mathrm{d}m}\left[\frac{\mathrm{nb}\,c^2}{\mathrm{MeV}}\right]$	Δ
2054.47	10.4	1.2	2094.99	27.4	1.3	2135.51	22.8	1.1
2055.48	21.6	1.7	2096.00	26.8	1.2	2136.52	21.6	1.1
2056.49	24.3	1.7	2097.01	26.5	1.2	2137.53	20.7	1.1
2057.51	26.8	1.7	2098.03	26.2	1.2	2138.55	19.2	1.0
2058.52	28.5	1.7	2099.04	25.4	1.2	2139.56	22.0	1.1
2059.53	27.8	1.6	2100.05	27.3	1.2	2140.57	19.3	1.0
2060.54	28.4	1.5	2101.06	27.2	1.2	2141.58	18.4	1.0
2061.56	28.2	1.5	2102.08	26.1	1.2	2142.60	18.6	1.0
2062.57	29.0	1.5	2103.09	25.8	1.2	2143.61	18.5	1.0
2063.58	27.6	1.4	2104.10	27.2	1.2	2144.62	19.5	1.0
2064.60	27.5	1.4	2105.12	28.0	1.2	2145.64	19.6	1.0
2065.61	30.0	1.5	2106.13	27.0	1.2	2146.65	17.5	1.0
2066.62	28.4	1.4	2107.14	25.3	1.2	2147.66	16.7	0.9
2067.64	29.0	1.4	2108.16	25.3	1.2	2148.68	17.4	1.0
2068.65	29.1	1.4	2109.17	24.2	1.2	2149.69	16.0	0.9
2069.66	28.6	1.4	2110.18	26.3	1.2	2150.70	16.0	0.9
2070.67	31.2	1.5	2111.19	28.4	1.3	2151.71	16.5	0.9
2071.69	29.2	1.4	2112.21	24.4	1.1	2152.73	16.0	0.9
2072.70	28.9	1.4	2113.22	24.4	1.2	2153.74	14.7	0.9
2073.71	27.1	1.3	2114.23	25.0	1.2	2154.75	14.0	0.9
2074.73	30.8	1.4	2115.25	24.5	1.1	2155.77	14.8	0.9
2075.74	28.6	1.3	2116.26	23.2	1.1	2156.78	15.2	0.9
2076.75	30.0	1.4	2117.27	24.9	1.2	2157.79	13.6	0.9
2077.77	28.1	1.3	2118.29	25.3	1.2	2158.81	14.1	0.9
2078.78	28.5	1.3	2119.30	26.2	1.2	2159.82	12.7	0.8
2079.79	28.2	1.3	2120.31	26.3	1.2	2160.83	13.5	0.9
2080.80	28.0	1.3	2121.32	25.0	1.2	2161.84	12.9	0.9
2081.82	28.9	1.3	2122.34	23.7	1.1	2162.86	11.5	0.8
2082.83	29.4	1.3	2123.35	25.4	1.2	2163.87	11.5	0.8
2083.84	25.5	1.2	2124.36	24.2	1.1	2164.88	11.1	0.8
2084.86	28.1	1.3	2125.38	25.9	1.2	2165.90	10.5	0.8
2085.87	28.7	1.3	2126.39	23.3	1.1	2166.91	10.6	0.8
2086.88	26.6	1.2	2127.40	25.0	1.2	2167.92	8.1	0.7
2087.90	30.2	1.4	2128.42	23.3	1.1	2168.94	9.6	0.8
2088.91	26.7	1.2	2129.43	27.8	1.3	2169.95	6.6	0.6
2089.92	28.9	1.3	2130.44	24.7	1.2	2170.96	7.5	0.7
2090.93	27.8	1.3	2131.45	22.9	1.1	2171.97	4.9	0.6
2091.95	25.3	1.2	2132.47	20.9	1.1	2172.99	5.2	0.6
2092.96	27.2	1.2	2133.48	21.9	1.1	2174.00	3.5	0.5
2093.97	26.1	1.2	2134.49	22.5	1.1	2175.01	0.7	0.3

Table B.5.: $p\Lambda$ invariant mass distribution for $0 < \cos\theta_{pK}^{p\Lambda} < 0.5$.

$m_{p\Lambda}\left[\frac{\mathrm{MeV}}{c^2}\right]$	$\frac{\mathrm{d}\sigma}{\mathrm{d}m}\left[\frac{\mathrm{nb}\,c^2}{\mathrm{MeV}}\right]$	Δ	$m_{p\Lambda}\left[\frac{\mathrm{MeV}}{c^2}\right]$	$\frac{\mathrm{d}\sigma}{\mathrm{d}m}\left[\frac{\mathrm{nb}\,c^2}{\mathrm{MeV}}\right]$	Δ	$m_{p\Lambda}\left[\frac{\mathrm{MeV}}{c^2}\right]$	$\frac{\mathrm{d}\sigma}{\mathrm{d}m}\left[\frac{\mathrm{nb}\,c^2}{\mathrm{MeV}}\right]$	Δ
2054.47	14.0	1.5	2094.99	28.6	1.3	2135.51	20.3	1.0
2055.48	20.6	1.6	2096.00	26.2	1.2	2136.52	21.0	1.1
2056.49	23.5	1.6	2097.01	30.1	1.3	2137.53	20.4	1.0
2057.51	24.7	1.6	2098.03	26.7	1.2	2138.55	20.6	1.1
2058.52	31.0	1.8	2099.04	28.0	1.3	2139.56	21.0	1.1
2059.53	28.4	1.6	2100.05	27.7	1.2	2140.57	20.9	1.1
2060.54	31.4	1.7	2101.06	24.8	1.2	2141.58	19.4	1.0
2061.56	30.9	1.6	2102.08	24.0	1.1	2142.60	19.8	1.0
2062.57	30.0	1.5	2103.09	26.3	1.2	2143.61	18.6	1.0
2063.58	31.6	1.6	2104.10	27.1	1.2	2144.62	19.0	1.0
2064.60	29.1	1.5	2105.12	25.6	1.2	2145.64	19.6	1.0
2065.61	31.5	1.5	2106.13	25.7	1.2	2146.65	20.0	1.0
2066.62	29.2	1.4	2107.14	27.0	1.2	2147.66	16.6	0.9
2067.64	27.4	1.4	2108.16	26.6	1.2	2148.68	16.9	1.0
2068.65	32.5	1.5	2109.17	26.1	1.2	2149.69	19.7	1.1
2069.66	28.6	1.4	2110.18	25.0	1.2	2150.70	16.6	1.0
2070.67	33.9	1.6	2111.19	23.7	1.1	2151.71	16.5	1.0
2071.69	30.6	1.4	2112.21	23.8	1.1	2152.73	16.0	0.9
2072.70	28.6	1.3	2113.22	23.7	1.1	2153.74	16.2	1.0
2073.71	28.9	1.3	2114.23	24.9	1.1	2154.75	17.1	1.0
2074.73	29.4	1.3	2115.25	25.6	1.2	2155.77	15.6	0.9
2075.74	29.9	1.4	2116.26	23.0	1.1	2156.78	16.7	1.0
2076.75	30.5	1.4	2117.27	25.2	1.2	2157.79	14.8	0.9
2077.77	29.2	1.3	2118.29	25.0	1.2	2158.81	13.8	0.9
2078.78	28.6	1.3	2119.30	23.0	1.1	2159.82	14.4	0.9
2079.79	29.3	1.3	2120.31	22.6	1.1	2160.83	13.2	0.9
2080.80	31.2	1.4	2121.32	25.3	1.2	2161.84	12.5	0.8
2081.82	31.1	1.4	2122.34	22.4	1.1	2162.86	10.6	0.8
2082.83	30.0	1.3	2123.35	24.3	1.1	2163.87	10.7	0.8
2083.84	28.9	1.3	2124.36	26.3	1.2	2164.88	11.6	0.8
2084.86	27.4	1.3	2125.38	24.3	1.1	2165.90	10.5	0.8
2085.87	29.3	1.3	2126.39	24.8	1.2	2166.91	10.8	0.8
2086.88	27.8	1.2	2127.40	24.6	1.2	2167.92	9.6	0.8
2087.90	30.8	1.4	2128.42	26.1	1.2	2168.94	8.8	0.7
2088.91	28.5	1.3	2129.43	23.6	1.1	2169.95	7.8	0.7
2089.92	28.1	1.3	2130.44	23.7	1.1	2170.96	6.5	0.6
2090.93	27.7	1.3	2131.45	23.5	1.1	2171.97	4.5	0.5
2091.95	27.2	1.2	2132.47	21.3	1.0	2172.99	3.9	0.5
2092.96	30.6	1.3	2133.48	21.5	1.1	2174.00	4.0	0.5
2093.97	27.7	1.3	2134.49	23.4	1.1	2175.01	0.6	0.3

Table B.6.: $p\Lambda$ invariant mass distribution for $-0.5 < \cos\theta_{pK}^{p\Lambda} < 0$.

$m_{p\Lambda}\left[\frac{\mathrm{MeV}}{c^2}\right]$	$\frac{\mathrm{d}\sigma}{\mathrm{d}m}\left[\frac{\mathrm{nb}\,c^2}{\mathrm{MeV}}\right]$	Δ	$m_{p\Lambda}\left[\frac{\mathrm{MeV}}{c^2}\right]$	$\frac{\mathrm{d}\sigma}{\mathrm{d}m}\left[\frac{\mathrm{nb}\,c^2}{\mathrm{MeV}}\right]$	Δ	$m_{p\Lambda}\left[\frac{\mathrm{MeV}}{c^2}\right]$	$\frac{\mathrm{d}\sigma}{\mathrm{d}m}\left[\frac{\mathrm{nb}\,c^2}{\mathrm{MeV}}\right]$	Δ
2054.47	9.8	1.2	2094.99	24.3	1.2	2135.51	18.3	1.0
2055.48	18.8	1.5	2096.00	21.4	1.1	2136.52	19.7	1.0
2056.49	22.4	1.5	2097.01	23.1	1.1	2137.53	19.4	1.0
2057.51	22.7	1.4	2098.03	24.1	1.2	2138.55	17.8	1.0
2058.52	26.5	1.5	2099.04	24.0	1.2	2139.56	21.0	1.1
2059.53	26.0	1.4	2100.05	21.6	1.1	2140.57	19.6	1.0
2060.54	30.4	1.6	2101.06	21.7	1.1	2141.58	18.9	1.0
2061.56	29.2	1.5	2102.08	22.7	1.1	2142.60	19.0	1.0
2062.57	24.1	1.3	2103.09	22.4	1.1	2143.61	19.8	1.0
2063.58	29.1	1.5	2104.10	23.6	1.1	2144.62	20.0	1.1
2064.60	26.2	1.4	2105.12	21.3	1.1	2145.64	19.0	1.0
2065.61	27.5	1.4	2106.13	20.0	1.0	2146.65	17.7	1.0
2066.62	27.2	1.4	2107.14	22.3	1.1	2147.66	17.4	1.0
2067.64	26.3	1.3	2108.16	23.2	1.1	2148.68	16.2	0.9
2068.65	25.2	1.3	2109.17	21.7	1.1	2149.69	18.0	1.0
2069.66	27.9	1.4	2110.18	21.1	1.0	2150.70	17.4	1.0
2070.67	24.6	1.3	2111.19	22.2	1.1	2151.71	16.0	1.0
2071.69	24.8	1.3	2112.21	20.2	1.0	2152.73	16.5	1.0
2072.70	22.0	1.1	2113.22	20.4	1.0	2153.74	14.6	0.9
2073.71	25.1	1.2	2114.23	21.4	1.0	2154.75	15.2	0.9
2074.73	23.7	1.2	2115.25	20.9	1.0	2155.77	15.2	0.9
2075.74	26.0	1.3	2116.26	22.4	1.1	2156.78	13.9	0.9
2076.75	23.1	1.2	2117.27	19.3	1.0	2157.79	15.8	1.0
2077.77	24.0	1.2	2118.29	21.7	1.1	2158.81	15.3	1.0
2078.78	24.8	1.2	2119.30	20.9	1.0	2159.82	13.5	0.9
2079.79	22.8	1.2	2120.31	19.5	1.0	2160.83	13.1	0.9
2080.80	24.6	1.2	2121.32	20.6	1.0	2161.84	11.7	0.8
2081.82	26.7	1.3	2122.34	23.4	1.1	2162.86	10.8	0.8
2082.83	23.5	1.2	2123.35	21.7	1.1	2163.87	10.1	0.8
2083.84	22.0	1.1	2124.36	22.1	1.1	2164.88	12.7	0.9
2084.86	22.5	1.1	2125.38	20.8	1.0	2165.90	10.0	0.8
2085.87	23.1	1.2	2126.39	20.7	1.0	2166.91	8.9	0.7
2086.88	22.6	1.1	2127.40	23.4	1.1	2167.92	9.0	0.8
2087.90	24.8	1.2	2128.42	20.8	1.0	2168.94	8.1	0.7
2088.91	22.7	1.1	2129.43	21.9	1.1	2169.95	8.9	0.8
2089.92	22.9	1.1	2130.44	22.7	1.1	2170.96	6.2	0.6
2090.93	24.8	1.2	2131.45	20.8	1.1	2171.97	5.4	0.6
2091.95	24.1	1.2	2132.47	20.0	1.0	2172.99	4.9	0.6
2092.96	22.7	1.1	2133.48	19.6	1.0	2174.00	2.9	0.4
2093.97	22.1	1.1	2134.49	21.3	1.1	2175.01	1.2	0.4

Table B.7.: $p\Lambda$ invariant mass distribution for $\cos\theta_{pK}^{p\Lambda} < -0.5$.

B.4. Data Tables for the Angular Distributions

$\cos\theta_K^{\mathrm{CMS}}$	$\frac{d\sigma}{d\Omega}\left[\frac{\mu b}{sr}\right]$	$\Delta\left[\frac{\mu b}{sr}\right]$	$\cos\theta_K^{\mathrm{CMS}}$	$\frac{d\sigma}{d\Omega}\left[\frac{\mu b}{sr}\right]$	$\Delta\left[\frac{\mu b}{sr}\right]$	$\cos\theta_K^{\mathrm{CMS}}$	$\frac{d\sigma}{d\Omega}\left[\frac{\mu b}{sr}\right]$	$\Delta\left[\frac{\mu b}{sr}\right]$
-0.99	0.796	0.028	-0.33	0.817	0.019	0.33	0.778	0.018
-0.97	0.746	0.024	-0.31	0.781	0.018	0.35	0.787	0.018
-0.95	0.728	0.023	-0.29	0.804	0.019	0.37	0.786	0.018
-0.93	0.759	0.022	-0.27	0.798	0.019	0.39	0.785	0.018
-0.91	0.769	0.022	-0.25	0.789	0.018	0.41	0.803	0.019
-0.89	0.739	0.021	-0.23	0.776	0.018	0.43	0.777	0.018
-0.87	0.791	0.021	-0.21	0.797	0.019	0.45	0.830	0.019
-0.85	0.782	0.021	-0.19	0.801	0.019	0.47	0.818	0.019
-0.83	0.777	0.021	-0.17	0.774	0.018	0.49	0.820	0.019
-0.81	0.789	0.021	-0.15	0.833	0.019	0.51	0.825	0.019
-0.79	0.799	0.021	-0.13	0.822	0.019	0.53	0.814	0.019
-0.77	0.749	0.020	-0.11	0.800	0.018	0.55	0.850	0.020
-0.75	0.807	0.020	-0.09	0.794	0.018	0.57	0.837	0.020
-0.73	0.806	0.020	-0.07	0.785	0.018	0.59	0.811	0.019
-0.71	0.762	0.019	-0.05	0.797	0.018	0.61	0.853	0.020
-0.69	0.786	0.020	-0.03	0.783	0.018	0.63	0.854	0.020
-0.67	0.769	0.020	-0.01	0.824	0.019	0.65	0.852	0.020
-0.65	0.782	0.019	0.01	0.801	0.018	0.67	0.836	0.020
-0.63	0.812	0.020	0.03	0.812	0.018	0.69	0.830	0.020
-0.61	0.821	0.020	0.05	0.755	0.018	0.71	0.862	0.020
-0.59	0.791	0.019	0.07	0.799	0.018	0.73	0.833	0.020
-0.57	0.791	0.019	0.09	0.798	0.018	0.75	0.896	0.021
-0.55	0.779	0.019	0.11	0.776	0.018	0.77	0.870	0.021
-0.53	0.795	0.019	0.13	0.801	0.018	0.79	0.861	0.021
-0.51	0.825	0.019	0.15	0.788	0.018	0.81	0.801	0.020
-0.49	0.816	0.019	0.17	0.781	0.018	0.83	0.874	0.021
-0.47	0.807	0.019	0.19	0.783	0.018	0.85	0.858	0.021
-0.45	0.825	0.019	0.21	0.790	0.018	0.87	0.833	0.021
-0.43	0.822	0.019	0.23	0.813	0.018	0.89	0.844	0.021
-0.41	0.811	0.019	0.25	0.753	0.017	0.91	0.763	0.020
-0.39	0.782	0.018	0.27	0.784	0.018	0.93	0.767	0.020
-0.37	0.795	0.019	0.29	0.835	0.019	0.95	0.752	0.020
-0.35	0.787	0.019	0.31	0.788	0.018	0.97	0.687	0.020
						0.99	0.301	0.015

Table B.8.: Kaon CMS distribution.

$\cos\theta_{\Lambda}^{\mathrm{CMS}}$	$\frac{\mathrm{d}\sigma}{\mathrm{d}\Omega}\left[\frac{\mu\mathrm{b}}{\mathrm{sr}}\right]$	$\Delta\left[\frac{\mu\mathrm{b}}{\mathrm{sr}}\right]$	$\cos\theta_{\Lambda}^{\mathrm{CMS}}$	$\frac{\mathrm{d}\sigma}{\mathrm{d}\Omega}\left[\frac{\mu\mathrm{b}}{\mathrm{sr}}\right]$	$\Delta\left[\frac{\mu\mathrm{b}}{\mathrm{sr}}\right]$	$\cos\theta_{\Lambda}^{\mathrm{CMS}}$	$\frac{\mathrm{d}\sigma}{\mathrm{d}\Omega}\left[\frac{\mu\mathrm{b}}{\mathrm{sr}}\right]$	$\Delta\left[\frac{\mu\mathrm{b}}{\mathrm{sr}}\right]$
-0.99	0.903	0.026	-0.33	0.741	0.018	0.33	0.729	0.017
-0.97	0.898	0.026	-0.31	0.756	0.018	0.35	0.752	0.017
-0.95	0.888	0.025	-0.29	0.757	0.018	0.37	0.729	0.017
-0.93	0.865	0.024	-0.27	0.756	0.018	0.39	0.739	0.017
-0.91	0.878	0.024	-0.25	0.707	0.017	0.41	0.748	0.018
-0.89	0.883	0.023	-0.23	0.740	0.018	0.43	0.777	0.018
-0.87	0.923	0.024	-0.21	0.705	0.017	0.45	0.764	0.018
-0.85	0.865	0.023	-0.19	0.719	0.017	0.47	0.750	0.018
-0.83	0.922	0.023	-0.17	0.716	0.017	0.49	0.779	0.018
-0.81	0.900	0.023	-0.15	0.702	0.017	0.51	0.774	0.018
-0.79	0.930	0.023	-0.13	0.701	0.017	0.53	0.794	0.019
-0.77	0.924	0.023	-0.11	0.668	0.016	0.55	0.815	0.019
-0.75	0.925	0.022	-0.09	0.711	0.017	0.57	0.810	0.019
-0.73	0.896	0.022	-0.07	0.690	0.017	0.59	0.812	0.019
-0.71	0.912	0.022	-0.05	0.691	0.017	0.61	0.846	0.019
-0.69	0.864	0.021	-0.03	0.713	0.017	0.63	0.801	0.019
-0.67	0.896	0.022	-0.01	0.659	0.016	0.65	0.836	0.019
-0.65	0.857	0.021	0.01	0.705	0.017	0.67	0.820	0.019
-0.63	0.871	0.021	0.03	0.727	0.017	0.69	0.907	0.021
-0.61	0.878	0.021	0.05	0.690	0.017	0.71	0.875	0.020
-0.59	0.856	0.021	0.07	0.687	0.017	0.73	0.871	0.020
-0.57	0.864	0.020	0.09	0.674	0.016	0.75	0.860	0.020
-0.55	0.872	0.021	0.11	0.696	0.017	0.77	0.859	0.020
-0.53	0.844	0.020	0.13	0.703	0.017	0.79	0.892	0.021
-0.51	0.827	0.020	0.15	0.693	0.017	0.81	0.845	0.020
-0.49	0.828	0.020	0.17	0.695	0.017	0.83	0.879	0.021
-0.47	0.831	0.020	0.19	0.697	0.017	0.85	0.848	0.020
-0.45	0.820	0.019	0.21	0.738	0.017	0.87	0.888	0.021
-0.43	0.761	0.018	0.23	0.722	0.017	0.89	0.874	0.021
-0.41	0.782	0.019	0.25	0.718	0.017	0.91	0.870	0.022
-0.39	0.802	0.019	0.27	0.692	0.017	0.93	0.810	0.021
-0.37	0.784	0.019	0.29	0.734	0.017	0.95	0.797	0.021
-0.35	0.779	0.019	0.31	0.721	0.017	0.97	0.774	0.021
						0.99	0.706	0.020

Table B.9.: Λ CMS distribution.

$\cos\theta_p^{\mathrm{CMS}}$	$\frac{\mathrm{d}\sigma}{\mathrm{d}\Omega}\left[\frac{\mu\mathrm{b}}{\mathrm{sr}}\right]$	$\Delta\left[\frac{\mu\mathrm{b}}{\mathrm{sr}}\right]$	$\cos\theta_p^{\mathrm{CMS}}$	$\frac{\mathrm{d}\sigma}{\mathrm{d}\Omega}\left[\frac{\mu\mathrm{b}}{\mathrm{sr}}\right]$	$\Delta\left[\frac{\mu\mathrm{b}}{\mathrm{sr}}\right]$	$\cos\theta_p^{\mathrm{CMS}}$	$\frac{\mathrm{d}\sigma}{\mathrm{d}\Omega}\left[\frac{\mu\mathrm{b}}{\mathrm{sr}}\right]$	$\Delta\left[\frac{\mu\mathrm{b}}{\mathrm{sr}}\right]$
-0.99	0.807	0.024	-0.33	0.647	0.016	0.33	0.711	0.018
-0.97	1.048	0.024	-0.31	0.694	0.017	0.35	0.682	0.017
-0.95	1.144	0.025	-0.29	0.663	0.016	0.37	0.673	0.017
-0.93	1.123	0.024	-0.27	0.679	0.016	0.39	0.693	0.018
-0.91	1.120	0.024	-0.25	0.649	0.016	0.41	0.659	0.017
-0.89	1.095	0.023	-0.23	0.620	0.016	0.43	0.712	0.018
-0.87	1.104	0.023	-0.21	0.628	0.016	0.45	0.702	0.018
-0.85	1.066	0.023	-0.19	0.615	0.016	0.47	0.732	0.018
-0.83	1.063	0.022	-0.17	0.633	0.016	0.49	0.720	0.019
-0.81	0.978	0.021	-0.15	0.633	0.016	0.51	0.777	0.019
-0.79	0.984	0.021	-0.13	0.609	0.015	0.53	0.759	0.019
-0.77	0.963	0.021	-0.11	0.625	0.016	0.55	0.783	0.020
-0.75	0.921	0.020	-0.09	0.603	0.015	0.57	0.805	0.020
-0.73	0.902	0.020	-0.07	0.595	0.015	0.59	0.803	0.020
-0.71	0.920	0.020	-0.05	0.633	0.016	0.61	0.843	0.021
-0.69	0.850	0.019	-0.03	0.620	0.016	0.63	0.822	0.020
-0.67	0.832	0.019	-0.01	0.623	0.016	0.65	0.865	0.021
-0.65	0.836	0.019	0.01	0.626	0.016	0.67	0.899	0.022
-0.63	0.844	0.019	0.03	0.615	0.016	0.69	0.915	0.022
-0.61	0.790	0.018	0.05	0.650	0.016	0.71	0.946	0.023
-0.59	0.801	0.018	0.07	0.623	0.016	0.73	0.953	0.023
-0.57	0.799	0.018	0.09	0.645	0.016	0.75	0.993	0.024
-0.55	0.746	0.017	0.11	0.650	0.017	0.77	1.050	0.025
-0.53	0.739	0.017	0.13	0.616	0.016	0.79	1.006	0.024
-0.51	0.725	0.017	0.15	0.632	0.016	0.81	1.060	0.025
-0.49	0.746	0.017	0.17	0.639	0.017	0.83	1.125	0.026
-0.47	0.700	0.017	0.19	0.632	0.016	0.85	1.069	0.026
-0.45	0.733	0.017	0.21	0.644	0.017	0.87	1.180	0.028
-0.43	0.731	0.017	0.23	0.618	0.016	0.89	1.180	0.028
-0.41	0.704	0.017	0.25	0.670	0.017	0.91	1.240	0.029
-0.39	0.696	0.016	0.27	0.661	0.017	0.93	1.189	0.028
-0.37	0.687	0.016	0.29	0.656	0.017	0.95	1.153	0.028
-0.35	0.685	0.016	0.31	0.654	0.017	0.97	0.819	0.024
						0.99	0.177	0.017

Table B.10.: Proton CMS distribution.

$\cos\theta_p^{p\Lambda}$	$\frac{\mathrm{d}\sigma}{\mathrm{d}\Omega}\left[\frac{\mu\mathrm{b}}{\mathrm{sr}}\right]$	$\Delta\left[\frac{\mu\mathrm{b}}{\mathrm{sr}}\right]$	$\cos\theta_p^{p\Lambda}$	$\frac{\mathrm{d}\sigma}{\mathrm{d}\Omega}\left[\frac{\mu\mathrm{b}}{\mathrm{sr}}\right]$	$\Delta\left[\frac{\mu\mathrm{b}}{\mathrm{sr}}\right]$	$\cos\theta_p^{p\Lambda}$	$\frac{\mathrm{d}\sigma}{\mathrm{d}\Omega}\left[\frac{\mu\mathrm{b}}{\mathrm{sr}}\right]$	$\Delta\left[\frac{\mu\mathrm{b}}{\mathrm{sr}}\right]$
-0.99	1.046	0.026	-0.33	0.665	0.016	0.33	0.691	0.017
-0.97	1.033	0.025	-0.31	0.641	0.016	0.35	0.668	0.017
-0.95	1.042	0.024	-0.29	0.672	0.016	0.37	0.683	0.017
-0.93	1.007	0.023	-0.27	0.653	0.016	0.39	0.731	0.018
-0.91	1.009	0.023	-0.25	0.656	0.016	0.41	0.703	0.018
-0.89	1.055	0.023	-0.23	0.653	0.016	0.43	0.702	0.018
-0.87	1.013	0.022	-0.21	0.634	0.016	0.45	0.760	0.019
-0.85	0.987	0.022	-0.19	0.639	0.016	0.47	0.753	0.019
-0.83	0.976	0.021	-0.17	0.647	0.016	0.49	0.766	0.019
-0.81	0.954	0.021	-0.15	0.609	0.015	0.51	0.756	0.019
-0.79	0.930	0.021	-0.13	0.620	0.016	0.53	0.775	0.019
-0.77	0.925	0.020	-0.11	0.600	0.015	0.55	0.749	0.019
-0.75	0.921	0.020	-0.09	0.619	0.016	0.57	0.811	0.020
-0.73	0.904	0.020	-0.07	0.630	0.016	0.59	0.801	0.020
-0.71	0.862	0.019	-0.05	0.582	0.015	0.61	0.823	0.020
-0.69	0.873	0.020	-0.03	0.603	0.015	0.63	0.842	0.021
-0.67	0.863	0.019	-0.01	0.637	0.016	0.65	0.883	0.021
-0.65	0.850	0.019	0.01	0.589	0.015	0.67	0.906	0.022
-0.63	0.814	0.018	0.03	0.610	0.016	0.69	0.922	0.022
-0.61	0.816	0.019	0.05	0.602	0.016	0.71	0.929	0.022
-0.59	0.781	0.018	0.07	0.622	0.016	0.73	0.947	0.023
-0.57	0.803	0.018	0.09	0.633	0.016	0.75	0.976	0.023
-0.55	0.763	0.018	0.11	0.612	0.016	0.77	0.988	0.024
-0.53	0.762	0.018	0.13	0.635	0.016	0.79	1.048	0.025
-0.51	0.734	0.017	0.15	0.583	0.015	0.81	0.995	0.024
-0.49	0.730	0.017	0.17	0.636	0.016	0.83	1.077	0.026
-0.47	0.744	0.017	0.19	0.619	0.016	0.85	1.118	0.027
-0.45	0.703	0.017	0.21	0.650	0.016	0.87	1.113	0.027
-0.43	0.698	0.017	0.23	0.670	0.017	0.89	1.122	0.028
-0.41	0.691	0.017	0.25	0.645	0.016	0.91	1.132	0.028
-0.39	0.685	0.016	0.27	0.640	0.017	0.93	1.101	0.028
-0.37	0.684	0.017	0.29	0.655	0.017	0.95	1.118	0.030
-0.35	0.666	0.016	0.31	0.645	0.017	0.97	1.103	0.031
						0.99	0.955	0.030

Table B.11.: Proton Jackson angle in the $p\Lambda$ rest frame.

$\cos\theta_K^{K\Lambda}$	$\frac{\mathrm{d}\sigma}{\mathrm{d}\Omega}\left[\frac{\mu\mathrm{b}}{\mathrm{sr}}\right]$	$\Delta\left[\frac{\mu\mathrm{b}}{\mathrm{sr}}\right]$	$\cos\theta_K^{K\Lambda}$	$\frac{\mathrm{d}\sigma}{\mathrm{d}\Omega}\left[\frac{\mu\mathrm{b}}{\mathrm{sr}}\right]$	$\Delta\left[\frac{\mu\mathrm{b}}{\mathrm{sr}}\right]$	$\cos\theta_K^{K\Lambda}$	$\frac{\mathrm{d}\sigma}{\mathrm{d}\Omega}\left[\frac{\mu\mathrm{b}}{\mathrm{sr}}\right]$	$\Delta\left[\frac{\mu\mathrm{b}}{\mathrm{sr}}\right]$
-0.99	0.679	0.021	-0.33	0.846	0.019	0.33	0.794	0.019
-0.97	0.670	0.021	-0.31	0.868	0.020	0.35	0.817	0.019
-0.95	0.709	0.021	-0.29	0.859	0.019	0.37	0.805	0.019
-0.93	0.658	0.020	-0.27	0.852	0.019	0.39	0.784	0.019
-0.91	0.709	0.021	-0.25	0.881	0.020	0.41	0.812	0.019
-0.89	0.703	0.020	-0.23	0.869	0.019	0.43	0.809	0.019
-0.87	0.704	0.020	-0.21	0.856	0.019	0.45	0.822	0.019
-0.85	0.740	0.020	-0.19	0.844	0.019	0.47	0.786	0.019
-0.83	0.726	0.020	-0.17	0.826	0.019	0.49	0.800	0.019
-0.81	0.791	0.021	-0.15	0.872	0.019	0.51	0.808	0.019
-0.79	0.758	0.020	-0.13	0.856	0.019	0.53	0.812	0.019
-0.77	0.817	0.021	-0.11	0.845	0.019	0.55	0.813	0.019
-0.75	0.767	0.020	-0.09	0.841	0.019	0.57	0.815	0.019
-0.73	0.781	0.020	-0.07	0.805	0.018	0.59	0.761	0.019
-0.71	0.791	0.020	-0.05	0.872	0.019	0.61	0.767	0.019
-0.69	0.778	0.019	-0.03	0.854	0.019	0.63	0.825	0.020
-0.67	0.792	0.019	-0.01	0.823	0.019	0.65	0.830	0.020
-0.65	0.810	0.020	0.01	0.836	0.019	0.67	0.820	0.020
-0.63	0.837	0.020	0.03	0.815	0.018	0.69	0.766	0.019
-0.61	0.820	0.020	0.05	0.850	0.019	0.71	0.789	0.020
-0.59	0.850	0.020	0.07	0.872	0.019	0.73	0.819	0.020
-0.57	0.811	0.019	0.09	0.844	0.019	0.75	0.771	0.020
-0.55	0.839	0.020	0.11	0.792	0.019	0.77	0.752	0.020
-0.53	0.824	0.019	0.13	0.818	0.018	0.79	0.787	0.020
-0.51	0.859	0.020	0.15	0.844	0.019	0.81	0.750	0.020
-0.49	0.817	0.019	0.17	0.861	0.019	0.83	0.720	0.019
-0.47	0.806	0.019	0.19	0.810	0.020	0.85	0.727	0.020
-0.45	0.830	0.019	0.21	0.798	0.019	0.87	0.714	0.020
-0.43	0.840	0.019	0.23	0.805	0.019	0.89	0.715	0.020
-0.41	0.848	0.019	0.25	0.799	0.019	0.91	0.697	0.020
-0.39	0.851	0.019	0.27	0.830	0.019	0.93	0.644	0.019
-0.37	0.831	0.019	0.29	0.799	0.019	0.95	0.691	0.021
-0.35	0.876	0.020	0.31	0.830	0.019	0.97	0.626	0.020
						0.99	0.540	0.019

Table B.12.: Kaon Jackson angle in the $K\Lambda$ rest frame.

$\cos\theta_K^{Kp}$	$\frac{\mathrm{d}\sigma}{\mathrm{d}\Omega}\left[\frac{\mu\mathrm{b}}{\mathrm{sr}}\right]$	$\Delta\left[\frac{\mu\mathrm{b}}{\mathrm{sr}}\right]$	$\cos\theta_K^{Kp}$	$\frac{\mathrm{d}\sigma}{\mathrm{d}\Omega}\left[\frac{\mu\mathrm{b}}{\mathrm{sr}}\right]$	$\Delta\left[\frac{\mu\mathrm{b}}{\mathrm{sr}}\right]$	$\cos\theta_K^{Kp}$	$\frac{\mathrm{d}\sigma}{\mathrm{d}\Omega}\left[\frac{\mu\mathrm{b}}{\mathrm{sr}}\right]$	$\Delta\left[\frac{\mu\mathrm{b}}{\mathrm{sr}}\right]$
-0.99	0.874	0.023	-0.33	0.794	0.019	0.33	0.677	0.016
-0.97	0.946	0.025	-0.31	0.761	0.018	0.35	0.681	0.016
-0.95	0.900	0.024	-0.29	0.753	0.018	0.37	0.714	0.017
-0.93	0.925	0.025	-0.27	0.750	0.018	0.39	0.696	0.017
-0.91	0.927	0.024	-0.25	0.765	0.018	0.41	0.695	0.017
-0.89	0.957	0.025	-0.23	0.780	0.019	0.43	0.713	0.017
-0.87	0.961	0.025	-0.21	0.764	0.018	0.45	0.720	0.017
-0.85	0.977	0.025	-0.19	0.743	0.018	0.47	0.744	0.018
-0.83	0.951	0.024	-0.17	0.750	0.018	0.49	0.756	0.018
-0.81	0.966	0.024	-0.15	0.701	0.017	0.51	0.738	0.017
-0.79	0.941	0.023	-0.13	0.701	0.017	0.53	0.761	0.018
-0.77	0.951	0.023	-0.11	0.705	0.017	0.55	0.752	0.018
-0.75	0.917	0.023	-0.09	0.723	0.017	0.57	0.777	0.018
-0.73	0.929	0.023	-0.07	0.762	0.018	0.59	0.766	0.018
-0.71	0.898	0.022	-0.05	0.700	0.017	0.61	0.787	0.018
-0.69	0.898	0.022	-0.03	0.705	0.017	0.63	0.812	0.019
-0.67	0.914	0.022	-0.01	0.691	0.017	0.65	0.841	0.019
-0.65	0.890	0.021	0.01	0.673	0.017	0.67	0.832	0.019
-0.63	0.885	0.021	0.03	0.729	0.017	0.69	0.866	0.020
-0.61	0.911	0.022	0.05	0.703	0.017	0.71	0.860	0.020
-0.59	0.866	0.021	0.07	0.697	0.017	0.73	0.899	0.020
-0.57	0.861	0.021	0.09	0.681	0.017	0.75	0.866	0.020
-0.55	0.825	0.020	0.11	0.712	0.017	0.77	0.873	0.020
-0.53	0.842	0.020	0.13	0.678	0.017	0.79	0.874	0.020
-0.51	0.802	0.019	0.15	0.694	0.017	0.81	0.881	0.020
-0.49	0.826	0.020	0.17	0.677	0.017	0.83	0.850	0.020
-0.47	0.834	0.020	0.19	0.713	0.017	0.85	0.872	0.021
-0.45	0.803	0.019	0.21	0.710	0.017	0.87	0.841	0.020
-0.43	0.822	0.020	0.23	0.687	0.017	0.89	0.848	0.021
-0.41	0.779	0.019	0.25	0.688	0.017	0.91	0.845	0.021
-0.39	0.790	0.019	0.27	0.688	0.017	0.93	0.816	0.021
-0.37	0.768	0.019	0.29	0.714	0.017	0.95	0.755	0.020
-0.35	0.780	0.019	0.31	0.684	0.017	0.97	0.740	0.020
						0.99	0.639	0.019

Table B.13.: Kaon Jackson angle in the Kp rest frame.

$\cos\theta^{p\Lambda}_{pK}$	$\frac{d\sigma}{d\Omega}\left[\frac{\mu b}{sr}\right]$	$\Delta\left[\frac{\mu b}{sr}\right]$	$\cos\theta^{p\Lambda}_{pK}$	$\frac{d\sigma}{d\Omega}\left[\frac{\mu b}{sr}\right]$	$\Delta\left[\frac{\mu b}{sr}\right]$	$\cos\theta^{p\Lambda}_{pK}$	$\frac{d\sigma}{d\Omega}\left[\frac{\mu b}{sr}\right]$	$\Delta\left[\frac{\mu b}{sr}\right]$
-0.99	0.731	0.020	-0.33	0.853	0.020	0.33	0.830	0.019
-0.97	0.749	0.020	-0.31	0.859	0.020	0.35	0.815	0.019
-0.95	0.775	0.020	-0.29	0.871	0.020	0.37	0.819	0.019
-0.93	0.734	0.019	-0.27	0.859	0.020	0.39	0.769	0.018
-0.91	0.730	0.019	-0.25	0.878	0.020	0.41	0.806	0.019
-0.89	0.790	0.020	-0.23	0.870	0.020	0.43	0.822	0.019
-0.87	0.778	0.019	-0.21	0.826	0.019	0.45	0.830	0.020
-0.85	0.783	0.019	-0.19	0.853	0.020	0.47	0.792	0.019
-0.83	0.767	0.019	-0.17	0.863	0.020	0.49	0.789	0.019
-0.81	0.777	0.019	-0.15	0.889	0.020	0.51	0.810	0.019
-0.79	0.794	0.019	-0.13	0.816	0.019	0.53	0.755	0.018
-0.77	0.792	0.019	-0.11	0.846	0.020	0.55	0.809	0.019
-0.75	0.791	0.019	-0.09	0.855	0.020	0.57	0.789	0.019
-0.73	0.823	0.020	-0.07	0.864	0.020	0.59	0.726	0.018
-0.71	0.798	0.019	-0.05	0.876	0.020	0.61	0.755	0.019
-0.69	0.807	0.019	-0.03	0.856	0.020	0.63	0.755	0.019
-0.67	0.785	0.019	-0.01	0.900	0.020	0.65	0.735	0.018
-0.65	0.809	0.019	0.01	0.850	0.020	0.67	0.766	0.019
-0.63	0.831	0.020	0.03	0.846	0.020	0.69	0.739	0.018
-0.61	0.850	0.020	0.05	0.862	0.020	0.71	0.731	0.018
-0.59	0.817	0.019	0.07	0.831	0.019	0.73	0.687	0.018
-0.57	0.842	0.020	0.09	0.873	0.020	0.75	0.707	0.018
-0.55	0.844	0.020	0.11	0.863	0.020	0.77	0.709	0.018
-0.53	0.846	0.020	0.13	0.870	0.020	0.79	0.726	0.018
-0.51	0.833	0.020	0.15	0.867	0.020	0.81	0.690	0.018
-0.49	0.817	0.019	0.17	0.867	0.020	0.83	0.690	0.018
-0.47	0.861	0.020	0.19	0.842	0.019	0.85	0.664	0.018
-0.45	0.824	0.019	0.21	0.874	0.020	0.87	0.682	0.018
-0.43	0.855	0.020	0.23	0.808	0.019	0.89	0.660	0.018
-0.41	0.848	0.020	0.25	0.822	0.019	0.91	0.612	0.017
-0.39	0.839	0.020	0.27	0.866	0.020	0.93	0.594	0.017
-0.37	0.860	0.020	0.29	0.859	0.020	0.95	0.603	0.018
-0.35	0.834	0.020	0.31	0.806	0.019	0.97	0.536	0.017
						0.99	0.520	0.018

Table B.14.: Proton to Kaon helicity angle in the $p\Lambda$ rest frame.

$\cos\theta_{p\Lambda}^{K\Lambda}$	$\frac{\mathrm{d}\sigma}{\mathrm{d}\Omega}\left[\frac{\mu\mathrm{b}}{\mathrm{sr}}\right]$	$\Delta\left[\frac{\mu\mathrm{b}}{\mathrm{sr}}\right]$	$\cos\theta_{p\Lambda}^{K\Lambda}$	$\frac{\mathrm{d}\sigma}{\mathrm{d}\Omega}\left[\frac{\mu\mathrm{b}}{\mathrm{sr}}\right]$	$\Delta\left[\frac{\mu\mathrm{b}}{\mathrm{sr}}\right]$	$\cos\theta_{p\Lambda}^{K\Lambda}$	$\frac{\mathrm{d}\sigma}{\mathrm{d}\Omega}\left[\frac{\mu\mathrm{b}}{\mathrm{sr}}\right]$	$\Delta\left[\frac{\mu\mathrm{b}}{\mathrm{sr}}\right]$
-0.99	0.414	0.016	-0.33	0.707	0.018	0.33	0.837	0.019
-0.97	0.454	0.015	-0.31	0.706	0.018	0.35	0.902	0.020
-0.95	0.479	0.016	-0.29	0.724	0.018	0.37	0.883	0.020
-0.93	0.486	0.015	-0.27	0.728	0.018	0.39	0.867	0.020
-0.91	0.512	0.016	-0.25	0.717	0.018	0.41	0.911	0.021
-0.89	0.541	0.016	-0.23	0.746	0.018	0.43	0.883	0.020
-0.87	0.521	0.015	-0.21	0.741	0.018	0.45	0.919	0.021
-0.85	0.548	0.016	-0.19	0.739	0.018	0.47	0.881	0.020
-0.83	0.564	0.016	-0.17	0.761	0.018	0.49	0.894	0.020
-0.81	0.581	0.016	-0.15	0.725	0.018	0.51	0.916	0.021
-0.79	0.566	0.016	-0.13	0.748	0.018	0.53	0.915	0.021
-0.77	0.588	0.016	-0.11	0.717	0.018	0.55	0.921	0.021
-0.75	0.568	0.016	-0.09	0.772	0.018	0.57	0.953	0.021
-0.73	0.581	0.016	-0.07	0.764	0.018	0.59	0.944	0.021
-0.71	0.609	0.016	-0.05	0.735	0.018	0.61	0.970	0.022
-0.69	0.642	0.017	-0.03	0.755	0.018	0.63	0.956	0.021
-0.67	0.598	0.016	-0.01	0.816	0.019	0.65	0.973	0.022
-0.65	0.587	0.016	0.01	0.786	0.019	0.67	0.940	0.021
-0.63	0.604	0.016	0.03	0.796	0.019	0.69	1.006	0.022
-0.61	0.643	0.017	0.05	0.766	0.018	0.71	1.035	0.023
-0.59	0.655	0.017	0.07	0.751	0.018	0.73	1.029	0.023
-0.57	0.625	0.016	0.09	0.783	0.019	0.75	1.046	0.023
-0.55	0.629	0.016	0.11	0.798	0.019	0.77	1.078	0.024
-0.53	0.642	0.017	0.13	0.777	0.019	0.79	1.059	0.023
-0.51	0.651	0.017	0.15	0.794	0.019	0.81	1.091	0.024
-0.49	0.644	0.017	0.17	0.805	0.019	0.83	1.095	0.024
-0.47	0.647	0.017	0.19	0.798	0.019	0.85	1.108	0.024
-0.45	0.693	0.017	0.21	0.851	0.020	0.87	1.146	0.025
-0.43	0.690	0.017	0.23	0.817	0.019	0.89	1.173	0.026
-0.41	0.694	0.017	0.25	0.834	0.019	0.91	1.155	0.025
-0.39	0.689	0.017	0.27	0.804	0.019	0.93	1.207	0.026
-0.37	0.682	0.017	0.29	0.851	0.020	0.95	1.220	0.027
-0.35	0.700	0.017	0.31	0.831	0.019	0.97	1.272	0.027
						0.99	1.228	0.027

Table B.15.: Proton to Λ helicity angle in the $K\Lambda$ rest frame.

$\cos\theta^{pK}_{K\Lambda}$	$\frac{\mathrm{d}\sigma}{\mathrm{d}\Omega}\left[\frac{\mu\mathrm{b}}{\mathrm{sr}}\right]$	$\Delta\left[\frac{\mu\mathrm{b}}{\mathrm{sr}}\right]$	$\cos\theta^{pK}_{K\Lambda}$	$\frac{\mathrm{d}\sigma}{\mathrm{d}\Omega}\left[\frac{\mu\mathrm{b}}{\mathrm{sr}}\right]$	$\Delta\left[\frac{\mu\mathrm{b}}{\mathrm{sr}}\right]$	$\cos\theta^{pK}_{K\Lambda}$	$\frac{\mathrm{d}\sigma}{\mathrm{d}\Omega}\left[\frac{\mu\mathrm{b}}{\mathrm{sr}}\right]$	$\Delta\left[\frac{\mu\mathrm{b}}{\mathrm{sr}}\right]$
-0.99	1.244	0.032	-0.33	0.822	0.019	0.33	0.685	0.017
-0.97	1.264	0.029	-0.31	0.828	0.019	0.35	0.653	0.017
-0.95	1.257	0.028	-0.29	0.811	0.019	0.37	0.675	0.017
-0.93	1.223	0.027	-0.27	0.798	0.019	0.39	0.659	0.017
-0.91	1.217	0.027	-0.25	0.809	0.019	0.41	0.656	0.017
-0.89	1.191	0.026	-0.23	0.815	0.019	0.43	0.656	0.017
-0.87	1.186	0.026	-0.21	0.788	0.019	0.45	0.653	0.017
-0.85	1.136	0.025	-0.19	0.811	0.019	0.47	0.638	0.016
-0.83	1.142	0.025	-0.17	0.746	0.018	0.49	0.673	0.017
-0.81	1.121	0.024	-0.15	0.789	0.019	0.51	0.648	0.017
-0.79	1.036	0.023	-0.13	0.787	0.019	0.53	0.650	0.017
-0.77	1.092	0.024	-0.11	0.764	0.018	0.55	0.654	0.017
-0.75	1.011	0.023	-0.09	0.765	0.018	0.57	0.640	0.017
-0.73	1.039	0.023	-0.07	0.785	0.019	0.59	0.670	0.017
-0.71	1.002	0.022	-0.05	0.768	0.018	0.61	0.629	0.017
-0.69	0.982	0.022	-0.03	0.732	0.018	0.63	0.631	0.017
-0.67	0.941	0.021	-0.01	0.748	0.018	0.65	0.635	0.017
-0.65	0.919	0.021	0.01	0.751	0.018	0.67	0.656	0.017
-0.63	0.953	0.021	0.03	0.790	0.019	0.69	0.656	0.017
-0.61	0.933	0.021	0.05	0.740	0.018	0.71	0.614	0.016
-0.59	0.922	0.021	0.07	0.709	0.017	0.73	0.635	0.017
-0.57	0.880	0.020	0.09	0.757	0.018	0.75	0.640	0.017
-0.55	0.926	0.021	0.11	0.710	0.017	0.77	0.625	0.017
-0.53	0.893	0.020	0.13	0.708	0.017	0.79	0.628	0.017
-0.51	0.881	0.020	0.15	0.709	0.017	0.81	0.619	0.017
-0.49	0.867	0.020	0.17	0.755	0.018	0.83	0.616	0.017
-0.47	0.910	0.020	0.19	0.676	0.017	0.85	0.625	0.017
-0.45	0.839	0.019	0.21	0.690	0.017	0.87	0.613	0.017
-0.43	0.837	0.020	0.23	0.710	0.017	0.89	0.640	0.017
-0.41	0.862	0.020	0.25	0.694	0.017	0.91	0.579	0.017
-0.39	0.821	0.019	0.27	0.684	0.017	0.93	0.578	0.017
-0.37	0.831	0.019	0.29	0.685	0.017	0.95	0.594	0.018
-0.35	0.836	0.019	0.31	0.689	0.017	0.97	0.590	0.018
						0.99	0.546	0.018

Table B.16.: Kaon to Λ helicity angle in the pK rest frame.

B.5. Data Tables for the Λ Polarization

$\cos\theta_{\Lambda}^{\mathrm{CMS}}$	P_{Λ}	ΔP_{Λ}	$\cos\theta_{\Lambda}^{\mathrm{CMS}}$	P_{Λ}	ΔP_{Λ}
-0.9375	-0.110	0.031	0.0625	-0.046	0.027
-0.8125	-0.223	0.028	0.1875	0.080	0.027
-0.6875	-0.155	0.027	0.3125	0.110	0.027
-0.5625	-0.179	0.027	0.4375	0.147	0.027
-0.4375	-0.139	0.027	0.5625	0.199	0.026
-0.3125	-0.072	0.027	0.6875	0.188	0.026
-0.1875	-0.089	0.028	0.8125	0.217	0.026
-0.0625	-0.034	0.028	0.9375	0.219	0.029

Table B.17.: Λ polarization dependence on $\cos\theta_{\Lambda}^{\mathrm{CMS}}$.

x_F	P_{Λ}	ΔP_{Λ}	x_F	P_{Λ}	ΔP_{Λ}	x_F	P_{Λ}	ΔP_{Λ}
-0.9	-0.284	0.089	-0.25	-0.077	0.024	0.35	0.159	0.025
-0.75	-0.183	0.055	-0.15	-0.055	0.023	0.45	0.209	0.027
-0.65	-0.311	0.039	-0.05	-0.042	0.023	0.55	0.228	0.030
-0.55	-0.237	0.032	0.05	-0.007	0.023	0.65	0.282	0.036
-0.45	-0.178	0.028	0.15	0.064	0.023	0.75	0.292	0.046
-0.35	-0.152	0.026	0.25	0.130	0.024	0.9	0.334	0.067

Table B.18.: Λ polarization dependence on the scaling variable $x_F = \frac{p_{||}^{\mathrm{CMS}}}{p_{||\max}^{\mathrm{CMS}}}(\Lambda)$.

p_T	P_Λ	ΔP_Λ	p_T	P_Λ	ΔP_Λ	p_T	P_Λ	ΔP_Λ
20	0.001	0.051	150	0.015	0.025	270	-0.000	0.026
50	0.065	0.046	170	0.027	0.024	290	-0.007	0.027
70	0.043	0.038	190	-0.009	0.023	310	-0.006	0.030
90	-0.019	0.033	210	0.026	0.023	330	-0.008	0.034
110	0.082	0.029	230	0.011	0.024	350	0.048	0.043
130	0.022	0.026	250	-0.021	0.024	380	-0.073	0.054

Table B.19.: Λ polarization dependence on the transverse momentum $p_T(\Lambda)$ without constraint on x_F.

p_T	P_Λ	ΔP_Λ	p_T	P_Λ	ΔP_Λ
40	0.116	0.036	220	0.147	0.023
100	0.138	0.030	260	0.184	0.024
140	0.115	0.025	300	0.166	0.028
180	0.115	0.023	360	0.122	0.034

Table B.20.: Λ polarization dependence on the transverse momentum $p_T(\Lambda)$ for $x_F > 0$.

p_T	P_Λ	ΔP_Λ	p_T	P_Λ	ΔP_Λ
40	-0.034	0.036	220	-0.121	0.024
100	-0.068	0.031	260	-0.223	0.025
140	-0.084	0.026	300	-0.197	0.029
180	-0.105	0.024	360	-0.133	0.034

Table B.21.: Λ polarization dependence on the transverse momentum $p_T(\Lambda)$ for $x_F < 0$.

B.6. Data Tables for the Analyzing Power of the Final State Particles

$\cos\theta_p^{\mathrm{CMS}}$	$A_N(p)$	$\Delta A_N(p)$	$\cos\theta_p^{\mathrm{CMS}}$	$A_N(p)$	$\Delta A_N(p)$
-0.875	-0.048	0.010	0.125	-0.043	0.013
-0.625	-0.038	0.011	0.375	-0.048	0.013
-0.375	-0.044	0.012	0.625	-0.013	0.012
-0.125	-0.048	0.012	0.875	-0.006	0.012

Table B.22.: Proton analyzing power dependence on $\cos\theta_p^{\mathrm{CMS}}$.

$\cos\theta_\Lambda^{\mathrm{CMS}}$	$A_N(\Lambda)$	$\Delta A_N(\Lambda)$	$\cos\theta_\Lambda^{\mathrm{CMS}}$	$A_N(\Lambda)$	$\Delta A_N(\Lambda)$
-0.875	-0.020	0.013	0.125	-0.077	0.012
-0.625	-0.035	0.012	0.375	-0.076	0.011
-0.375	-0.062	0.012	0.625	-0.116	0.011
-0.125	-0.066	0.012	0.875	-0.094	0.012

Table B.23.: Λ analyzing power dependence on $\cos\theta_\Lambda^{\mathrm{CMS}}$.

$\cos\theta_K^{\mathrm{CMS}}$	$A_N(K)$	$\Delta A_N(K)$	$\cos\theta_K^{\mathrm{CMS}}$	$A_N(K)$	$\Delta A_N(K)$
-0.875	0.116	0.014	0.125	0.132	0.011
-0.625	0.172	0.012	0.375	0.076	0.011
-0.375	0.151	0.011	0.625	0.056	0.011
-0.125	0.186	0.011	0.875	0.023	0.013

Table B.24.: Kaon analyzing power dependence on $\cos\theta_K^{\mathrm{CMS}}$.

$\cos\theta_K^{\mathrm{CMS}}$	$A_N(K)$	$\Delta A_N(K)$	$\cos\theta_K^{\mathrm{CMS}}$	$A_N(K)$	$\Delta A_N(K)$
-0.875	0.038	0.126	0.125	-0.019	0.058
-0.625	0.323	0.071	0.375	-0.044	0.061
-0.375	0.155	0.062	0.625	0.045	0.063
-0.125	0.188	0.058	0.875	-0.089	0.084

Table B.25.: Kaon analyzing power dependence on $\cos\theta_K^{\mathrm{CMS}}$ for $m_{p\Lambda} < m_p + m_\Lambda + 5\,\mathrm{MeV}/c^2$.

$m_{p\Lambda}\left[\frac{\mathrm{MeV}}{c^2}\right]$	$-\alpha_K$	$\Delta\alpha_K$	β_K	$\Delta\beta_K$
2056.46	0.104	0.027	0.097	0.023
2061.46	0.143	0.021	0.153	0.018
2066.46	0.126	0.021	0.082	0.018
2071.46	0.081	0.021	0.097	0.017
2076.46	0.139	0.021	0.087	0.017
2081.46	0.129	0.021	0.055	0.016
2086.46	0.130	0.021	0.040	0.016
2091.46	0.165	0.021	0.040	0.016
2096.46	0.136	0.021	0.042	0.016
2101.46	0.179	0.021	0.036	0.017
2106.46	0.156	0.021	0.043	0.016
2111.46	0.154	0.022	0.044	0.017
2116.46	0.127	0.022	-0.006	0.017
2121.46	0.161	0.022	-0.006	0.017
2126.46	0.071	0.022	0.010	0.017
2131.46	0.224	0.023	0.016	0.017
2136.46	0.169	0.024	0.020	0.018
2141.46	0.174	0.024	0.014	0.019
2146.46	0.126	0.026	0.008	0.020
2151.46	0.184	0.027	0.008	0.021
2156.46	0.206	0.029	-0.048	0.023
2161.46	0.121	0.032	0.036	0.025
2166.46	0.083	0.037	-0.014	0.030
2171.46	0.076	0.050	-0.038	0.043

Table B.26.: $-\alpha$ and β contribution to the kaon analyzing power dependent on the $p\Lambda$ invariant mass.

B.7. Data Table Modified $m_{p\Lambda}$ Distribution

$m_{p\Lambda}\left[\frac{\mathrm{MeV}}{c^2}\right]$	$\frac{\mathrm{d}\sigma}{\mathrm{d}m}\,\alpha_K$[a. U.]	Δ	$m_{p\Lambda}\left[\frac{\mathrm{MeV}}{c^2}\right]$	$\frac{\mathrm{d}\sigma}{\mathrm{d}m}\,\alpha_K$[a. U.]	Δ
2056.46	9.2	2.4	2116.46	11.9	2.1
2061.46	16.8	2.4	2121.46	14.7	2.1
2066.46	14.4	2.3	2126.46	6.7	2.1
2071.46	9.0	2.3	2131.46	20.1	2.0
2076.46	15.2	2.3	2136.46	13.9	1.9
2081.46	14.1	2.3	2141.46	13.2	1.9
2086.46	14.0	2.2	2146.46	9.1	1.8
2091.46	17.4	2.2	2151.46	11.6	1.8
2096.46	14.2	2.2	2156.46	11.8	1.7
2101.46	17.6	2.1	2161.46	5.6	1.5
2106.46	15.0	2.1	2166.46	3.1	1.4
2111.46	14.5	2.1	2171.46	1.9	1.2

Table B.27.: $p\Lambda$ invariant mass distribution multiplied with the contribution of the Legendre polynomial P_1^1 to the kaon analyzing power

C. Other Plots for the Effective Scattering Length Determination

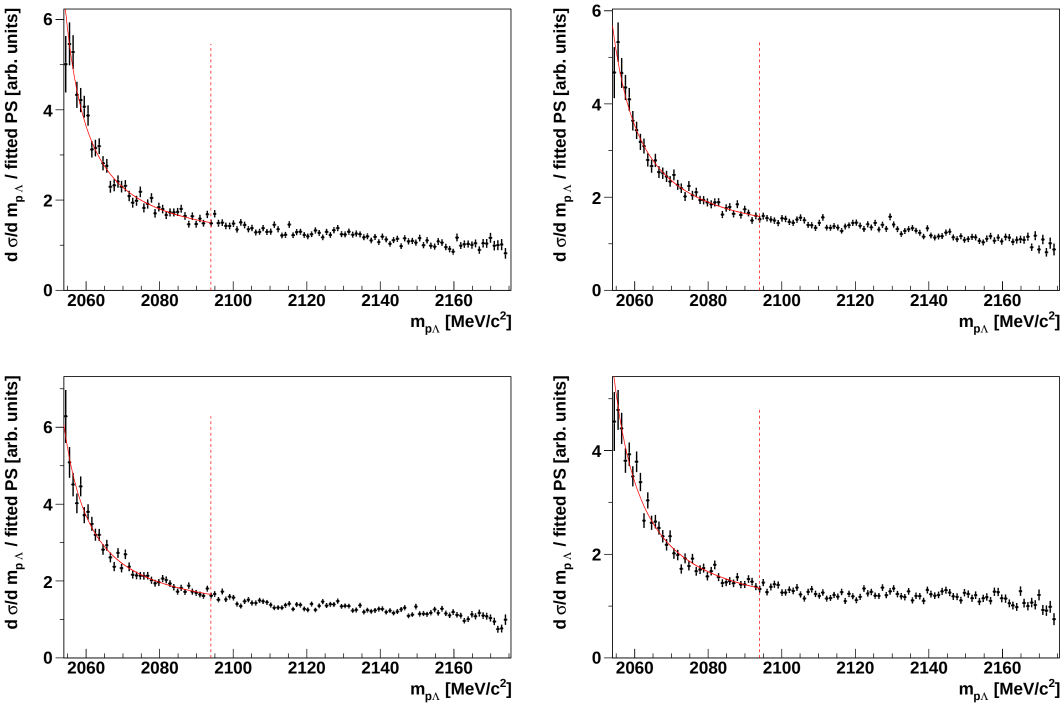

Figure C.1.: $m_{p\Lambda}$ invariant mass distributions from Figure 8.3 divided by the fitted phase space. The ranges of the helicity angle $\cos\theta_{pK}^{p\Lambda}$ in the plots are: $\cos\theta_{pK}^{p\Lambda} > 0.5$ (upper left), $0 < \cos\theta_{pK}^{p\Lambda} < 0.5$ (upper right), $-0.5 < \cos\theta_{pK}^{p\Lambda} < 0$ (lower left) and $\cos\theta_{pK}^{p\Lambda} < -0.5$ (lower right). The red line in each plot shows the final state fit divided by the phase space function. The vertical red dashed line marks the upper limit of the FSI fit.

Acronyms

A	Analyzing power for the pp elastic scattering
$A_N(K)$	Kaon Analyzing power
$A_N(\Lambda)$	Λ Analyzing power
$A_N(p)$	Proton Analyzing power
P_Λ	Λ Polarization
$\tilde{a}$	Effective $p\Lambda$ scattering length
a_t	Spin Triplet $p\Lambda$ scattering length
p_b	Beam Polarization
ADC	Analog to Digital Converter
ChEFT	Chiral Effective Field Theory
CMS	Center Of Mass System
COSY	COoler SYnchroton
COSY-TOF	COSY TOF Detector
DAQ	Data AQuisition
FSI	Final State Interaction
FWHM	Full Width Half Maximum
JULIC	JUeLIch Cyclotron
QCD	Quantum Chromo Dynamics
SQT	Silicon Quirl Telescope
STT	Straw Tube Tracker
TDC	Time to Digital Converter
TOF	Time Of Flight

VME	Versa Module European Bus

List of Figures

List of Tables

Bibliography

[Ale68] Alexander G., et al., *Study of $\Lambda - N$ System in Low-Energy $\Lambda - p$ Elastic Scattering*, Phys. Rev. **173**(1968), 1452.

[And79] Andersson B., et al., *A semiclassical model for the polarization on inclusively produced Λ^0-particles at high energies*, Phys. Lett. B**85**(1979), 417.

[Ani07a] Anisovich A.V., et al., *Nucleon-nucleon interaction amplitudes in the framework of spin-momentu operator expansion method*, arxiv:hep-ph/0703216.

[Ani07b] Anisovich A.V., et al., *Baryon resonances and polarization transfer in hyperon photoproduction*, Eur. Phys. J. A**34**(2007), 243-254.

[ATLAS12] ATLAS Collaboration, *Observation of a new particle in the search for the Standard Model Higgs boson with the ATLAS detector at the LHC*, Phys. Lett. B**716**(2012), 1-29.

[Bea12] Beane S.R., et al., *Hyperon-Nucleon Interactions from Quantum Chromodynamics and the Composition of Dense Nuclear Matter*, Phys. Rev. Lett. **109**(2012), 172001.

[Bea13a] Beane S.R., et al., *Light Nuclei and Hypernuclei from Quantum Chromodynamics in the Limit of SU(3) Flavor Symmetry*, Phys. Rev. D**87**(2013), 034506.

[Bea13b] Beane S.R., et al., *Nucleon-Nucleon Scattering Parameters in the Limit of SU(3) Flavor Symmetry*, Phys. Rev. C**88**(2013), 024003.

[Bes79] Besset D., et al., *A set of efficient estimators for polarization measurements*, Nucl. Instrum. Meth. **166**(1979), 515-520.

[Bla85] Blankleider B. and Afnan I.R., *Relationship between partial wave amplitudes and polarization observables in $pp \to d\pi^+$ and $\pi d \to \pi d$*, Phys. Rev. C**31**(1985), 1380.

[Bun76] Bunce G., et al., Λ^0 *Hyperon Polarisation in Inclusive Production by* 300 *GeV Protons on Beryllium*, Phys. Rev. Lett. **36**(1976), 1113.

[Byc00] Byckling. E. and Kajantie K., *Particle Kinematics*, John Wiley & Sons, London, 1973.

[Cas06] Castelijns R., tofStraw1.0 library, COSY-TOF Internal Documentation, Jülich 2006.

[CMS12] CMS Collaboration, *Observation of a new boson at a mass of* 125 *GeV with the CMS experiment at the LHC*, Phys. Lett. B**716**(2012), 30.

[C1196] COSY-11 Collaboration, Balewski J., et al., Λ-*Hyperon Production via the* $pp \rightarrow pK^+\Lambda$ *Reaction* 2 *MeV above Threshold*, Phys. Lett. B**388**(1996), 859.

[C1197] COSY-11 Collaboration, Balewski J., et al., *Threshold measurements at the internal experimental facility COSY-11*, Nucl. Phys. A**626**(1997), 85c-92c.

[C1198a] COSY-11 Collaboration, Balewski J., et al., *Total Cross Section of the Reaction* $pp \rightarrow pK^+\Lambda$ *Close to Threshold*, Phys. Lett. B**420**(1998), 211.

[C1198b] COSY-11 Collaboration, Balewski J., et al., *Low Energy* $p - \Lambda$ *Scattering Parameters from the* $pp \rightarrow pK^+\Lambda$ *Reaction*, Eur. Phys. J. A**2**(1998), 99-104.

[C1199] COSY-11 Collaboration, Severin S., et al., *Comparison of* Λ *and* Σ^0 *threshold production in proton-proton collisions*, Phys. Rev. Lett. **83**(1999), 682-685.

[C1104] COSY-11 Collaboration, Kowina P., et al., *Energy dependence of the* Λ/Σ^0 *production cross section ratio in p-p collisions*, Eur. Phys. J. A**22**(2004), 293-299.

[CTOF98a] COSY-TOF Collaboration, Bilger R., et al., *Strangeness production in reaction* $pp \rightarrow K^+\Lambda p$ *near threshold*, Phys. Lett. B**420**(1998), 217.

[CTOF98b] COSY-TOF Collaboration, Bilger R., et al., *Proton proton bremsstrahlung at* 797 *MeV/c*, Phys. Lett. B**429**(1998), 195.

[CTOF00] COSY-TOF Collaboration, Böhm A., et al., *The COSY-TOF barrel detector*, Nucl. Inst. Meth. A**443**(2000), 238-253.

[CTOF06a] COSY-TOF Collaboration, Abd El-Samad S., et al., *Hyperon Production in the channel* $pp \rightarrow K^+\Lambda p$ *near the reaction threshold*, Phys. Lett. B**632**(2006), 27-34.

[CTOF06b] COSY-TOF Collaboration, Abdel-Bary M., et al., *Study of spectator tagging in the reaction* $np \rightarrow pp\pi$ *with a deuteron beam*, Eur. Phys. J. A**29**(2006), 353-361.

[CTOF06c] COSY-TOF Collaboration, tof++ Software, COSY-TOF Internal Note, Jülich 2006.

[CTOF07] COSY-TOF Collaboration, *Strangeness Physics at COSY-TOF*, PAC 34, FZ Jülich, 2007, donald.cc.kfa-juelich.de/wochenplan/documents/PAC34/TOF_perspectives_final.pdf

[CTOF08] COSY-TOF Collaboration, *Commissioning of the COSY-TOF Straw Tracker*, IKP Annual Report Highlights, FZ Jülich, 2008.

[CTOF09] COSY-TOF Collaboration, *First measurements with the upgraded COSY-TOF detector*, IKP Annual Report, FZ Jülich, 2009.

[CTOF10a] COSY-TOF Collaboration, Abdel-Bary M., et al., *Production of* Λ *and* Σ^0 *hyperons in proton-proton collisions*, Eur. Phys. J. A**46**(2010), 27-44.

[CTOF10b] COSY-TOF Collaboration, Abd El-Samad S., et al., *Influence of* N^**-resonances on hyperon production in the channel* $pp \to K^+\Lambda p$ *at* 2.95, 3.20 *and* 3.30 *GeV/c beam momentum*, Phys. Lett. B**688**(2010), 142-149.

[CTOF13a] COSY-TOF Collaboration, Abd El-Samad S., et al., *On the* ΣN *cusp in the* $pp \to pK^+\Lambda$ *reaction*, Eur. Phys. J. A**49**(2013), 41.

[CTOF13b] COSY-TOF Collaboration, Roeder M., et al., *Final-State Interactions in the Process* $\vec{p}p \to pK^+\Lambda$, Eur. Phys. J. A**49**(2013), 157.

[Cza94] Czarnecki T., *Bau und Test eines Szintillationsfaserhodoskops für ein Hyperonexperiment an COSY*, Diploma Thesis, University of Erlangen, 1994.

[Dah94] Dahmen M., et al., *A Three Layer Circular Scintillator Hodoscope*, Nucl. Inst. Meth. A**348**(1994), 97.

[Dal53] Dalitz R.H., *On the analysis of* τ*-meson data and the nature of the* τ*-meson*, Phil. Mag. Series 7 Vol.**44**(1953), 1068.

[Dzh12] Dzhygadlo R., *Differential Cross Section Distributions and Polarization Observables in the Reaction* $\vec{p}p \to pK^0\Sigma^+$ *at* $p_{\vec{p}} = 2.95$ *GeV/c*, PhD Thesis, University of Bonn, 2012.

[DIS99a] DISTO Collaboration, Balestra F., et al., *DISTO: a large acceptance multiparticle spectrometer for* $1-3$ *GeV proton beams*, Nucl. Inst. Meth. A**426**(1999), 385.

[DIS01b] DISTO Collaboration, Balestra F., et al., *DISTO: Spin Observables for* Λ *Hyperons in pp scattering*, Nucl. Phys. B(Proc. Suppl.) **93**(2001), 58.

[Dud72] Duda R. O. and Hart P. E., *Use of the Hough transformation to detect lines and curves in picture*, Communiations of the ACL Vol 15, N.**1**(1972), 11-15.

[Epe09] Epelbaum E., et al., *Modern theory of nuclear forces*, Rev. Mod Phys. **81**(2009), 1773.

[Eyr10] Eyrich W., University of Erlangen, private communication 2010.

[Fae97] Fäldt G. and Wilkin C., *Comparision of the Near-threshold Production of η- and K-Mesons in Proton-Proton Collisions*, Z. Phys. A**357**(1997), 241-243.

[FB] FASTBUS modular high-speed data acquisition and control system, IEEE standard 960-1986.

[Fel96] Felix J., et al., *Study of Λ^0 polarization in $pp \to p\Lambda^0 K^+\pi^+\pi^-\pi^+\pi^-$ at* 27.5 *GeV/c*, Phys. Rev. Lett. **76**(1996), 22-25.

[Fel99] Felix J., et al., *Study of Λ^0 polarization in four different exclusive pp reactions at* 27.5 *GeV/c*, Phys. Rev. Lett. **82**(1999), 5213-5216.

[Fer60] Ferrari E., *Asssociated Production in Proton-Proton-Collisions*, Phys. Rev. **120**(1960), 988.

[Feu98] Feuster T. and Mosel U., *Unitary model for meson-nucleon scattering*, Phys. Rev. C**58**(1998), 457.

[Fic62] Fickinger W.J., et al., *p-p Interactions at* 2 *BeV. I. Single-Pion Production*, Phys. Rev. **125**(1962), 2085.

[Fla84] Flamino V., et al., *Compilation of Cross Sections I*, CERN-HERA 84-01, 1984.

[Fri02] Fritsch M., *Assoziierte Strangenessproduktion in den Reaktionen $pp \to K^+\Lambda p$ und $pp \to K^+\Sigma^0 p$ am COSY-Flugzeitspektrometer*, PhD Thesis, University of Erlangen, 2002.

[Fuj07] Fujiwara Y., et al., *Baryon-baryon interactions in the SU(6) quark model and their applications to light nuclear systems*, Prog. Part. Nucl. Phys. **58**(2007), 439-520.

[Gas00] Gasparian A., et al., *The reactions $pp \to p\Lambda K^+$ and $pp \to p\Sigma^0 K^+$ near their thresholds*, Phys. Lett. B**480**(2000), 273.

[Gas01] Gasparian A., et al., *Near threshold Λ and Σ production in pp collisions*, Nucl. Phys. A**684**(2001), 397c.

[Gas04] Gasparian A., et al., *How to extract the ΛN scattering length from production reactions*, Phys. Rev. C**69**(2004), 034006.

[Gas05] Gasparian A., et al., *Extraction of scattering lengths from final-state interactions*, Phys. Rev. C**72**(2005), 034006.

[GEANT] GEANT, GEANT 3.2.1 detector description and simulation tool, wwwasdoc.web.cern.ch/wwwasdoc/pdfdir/geant.pdf

[Gil64] Gillespie J., *Final-state Interactions*, Holden-Day, Amsterdam, 1964.

[Gol64] Goldberger M.L., Watson K.M., *Collision Theory*, John Wiley, New York, 1964.

[Got64] Gottfried K. and Jackson J.D., *On the connection between production mechanism and decay of resonances at high energy*, Nuovo Cimento **33**(1964), 309.

[GSL] GNU Scientific Library GSL, Reference Manual, 2013, www.gnu.org/software/gsl/manual/html_node/

[Hai05] Haidenbauer J., et al., *Jülich hyperon-nucleon model revisited*, Phys. Rev. C**72**(2005), 044005.

[Hai13] Haidenbauer J., et al., *Hyperon-nucleon interaction at next-to-leading order in chiral effective field theory*, Nucl. Phys. A**915**(2013), 24-58.

[Han04] Hanhart C., *Meson production in nucleon-nucleon collisions close to the threshold*, Phys. Rept. **397**(2004), 155.

[Hau13] Hauenstein F., *Study of the beam polarization with COSY-TOF*, IKP Annual Report, FZ Jülich, 2013, http://www.fz-juelich.de/ikp/EN/Aktuelles/ar2013.html

[Hau14] Hauenstein F., et al., *How to Extract the Spin Transfer Coefficient D_{NN} from Data Measured with a Full Acceptance Detector*, to be published, 2014.

[Her97] Herrmann P., *Messung des differentiellen Wirkungsquerschnitts der Reaktion $pp \to pp\gamma$ mit dem COSY-TOF-Spektrometer*, PhD Thesis, Ruhr-University of Bochum, 1997.

[Hes01] Hesselbarth D., *Experimentelle Untersuchung zur Hyperonen-Produktion im Proton-Proton-Stoß*, PhD Thesis, University Bonn, 2001.

[Hin04] Hinterberger F., Sibirtsev A., *Analysis of the Λp Final State Interaction in the Reaction $p + p \to K^+(\Lambda p)$*, Eur. Phys. J. A**21**(2004), 313.

[HIR10] HIRES Collaboration, Budzanowski A., et al., *High resolution study of the Λp final state interaction in the reaction $p + p \to K^+(\Lambda p)$*, Phys. Lett. B**687**(2010), 31-35.

[Hou62] Hough P.V.C., *Method and means of recognizing complex patterns*, U.S. Patent 3,069,654, 1962.

[Jae94] Jaeckle V., et al., *A Liquid Hydrogen/Deuterium Target With Very Thin Windows*, Nucl. Inst. Meth. **A349**(1994), 15.

[Jos47] Jost R., *Über die falschen Nullstellen der Eigenwerte der S-Matrix*, Helv. Phys. Acta **20**(1947), 356.

[Jos52] Jost R., Kohn W., *Construction of a Potential from a Phase Shift*, Phys. Rev. **87**(1952), 977

[Jow12] Jowzaee S., *Calibration of the COSY-TOF Straw Tube Tracker*, IKP Annual Report, FZ Jülich, 2012, http://www.fz-juelich.de/ikp/EN/Aktuelles/ar2012.html

[Jow13a] Jowzaee S., *Calibration of a modular Straw Tube Tracker for the COSY-TOF experiment*, Acta Phys. Polo. B**6**(2013) .

[Jow13b] Jowzaee S., *Improvement in position and spatial resolution determination of the COSY-TOF Straw Tube Tracker*, IKP Annual Report, FZ Jülich, 2013, http://www.fz-juelich.de/ikp/EN/Aktuelles/ar2013.html

[Jow14] Jowzaee S., *Self-supporting straw tube detectors for the COSY-TOF and PANDA experiments*, PhD Thesis in preparation, Jagiellonian University Crakow, 2014.

[Jow14b] Jowzaee S., private communication, 2014.

[Jur73] Jurič M., et al., *A new determination of the binding-energy values of the light hypernuclei ($A \leq 15$)*, Nucl. Phys. B**52**(1973), 1–30.

[Kad71] Kadyk J.A., et al., *Λp interactions in momentum range 300 to 1500 MeV/c*, Nucl. Phys. B**27**(1971), 13.

[Kil13] Kilian K., private communication, 2013.

[Kin02] Kingsberry P., *Depolarisation and Spin Transfer in $\bar{p}p \rightarrow \bar{\Lambda}\Lambda$ with Polarised Target at 1.525 GeV/c*, PhD Thesis, University of New Mexico, 2002.

[Kir94] Kirsch M., *Entwicklung und Aufbau eines Detektorsystems zur Messung der assoziierten Strangenessproduktion im Proton-Proton-Stoß*, PhD Thesis, University of Erlangen, 1994.

[Kle96] Kleefeld F., et al., *Proton induced K^+ production and the $s\bar{s}$ content of the proton*, Act. Phys. Pol. B**27**(1996), 2867.

[Kra06] Krapp M., *Entwicklung von rechnergestützten graphischen Analysemethoden bei der assoziierten Strangeness-Produktion am Flugzeitspektrometer COSY-TOF*, Diploma Thesis, University of Erlangen, 2006.

[Lag91] Laget J.M., *Strangeness Production in nucleon-nucleon collisions*, Phys. Lett. B**259**(1991), 24.

[Lor13] Lorentz B., private communication, 2013.

[Mac87] Machleidt R., et al., *The Bonn Meson-Exchange Model for the Nucleon-Nucleon Interaction*, Phys. Rep. **149**(1987), 1.

[Mac89] Machleidt R., *The Meson Theory of Nuclear Forces and Nuclear Structure*, Adv. Nucl. Phys. **19**(1989), 189.

[Mac11] Machleidt R. and Entem D.R., *Chiral effective field theory and nuclear forces*, Phys. Rept. **503**(2011), 1-75.

[Mag99] Maggiora M., *First measurements of spin observables for Λ produced in exclusive channels*, PhD Thesis, University of Torino, Italy, 1999.

[Mah09] Mahan G.D., *Quantum Mechanics in a Nutshell*, Princeton University Press, Princeton, 2009.

[Mai97] Maier R., *Cooler Synchrotron COSY - performance and perspectives*, Nucl. Inst. Meth. A**390**(1997), 1.

[Mel65] Melissinos A.C., et al., *Observation of the low-energy Λp interaction*, Phys. Rev. Lett. **14**(1965), 604.

[Mes67] Messiah A., *Quantum Mechanics Volume 1*, North-Holland Publishing Company, Amsterdam, 1967.

[Met94] Metzger A., *Monte-Carlo-Simulation eines Experiments zur Hyperonproduktion am COSY-Flugzeit-Spektrometer*, Diploma Thesis, University of Erlangen, 1994.

[Met98] Metzger A., *Untersuchung der schwellennahen assoziierten Strangenessproduktion in der Reaktion $pp \rightarrow pK^+\Lambda$ am COSY-Flugzeitspektrometer*, PhD Thesis, University of Erlangen, 1998.

[Mig55] Migdal A.B., *The theory of nuclear reactions with production of slow particles*, Sov. Phys. JETP **1**(1955), 2-6.

[MINUIT] James F. and Roos M., *Minuit: A System for Function Mimimization and Analysis of the Parameter Errors and Correlations*, Comput. Phys. Commun. **10**(1975), 343-367.

[Nak93] Nake C., *Optimierung eines Flüssig-Wasserstoff/Deuterium-Targets mit äusserst dünnen Folienfenstern*, Diploma Thesis, University of Bonn, 1993.

[Ohl73] Ohlsen G., *Techniques for measurement of spin-1/2 and spin-1 polarization analyzing tensors*, Nucl. Inst. Meth **109**(1973), 41-59.

[NE90] Plastic Scintillators, NE Technology Limited, Edinburgh.

[Par92] Parsch A., *Monte-Carlo-Simulation eines Experiments zur Hyperonproduktion an COSY*, Diploma Thesis, University of Erlangen, 1992.

[Pau96] Paul N., COSY Zeichnung, FZ Jülich, 1996.

[PDG2012] Particle Data Group, Beringer J., et al., Phys. Rev. D **86**(2012), 010001.

[Phi90] Photomultipliers Data Handbook, Philips Components, 1990.

[Piz07] Pizzolotto C., *Measurement of Λ polarization observables at the COSY-TOF spectrometer*, PhD Thesis, University of Erlangen, 2007.

[Pol06] Polinder H., et al., *Hyperon–nucleon interactions — a chiral effective field theory approach*, Nucl. Phys. A**779**(2006), 244.

[Pra14] Prasuhn D., private communication, 2014.

[Reu94] Reuber A., et al., *Meson-exchange hyperon-nucleon interactions in free scattering and nuclear matter*, Nucl. Phys. A**570**(1994), 543.

[Rij99] Rijken T. A., et al., *Soft-core hyperon-nucleon potentials*, Phys. Rev. C**59**(1999), 21.

[Rod08] Roderburg E., *Including the Straw Detector into the software analysis package of the COSY-TOF detector*, COSY-TOF reports for the IKP annual report, Jülich 2008.

[Rod14] Roderburg E., private communication, 2014.

[Roe11] Röder M., *Final State Interaction and Polarization Variables in the Reaction $\vec{p}p \to pK^+\Lambda$ Close to Threshold*, PhD Thesis, Ruhr-University Bochum, 2011.

[Roe12] Röder M., private communication, 2012.

[ROOT] ROOT, Data-Analyse-Framework, http://root.cern.ch/drupal/

[Ros54] Rosenfeld A.H., *Production of Pions in Nucleon-Nucleon Collisions at Cyclotron Energies*, Phys. Rev. **96**(1954), 139.

[SAID] Online SAID data base: http://gwdac.phys.gwu.edu, SP07 solution: Arndt R.A., et al., *Updated Analysis of NN elastic scattering to* 3 *GeV*, Phys. Rev. C**76**(2007), 025209.

[Sar05] Sarantsev A.V., et al., *Decays of baryon resonances into ΛK^+, $\Sigma^0 K^+$ and $\Sigma^+ K^0$*, Eur. Phys. J. A**25**(2005), 441-453.

[Sch97] Schönmeier P., *Erweiterung der Datenerfassungssoftware für das COSY-TOF-Spektrometer*, Diploma Thesis, TU Dresden, 1997.

[Schr98] Schröder W., *Entwicklung und Bau eines Vetodetektorsystems für das COSY-TOF-Experiment am FZ Jülich*, Diploma Thesis, University of Erlangen, 1998.

[Schr03] Schröder W., *Untersuchung der assoziierten Strangeness-Produktion in den Reaktionen* $pp \to pK^+\Lambda$ *und* $pp \to pK^+\Sigma^0$ *am Flugzeitspektrometer COSY-TOF*, PhD Thesis, University of Erlangen, 2003.

[Sec68] Sechi-Zorn B., et al., *Low energy* Λ*-Proton Scattering*, Phys. Rev.**175**(1968), 1735.

[Sew99] Sewerin S., *Schwellennahe Hyperonproduktion in den Reaktionskanälen* $pp \to pK^+\Lambda$ *und* $pp \to pK^+\Sigma^0$ *am Experiment COSY-11*, PhD Thesis, University of Bonn, 1999.

[Shy99] Shyam R., $pp \to pK^+\Lambda$ *reaction in an effective Lagrangian model*, Phys. Rev. C**60**(1999), 055213.

[Shy01] Shyam R., et al., *Role of* $N^*(1650)$ *in the near threshold* $pp \to p\Lambda K^+$ *and* $pp \to p\Sigma^0 K^+$ *reactions*, Phys. Rev. C**63**(2001), 022202(R).

[Sib95] Sibirtsev A., *Internal nuclear momentum and subthreshold kaon production*, Phys. Lett. B**359**(1995), 29.

[Sib98a] Sibirtsev A., et al., *A clue to the mechanism of* ΛK^+ *production in pp-reactions*, Phys. Lett. B**421**(1998), 59.

[Sib98b] Sibirtsev A. and Cassing W., *Final State Interactions in the Near-Threshold Production of Kaons from Proton-Proton Collisions*, arxiv:nucl-th/9802025.

[Sib98c] Sibirtsev A. and Cassing W., *Strangeness production in proton-proton collisions*, arxiv:nucl-th/9802019.

[Sib98d] Sibirtsev A. and Cassing W., *Final State Interactions in Near Threshold Meson Production from pp Collisions*, European Phys. Journal A**2**, (1998), 333.

[Sib99] Sibirtsev A., et al., *The Role of* $P_{11}(1710)$ *in the* $NN \to N\Sigma K$ *reaction*, Nucl. Phys A**646**(1999), 427.

[Sib00] Sibirtsev A., et al., *On the* Λ *to* Σ^0 *ratio from proton-proton collisions*, arxiv:nucl-th/0004022.

[Sib02] Sibirtsev A., *Simple model for Dalitz plot analysis*, COSY-TOF internal note, FZ Jülich 2002.

[Sib05] Sibirtsev A., et al., *Resonances and final state interactions in the reaction* $pp \to pK^+\Lambda$, arxiv:nucl-th/0512059.

[Sie94] Siebert R., et al., *High-resolution study of hyperon-nucleon interactions by associated strangeness production in pp collisions*, Nucl. Phys. A**567**(1994), 819.

[Sof99] Soffer J., *Is the riddle of the hyperon polarization solved?*, arxiv:hep-ph/9911373.

[Tan69] Tan. T., *Study of Hyperon-Nucleon interaction in the reaction* $K^-d \to \pi^-p\Lambda$ *at rest*, Phys. Rev. Lett. **23**(1969), 395.

[Tsu97] Tsushima K., et al., *Resonance model study of strangeness production in pp collision*, Phys. Lett. B**390**(1997), 29.

[Tsu99] Tsushima K., et al., *Resonance model study of kaon production in baryon baryon reactions for heavy ion collisions*, Phys. Rev. C**59**(1999), p369, Erratum: Phys. Rev. C**61**(2000), 029903(E).

[Uca06] Ucar A., *Developments for the TOF Straw Tracker*, PhD Thesis, University of Bonn, 2006.

[Val07] Valdau Y.,et al., *The* $pp \to K^+n\Sigma^+$ *reaction near threshold*, Phys. Lett. B**652**(2007), 245.

[VME] IEEE Standard for a Versatile Backplane Bus: VMEbus, IEEE Standard 1014-1987.

[Voigt09] Voigtländer P., *Kalibration des COSY-TOF Straw-Tube-Tracker*, Diploma Thesis, Ruhr-University of Bochum, 2009.

[Wat52] Watson. K.M, *The Effect of Final State Interactions on Reaction Cross Sections*, Phys. Rev. **88**(1952), 1163.

[Wei90] Weinberg S., *Nuclear forces from chiral Langrangians*, Phys. Lett. B**251**(1990), 288-292.

[Wei91] Weinberg S., *Effective chiral Lagrangians for nucleon-pion interactions and nuclear forces*, Nucl. Phys. B**363**(1991), 3.

[Wiki13] Wikipedia, Standard Model, http://en.wikipedia.org/wiki/Standard_model, 2013, Image Credit: Miss MJ.

Acknowledgement

Here, I would like to thank all the people, which made this thesis possible. Especially I would like to thank

my doctor father Wolfgang Eyrich, who give me the possibility to work quite freely on the thesis topic and to stay for my thesis mainly at the research center Juelich. This is not usual and thats why I could finish the thesis in about three years. Furthermore, I would like to thank him for the detailed discussions and corrections when writing the thesis.

Eduard Roderburg for his supervision at the research center and his answers for the over one million questions, which I asked him.

Jim Ritman for the possibility to stay at the research center Juelich for the thesis, the discussions of the results and reading of my thesis.

Matthias Roeder for his explanations of every part of the software and the calibration procedure of the straws.

Kurt Kilian for his enthusiasm about the COSY-TOF experiment and the detailed discussions and explanations of kinematics and beam analysis.

the other former and actual COSY-TOF colleagues in Juelich, Ekaterina Borodina, Roman Dzhygadlo, Werner Gast, Albrecht Gillitzer, Dieter Gzonka, Sedigheh Jowzaee, Pawel Klaja, Norbert Paul, Peter Wintz, Peter Wuestner and Juergen Uehlemann for the fruitful analysis meetings and discussions, their support if I need something and their answers to questions about any part of COSY-TOF.

Johann Haidenbauer and Christoph Hanhardt from the theory group to be available anytime to answer my questions concerning the spin triplet extraction and polarization observables.

Hartmut Machner for his explanations of final state interactions and the useful discussions about the various approaches.

Guenther Sterzenbach for helping me anytime if I had some problems with my computer.

Erhard Steffens to be my second referee and a quite fast preparation of the report.

the other former and actual colleagues in Juelich, Andre, Andreas, Dan, Daniel, Dariusch, Elisabetta, Farha, Joanna, Lu, Ludo, Maria, Marius, Rene, Simone, Susan, Thomas, Tobias and Xuagen for the nice atmosphere in the institut and during lunch and the various non physics related celebrations and meetings, especially in the pub.

the COSY crew for the high polarized and high intensity beam during my beam time with very few shutdowns.

my colleagues at the university, Adrian, Albert, Alex, Christoph, Christopher, Fred, Liwen and Martin for the usuful discussions and support when I was at the university.

all other people, which I forget to mention explicitly.

and finally my family for their love and support and tolerating all of my habits.